PMFSEL REPORT NO. 87-9
MAY 1987

ULTIMATE STRENGTH OF DOUBLE-TEE TUBULAR JOINTS : INTERACTION EFFECTS

By

Kurt D. Swensson

Joseph A. Yura

A C K N O W L E D G E M E N T S

The technical advisory committee consisting of K. Chang, C. Caracostis, P. Durning, M. Dwyer, J. Hansford, T. M. Hsu, David F. Grimm, D. K. Y. Kan, J. Saunders, J. Teymourian, W.J. Wang, J. P. Wilbourn, W. Yu, and N. Zettlemoyer, representing the project sponsors, was active and helpful in guiding this research.

The tests were conducted at the Phil M. Ferguson Structural Engineering Laboratory, Department of Civil Engineering, The University of Texas at Austin. The help of the laboratory staff - Blake Stassney, Pat Ball, Jean Gehrke, Sharon Cunningham, and Gorham Hinckley - is greatly appreciated. A special thanks to Laurie Golding for getting what was needed when it was needed. The help of three research assistants - Jens Dossing, David Inlow, and Troy Madeley - who worked overtime to finish the experimentation on a tight schedule, is greatly appreciated.

The supervisory committee consisting of Dr. Eric B. Becker, Dr. Karl H. Frank, Dr. James O. Jirsa, Dr. John L. Tassoulas and Chairman Dr. Joseph A. Yura was active in the project, and their assistance and advise is appreciated. A special thanks to Dr. Yura for his day-to-day supervision and

help as proof reader and editor of this dissertation, which was essential in the completion of this project. Thanks are also extended to Dr. Richard E. Klingner and Dr. Eric B. Becker for their assistance in the use of the ABAQUS finite element program. Mr. Mark Wickham provided invaluable help in the use of a personal computer which greatly simplified the manipulation of the data files used in the finite element analysis.

ULTIMATE STRENGTH OF DOUBLE-TEE TUBULAR JOINTS:

INTERACTION EFFECTS

Publication No. _____

Kurt Dickenson Swensson, B.E., M.S., Ph.D.

The University of Texas at Austin, 1986

Supervising Professor: Dr. Joseph A. Yura

Twenty-seven double-tee (DT) tubular joints were tested under branch axial compression (P), in-plane bending (IPB), and out-of-plane bending (OPB), and various combinations of these branch loads. These test results along with test results published by Hoadley [14] were used to study the effect of the β ratio (O.D. of branch to O.D. of chord) on the interaction of branch loads in DT tubular joints. It was found that β did have an effect on the joints' interaction behavior and the following equation was developed as a reasonable lower bound to the data:

$$P/P_U + (M/M_U)^Y_{OPB} + (M/M_U)^Z_{IPB} = 1.0$$

$$Y = 2.35 - 1.35(\beta)^{0.63}$$

$$Z = 3.44(\beta) + 0.01(\beta)^{-5.60}$$

where P_U = ultimate axial strength of joint

M_U = ultimate bending strength of joint

Comparison of this equation, an interaction equation proposed by Hoadley, and the arcsine interaction equation which is recommended for design in the 15th edition of API RP 2A, using a data base of 65 T and DT interaction tests, showed that the proposed equation was the most accurate of the three equations. Hoadley's equation provided a lower bound to the data when P_U and M_U were based on the experimental results. When P_U and M_U were based on the values predicted using the ultimate strength equations given in the 15th edition of the API RP 2A, the proposed equation provided the most accurate strength predictions, however the accuracy of all three equations was very similar. Further comparison showed that there was very little difference between the results of the three interaction equations in terms of the amount of material required for a particular joint and load, therefore Hoadley's equation is recommended for design based on its simplicity. During the course of the comparison, it was found that a greater increase in the reliability of interaction design can be gained by increasing the accuracy of the ultimate strength equations than by increasing the accuracy of the interaction equations.

Investigation of the experimental scatter present in replicate branch axial and OPB tests on β=1.0 joints indicated that the distance between the weld toes at the saddle points, or gap, has a significant effect on the behavior of β=1.0 joints. Comparison of the gap size and the compressive capacity of the joint showed that the compressive capacity of the joint can be predicted when the gap is treated as a column. This conclusion was supported by a finite element analysis. Based on this analysis and because measurements showed a significant variation in the gap sizes on nominally identical joints, it is recommended that the variation in the gap be accounted for in the factor of safety applied to a mean design equation.

Due to the paucity of experimental data a simplified finite element model was developed to analyze the ultimate strength behavior of tubular joints to provide additional insight into joint behavior. Comparison of the results of the finite element analysis and the experimental data showed that the model is both accurate and economical. The finite element model was first used to study the gap effect on the strength of joints with a β ratio close to unity as discussed earlier. Next, the model was used to predict the IPB strength of DT tubular joints and the results matched the experimental ultimate strengths well. In

addition, the data showed that the IPB strength of DT tubular joints is predicted accurately by Billington's equation for IPB strength adjusted for DT joints by Yura. The finite element model was used to develop AI interaction data for a $\beta = 0.67$ DT joint. the analytical interaction data matched the experimental data reasonably well, indicating that the finite element method can be used in further interaction studies. The developed finite element model proved to be both economical and widely applicable, and shows promise as a tool for the analysis of the ultimate strength behavior of tubular joints.

TABLE OF CONTENTS

T A B L E O F C O N T E N T S (continued)

T A B L E O F C O N T E N T S (continued)

T A B L E O F C O N T E N T S (continued)

T A B L E O F C O N T E N T S (continued)

CHAPTER 1

INTRODUCTION

1.1 History

As a structural element, the tubular cross section possesses many attractive properties including a high bending strength to weight ratio. The circular cross section increases the member's stability under compression and makes it very strong under torsional bending loads. The curved shape minimizes wind or wave forces transferred to the structure which makes the section ideal for structures exposed to the elements. In addition, circular sections can be combined to form aesthetically pleasing structures which is becoming more important in modern structural design.

The use of tubular steel members in major structural applications began in Great Britain in the 1800's [10]. At that point in time, tubular sections were mainly used in bridges. In these early structures, the tubular section was created by riveting together sections of curved steel plate. Late in that same century, rudimentary methods of welding were used to create circular hollow sections. The development of the continuous welding process by Fretz-Moon in 1930 greatly increased the importance of the tubular sections by simplifying fabrication [35]. In the 1940's the offshore oil industry took advantage of

the properties of tubular members and the first offshore drilling platforms were erected in the Gulf of Mexico [10]. To this date thousands of tubular structures have been built for offshore oil drilling [24] .

One problem with the use of tubular members in structures occurs at the connections. The circular shapes create a complicated geometry at the intersections of members which increases fabrication costs. However, in the 1960's, automated fabrication techniques were applied to tubular connections and today tubular structures can be fabricated with relative ease. However, as with many other structural systems, the industry has developed construction and fabrication techniques faster than the knowledge of behavior has been developed and transmitted to the designer.

When the first offshore structures were erected in the 1940's the designers had little more than an educated guess to use as a basis for design. In the 1960's pilot research on simple joints under simple loadings began and this research continued into the 1970's and a rather substantial database was developed. From this database, empirical formulae were developed to predict the ultimate strength of tubular connections, but for only the simplest of conditions. So far this decade, experimental investigation on more complicated geometries and loadings has begun and much of the old data has been critically analyzed and

organized. Today, ultimate strength design is still almost totally empirical, and the forms of recommended strength equations vary greatly from code to code. In addition, the analysis techniques available for predicting ultimate strength for anything but the simplest cases are either inadequate or too expensive for general use.

1.2 General Information

Tubular joints consist of one member which runs uninterrupted through the joint, known as the chord, and one or more members which are welded to the chord, known as branches or braces. Two typical joints are shown in Fig. 1.1. Two important locations on a joint are the crown and saddle positions which are shown in Fig. 1.1. There are four basic categories of tubular joints:

1. Simple welded joints
2. Complex welded joints
3. Cast steel joints
4. Composite joints

A simple welded joint must consist of two or more tubular members in a single plane. A simple joint cannot have overlaps in the branch members or contain gussets, diaphragms, stiffeners or grout. Examples of simple welded joints are shown in Fig. 1.1. A complex welded joint may be multiplanar, and may have overlapping

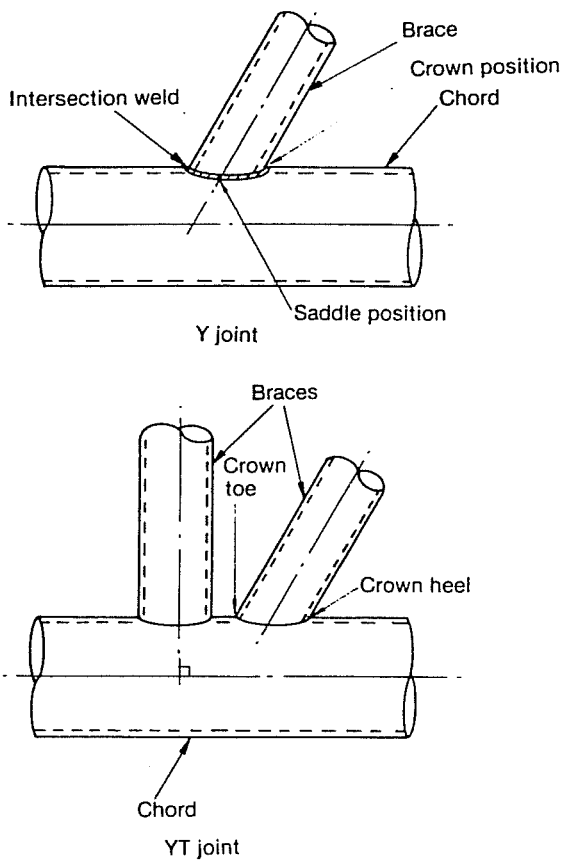

Fig.1.1 Typical Tubular Joint Geometries

brace members, stiffeners, gussets, or diaphragms. Examples of complex welded joints are shown in Fig. 1.2. Cast steel joints are tubular joints formed by a casting process. Composite joints are tubular joints in which the chord member is either fully filled with grout, serves as a sleeve for a pile or contains a grouted annulus. This type of joint is shown in Fig. 1.3.

This discussion will deal only with simple welded tubular joints. Within the category of simple tubular joints, there are several different joint configurations (T, DT, Y, DY, K, DK, YT, X, DYT YK, and DKDT) which are shown in Fig. 1.4.

1.2.1 Basic Dimensions and Parameters

The basic dimensions used to describe a simple tubular joint are shown in Fig. 1.5. These dimensions include:

D - Chord outside diameter

d - Branch outside diameter

T - Chord wall thickness

t - Branch wall thickness

θ - Included angle between branch and chord

g - Gap between brace toes for K and KT joints

L - Chord length

Several nondimensional parameters based on the above dimensions have been developed for use in design equations and for comparison of experimental data. These parameters include the

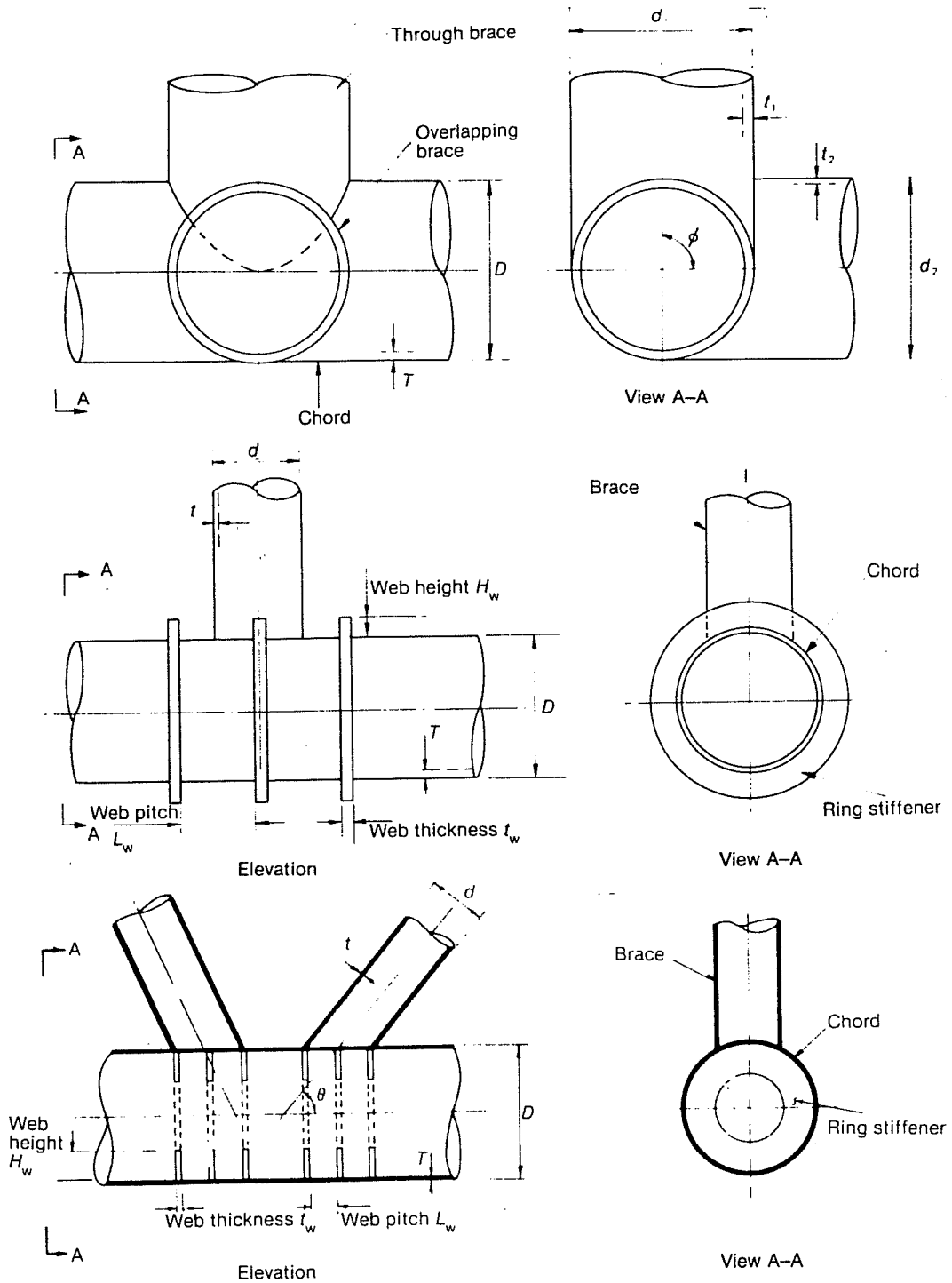

Fig. 1.2 Example of Complex Welded Tubular Joint

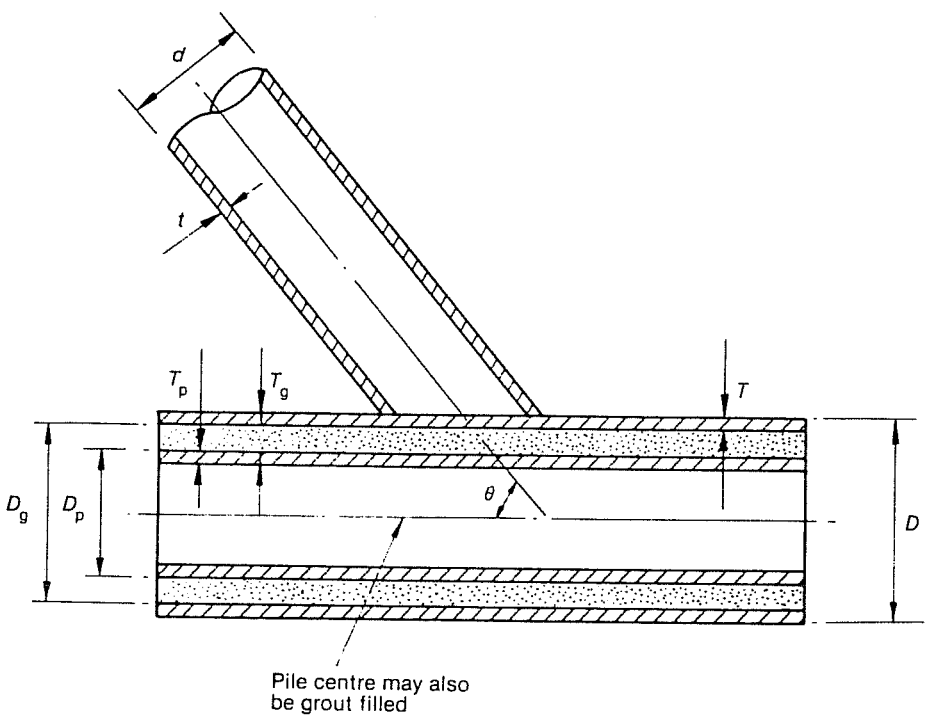

Fig. 1.3 Example of Composite Tubular Joint

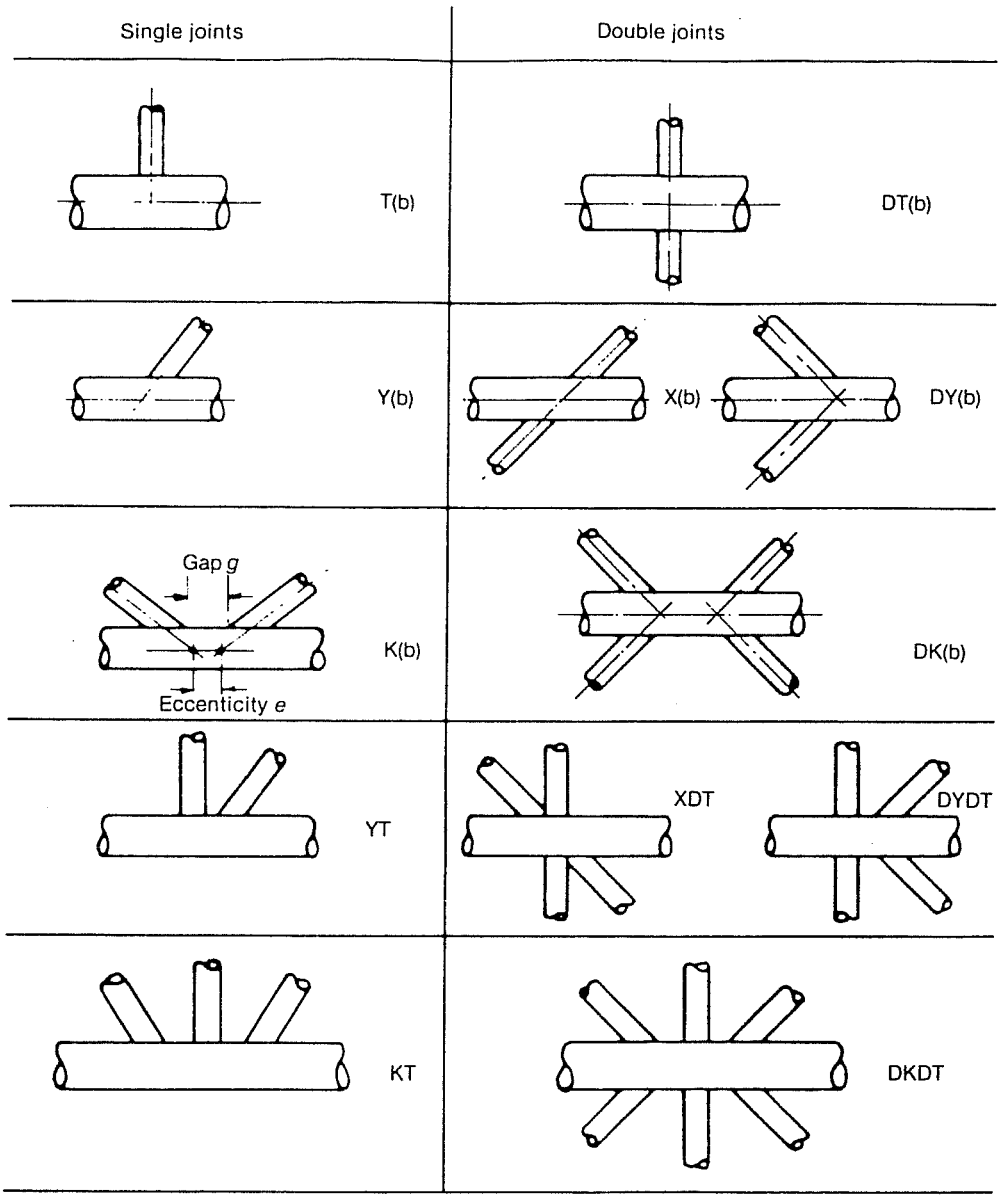

Fig. 1.4 Definition of Tubular Joint Configurations

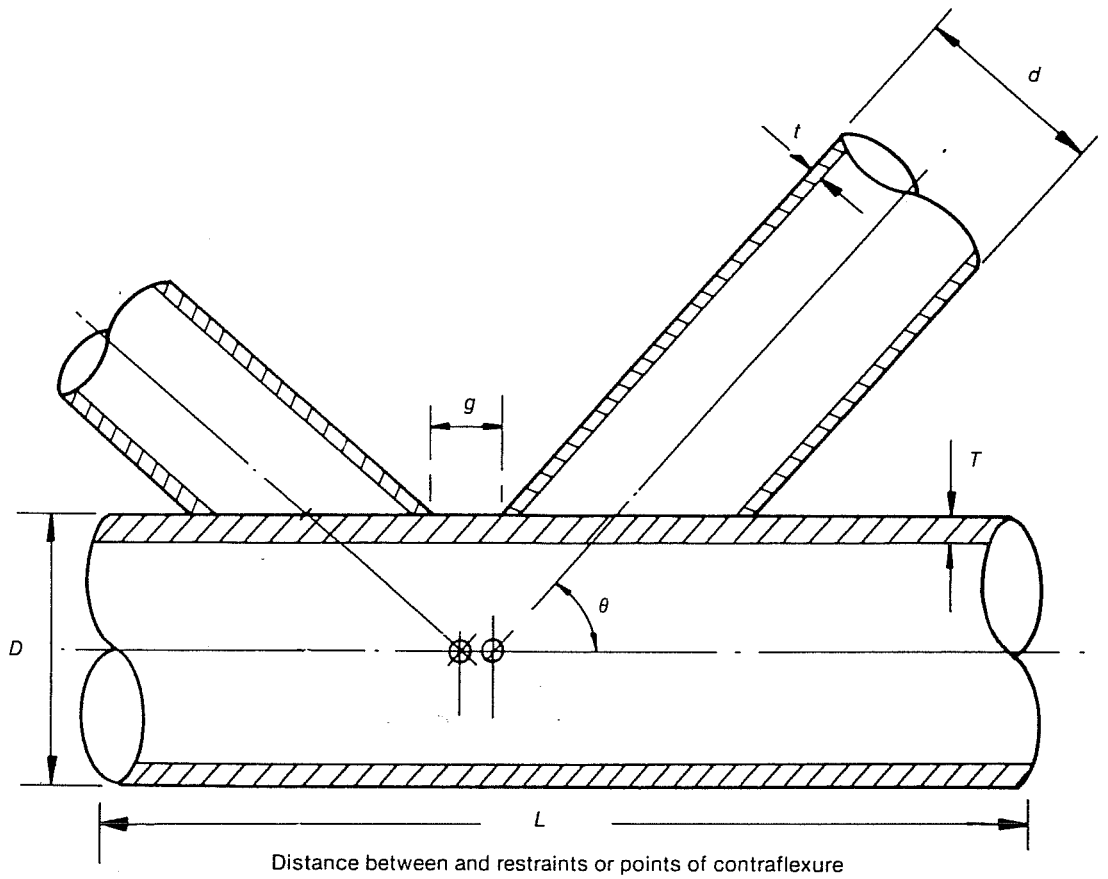

Geometric ratios: $\alpha = \frac{2L}{D}$ $\beta = \frac{d}{D}$ $\gamma = \frac{D}{2T}$ $\tau = \frac{t}{T}$ $\zeta = \frac{g}{D}$

Fig. 1.5 Definition of Basic Dimensions

following:

1. Chord length parameter (α)- ratio of chord length to the chord radius (2L/D). This parameter gives an indication of the effect end conditions may have on the strength of a joint, and of any beam bending which may be present in the chord.
2. Diameter ratio (β) - ratio of branch diameter to chord diameter (d/D). This parameter varies from 0 to 1.0 and gives an indication of the compactness of the joint.
3. Chord thickness ratio (γ) - ratio of chord radius to chord thickness (D/2T). This parameter gives an indication of the radial stiffness of the chord.
4. Wall thickness ratio (τ) - ratio of branch wall thickness to chord wall thickness (t/T). This parameter is used to determine the possibility of the branch fracturing before the chord wall fails.
5. Gap parameter (ξ) - ratio of the gap to the chord diameter (g/D). This parameter is used in joints involving the K geometry to determine the proximity of the various branch members.

1.2.2 Basic Loadings. Tubular joints are subjected to loads on both the branch and chord members. The basic loadings are axial compression and tension, in-plane bending (IPB) and

out-of-plane bending (OPB). These loadings are illustrated in Fig. 1.6. In most cases the failure of the joint is controlled by branch loadings; however, chord loadings do effect the strength of the joint. In practice, the joint is usually subjected to combinations of these basic loadings.

1.3 Modes of Failure

The mode of failure of a tubular joint is determined by the type of loading, the geometry of the joint, and the material properties of the joint. In offshore structures which are subjected to cyclic wave loadings fatigue failure may be the controlling mode of failure. This report, however, concentrates on the static ultimate strength of tubular joints which represents the maximum one time load which can be resisted by the joint.

The modes of failure exhibited by joints subjected to branch axial loads are shown in Fig. 1.7. Local chord wall collapse is the most common mode of failure for joints subjected to branch axial compression. Punching shear type failures are more common in tension loaded joints with small β ratios. Local buckling of the chord wall away from the branch-chord intersection occurs with thin walled chords when chord bending or axial stresses result from branch loadings (T joints with high α values). Shear failure of the chord wall at the gap occurs with

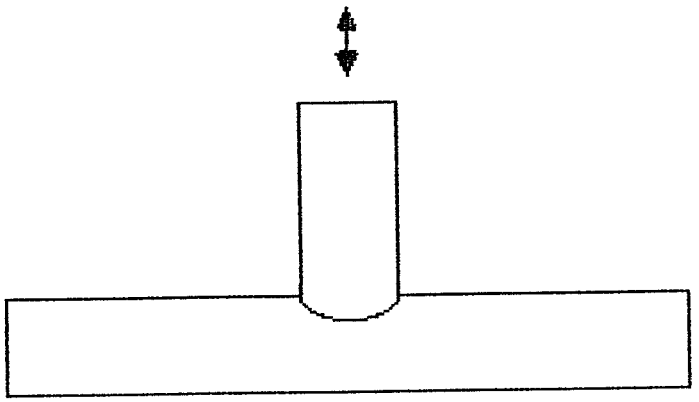

Axial Compression or Tension

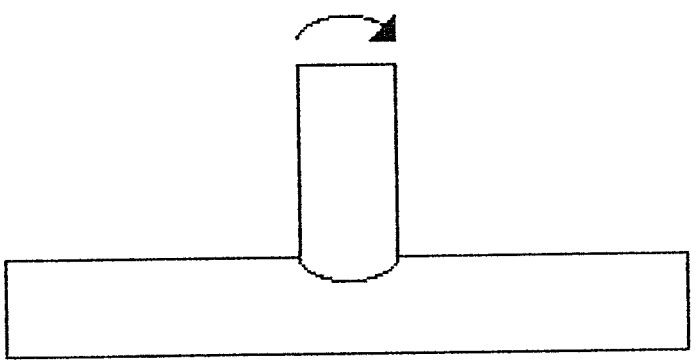

In-Plane Bending (IPB)

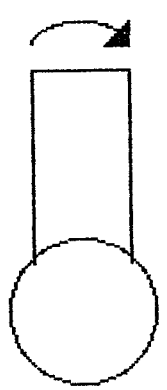

Out-of-Plane Bending (OPB)

Fig. 1.6 Basic Joint Loadings

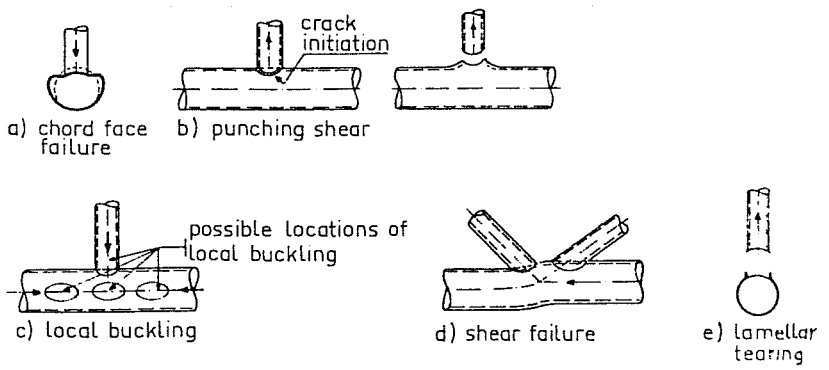

Fig. 1.7 Typical Modes of Failure for Branch Axial Loads

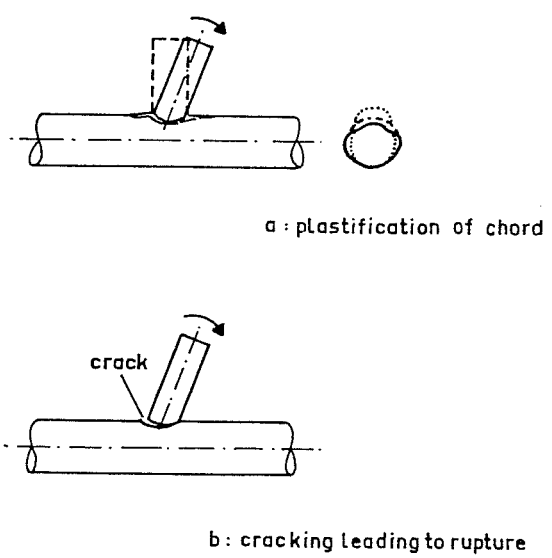

Fig. 1.8 Typical Modes of Failure for Branch Bending Loads

large β ratios. Lamellar tearing is mainly a problem for joints with thick walled chords (low γ values).

The modes of failure exhibited by branch moment loaded joints are shown in Fig. 1.8. Yielding of the chord wall on the compression side of the joint generally controls for joints constructed of ductile metals. Fracture along the branch-chord intersection on the tension side of the joint may control for joints made of high strength steel or with small β ratios. However, because tubular joints subjected to branch bending show a great deal of ductility the fracture of the chord wall usually does not occur until the rotations of the joint are very large. In addition to these, lamellar tearing on the tension side of the joint is also a possibility.

1.4 Prediction of Static Ultimate Strength

The static ultimate strength of a tubular joint is determined by the ability of the chord wall to resist the loads applied by the branch members. These branch forces are resisted by a combination of plate and membrane action in the chord wall as shown in Fig1.9. Plate action occurs mainly in the crown region of the joint where the branch loads are resisted by transverse shear and bending in the chord wall much like a flat plate subjected to perpendicular loads. Membrane action dominates in the saddle region of the joints with large diameter ratios

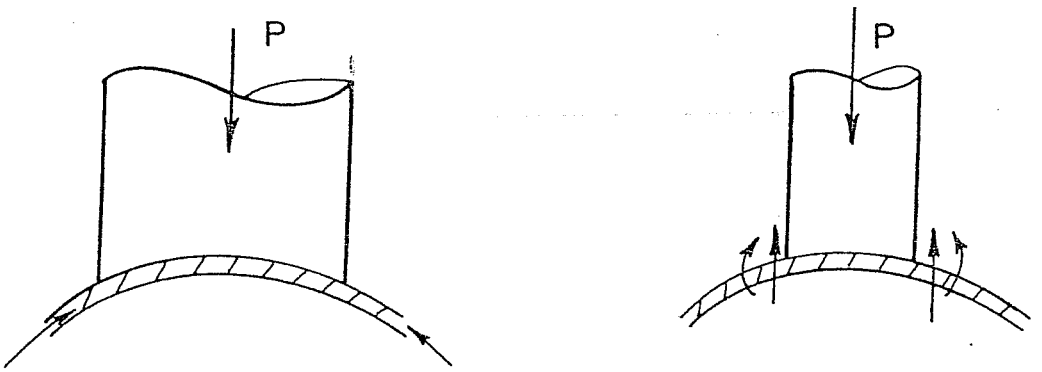

(a) membrane action (b) plate action

Fig. 1.9 Schematic of Plate and Membrane Action in Chord Wall

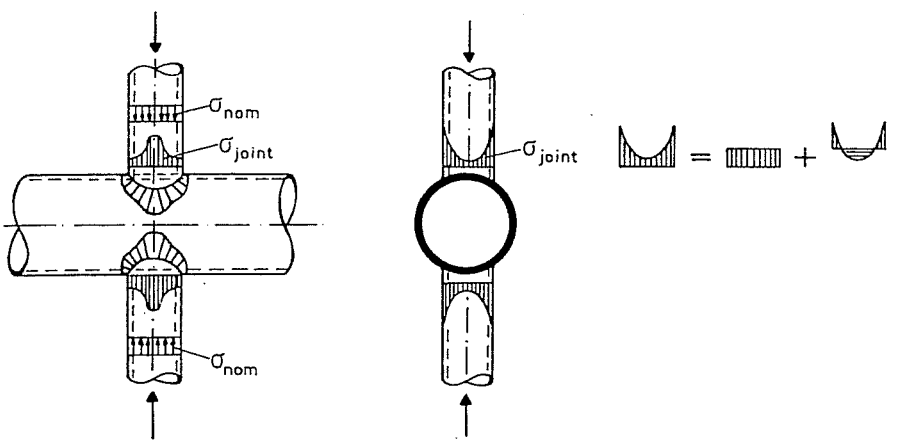

Fig. 1.10 Example Elastic Stress Distribution for T Joint Under Axial Compression

where the branch loads are resisted by axial forces in the chord wall, thus the chord wall in this region acts much like a column. The fact that the chord wall is stiffer in membrane action than in plate action results in a nonuniform distribution of stresses around the branch-chord intersection when branch loads are applied. For example an elastic stress distribution for a DT joint under axial compression is shown in Fig. 1.10. From this example it can be seen that there is a large concentration of stress (load) around the saddle region. These stress concentrations are typical of all types of tubular joints and can cause fatigue failure of a joint. The problem of fatigue is not addressed here but more information can be found in Refs. 32 and 34.

1.4.1 Factors Affecting Static Ultimate Strength. The static strength of a tubular joint, is a function of the material strength of the chord, the geometry of the connected members, and the type of loading applied. The material strength is represented by the tensile strength of the chord or branch wall, and its effect is fairly straightforward. The geometry of the joint is represented by several nondimensional parameters which were introduced earlier.

One of the most important parameters in determining the ultimate strength of a tubular joint is the diameter ratio, β. For small β ratios, the branch member is much smaller than the

chord so the branch loads are resisted mainly by plate action in the chord wall. As the β ratio increases, the branch approaches the same size as the chord, more of the branch loads are resisted by membrane action and the strength of the joint increases. The increase in strength is not generally significant until β is larger than 0.6. Another influence of the β ratio is that as the β ratio increases, there is relatively more weld length, due to the saddle shape of the joint, to transfer the branch loads.

The ultimate strength of a tubular joint is also affected by the chord thickness ratio, γ. The chord thickness ratio is a measure of the radial flexibility of the joint. As γ decreases, the chord becomes thicker in relation to its diameter so the radial stiffness of the chord increases, and thus the strength of the joint increases. However, many ultimate strength equations do not include the thickness ratio. This may be explained by the fact that the ultimate strength for several types of loadings are controlled mainly by the chord behavior near the intersection of the branch and chord. In this area, the chord wall is stiffened or reinforced by the presence of the branch; therefore, a change in the radial stiffness will not have a large effect on the ultimate strength of the joint. Recent evidence [39] indicates that γ has a significant effect on IPB.

The angle included between the branch and chord, θ, influences the strength of a tubular joint in several ways. First, due to the strength of the chord in membrane action, only the branch force components (perpendicular to the chord) need to be considered in axial loadings. For IPB moment loaded joints, the inclination of the branch does not significantly affect the strength of the joint. For OPB moment loaded joints, the moment can be separated into a pure OPB component and a component of torsion about the center of the branch-chord intersection [34]. The inclination of the branch also increases the length of the branch-chord intersection which can have a significant effect on the tensile capacity of a joint [15].

The gap parameter, ζ, is an important variable in the strength of joints with more than one branch on one side of the chord. For large gap values each branch-chord intersection can be treated as a separate joint. As the gap becomes smaller, the flexural stiffness of the chord wall between the branches increases. This increase in flexural stiffness results in an increase in the strength of the joint.

The static ultimate strength of a tubular joint is also influenced by the type of loading applied. The types of loadings include axial tension and compression, IPB moment, and OPB moment to either or both the branch and chord, and combinations of branch loads and or chord loads. As mentioned earlier, the

failure of most joints is controlled by the branch loadings. The type of loading is a determining factor in how much plate or membrane action is used to resist the branch loads. For example, axial loads are resisted mainly at the saddle area of a joint where membrane action dominates. The same joint will exhibit a much higher ultimate strength in tension than in compression as shown in Fig. 1.11 because the mode of failure is fracture in the heat affected zone along the weld profile and not plastic bending or buckling of the chord wall. In IPB on the other hand, because of the stress distribution in the branch, the highest branch loads are applied near the crown where plate action dominates. In addition, the type of loading determines the mode of failure of the joint. Also, a joint loaded in IPB will have a higher ultimate load and exhibit higher stiffness than when loaded in OPB, as shown in Fig. 1.12.

The presence of other loads, such as compressive stresses in the chord, or branch loadings in other directions will tend to effect the ultimate strength of a tubular joint. Compressive stresses in the chord cause a decrease in the strength of a joint by weakening the plate action of the chord wall [37]. The presence of more than one branch loading (load interaction) also tends to reduce the strength of the joint.

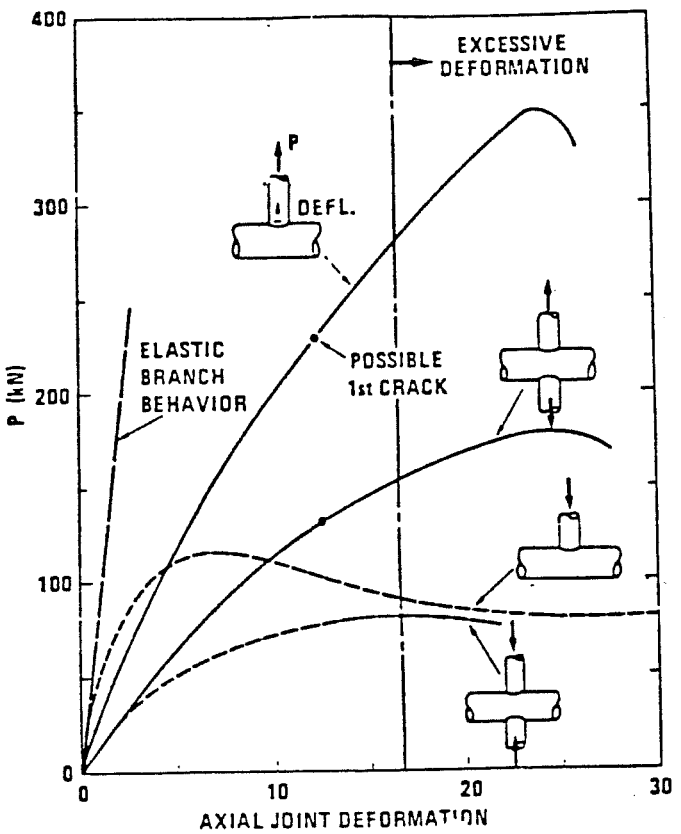

Fig. 1.11 Comparison of Axial Tension and Compression Stiffness

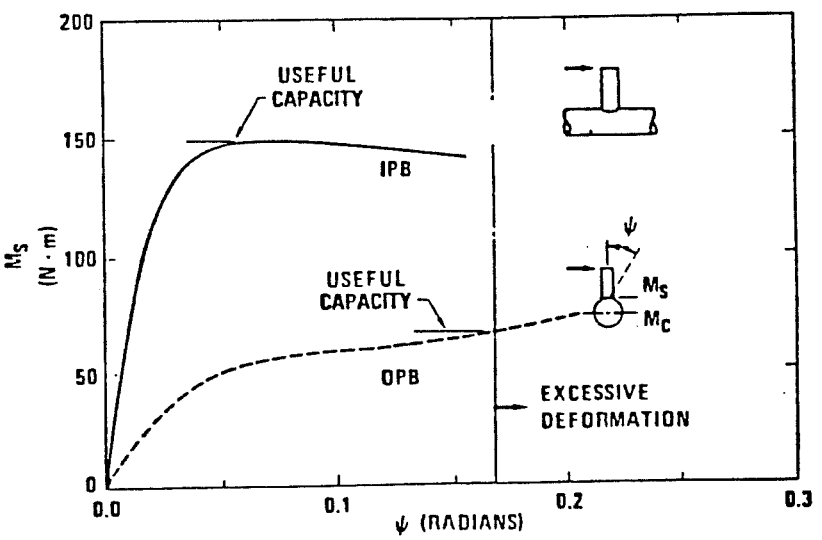

Fig. 1.12 Comparison of IPB and OPB Stiffness

1.4.2 Design Methods. At the present time, there is little uniformity among the equations recommended for the ultimate strength design of tubular joints. In a recent comprehensive study of tubular joint design, the Underwater Engineering Group [34] compiled and compared the various design code available and concluded that, "although some codes are 'closely related' to others, there are almost as many different design formulations as there are codes." The publication continues by suggesting a review of many of the existing codes so some consensus may be reached among the design regulating bodies. The one thing that the codes do have in common is that all of the design equations are based on curves fit to experimental data.

There are many empirical equations suggested for the design of simple tubular joints subjected to simple loadings [27, 26, 39, 17, 12, 6, 34]. Table 1.1 shows the various equations which have been recommended for the design of DT joints under compression. Even though the equations have many different forms the mean formulas all yield about the same results. As an example of basic design formulation, a recent set of proposed design equations is shown in Table 1.2 [39]. The general format of the equations includes a basic nondimensional strength term,

$$Fy\ T^2 / \sin\theta$$

T = chord thickness
Fy = Chord yield strength

Table 1.1 Example Ultimate Strength Formulae

1. Washio (1969) $P_u = F_y T^2[6.19/(1-0.833\beta)]$

2. Kurobane (1976) $P_u = F_y T^2[6.57/(1-0.81\beta)]$

   (1981) $P_u = F_y T^2[7.46/(1-0.812\beta)](D/T)^{-0.05}(F_y/F_u)^{-0.173}$

   or $P_u = F_y T^2[7.36/(1-0.811\beta)]$

   (1984) $P_u = F_y T^2[7.36/(1-0.813\beta)](D/T)^{-0.035}$

3. API (1978) $P_u = F_y T^2(12.57\beta)(D/2T)^{0.3}$ for $\beta<0.271$

   $P_u = F_y T^2[2.64/(1-5\beta/6)](D/2T)^{0.3}$ for $\beta>0.271$

4. DnV (1977) $P_u = F_y T^2[7.41/(1.2-\beta)]$

5. Dutch & French Spec. (1977) $P_u = F_y T^2[6.4/(1.2-\beta)]$

6. Pan (1976) $P_u = F_y T^2(16.31\beta^{0.64})$ for $0.2<\beta<0.8$

   $P_u = F_y T^2(30.0\beta^{3.42})$ for $0.8<\beta<1.0$

7. Yura, API Ds449 (1980) $P_u = F_y T^2[3.4 + 13\beta]Q_\beta$ (1984)

8. Billington (1980) $P_u = F_y T^2[3.0 + 15.2\beta]Q_\beta$

Table 1.2 Example Design Recommendations Ref. 39

Basic Strength: $P_u = Q_u[F_y T^2/\sin\theta]Q_f$ $\quad M_u = Q_u[dF_y T^2/\sin\theta]Q_f$

where: $Q_f = 1.0 - 0.045\gamma A^2$ for IPB
$Q_f = 1.0 - 0.030\gamma A^2$ for Axial
$Q_f = 1.0 - 0.021\gamma A^2$ for OPB
$A = F.S.\ (f_a^2 + f_b^2)^{0.5}/F_y$

and Q_u is given below; for Mean Strength

Joint Type	Compression	Tension	IPB	OPB
T	$3.1+20.9\beta$	$0.48\sqrt{3.1+20.9\beta}$	$6\gamma^{0.5}\beta$	$\frac{3.56}{(1.0-0.81\beta)}$
Cross	$(2.2+17.3\beta)Q_\beta$	$\frac{4.5\gamma^{0.32}}{(1.0-0.81\beta)}$		
K	$1.3[3.1+20.9\beta]Q_g$			

and for Lower Bound Strength

Joint Type	Compression	Tension	IPB	OPB
T	$2+21\beta$	$2+21\beta$	$5\gamma^{0.5}\beta$	$\frac{3.2}{(1.0-0.81\beta)}$
Cross	$(3.4+13\beta)Q_\beta$	$(3.4+13\beta)Q_\beta$		
K	$1.05[2+21\beta]Q_g$			

where: $Q_\beta = 0.3/[\beta(1-0.833\beta)]$ for $\beta>0.6$
$Q_\beta = 1.0$ for $\beta\leq 0.6$
$Q_g = 1.8-0.1g/T$ for $\gamma\leq 20$
$Q_g = 1.8-4g/D$ for $\gamma\leq 20$
$Q_g \geq 1.0$
For Load Interaction: $P/P_u + (M/M_u)_{OPB} + (M/M_u)^2_{IPB} \leq 1.0$

with factors Q_u to account for the type of load, and type of joint; and Q_f to account for any chord stress. The effects of the diameter ratio, β, and the thickness ratio, γ, are included in the Q_u term since the effect of these parameters varies with the joint loading and geometry. In addition the effect of the interaction of combined branch loads on the joint strength is accounted for by an interaction equation.

In general the recommended equations agree with the earlier discussion of the factors which influence the ultimate strength. But, as the database continues to grow, and the design philosophies change, the constants involved in the equations will continue to change. For example the American Petroleum Institute's (API) design guide has been revised 15 times to date since its first edition in 1971. This is one of the drawbacks to design using empirical equations. Further, only the simplest cases are tested in a laboratory, and the number of parameters which can be investigated are limited by cost and time. Finally, the use of empirical design tends to limit the understanding of joint behavior because an important variable in design may be missed or misunderstood because the variable has not been investigated experimentally. Therefore, it would be more advantageous to develop some generally applicable inexpensive analytical methods which could be used to investigate joint behavior.

1.4.3 Analytical Methods. The development of a generally applicable purely analytical model of tubular joint ultimate strength behavior is complicated by the complex geometry of the joints, the stress concentrations, and the presence of both plate and membrane actions. In addition, the large reserve capacity of tubular joints after first yield make the results of any elastic model unreasonably conservative. Therefore, even though the elastic models developed by Bijlaard [5] and Dundrova [3] are useful for some basic understanding of joint behavior, they are not applicable to the prediction of ultimate strength behavior. But two rather simple models, the punching shear and ring, have been used with some success to predict the ultimate strength of tubular joints. In addition, the finite element method has shown much promise in the analytical solution of ultimate strength problems in tubular joints.

1.4.3.1 The Punching Shear Model. The punching shear model is based on the assumption that the ultimate capacity of the joint is reached when the chord wall around the branch-chord intersection fails in shear as shown in Fig. 1.13. The shear stress in the chord wall is calculated based on the nominal axial stress in the branch. So that the basic shear stress in the chord wall is given by,

$$V_p = \tau f_v \tag{1.1}$$

To this basic equation a $\sin\theta$ term is added to account for the

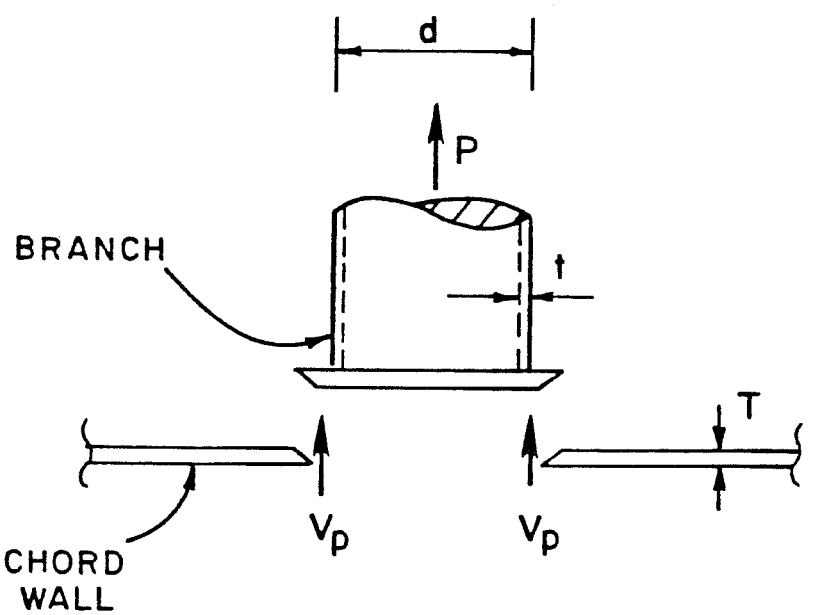

Fig. 1.13 Schematic of Punching Shear Failure

inclination of the branch. For bending loads in the branch a full plastic shear stress distribution is assumed.

The material shear yield is 0.58 of the tensile yield; however, this level of shear cannot be attained in thin shells. Therefore, a correction factor was developed by Marshall [22] which calculates the ultimate shear stress as a function of γ.

The punching shear method does not account for the membrane actions which are present in the chord wall. Because of this omission, the model is not applicable to joints with large β ratios where membrane action is significant. Thus, the basic formulation must be calibrated to experimental data. Since it does not consider membrane action or bending in the chord, the punching shear model does not seem to be a very accurate model of tubular joint behavior.

1.4.3.2 The Ring Model. The ring model was developed to predict the strength of DT tubular joints [15]. In this model the joint is reduced to a tube with the same dimensions and mechanical properties as the actual chord and with an effective length B_e as shown in Fig. 1.14. For branch axial loads, the branch loads are applied as two line loads equal to half of the branch load acting over the length of the tube or ring as shown in Fig. 1.14. At this point the axial (membrane) and shear stress effects on the the bending strength of the ring are neglected so that available equations for moments in a ring can be used to

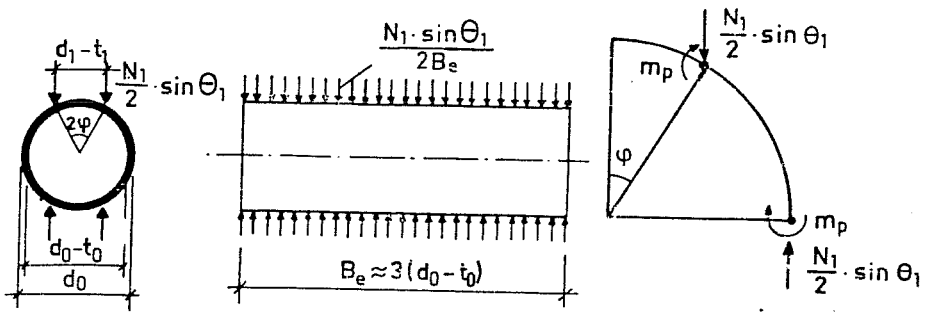

Fig. 1.14 Schematic of Ring Model and Effective Length Applied to Axial Loads

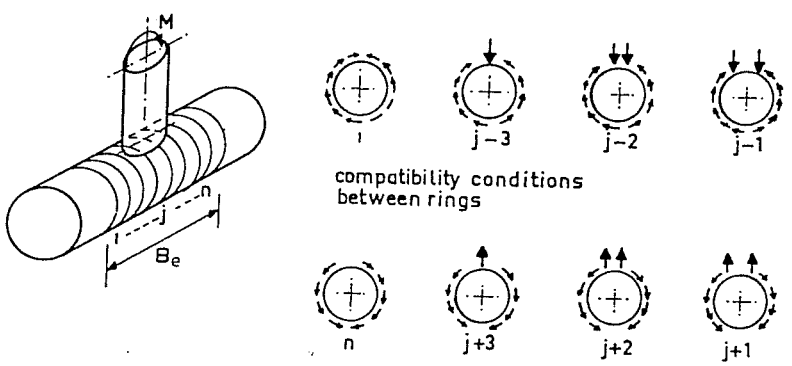

Fig. 1.15 Schematic of Ring Model and Effective Length Applied to IPB Loads

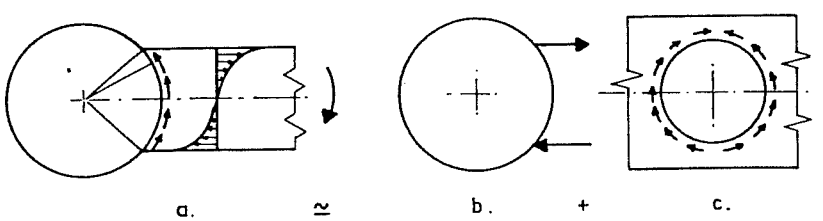

Fig. 1.16 Schematic of Ring Model and Effective Length Applied to OPB Loads

calculate the ultimate line loads. The ultimate strength is then equal to twice the ultimate line load times the effective length of the ring. However, the only way to determine the effective length B_e is by fitting the results of the analysis to experimental data. Thus, this analytical model is dependent on empirical data.

The ring model does not present a simple method for predicting the bending strength of tubular joints. One method for using this model to predict IPB behavior is illustrated in Fig. 1.15. The joint is divided into a series of independent rings with different loads. Then the capacity of the rings is integrated over some effective length to give an approximation of the strength of the joint. For OPB, the ring model can be used as shown in Fig. 1.16 where the moment is modeled as both a shear across the face of the intersection and a pair of line loads. But as with the other models an effective length must be determined experimentally.

1.4.3.3 Hoadley's Ring Model. Hoadley attempted to use the ring model to predict the ultimate strength behavior of DT tubular joints by dividing the chord into three separate sections which work to resist the branch forces as shown in Fig. 1.17 [15]. Hoadley used his model to develop a mean strength equation for DT joints in compression which is shown in Fig. 1.18 along with a mean strength equation given by Kurobane [18] which is

recommended for use by the International Institute of Welding (IIW). Comparison of the two curves shows that Hoadley's ring model produces fairly good predictions over a wide range of β ratios. However, since the ring model does not account for membrane action it becomes less applicable as β approaches 1.0.

Hoadley next attempted to apply his ring model to predict the OPB strength of a tube. In this model, it is assumed that the adjoining chord section will have no effect on the OPB strength as shown in Fig. 1.19. The model assumed the same transition zone length as the axial compression model. The prediction based on this model was 34% less than the experimental result. Upon further investigation with a simple finite element model, which will be discussed later, it was found that the transition zone should be made larger for OPB applications. With the adjustment in the transition zone length, Hoadley's model yielded reasonable predictions of the ultimate strength of the joint as shown in Fig. 1.20.

Finally Hoadley used his ring model to predict IPB ultimate strength. For IPB, Hoadley took the axial load model and applied tension to one half of the joint and compression to the other. The resulting IPB strength prediction was less than half of the experimental value. The inaccuracy of the model comes from the fact that it does not model the longitudinal strength of the

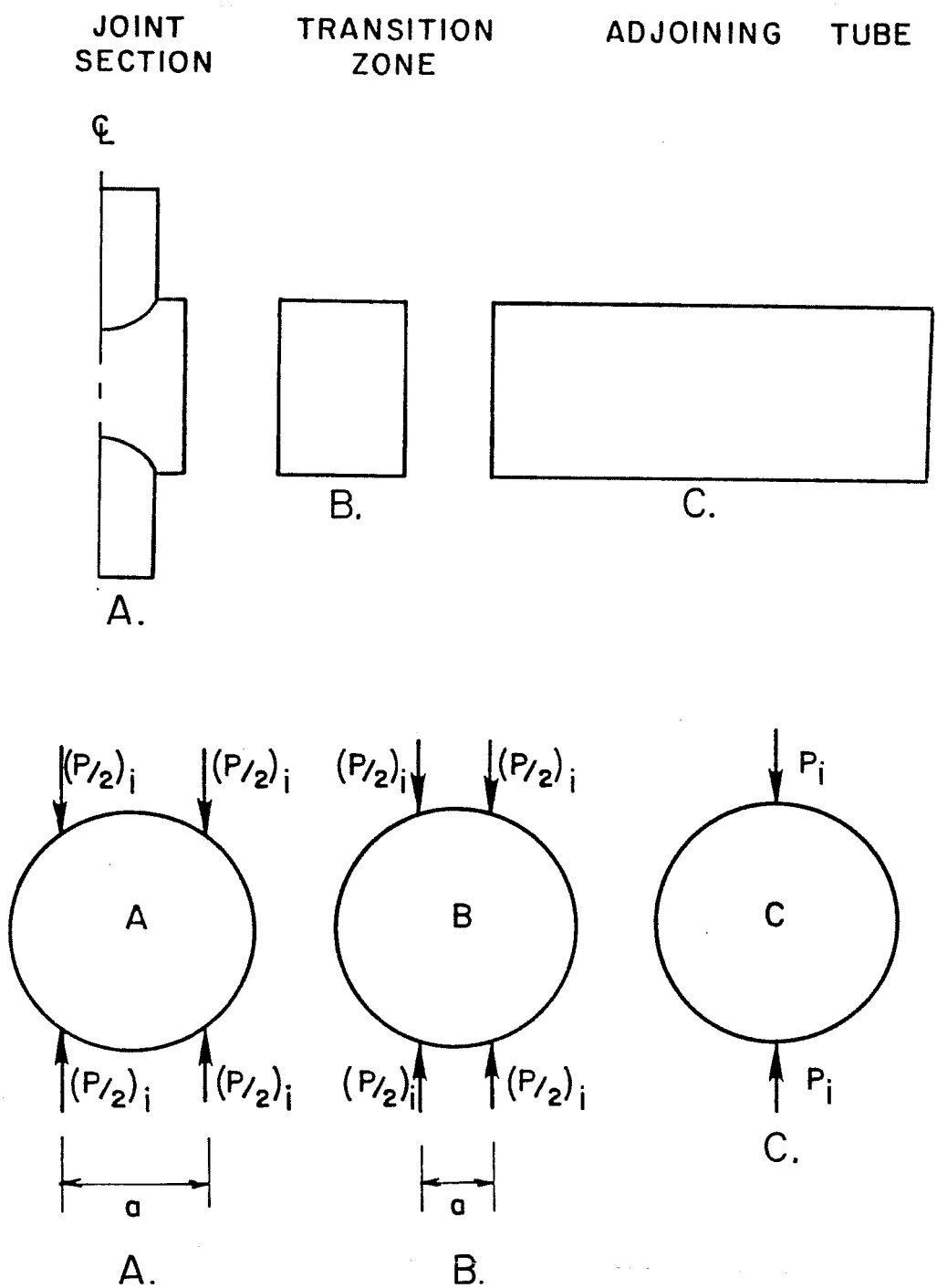

Fig. 1.17 Hoadley's Ring Model

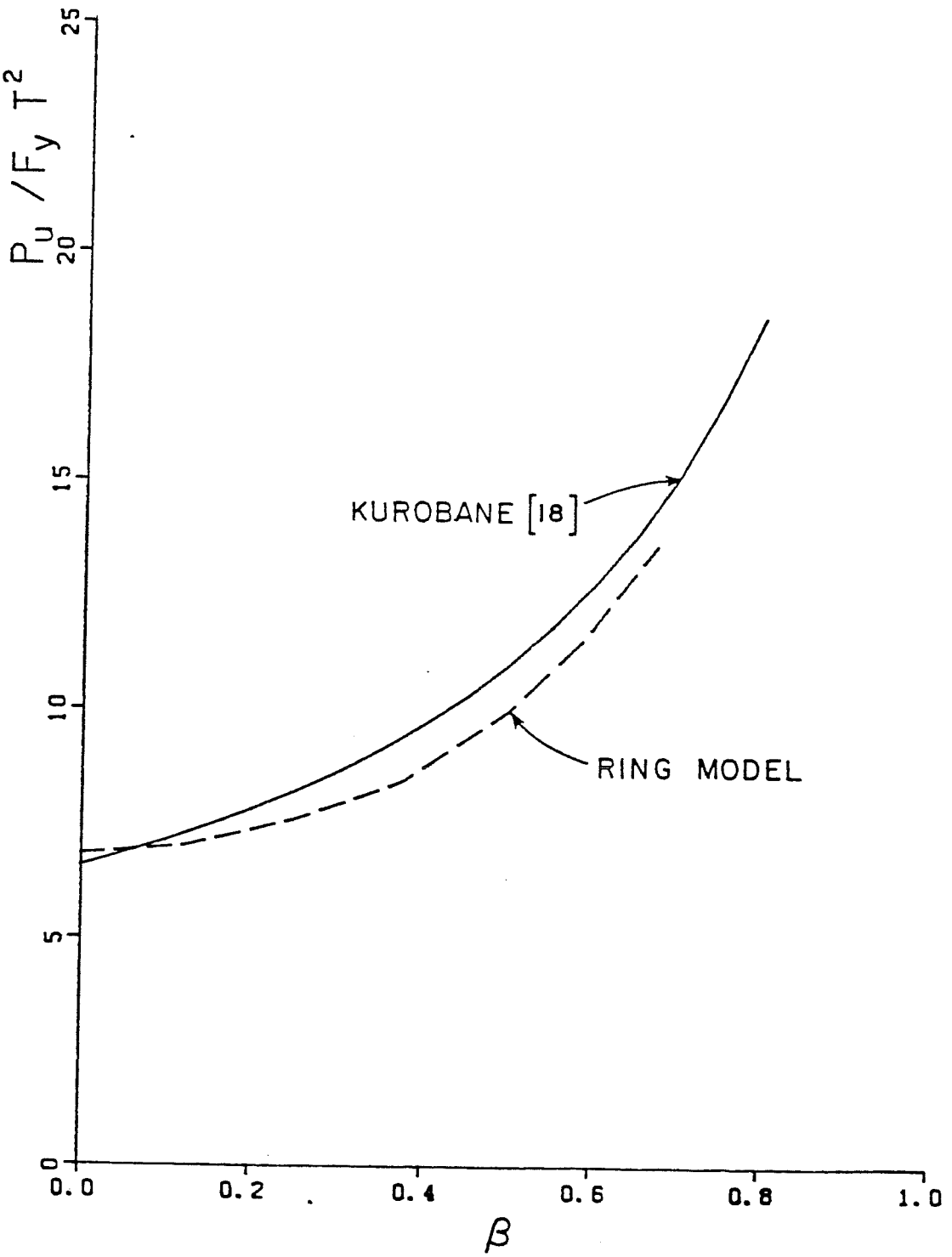

Fig. 1.18 Predictions of DT Axial Strength from Hoadley's Ring Model and Kurobane's Equation

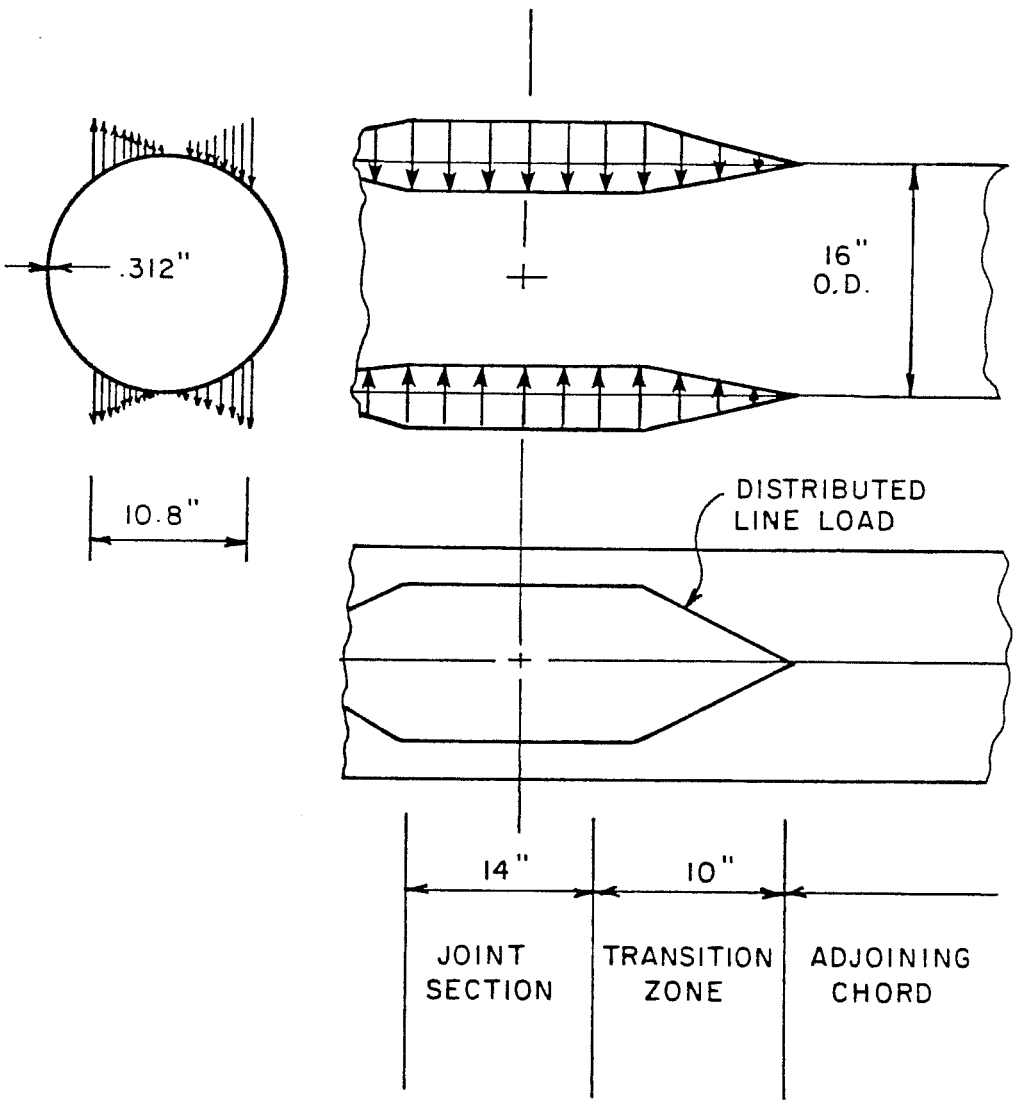

Fig. 1.19 Hoadley's OPB Ring Model

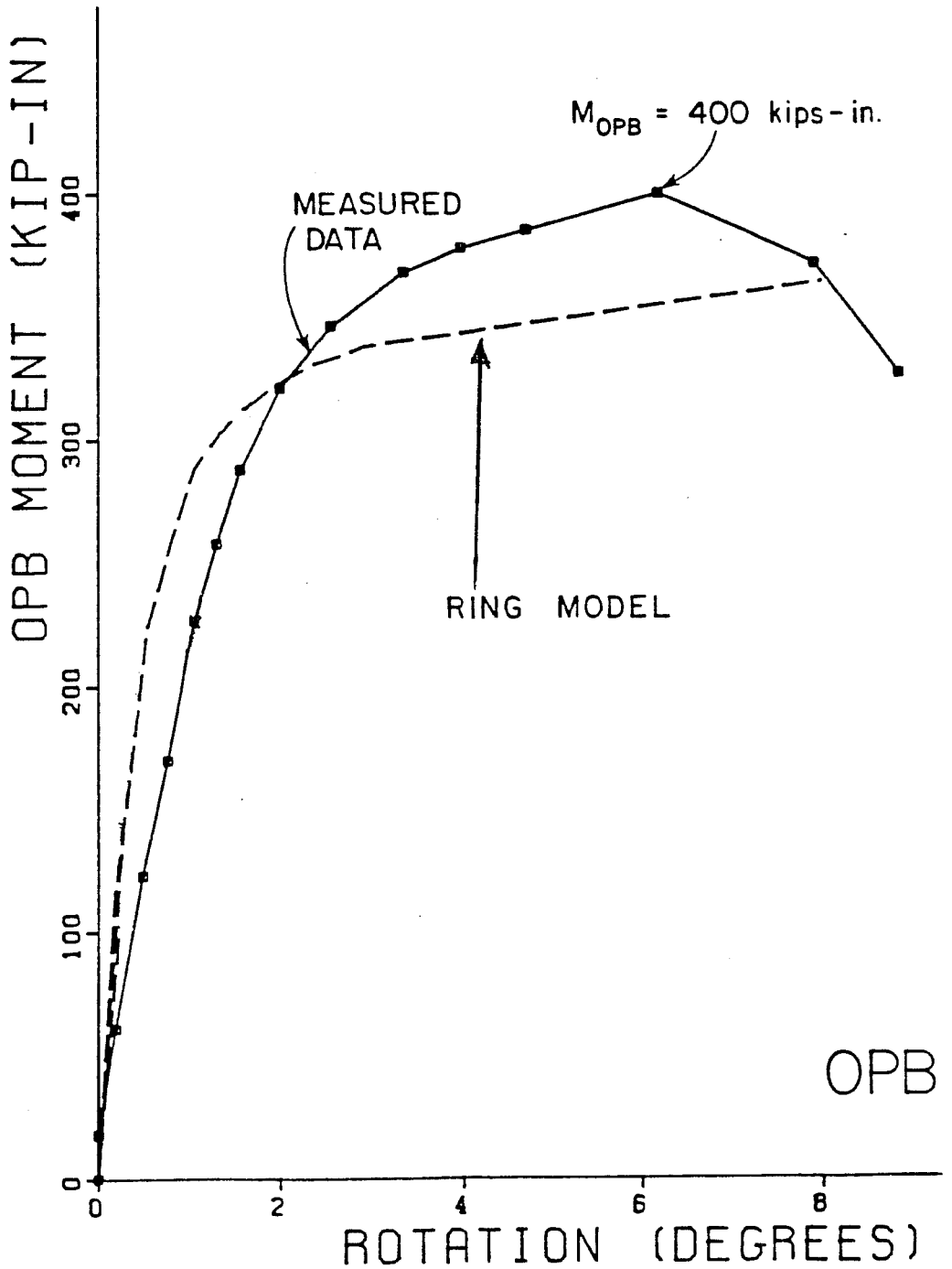

Fig. 1.20 OPB Moment vs. Rotation Curves from Test 08 and Predicted by Hoadley's Ring Model

a line normal to the original tangent plane of the element remains straight in the deformed state and (2) a line normal to the original tangent plane remains normal in the deformed state. Thus, Kirchoff's assumptions effectively neglect the transverse shear through the shell thickness. Mindlin's plate theory [20] includes the effect of transverse shear through the shell thickness as a rotation of the normal to tangent plane of the original element. Two elements which use Mindlin's plate theory are the Ahmad element and the complex semiloof element [34]. Both of these element types should yield reasonable results since the shear in thin shells, typical of chords in offshore structures, should not be very significant in ultimate strength applications. However, the use of shell elements does pose difficulties in modeling the weld around the joint. But it has been found that the use of three-dimensional solid elements may be used to solve this problem [34].

Stamenkovic and Holsgrove used the finite element method to predict ultimate strength of T joints subjected to axial compression and IPB [16]. The finite element model used the LUSAS finite element system [19]. This system is based on a non-linear semiloof shell element with geometric and material non-linearity. In addition, the material non-linearity was traced using a multi-layered shell formulation. The weld was modeled using a standard

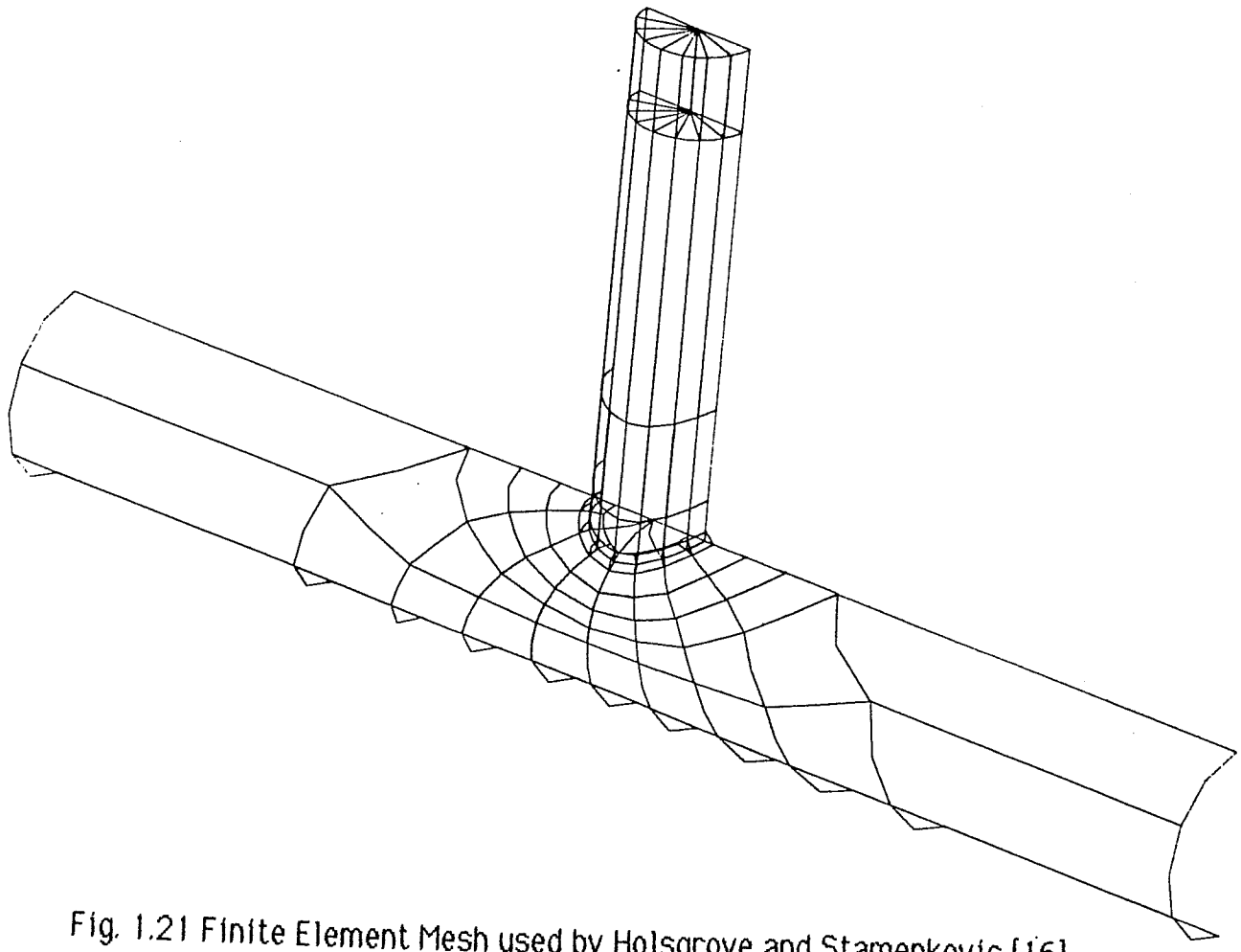

Fig. 1.21 Finite Element Mesh used by Holsgrove and Stamenkovic [16]

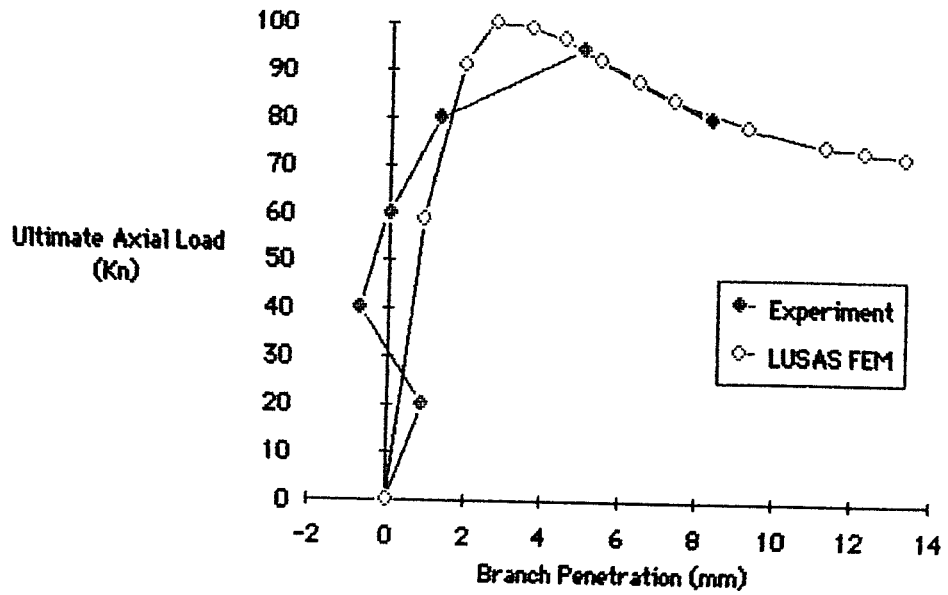

Fig. 1.22 Axial Load vs. Deflection Measured and Predicted by Holsgrove and Stamenkovic Finite Element Model

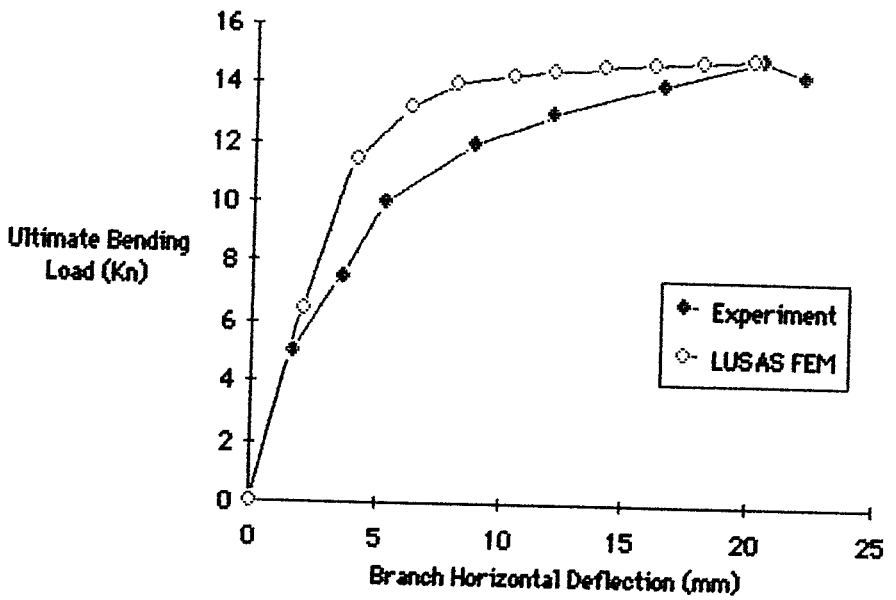

Fig. 1.23 IPB Moment vs. Rotation Measured and Predicted by Holsgrove and Stamenkovic Finite Element Model

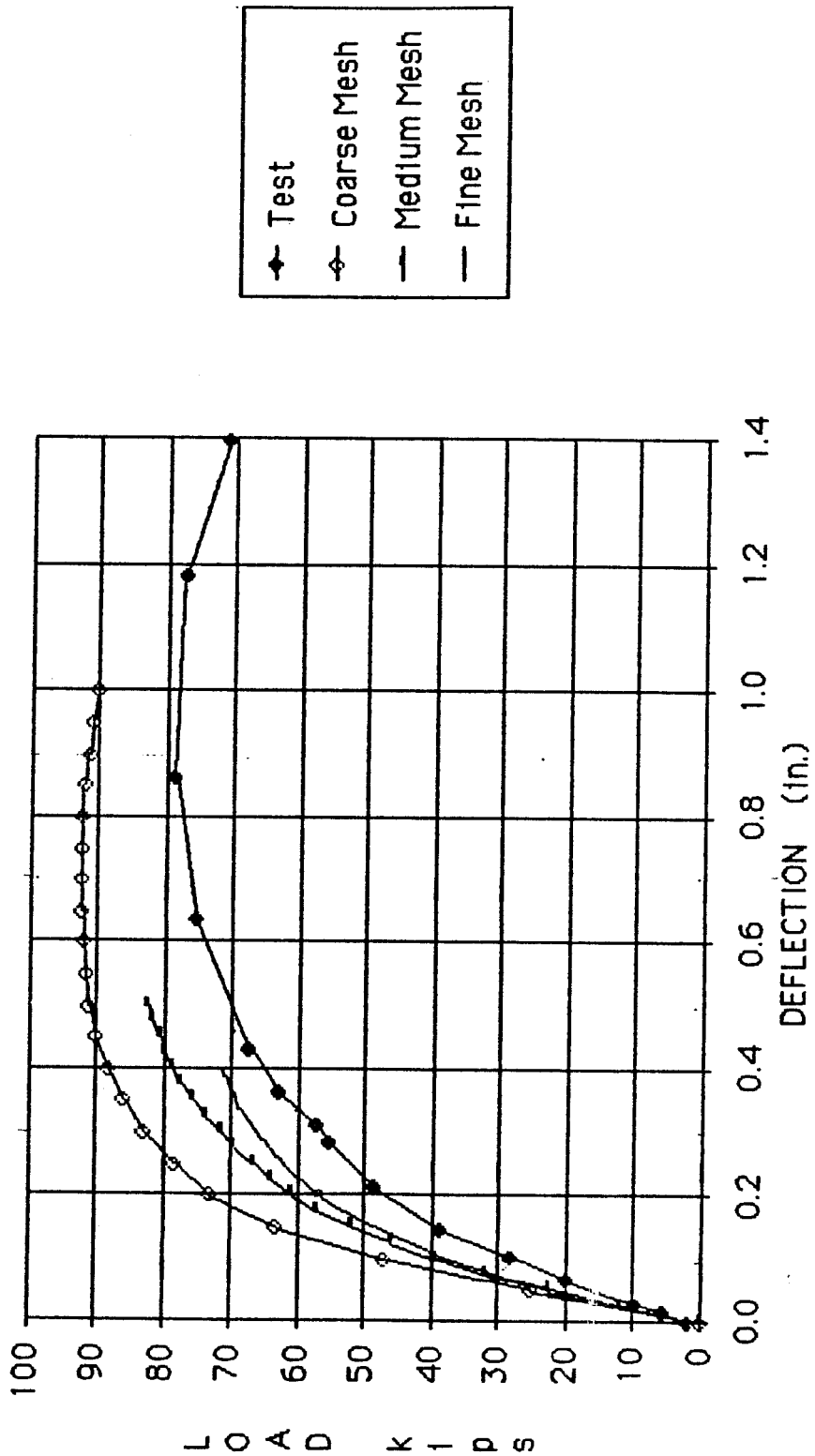

Fig. 1.24 Axial Load vs. Deflection Curves Reported by Hoadley and Predicted by Pan's Finite Element Model

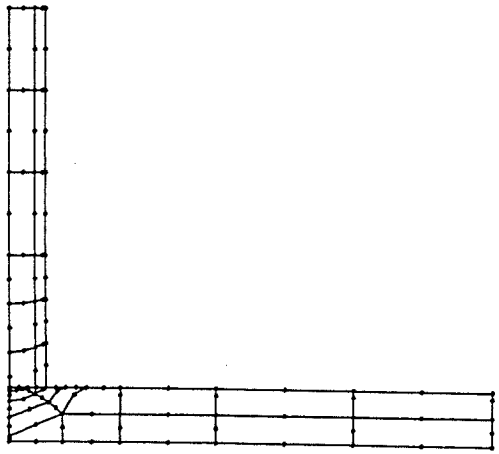

Fig. 1.25 "Coarse" Mesh used by Pan

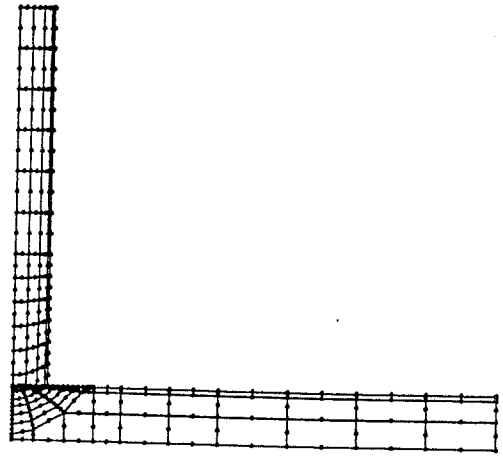

Fig. 1.26 "Medium" Mesh used by Pan

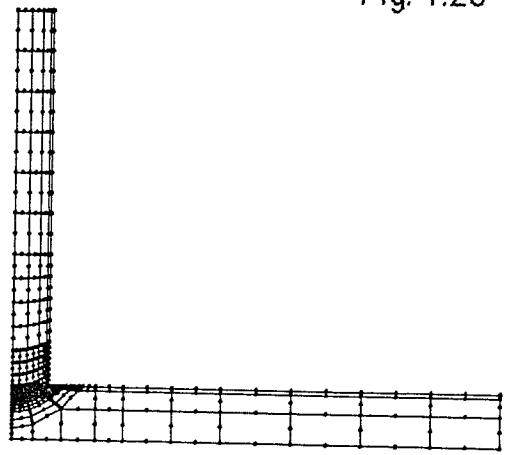

Fig. 1.27 "Fine" Mesh used by Pan

While developing the ring model discussed earlier, Hoadley utilized a simple finite element model and the ABAQUS finite element system [13] to predict the ultimate strength of a DT joint subjected to OPB and one subjected to IPB. Hoadley simplified the model greatly by eliminating the branch member and applying assumed branch forces directly to the chord surface. The chord was modeled using simple 4 noded reduced integration, doubly curved shell elements which follow Kirchoff's assumptions. OPB moment was modeled by two compressive and two tensile loads at the centerline of the joint as shown in Fig. 1.28. The prediction of OPB strength produced by this model was surprisingly good, even though the stiffness of the joint was incorrectly modeled as shown in Fig. 1.29. IPB was simulated by three equivalent compressive and tensile forces on either side of the joint as shown in Fig. 1.30. Unlike the OPB case, the finite element model's IPB strength prediction was almost 40% less than the experimental value; but, the stiffness of the joint in the elastic range was modeled reasonably well as shown in Fig. 1.31. The explanation for the inability of the model to predict IPB was that the assumed distribution of branch loads was inaccurate.

1.5 Prediction of Static Ultimate Strength : Interaction Effects

As discussed earlier, empirical design is restricted to the database upon which it is based. At the present time the

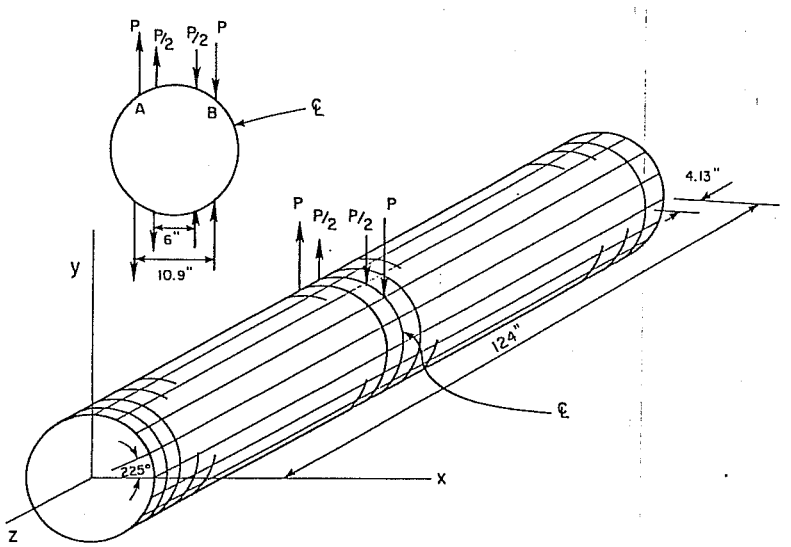

Fig. 1.28 OPB Finite Element Mesh used by Hoadley

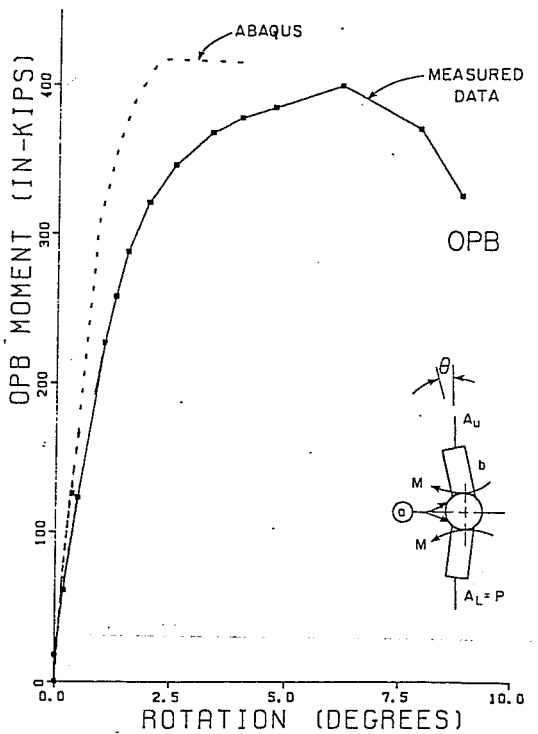

Fig. 1.29 OPB Moment vs. Rotation Curves for Test 08 and Predicted by Hoadley's Finite Element Model

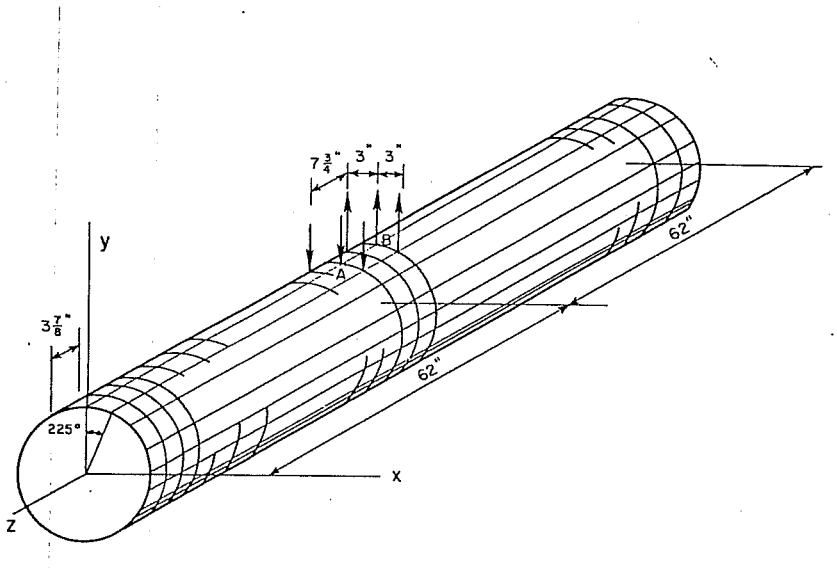

Fig. 1.30 IPB Finite Element Mesh used by Hoadley

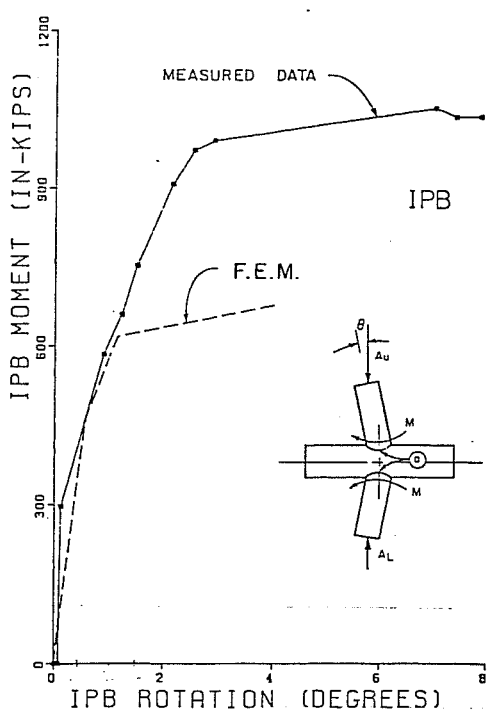

Fig. 1.31 IPB Moment vs. Rotation for Test 17 and Predicted by Hoadley's Finite Element Model

weakness in the database used for the ultimate strength design of tubular joints is that almost all of the tests involved simple joint geometries subjected to simple loadings; i.e., branch axial, IPB, or OPB. However, actual design involves combinations of axial and bending loads in the branches of a joint. At present there is very little experimental data to support any design method for the interaction of branch loadings.

The experimental history of tubular joints subjected to combinations of branch loadings is a short one. The first published tests dealing with the topic were reported by Stamenkovic in 1981 [29]. He tested approximately 105 small scale T joints with combinations of axial and IPB in the branches. The preliminary results of Stamenkovic's tests showed a linear interaction between the two branch loads. However, critical evaluation of Stamenkovic's data showed that the test setup and the definition of failure made this data invalid. A reanalysis of Stamenkovic's data by Marshall indicated that the data fell along an interaction curve based on the theoretical plastic strength of tubular member in bending [23]. This is known as the arcsine equation [35] and is given by :

$$P/P_u+(2/\pi)\text{Arcsine}[(M/M_u)^2_{IPB}+(M/M_u)^2_{OPB}]^{1/2}=1.0 \qquad (1.1)$$

where, P_u and M_u are the ultimate strengths of the joint subjected to axial and bending loads respectively.

The arcsine equation has been adopted by the American Petroleum Institute (API) in the 15th edition of API RP 2A for the interaction of branch axial and bending loads. Hoadley investigated the interaction of branch axial compression with IPB (AI), branch axial compression with OPB (AO), IPB with OPB (IO), and branch axial compression with IPB with OPB (AIO) in DT tubular joints with β=0.67 [14]. From these results Hoadley developed the interaction equation shown below:

$$P/P_u+(M/M_u)^{2.1}_{IPB}+(M/M_u)^{1.2}_{OPB}=1.0 \qquad (1.2)$$

His data showed that the arcsine equation (1.1) was slightly unconservative in most cases if experimental P_u and M_u values were used. However, the conservatism of the API predictions for P_u and M_u makes Eq.1.1 safe for design until more accurate ultimate strength formulae are adopted. Hoadley's data seems to give some experimental support to the present design method except for Axial-OPB interactions which fall below the Arcsine curve. Only joints with β=0.67 were included in the database, no experiments on joints with other β's were available.

Because of the weakness of the database in respect to combinations of branch loadings a research project which served as a continuation of Hoadley's work was sponsored by a consortium of 13 companies involved in the offshore oil field. The results of this research will be presented herein.

1.6 Scope of Work

This report presents the results of 27 ultimate strength tests on DT tubular joints. Sixteen joints had β ratios of 1.0 and ten had β ratios of 0.35. One additional ultimate strength test was done on a DT joint with a β=0.67 to provide a replicate for a reference test completed in Hoadley's research. The purpose of these tests was to determine the influence of the β ratio on the interaction of branch loadings in DT joints.

A description of the specimen geometry, test setup, and testing procedures used in this research are given in Chapter 2. The ultimate strength results for each test are given in Chapter 3. Chapter 4 contains a discussion of the tubular joint behaviors observed in this testing program along with a comparison of DT and T joint interactions. In Chapter 5, the test results along with the results of Hoadley's tests will be used to develop an interaction equation. This equation and other current interaction equations will be evaluated against available test results and an interaction equation will be recommended for design.

Due to the inadequacies of the empirical design method, and the unpromising results or restrictive costs of attempts at ultimate strength prediction using the present analytical methods, a simplified method of analyzing ultimate strength behavior in tubular joints using the finite element method is developed in Chapter 6. This model is evaluated and used to

predict ultimate strength behavior for tubular joints subjected to combinations of branch loadings. A summary of the results and conclusions of this research are given in Chapter 7.

CHAPTER 2

TEST SPECIMENS, SETUP, AND PROCEDURE

2.1 Specimens

All of the specimens used in this research have the DT joint geometry. The DT geometry was chosen because it allows for relatively simple loading arrangements even for testing with combined loadings. The β ratios of 0.35 and 1.0 were chosen to complement Hoadley's work on specimens with β = 0.67 and to bound the values of β typically encountered in offshore structures. Other aspects of the joint geometry, which are presented in more detail in Ref. [7], were chosen to meet design criteria specified at the beginning of the project. Details of the specimens are shown in Fig. 2.1. In this phase of the research chord flanges were only present on specimen subjected to IPB. One flange was present to apply IPB loads.

The specimens were fabricated by McDermott Incorporated, Morgan City, Louisiana. The chords are nominally API-5LX Grade 42, welded line pipe with a nominal 16 in. o.d. and a 0.312 in. wall thickness. The branches of the β=1.0 specimens are of the same material as the chords. The branches for the β=0.35 specimens are nominally ASTM A53 Grade B steel seamless pipe with nominal 5-9/16 in. o.d. and 0.258 in. wall thickness. Several tests were done to determine the material and dimensional properties of all the specimens used in this study. The average

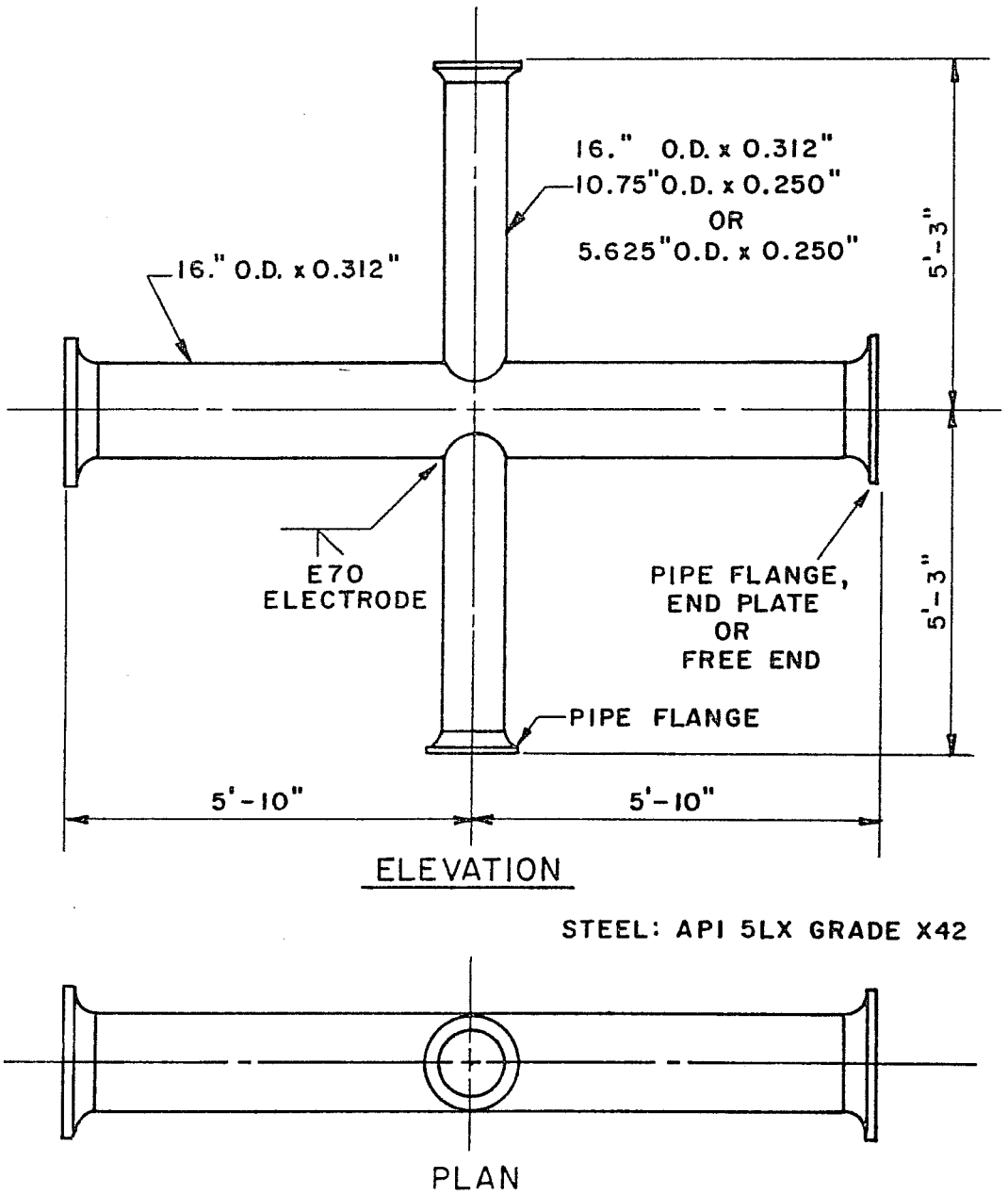

Fig. 2.1 Specimen Details

dimensional properties are presented in Table 2.1. The o.d. of the 16" x 0.312" pipe varied from 16.02 in. to 16.08 in. and the thickness varied from 0.306 in. to 0.325 in. for 26 samples. There was only one sample of the 10-3/4" x 0.258" pipe so there is no variation in dimensions. The o.d. of the 5-9/16" x 0.258" pipe varied from 5.60 in. to 5.63 in. and the thickness varied from 0.256 in. to 0.267 in. for nine samples. The small variations in the dimensions of the members should not influence variations in behavior between specimen.

The material properties of all of the specimens were determined by coupon tests using ASTM A370-71 Specifications for the testing of steel products [2]. A 2 in. gage length was used in all cases. Details of the testing procedure can be found in Ref. [36]. The static yield point of the tensile coupons was determined using the 0.2% offset method. A typical stress-strain plot for a tension coupon is shown in Fig. 2.2. A summary of the tensile coupon test results is given in Table 2.2

2.2 Test Setup

The test setup is capable of applying branch axial compression, IPB, and OPB independently or in a given proportion without restricting the deflections of the joint. The setup was used and perfected during Hoadley's work. Schematic drawings of the setup are presented in Figs. 2.3 and 2.4. A photo of the test

TABLE 2.1 MEASURED SPECIMEN DIMENSIONS AND SECTION PROPERTIES

Nominal Dimensions	Measured Dimensions			Sectional Properties				
	O.D. (in.)	I.D. (in.)	Thickness (in.)	Area ($in.^2$)	I ($in.^4$)	S ($in.^3$)	Z ($in.^3$)	P_y (kips)
16" x 0.312"	16.04	15.41	0.314	15.56	481	60.0	77.9	761
10-3/4" x 0.250"	10.80	10.28	0.260	8.61	120	22.1	28.9	413
5-9/16" x 0.258"	5.61	5.09	0.262	4.37	16	5.6	7.5	173

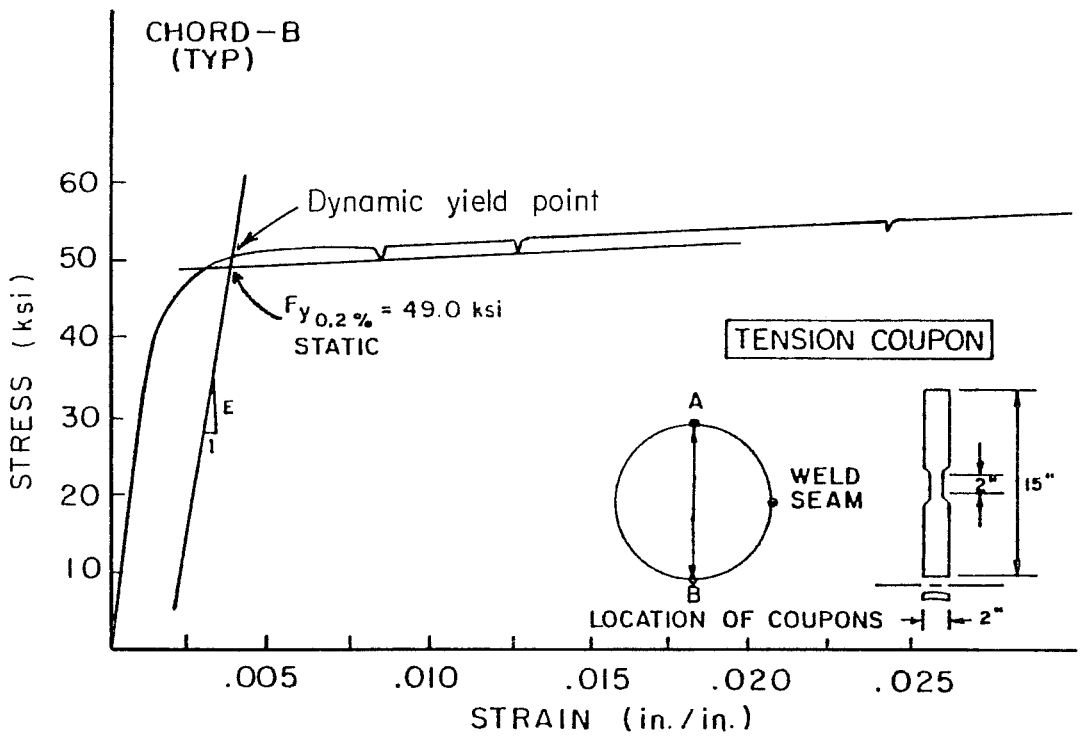

Fig. 2.2 Typical Tensile Coupon Stress-Strain Curve

TABLE 2.2 SUMMARY OF TENSION COUPON TEST RESULTS

Location of Coupon	Static Yield (ksi)	Dynamic Yield (ksi)	Ultimate Strength (ksi)	Elongation % (2 in. gages)
16" x 0.312"				
A-1	48.9	50.6	64.2	48
A-2	48.7	50.3	64.7	46
B-1	49.0	50.8	64.8	44
B-2	48.7	50.2	64.3	46
B-3	49.4	51.7	64.1	37
Average	48.9	50.7	64.4	44
Mill Report		47.0	75.5	36
API 5LX (min.)		42.0	60.0	24
10-3/4" x 0.250"*				
A-1	49.8	51.5	69.8	24
B-1	48.0	49.8	67.5	35
Average	48.9	50.7	68.7	30
API 5LX (min.)		42.0	60.0	20
5-9/16" x 0.258"				
A-1	39.2	43.6	70.9	43
A-2	37.9	40.6	73.5	45
B-1	41.8	44.3	72.1	--
Average	39.6	42.8	72.2	44
Mill Report		42.0	67.3	35
ASTM A53-GrB (min.)		35.0	60.0	23

*Mill report not available

setup is shown in Fig. 2.5. Because the test setup has been described in detail in Ref. 36; only a brief description will be provided herein. Other background information on the test setup can be found in Refs. 7, and 14.

2.2.1 Axial Loading Apparatus: The branch axial loading system consists of two 192 kip hydraulic rams located on the top and bottom of the specimen as shown in Fig. 2.3. The rams at both the top and bottom of the specimen are used to apply axial compression as well as to maintain the chord centerline elevation during bending loadings. The axial load is transferred from the ram to the branch thru a set of hemispherical bearings which allow the branch ends to rotate freely. For specimens subjected to axial compression loads close to ultimate, a ball and socket bracing attachment was placed on one end of the chord to prevent chord twisting due to small eccentricities in specimen fabrication. This attachment, which is discussed in more detail in Ref. 36, basically replaces the restraint which would be supplied by the rest of the chord member in an actual structure.

The only change in the axial loading system from Ref. 36, was for the β=0.35 specimens. This change involved the mounting of the male spherical heads of the bearings at the ends of the branch members. For the β=1.0 specimens, a large flange was fabricated on the branch ends and the male spherical heads were attached to a plate which was bolted to these flanges. The

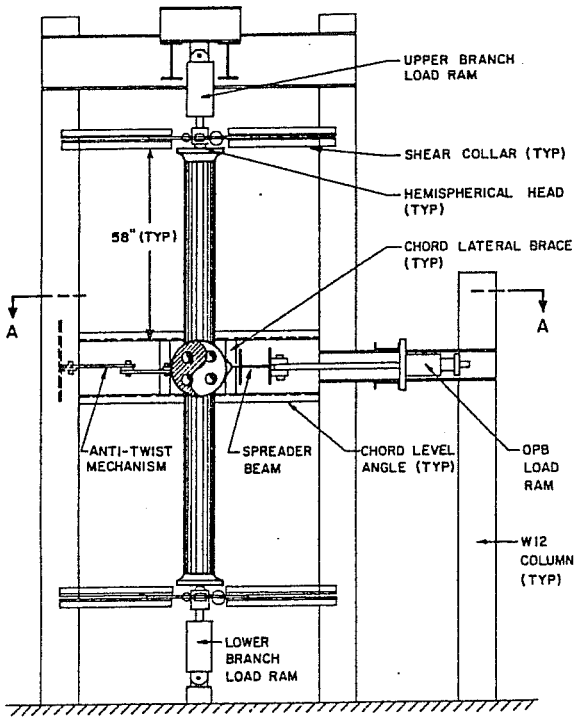

Fig. 2.3 Elevation of Test Setup

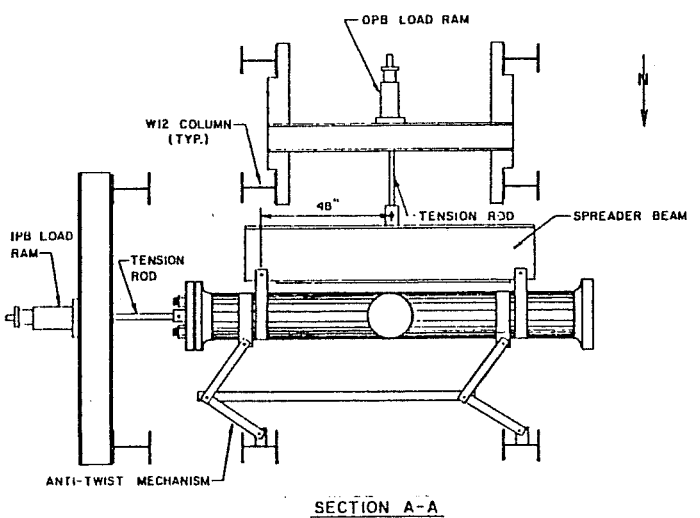

Fig. 2.4 Plan of Test Setup

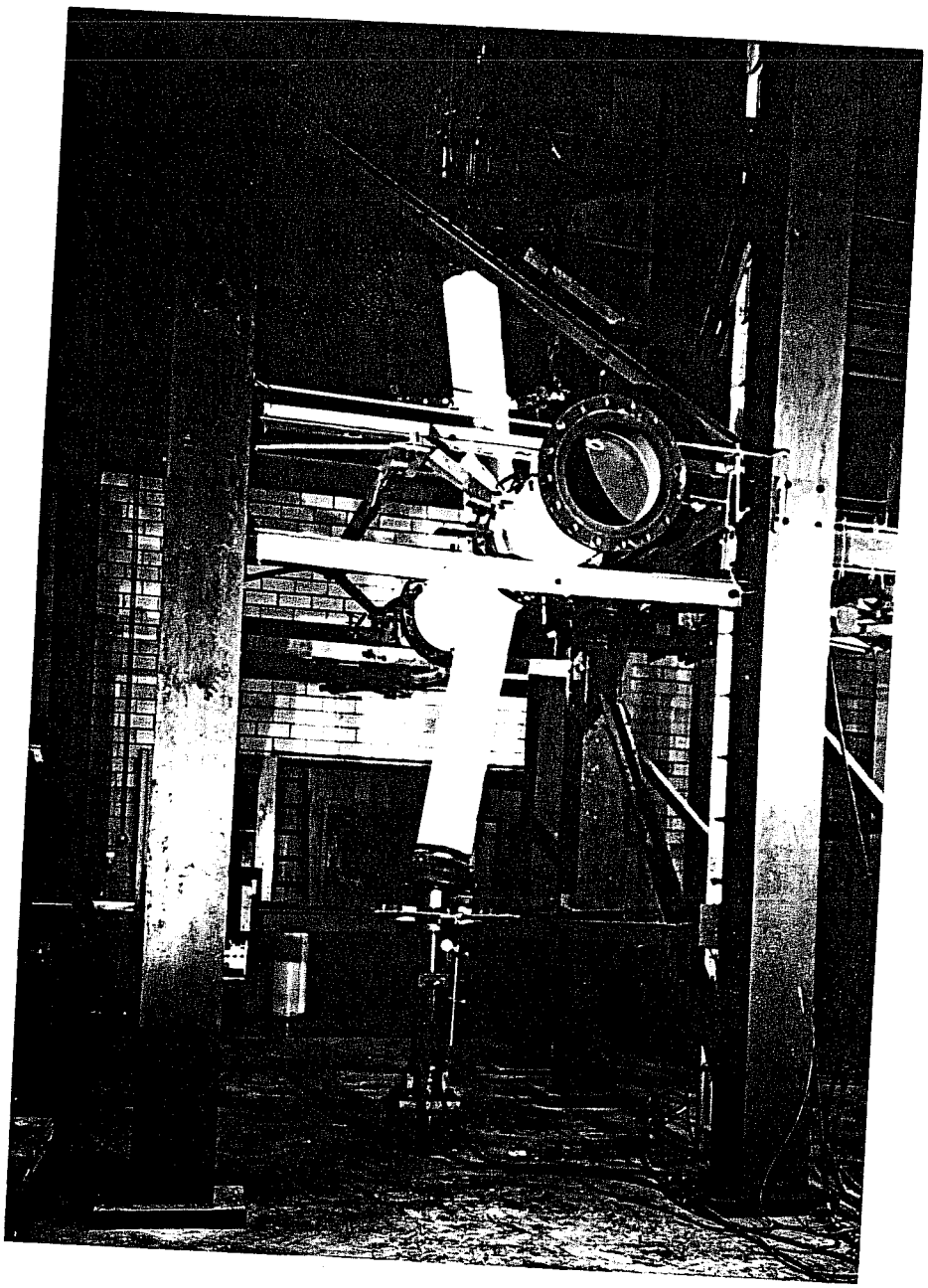

Fig. 2.5 Photo of Test Setup

branches of the β=0.35 specimens did not have flanges because of their small size; therefore, the male spherical head was attached to a plate which in turn was welded to a sleeve which fit over the open end of the branch. Two pictures of the attachment are shown in Fig. 2.6. The axial forces, which for the β=0.35 specimens were fairly small, were transferred thru friction forces developed along the sleeve and thru some end bearing on the open end of the branch. Measurements taken during the axial reference test (A40), in which the highest axial load of the test series was applied, showed no slipping between the sleeve and the branch.

2.2.2 Bending Load Apparatus: Bending in the branch members was developed by pulling the chord either in the plane of the chord and branch (IPB) or normal to the plane of the chord and branch (OPB) which developed shear forces at the top and bottom of the specimen. The piston of the axial rams travelled thru a set of roller bearings which allowed vertical but not horizontal movement. The roller bearings were attached to shear collars which resist the horizontal shear forces produced during bending. The combination of hemispherical and roller bearings at the end of the branches allowed for free rotation and compression of the joint. Thus, each branch acted like a cantilever beam with a restrained end at the joint and the load applied at the shear collar.

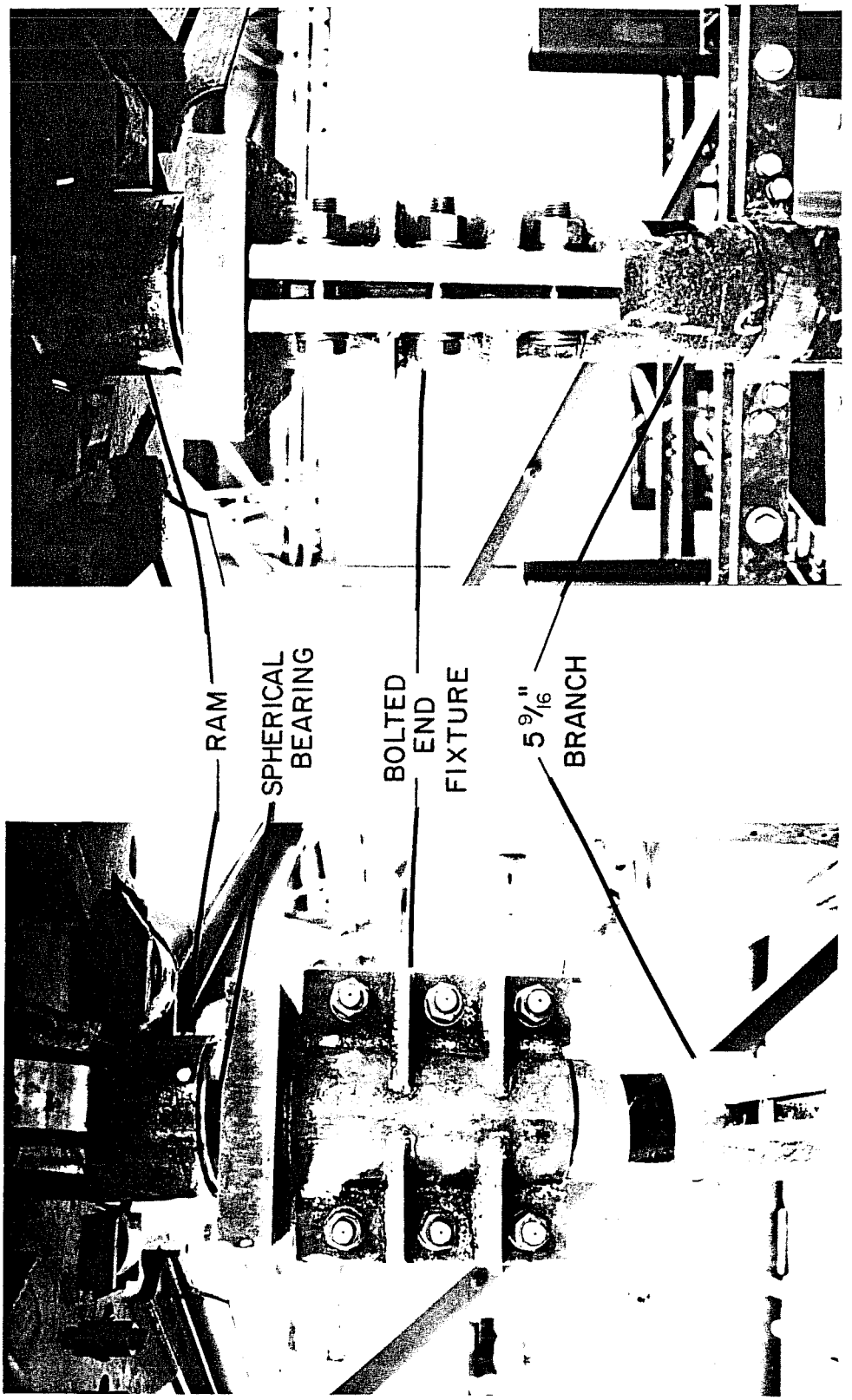

Fig. 2.6 Axial End Fixture for =0.35 joints

In addition to the apparatus described in Ref. 36, gravity load simulators or Roberts mechanisms were used to allow the specimen to move in both the in-plane and out-of-plane directions independently during loading. These mechanisms maintain the line of action of the load as the specimen deforms. That is, the OPB jack is always perpendicular to the longitudinal centerline of the chord and the IPB jack is always parallel to the longitudinal centerline of the chord. This simplifies the calculation of the forces and moments applied to the joints by eliminating the component forces which would result if the line of action is not constant as shown in Fig. 2.7. This simplification of the force calculations allows for more specific definitions of failure by uncoupling the effects of each loading source. It also allows for easier recognition of failure during actual testing which is very important for complicated loadings. A schematic drawing of a Robert's mechanism is given in Fig. 2.8. More details of the use of the Robert's mechanism in this test setup is given in Ref. 15. Details of the design of a Robert's mechanism and its use in structural testing are given in Ref. 38.

2.3 Loading System

A schematic of the typical loading diagram is shown in Fig 2.9. Hydraulic pressure is provided by a single electric pump and a multipressure load maintainer is used to control the pressure to each of the up to four hydraulic rams used during testing. The

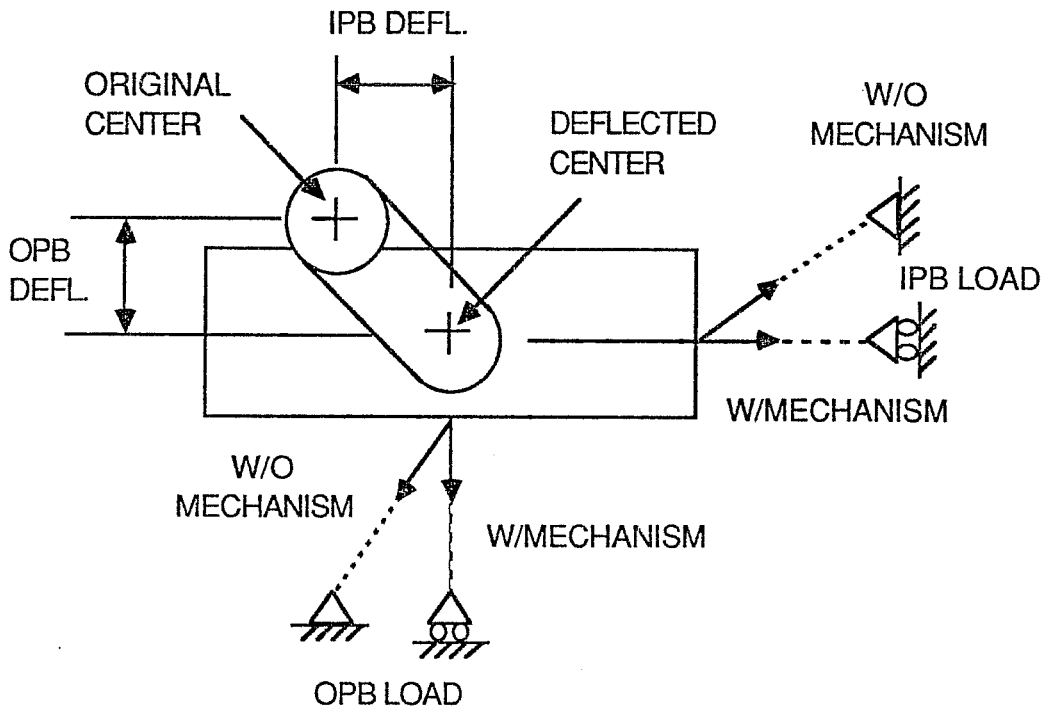

Fig. 2.7 Change in line of Action of Forces with and without Robert's Mechanism

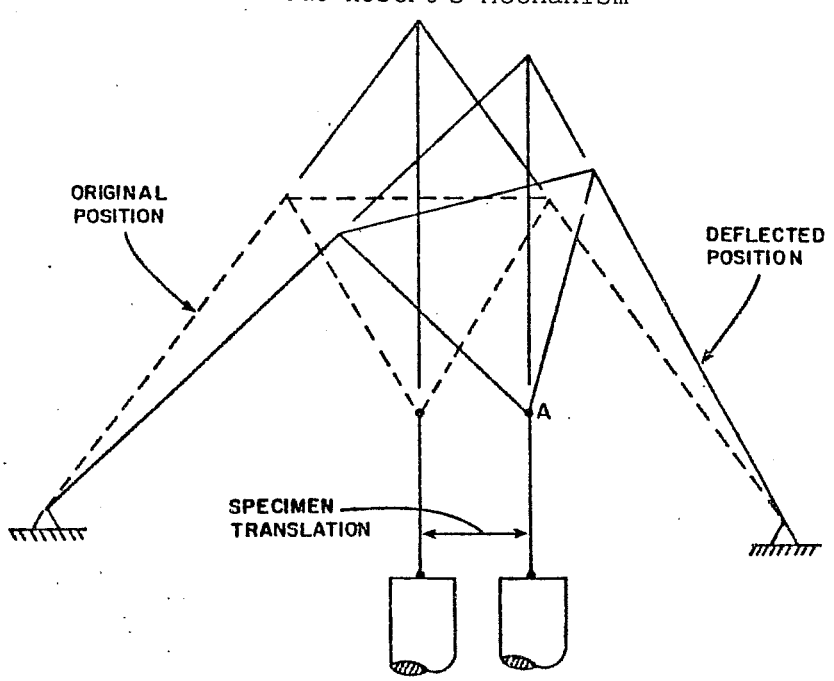

Fig. 2.8 Schematic of Robert's Mechanism

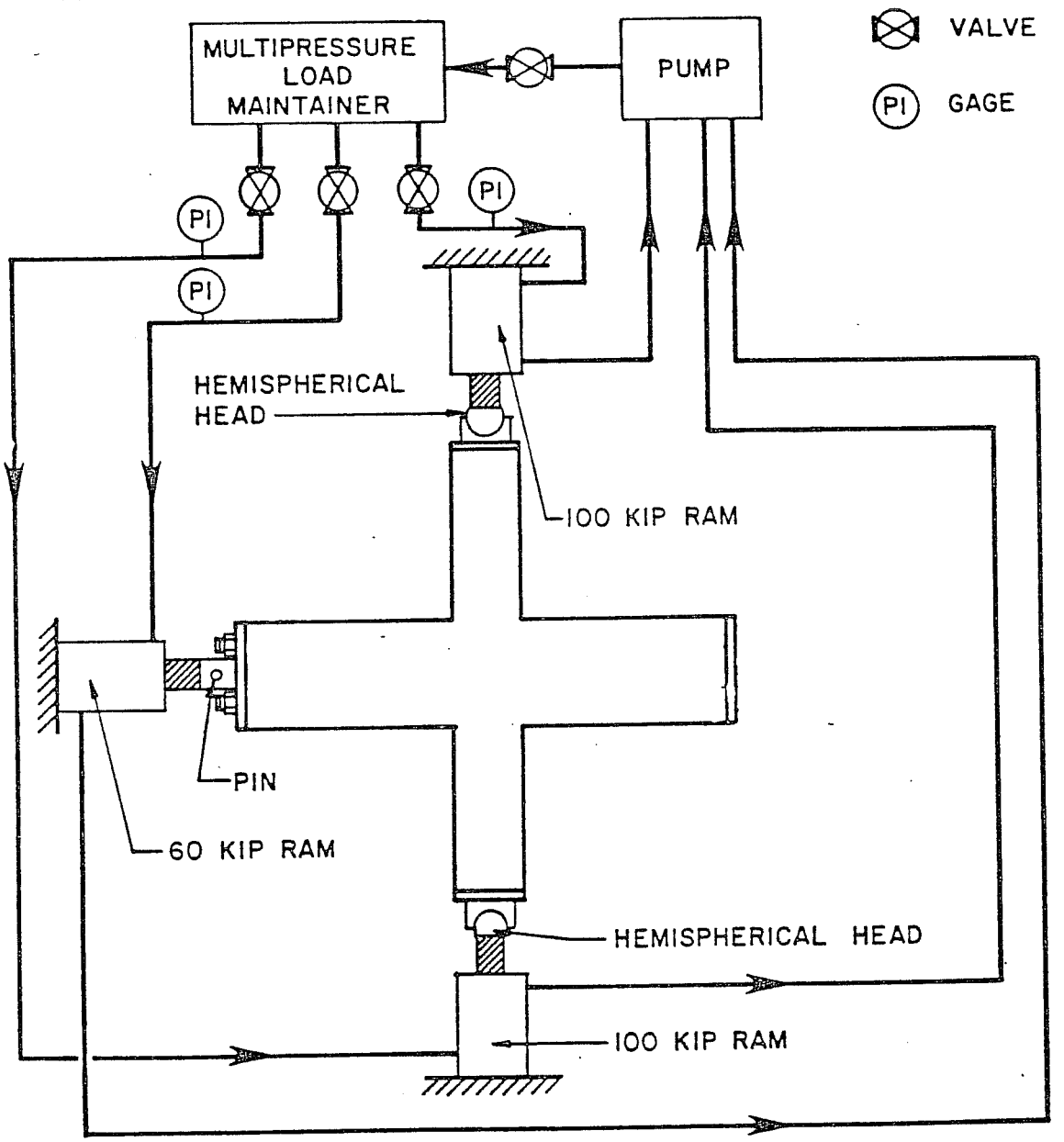

Fig. 2.9 Schematic of Loading System

pump, load maintainer, and rams were all connected using flexible pressure hoses. The heart of this system is the load maintainer which enables the operator to control each ram independently of the others, or to increase the pressure to any set of rams in a constant proportion, or to maintain a given differential in pressure between any set of rams while changing the overall pressure. More detailed discussion of the loading system is given in Ref. 15.

2.4 Instrumentation

The objective of each test was to establish a load-deflection curve from which the ultimate joint capacity could be determined. Each of the loads applied to the specimen was monitored by a pressure gage accurate to 25 psi and a pressure transducer accurate to 0.25%. The loads taken from the transducer readings are considered accurate to $\pm$0.5 kips. The output from the pressure transducers was monitored with a data acquisition system which translated the voltage readings into engineering units. For the axial loading tests, the reported loads are based on the load in the lower ram.

The deformation of the specimen was measured with mechanical dial gages accurate to 0.001 in. with stokes of 2 or 5 in. and with linear voltage displacement transducers (LVDT's) with strokes of 2 or 6 in.. The locations of the dial gages and LVDT's are indicated in Fig. 2.10. In addition to these gages,

transit readings were used as an independent verification of deflections. The axial deformations of the branches were monitored by gages at locations 1 and 2. In order to compare the results of several tests which failed by axial loading during interaction testing, it was found that the average of the top and bottom branch deflections gave a better indication of the joint behavior than the bottom deflection corrected for rigid body motion. Thus, the average of the readings at locations 1 and 2 is used to define the axial deformation presented in this report. Gages 3 and 4 were used to monitor the rigid body motions of the specimen during testing. The out-of-plane deflection of the branches was monitored with gages at locations 5 and 6. The average of these two readings defines the out-of-plane deflection at the centerline of the chord. Gages at location 7 measured the in-plane movement of the chord directly. The area of the joint was whitewashed prior to testing so that yielding could be visually identified during testing as the whitewash flaked away from the steel with the brittle mill scale. The references to the location and extent of yielding included in the test descriptions are based on observations of the pattern of whitewash flaking.

2.5 General Test Procedure

Except for the reference tests, all tests involved the interaction of two types of loading, axial with IPB, axial with

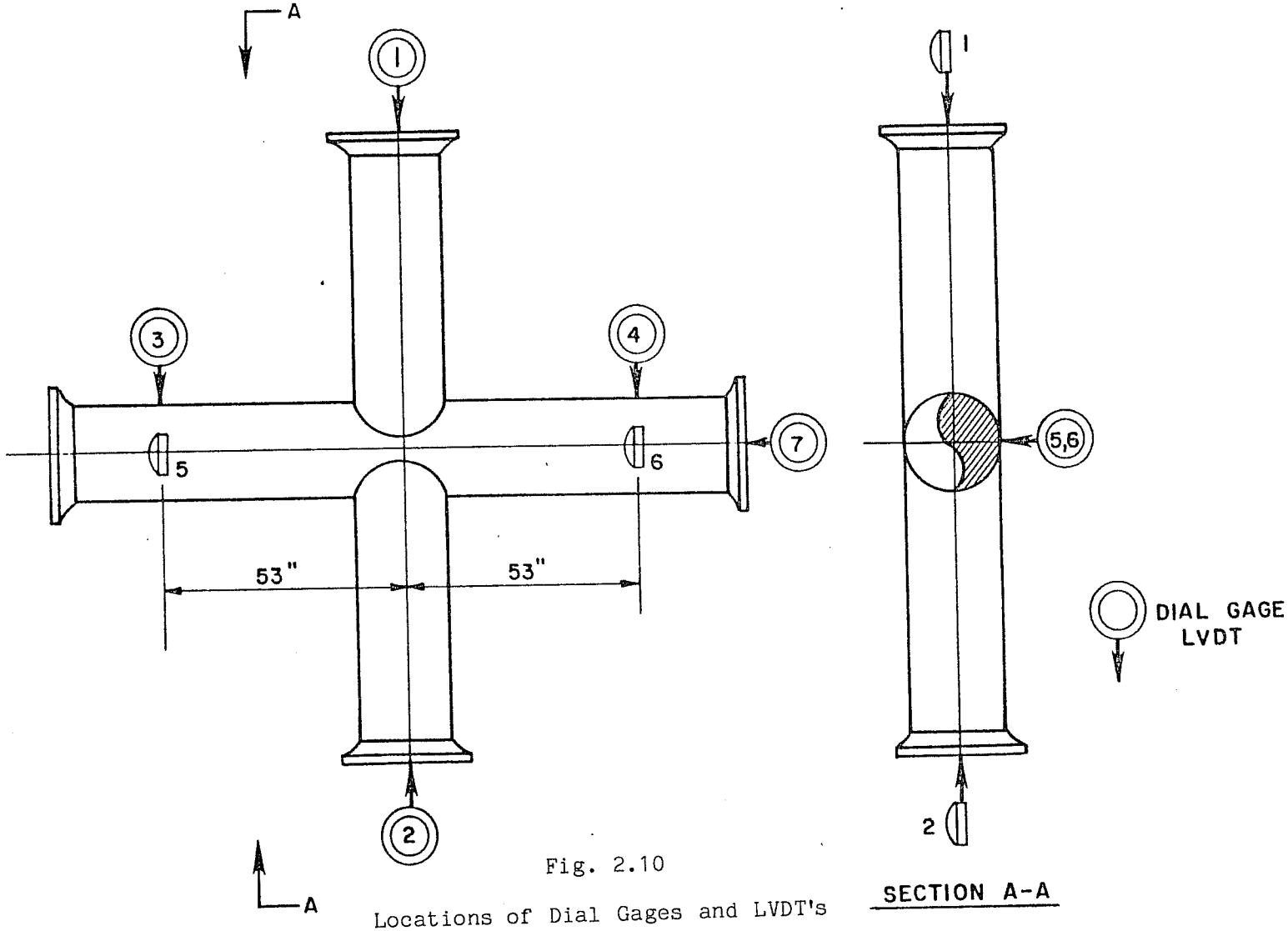

Fig. 2.10

Locations of Dial Gages and LVDT's

OPB, and IPB with OPB. The same general procedure was followed in the testing of all but two specimens. First, any axial load required to seat the specimen in the upper and lower hemispherical bearings was applied. In the interaction tests one type of loading (axial, IPB, or OPB) was applied first and held constant at a fraction of the ultimate load obtained in the reference test(s), then the other type of loading was increased from zero to failure. This procedure was used because; 1.) it enabled failure to be more easily established and, 2.) the resulting test data is more suitable for comparisons with theoretical results.

A proportional loading procedure was used for Tests AI50 and I026 in order to get data points on the interaction diagrams that represent large values of both loading variables. In the proportional loading procedure the load maintainer was set so that the two loading types increased in proportion to their respective ultimate strengths. As with the general test procedure, the bearings were first seated with a small axial load. Then, the loads in both directions were applied in the set proportion and increased until failure occurred. A detailed description of the criterion for failure is given in the next chapter.

Once first yielding was noted by the flaking of whitewash, static yield points were taken at each loading interval. The oil

flow to the pressure side of the loading ram(s) was shut off preventing any further loading in that direction, and the load was allowed to reduce to its static point after approximately 5 minutes. The same procedure was used during the testing of the tensile coupons to determine static yield points. The static load level is the load reported in the tabulated test data in Appendix B and is also used in the construction of the load-deflection curves presented in the next chapter.

CHAPTER 3

TEST RESULTS

Seventeen tests were conducted on specimens with DT joints using combinations of axial compression, IPB, or OPB in the branches. Eleven of the joints had a β ratio of 1.0, the remaining six joints had a β ratio of 0.35. The combinations of loadings included; branch axial compression with IPB (AI), branch axial compression with OPB (AO), and IPB with OPB (IO). A total of nine tests were used as reference cases. Five tests involved joints with β=1.0 and four involved joints with β=0.35. Three of the β=1.0 reference tests, A21, O23, and I24; and one β=0.35 reference test, A40, were reported earlier [37], but are included here for completeness. A complete outline of the testing program is shown in Tables 3.1 and 3.2.

The results of each test are presented in a tabular form in Appendix B along with the formulae used to calculate moments and rotations. The development of these equations was completed and reported with the results of Phase 2 [15]. It should be noted that the equations used to calculate moments include the secondary effects which become important in the moment calculation with large displacements.

TABLE 3.1 OUTLINE OF TESTING PROGRAM FOR β = 1.00 JOINTS

Test No.	% of Ultimate Axial at Failure	% of Ultimate OPB at Failure	% of Ultimate IPB at Failure
Reference Tests			
A21	100	---	---
A22	100	---	---
O23	---	100	---
O28	---	100	---
I24	---	---	100
Interaction Tests			
AO31	25	Failure	---
AO32	50	Failure	---
AO33	Failure	25	---
AI34	25	---	Failure
AI35	50	---	Failure
AI36	Failure	---	50
AI50	Failure	---	Failure
IO37	---	Failure	25
IO38	---	Failure	50
IO39	---	50	Failure
IO26	---	Failure	Failure

TABLE 3.2 OUTLINE OF TESTING PROGRAM FOR β = 0.35 AND 0.67 JOINTS

Test No.	% of Ultimate Axial at Failure	% of Ultimate OPB at Failure	% of Ultimate IPB at Failure
β = 0.35 Reference Tests			
A40	100	---	---
A41	100	---	---
O42	---	100	---
I43	---	---	100
Interaction Tests			
AO44	30	Failure	---
AO45	70	Failure	---
AI46	30	---	Failure
AI47	70	---	Failure
IO48	---	Failure	30
IO49	---	Failure	70
β = 0.67 Tests			
A51	100	---	---

3.1 Definition of Failure

Three independent criteria were used to determine failure. The first is a strength criterion by which failure is defined when the specimen can no longer maintain a maximum loading level. The second is a deformation criterion by which failure is defined when the specimen deforms past a certain predetermined limit. The third criterion is based on stability and defines failure when the specimen buckles out of the plane of loading. For example, failure by the third criterion would occur if the specimen began to deform in the out-of-plane direction due to axial loading while testing for in-plane strength.

The first and third failure criteria are fairly straightforward. The second criterion based on a deformation limit is much more subjective. The use of a deformation limit is particularly important in determining the ultimate strength of joints because the member moments and deflections in a framed structure are very sensitive to the flexibility and rotation capacity of the joint. A specific value for a useful deformation limit is difficult to define. In short, the deformation limit is reached when deflections are large enough to require the replacement of the member or when the geometry used in the structural analysis is significantly altered.

One concept of a useful deformation limit is described in Ref. 4. This useful deformation limit is based on a deflection of

four times that at yield. For branch bending, the deflection used is arbitrarily defined as the deflection at the centerline of a simply supported beam under a uniform load. This definition is intended to model the useful deflection of a branch member in an offshore structure subjected to wave loadings. From this assumption, the useful deformation limit in terms of rotation at the supports is defined by the following equation, assuming small rotations:

$$\theta_{useful} = 4\theta_y = (8/3)(F_y/E)(L/d) \qquad (3.1)$$

This limit, assuming a typical L/d of 30, was proposed for use in offshore tubular joint testing by Yura and Zettlemoyer [40]. F_y is taken as the chord yield stress. The resulting useful rotation limit is 7.73° for the joints used in this study.

To determine its applicability, the limit given by Eq. 3.1 was used in the analysis of a member in an offshore structure. An example analysis was done on an 18 in. o.d. horizontal member with a 45 ft. span attached to a 50 in. o.d. main vertical member, as shown in Fig. 3.1. If the 18 in. branch is subjected to a uniform wave load, in-plane bending loads will occur in the joint. An elastic-perfectly plastic moment-rotation curve as shown in Fig. 3.2 was assumed for the branch based on an F_y equal to that of the chord. The joint, circled in Fig. 3.1, is a DT type joint with β=0.36. The moment rotation information for

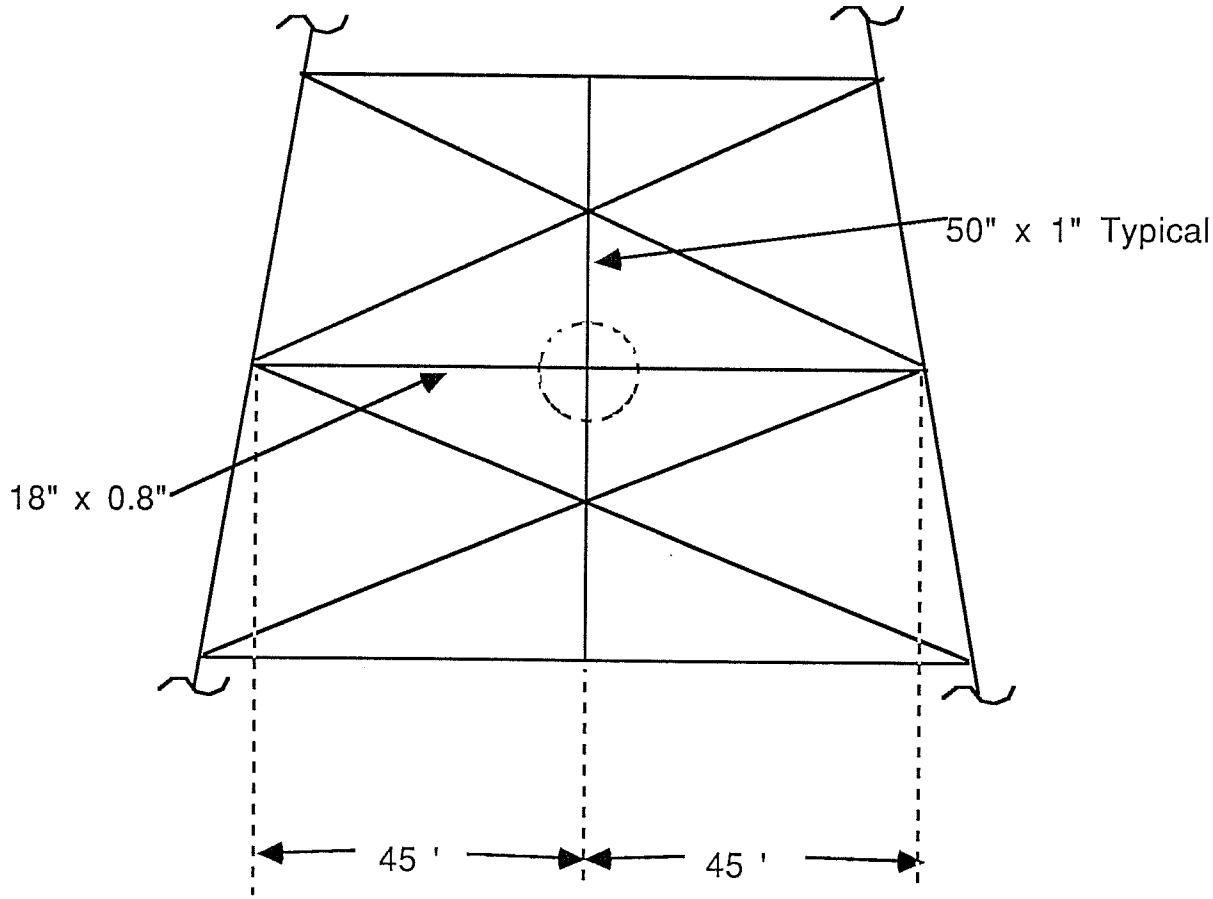

Fig. 3.1 Example Deformation Problem

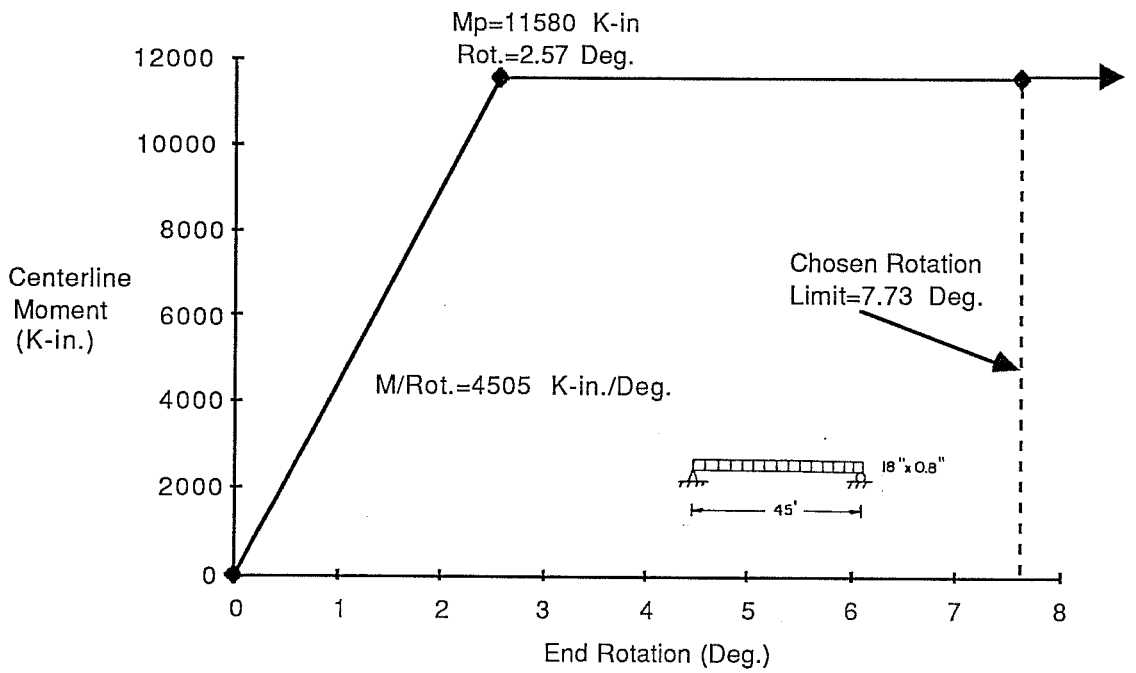

Fig. 3.2 Example Branch Centerline Moment-End Rotation Curve

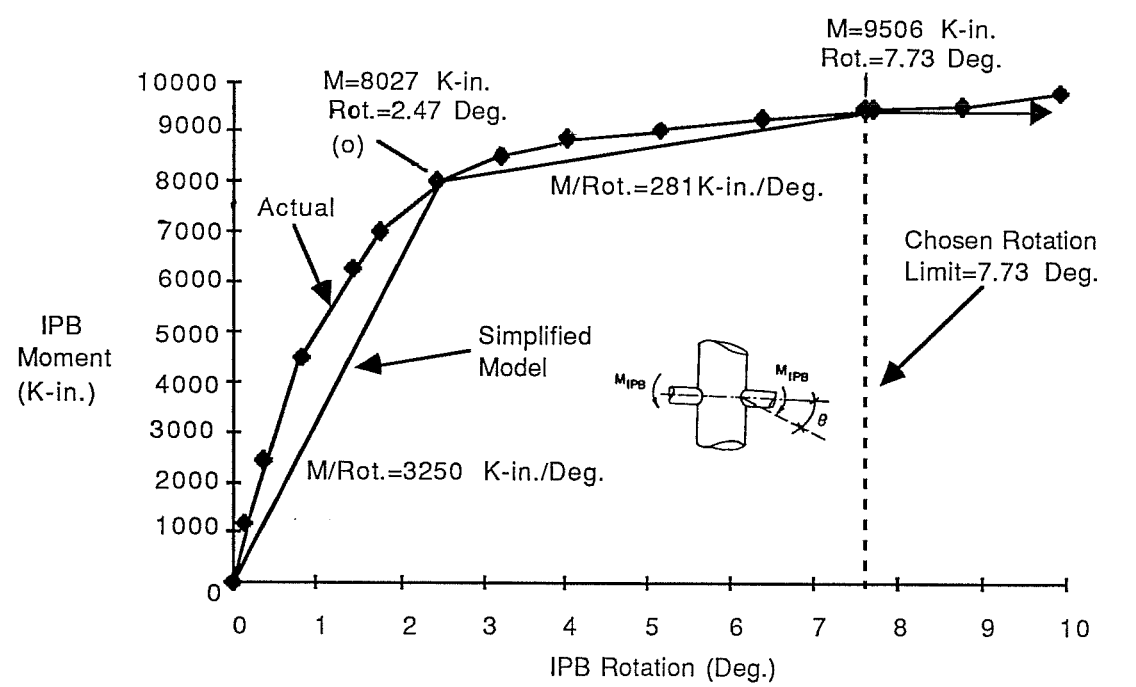

Fig. 3.3 Example Joint Moment Rotation Curve

the joint was taken from the results of an IPB reference test on a β=0.35 joint (I43). A simplified model of the joint loading curve is shown in Fig. 3.3 along with the actual moment-rotation curve for the joint. The member was analyzed with springs representing the joints. The purpose of this analysis was to determine how much the branch would have to deflect for the joint to reach its ultimate strength. The resulting uniform load vs. centerline deflection in the beam curve is plotted in Fig. 3.4. There are three points of interest in Fig. 3.4, when the beam reaches it plastic capacity and forms a hinge at the center (a), when the joint stiffness is reduced as indicated at point (o) in Fig. 3.3 (b)and in Fig. 3.4, and when the joint forms a plastic hinge (c). The curve shows that a centerline deflection of approximately 34 in., or an L/Δ of 15.8, is required to reach the ultimate capacity of the joint. The acceptability of this deformation limit in a failure type analysis is a matter for the designer to decide; however, for the purposes of this report the deformation limit given by Eq. 3.1 is used.

When used in testing joints with β=0.67 and 0.35, the deformation limit given by Eq. 3.1 seemed reasonable by visual inspection of the joints. But when loading the β=1.0 specimens in out-of-plane bending, there was considerable distress and gross distortion of the chord on the compression side of the joint at rotations of between 4° to 5°, as shown in Fig. 3.5, which is

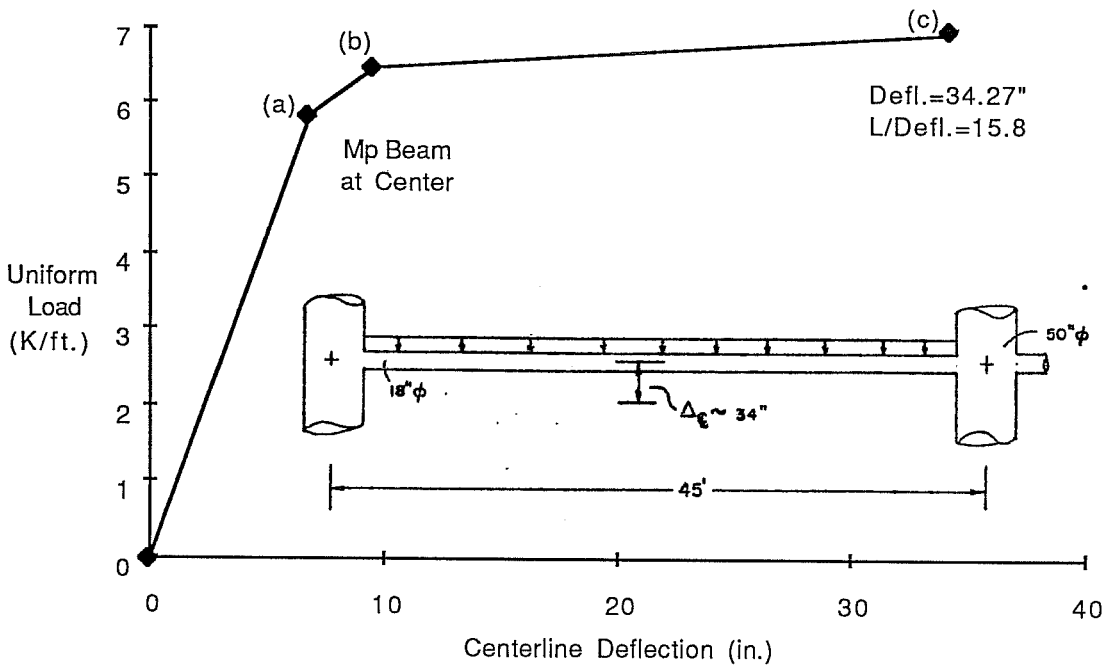

Fig. 3.4 Uniform Load vs. Centerline Deflection of Example Branch Member

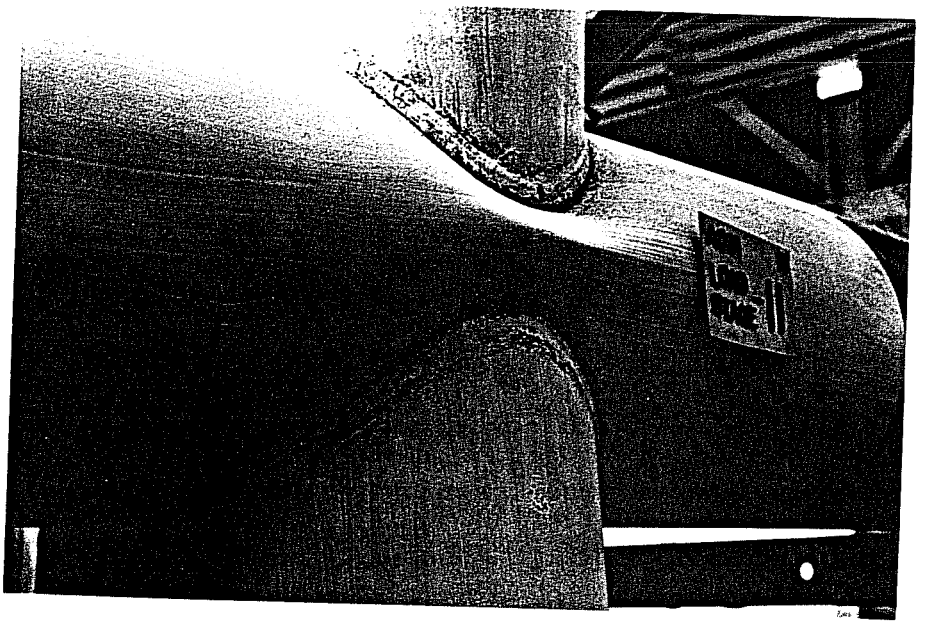

4° Rotation

7.75° Rotation

Fig. 3.5 Example of Joint Distortion for β=1.0 Specimen

considerably lower than the deformation limit of 7.73° given by Eq. 3.1. Since such local distortions are similar to local buckling in plate structures, it was felt that an additional useful limit should be imposed that considers the distortion of the chord material in the joint area.

The limit given by Eq. 3.1 is in terms of a rotation, but the distortion of the chord material is a result of the branch end displacements at the saddle region of the chord. As the branch diameter becomes larger, the deformation at the tips of the branches increases for a constant branch rotation. For example, the 7.73° rotation limit would require in a 0.76" rigid body movement of the branch in the saddle region in OPB for a β=0.35 joint while the same rotation creates a 2.18" movement in the β=1.0 joint. In addition, due to the geometry of the β=1.0 joint, there is much less material between the branches at the saddle points to absorb the deformations imposed by the branch movement than in the β=0.35 joint. For the β=1.0 joints, the distance between the branches at the saddle averaged 3.6", for a 7.73° rotation limit, each branch tip would move 2.18" or a total of 4.36". In order to reach the deformation limit given by Eq. 3.1, the branch tips on the compression side would have to overlap by almost 1" before failure. This definition is unreasonable. Therefore, an ultimate deformation limit for OPB was defined as the rotation at which the tips of the branches

would touch in OPB as shown in Fig. 3.6. With an average distance between the saddle points, or gap, of 3.6 in. and a diameter of 16 in., this rotation is 6.42°.

3.2 Reference Tests

3.2.1 Axial Loading-β=1.0

3.2.1.1 Test A21. The load-deflection curve for Test A21 is plotted in Fig. 3.7a. The lower axial load is plotted versus the average deflection of the branches as discussed in the instrumentation section of Chapter 2. First yielding occurred at Load Stage 9 at a load of 150.5 kips. The initial yielding occurred at the weld toe on the saddle position of the joint shown as point "a". An ultimate load of 172.7 kips was achieved at an average branch deflection of 0.339 in. During testing, yielding progressed from the saddle points to about 45° from the saddle of the joint. No yielding was apparent near the crown. Failure occurred when the chord wall between the weld toes at the saddles buckled. This type of failure is shown in Fig. 3.8. After the ultimate load was reached, yielding progressed into the chord region around the saddle points.

3.2.1.2 Test A22. The load-deflection curve for Test A22 is plotted in Fig. 3.7b. First yielding occurred at Load Stage 7 with a load of 133.8 kips in the lower ram. The initial yielding occurred at the weld toe on the saddle position of the joint

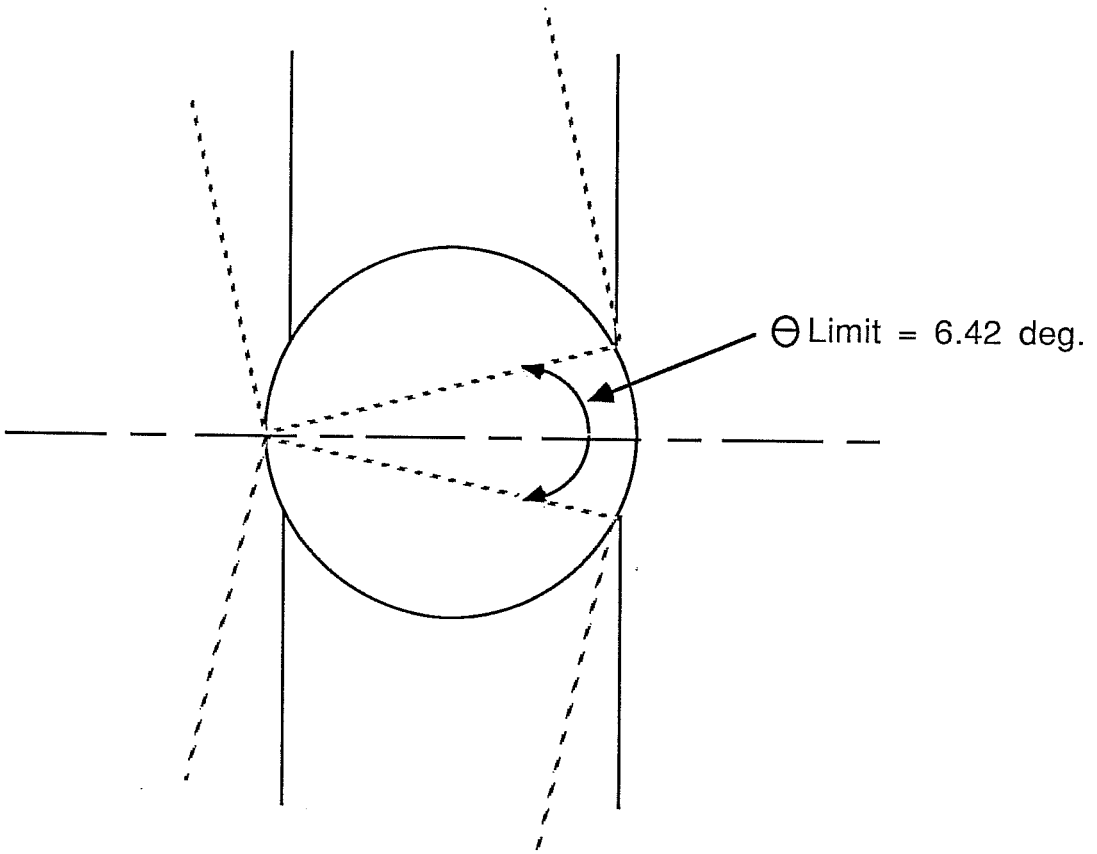

Fig. 3.6 Schematic of Definition of Deformation Limits for ß=1.0 Specimens

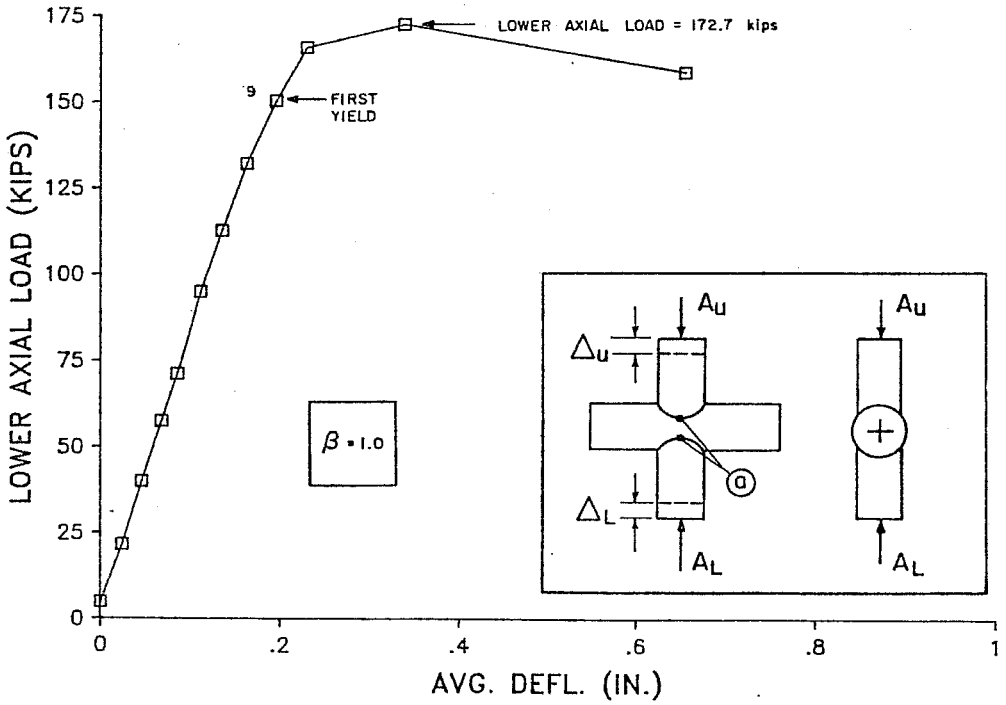

a.) Test A21

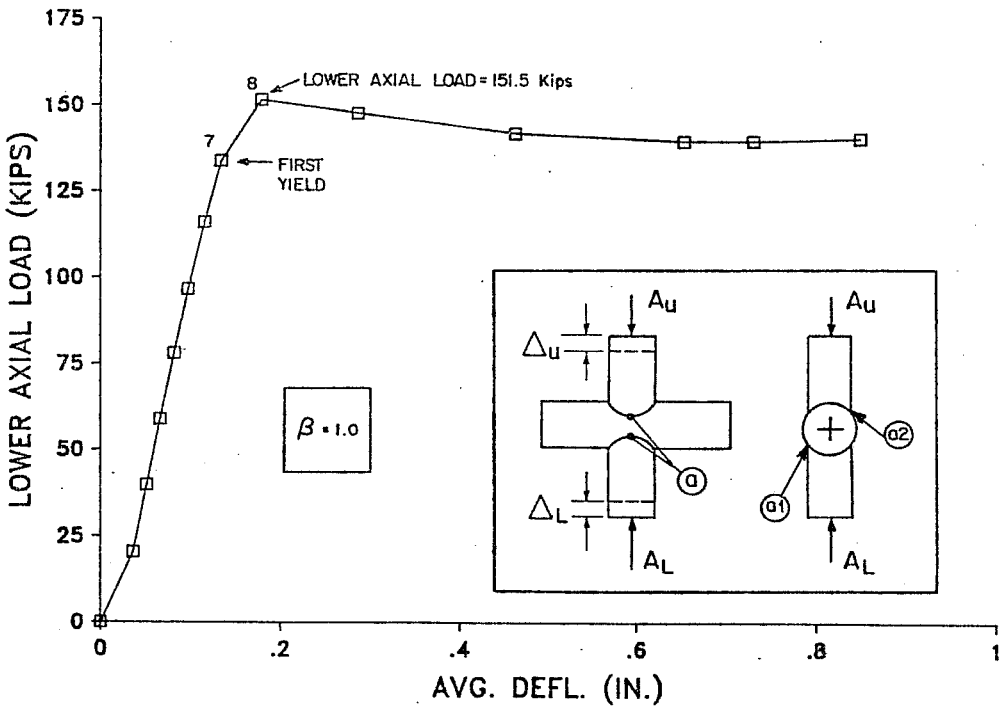

b.) Test A22

Fig. 3.7 Load-Deflection Curve for Tests A21 and A22

shown as point "a1" on the bottom of one side of the joint and the top of the other side "a2". This unsymmetrical yielding indicates that the branches of the specimen were not perfectly aligned on the chord. An ultimate load of 151.5 kips was achieved at an average branch deflection of 0.179 in. at Load Stage 8. During testing, yielding progressed from the saddle points to about 45° from the saddle of the joint. No yielding was apparent near the crown. Failure occurred when the branches began to rotate out of the plane of the chord and punch into the chord. This type of failure is shown schematically in Fig. 3.9. From measurements taken at the ends of the chord, it was shown that the twisting of the chord was localized in the joint region.

The ultimate load for Test A22 of 151.5 kips compares with 172.7 kips for Test A21. The difference between the two test results is 13.3% . For the purpose of the interaction equations discussed in the next chapter, the reference value will be the average of the two, 162.1 kips.

3.2.2 Axial Loading β=0.67

3.2.2.1 Test A51. This test is similar to Test A1 which was reported in Phase 2 [14]. Because specimens A51 and A1 were fabricated at different times, the exact material properties and specimen dimensions are not identical. The load-deflection curve for Test A51 is given in Fig. 3.10. First yielding occurred at Load Stage 4 with a load of 43.6 kips at the saddle points of the

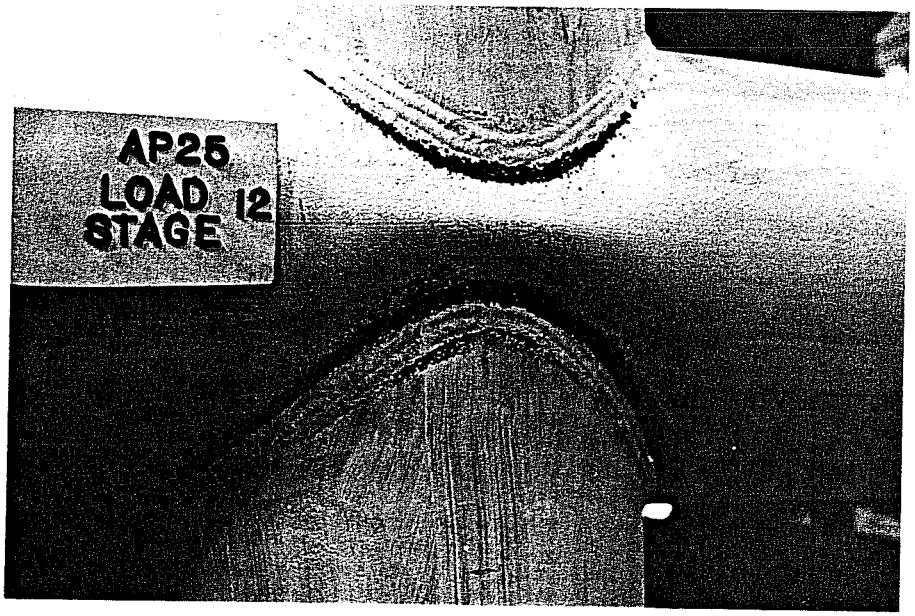

Fig. 3.8 Typical Compression Failure by Buckling of Chord Wall

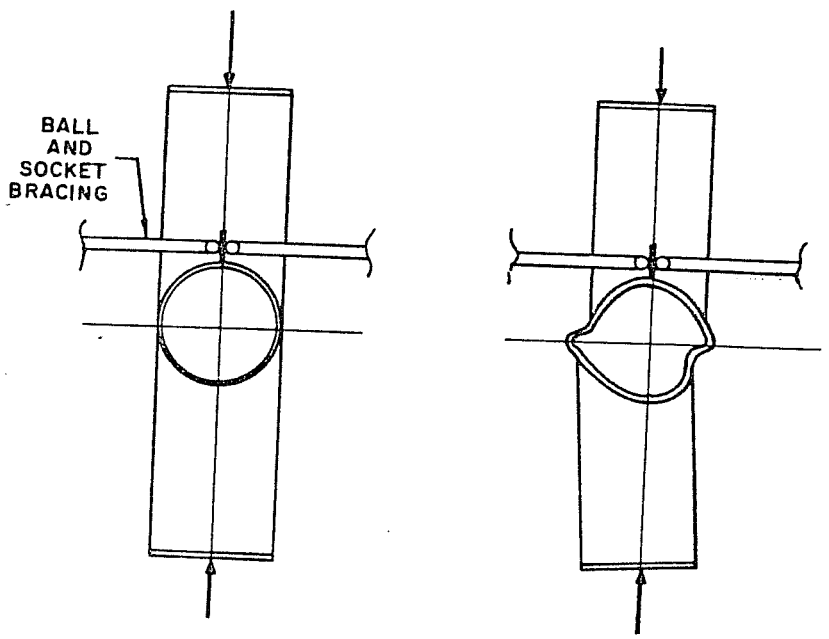

Fig. 3.9 Schematic of Chord Twisting Failure

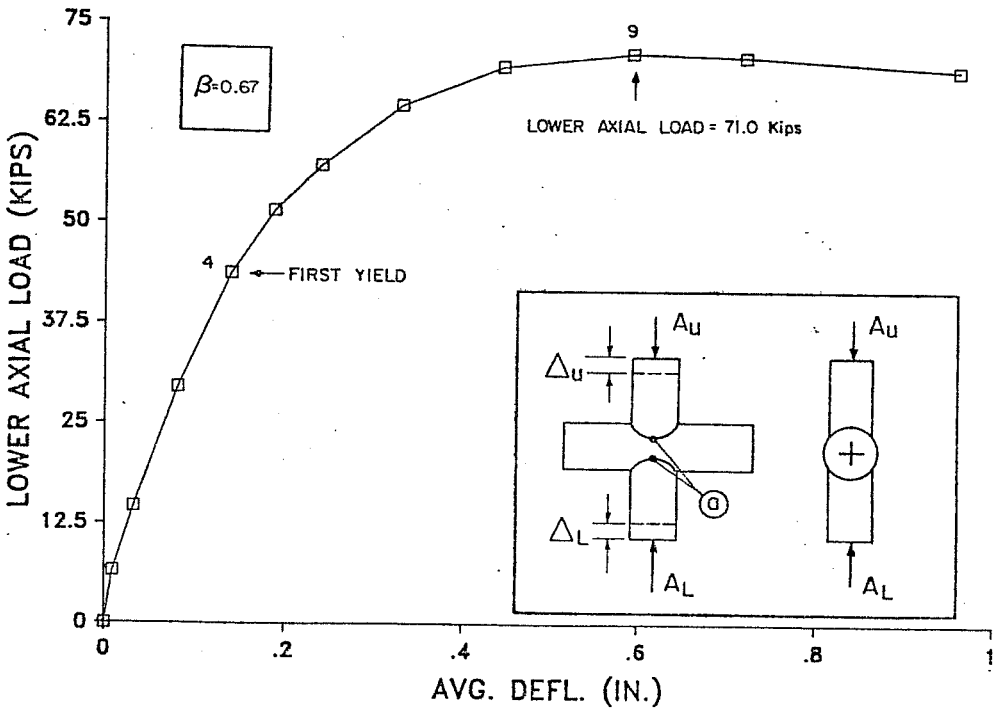

Fig. 3.10 Load-Deflection Curve for Test A51

joint. The ultimate load of 71.0 kips was reached at an average deflection of 0.594 in. at Load Stage 9. At ultimate, the yielding at one saddle was much more significant than at the other indicating a twisting type failure. This is probably a result of an initial out-of-plane displacement of about 0.35 in. due to fabrication. After ultimate, the top branch began to deflect much more than the bottom and yielding spread around the entire weld connecting the branch to the chord.

Due to the difference in material properties of the two specimens, the results of Tests A1 and A51 could not be simply averaged to determine a reference value. The ultimate loads were first nondimensionalized using the form P/T^2Fy. The nondimensionalized values were then averaged. The average nondimensionalized value was then transformed into a reference axial load using the material properties and specimen dimensions of the β=0.67 interaction tests which are given in Ref. 15. The resulting reference axial load is 73.9 kips.

3.2.3 Axial Loading β=0.35

3.2.3.1 Test A40. The load-deflection curve for Test A40 is plotted in Fig. 3.11a. First yield occurred at the saddle point of the joint during Load Stage 3 at an axial load of 27.1 kips in the lower ram. The ultimate load of 42.0 kips was reached at an average deflection of 0.616 in. at Load Stage 7. Yielding began on the top of the joint and spread from the saddle points

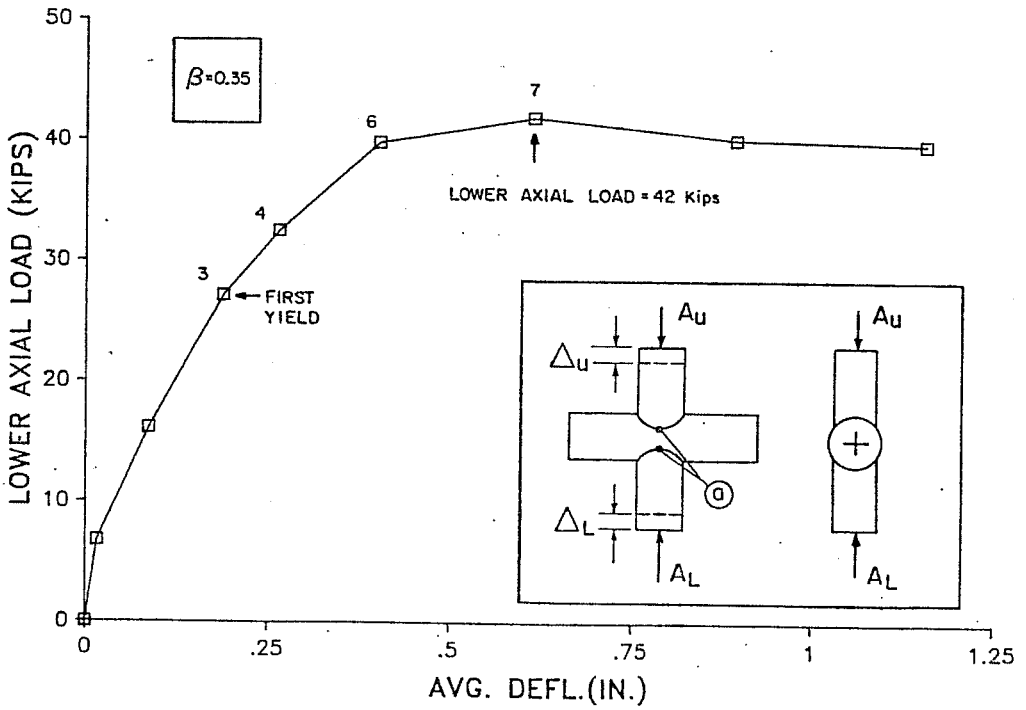

a.) Test A40

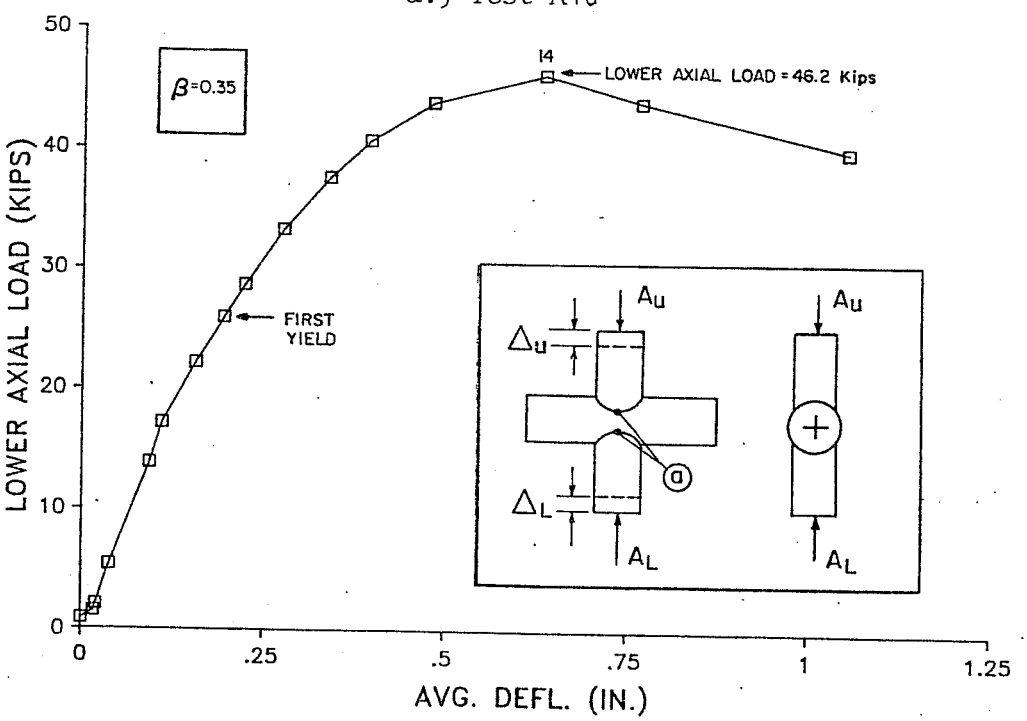

b.) Test A41

Fig. 3.11 Load-Deflection Curve for Tests A40 and A41

around the weld connecting the branch to chord. Yielding did not begin on the bottom of the joint until Load Stage 6. Failure occurred as the top branch began to punch into the chord wall. After failure, the branches began to rotate out-of-plane and the chord twisted by slipping in the chord anti-twist attachment. In addition, the chord rotated slightly about the joint centerline. The failed specimen is shown in Fig. 3.12.

3.2.3.2 Test A41. The load-deflection curve for Test A41 is plotted in Fig. 3.11b. First yield was detected at the saddle points at the top of the joint at a load of 25.9 kips. The ultimate load of 46.2 kips was attained at an average deflection of 0.585 in. at Load Stage 14. After the ultimate load was reached, yielding progressed around the branch-to-chord weld as shown in Fig. 3.13. Most of the deflection is due to gross bending of the chord wall very close to the branch.

The ultimate loads of Tests A40 and A41, 42.0 and 46.2 kips respectively, have a difference of 9.5%. The average of the ultimate strengths, 44.1 kips, will be used as a reference in the interaction equations.

3.2.4 OPB-β=1.0

3.2.4.1 Test 023. The moment-rotation curve for Test 023 is shown in Fig. 3.14a. First yielding occurred at the saddle of the lower branch connection at a moment of 819 kip-in. At Load Stages 8 and 9 yielding progressed around the bottom branch to

Fig. 3.12 Picture of Specimen A40 After Failure

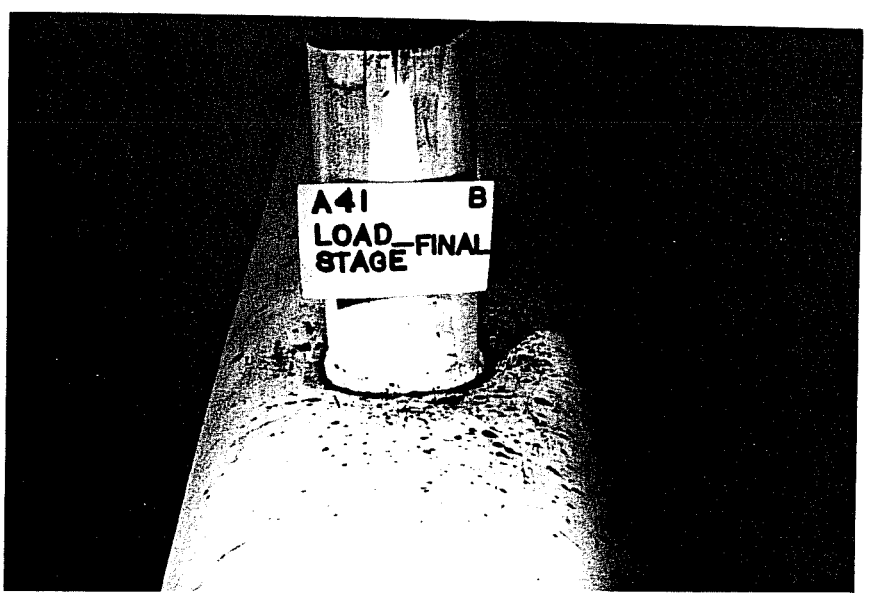

Fig. 3.13 Picture of Specimen A41 After Failure

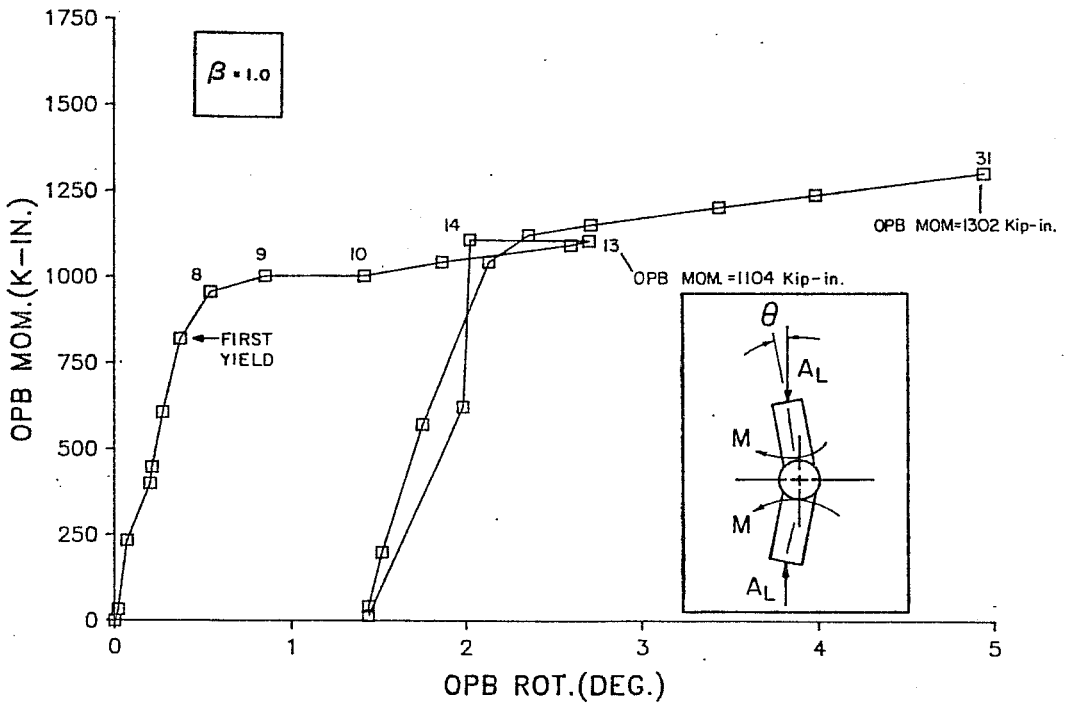

a.) Test 023

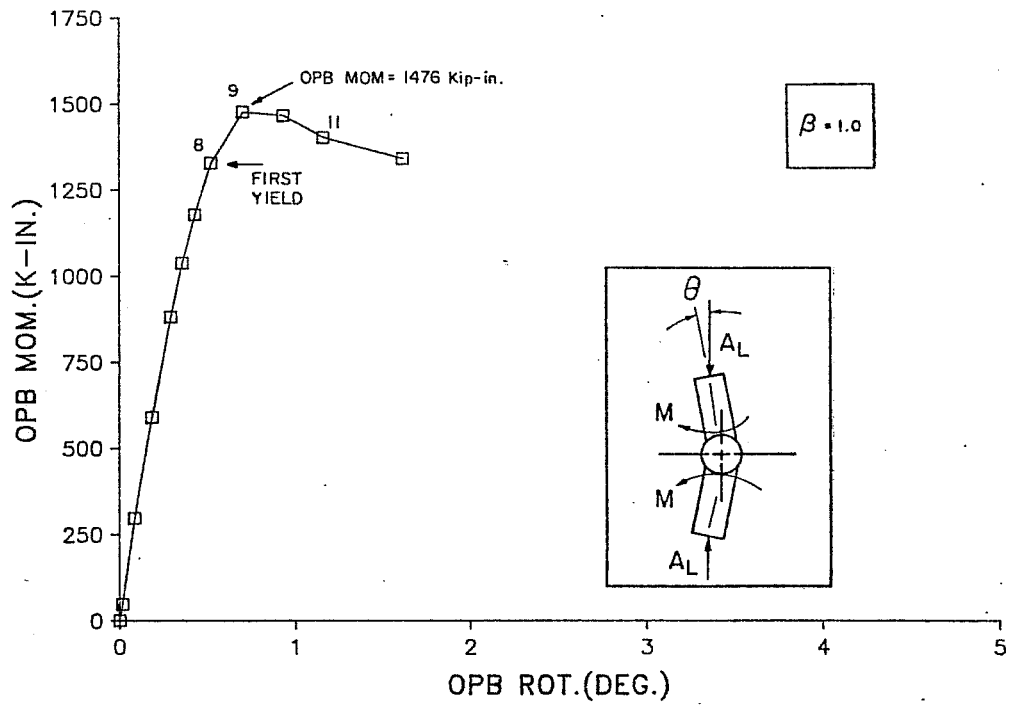

b.) Test 028

Fig. 3.14 Moment-Rotation Curve for Tests 023 and 028

about 45° from the saddle point on the connection. Buckling of the chord wall between the weld toes on the compression side began at Load Stage 10. Between Load Stages 13 and 14, an apparent instability failure of the joint occurred at a moment of 1104 kip-in. This behavior is discussed in detail in Ref. 36. At that point, the specimen was unloaded and then reloaded. Upon reloading, the specimen continued to resist increasing moments until the chord wall buckling became so excessive that the branches were nearly bearing against each other, as shown in Fig. 3.15. The test was stopped at Load Stage 31 with a moment of 1302 kip-in. and a rotation of 4.94° because the distortions of the chord between the saddle points became excessive. From this test result, it is hard to define failure. Upon analysis, it was found that the instability at Load Stage 13 was a result of a specific combination of geometric properties of the joint. This point with a moment of 1104 kip-in could be defined as failure. However it was felt that because the specimen carried larger moments upon reloading the ultimate strength of the joint is better represented by Load Stage 31 with a moment of 1302 kip-in.

3.4.2.2 Test 028. The moment-rotation curve for Test 028 is presented in Fig. 3.14b. First yielding occurred during Load Stage 8 at the saddle point of the lower branch weld on the compression side of the joint and a moment of 1327 kip-in. The ultimate moment of 1476 kip-in. was attained at a rotation of

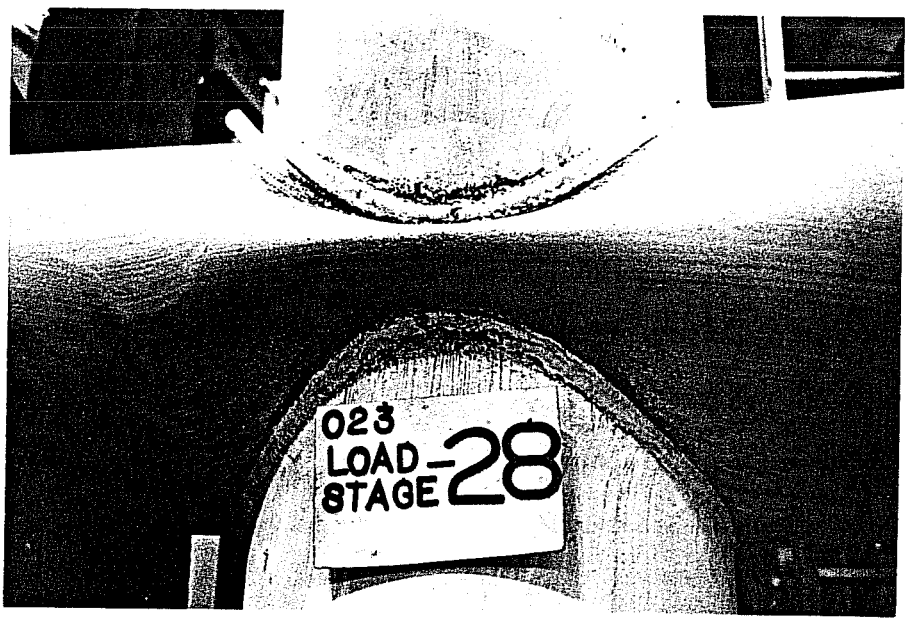

Fig. 3.15 Picture of Joint Distortion in Specimen 023

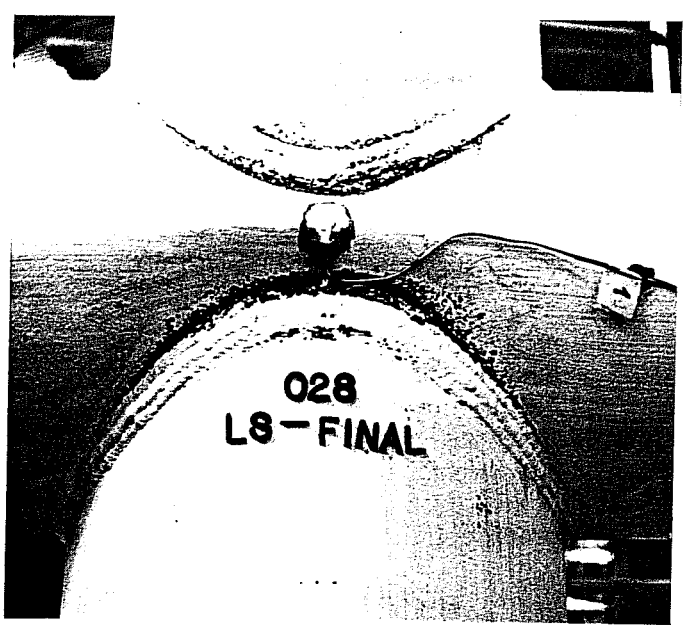

Fig. 3.16 Picture of Specimen 028 After Failure

0.70° during Load Stage 9. After the ultimate load, yielding progressed on the compression side of the joint and the chord wall between the saddle points buckled. In addition, the yielding began on the tension side of the joint at Load Stage 11 soon after the ultimate moment was reached. A picture of the failed specimen is shown in Fig. 3.16.

Comparison of the two tests, 023 and 028, shows a very significant difference in behavior. The reason for this is discussed in Chapter 4. The difference between the two ultimate moments, 1302 kip-in. for Test 023 and 1476 kip-in. for Test 028, is 12.5%. The average of the two ultimate moments, which will be used in interaction equations, is 1389 kip-in.

3.2.5 OPB-β=0.35

3.2.5.1 Test 042. The moment-rotation curve for Test 042 is shown in Fig. 3.17. The first yielding occurred during Load Stage 3 at a moment of 68 kip-in. The ultimate load of 118 kip-in. was reached at 6.27° rotation at Load Stage 9. At Load Stage 6 yielding was observed on the tension side of the joint at the saddle point and the yielding on the compression side began to approach the crown of the joint. Failure of the joint occurred when the branches punched into the chord on the compression side of the joint and significant yielding occurred on the tension side of the joint. After the maximum moment was reached, the .pa

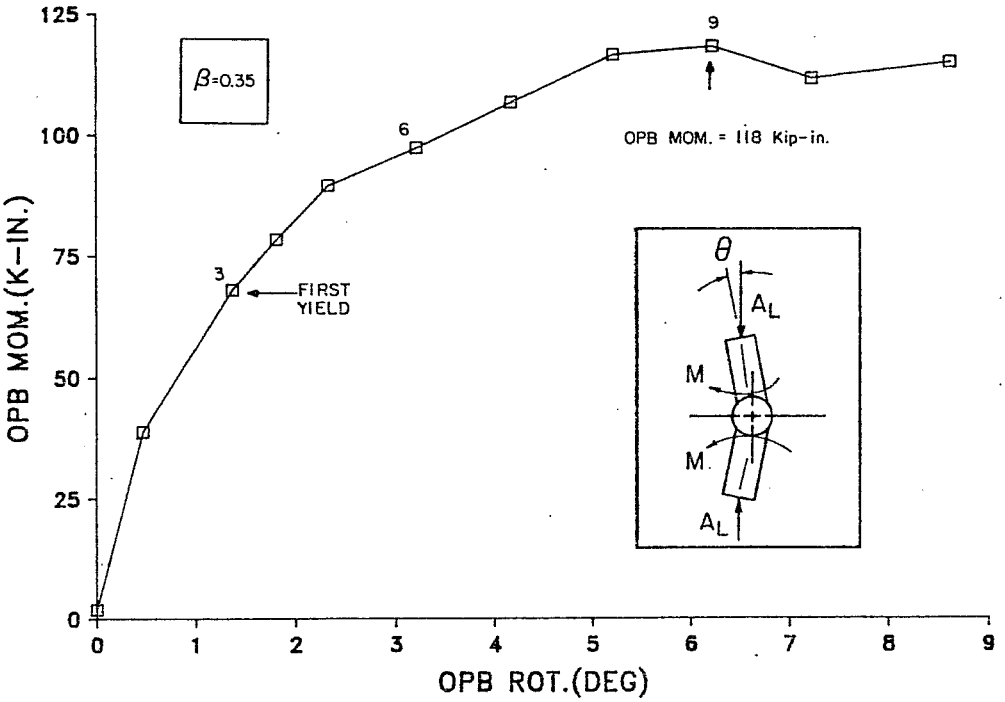

Fig. 3.17 Moment-Rotation Curve for Test 042

Fig. 3.18 Picture of Joint Yielding on Specimen 042

yield band continued completely around the compression side of the branch-chord connection, as shown in Fig. 3.18.

3.2.6 IPB-β=1.0

3.2.6.1 Test I24. The moment-rotation curve for Test I24 is shown in Fig. 3.19. First yielding was observed in the chord at location "a" near the saddle on the tension side of the joint at Load Stage 11 and a moment of 1725 kip-in. As the applied moment increased, chord ovalling on the tension side of the joint began followed by yielding along the welds at both the compression and tension crown points. As deformation continued, yielding began at points "b", and "c". These areas of yielding are shown as the dark patches in Fig. 3.20. The ultimate moment of 2265 kip-in. occurs at Load Stage 17 and a rotation of 5.67°. Failure occurred by two mechanisms. First, the chord on the tension side of the joint ovalled along a vertical axis with yielding along the center of the chord. Second, the chord on the compression side of the joint ovalled along a horizontal axis with a buckle in the chord wall near the crown area.

3.2.7 IPB-β=0.35

3.2.7.1 Test I43. The moment-rotation curve for Test I43 is plotted in Fig. 3.21. First yielding was observed in Load Stage 4 at a moment of 121 kip-in at the crown on the compression side of the joint. Failure of the joint, which is defined by the deformation limit, occurred at a moment of 257 kip-in. and a

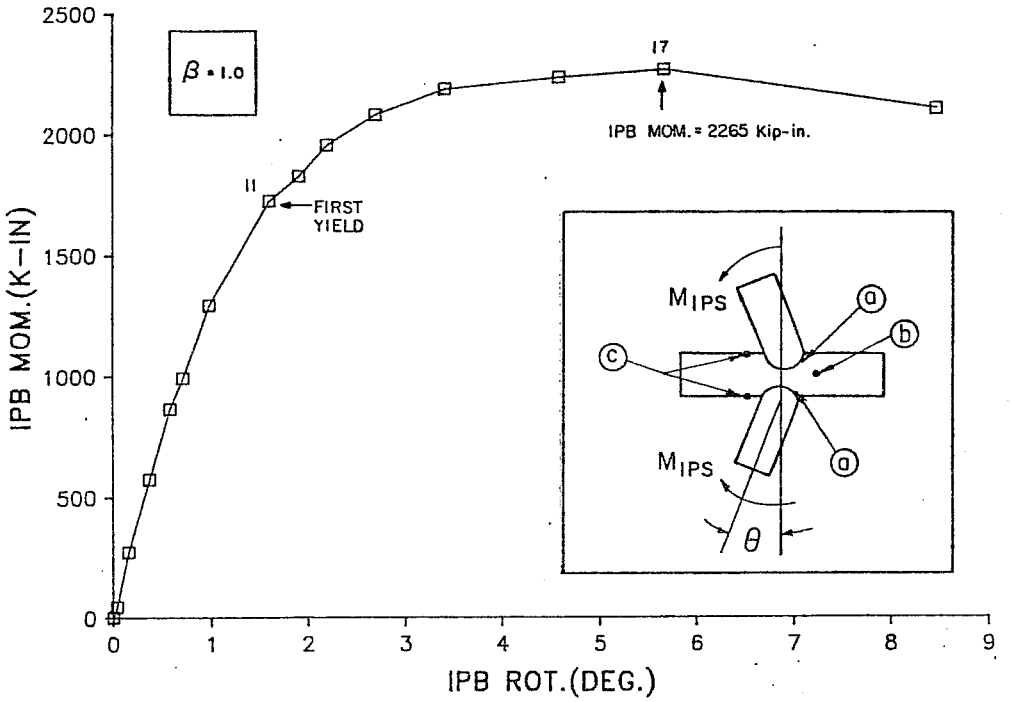

Fig. 3.19 Moment-Rotation Curve for Test I24

Fig. 3.20 Picture of Typical IPB Failure

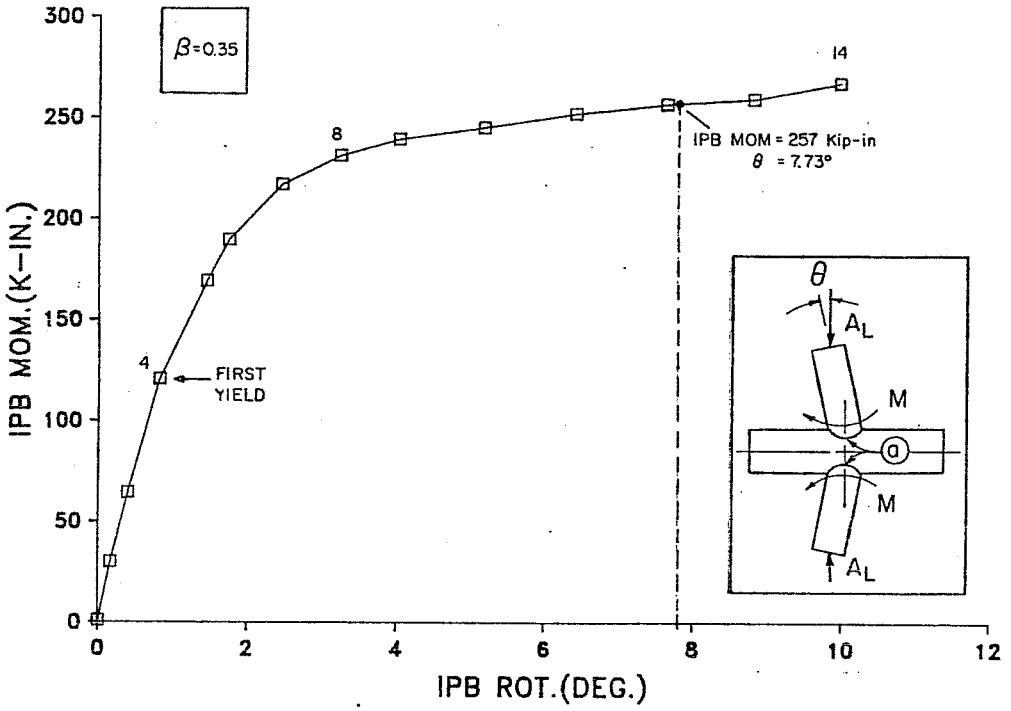

Fig. 3.21 Moment-Rotation Curve for Test I43

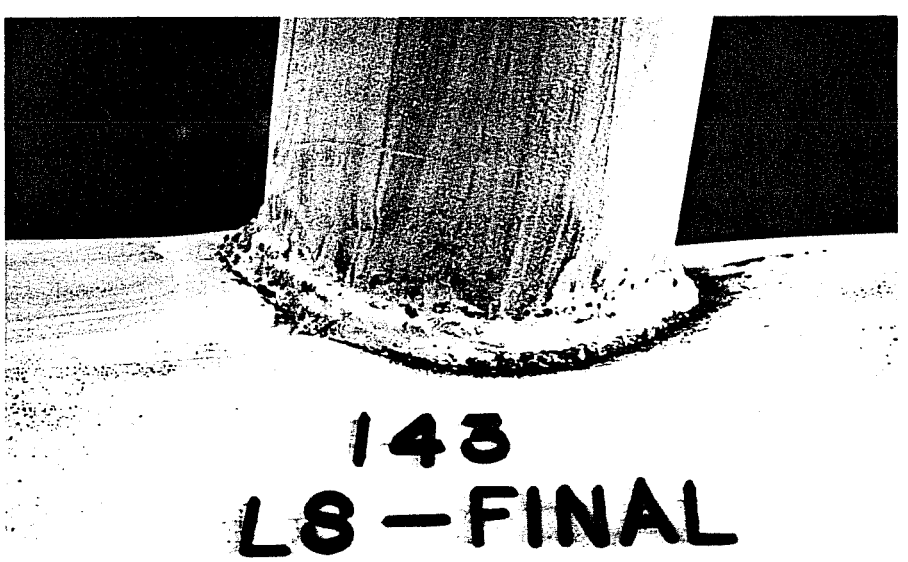

Fig. 3.22 Picture of Specimen I43 at Failure

rotation of 7.73°. After initial yielding, the joint continued to resist increasing moments to almost 10° rotation at which time the test was stopped at Load Stage 14. Yielding spread quickly around the compression side of the joint from saddle point on one side to saddle point on the other side of the joint. Yielding at the crown on the tension side of the side began at Load Stage 8 with a moment of 232 kip-in. A picture of the joint at failure is shown in Fig. 3.22.

After unloading, the test was continued by reversing the loading direction and applying an opposite moment to the joint. The moment-rotation curve for this additional loading is plotted in Fig. 3.23. The solid diamonds repeat the original M-θ diagram given in Fig. 3.21. The joint was loaded in the opposite direction from point (a) on the curve until the branches were almost vertical again at point (m) with a moment of 270 kip-in., as shown by the open circles. From that point, the specimen was unloaded to point (b) on the curve and the chord on the now tension side of the joint was cut off about 21 in. from the centerline of the joint. After the excess chord was removed, IPB moment was again applied to the joint as shown by the solid square data points. At point "c" a surface crack was found in the chord on the tension side of the joint about 45° from the saddle point along the weld toe. From this point, the joint continued the take moment until the chord of the specimen began to rotate

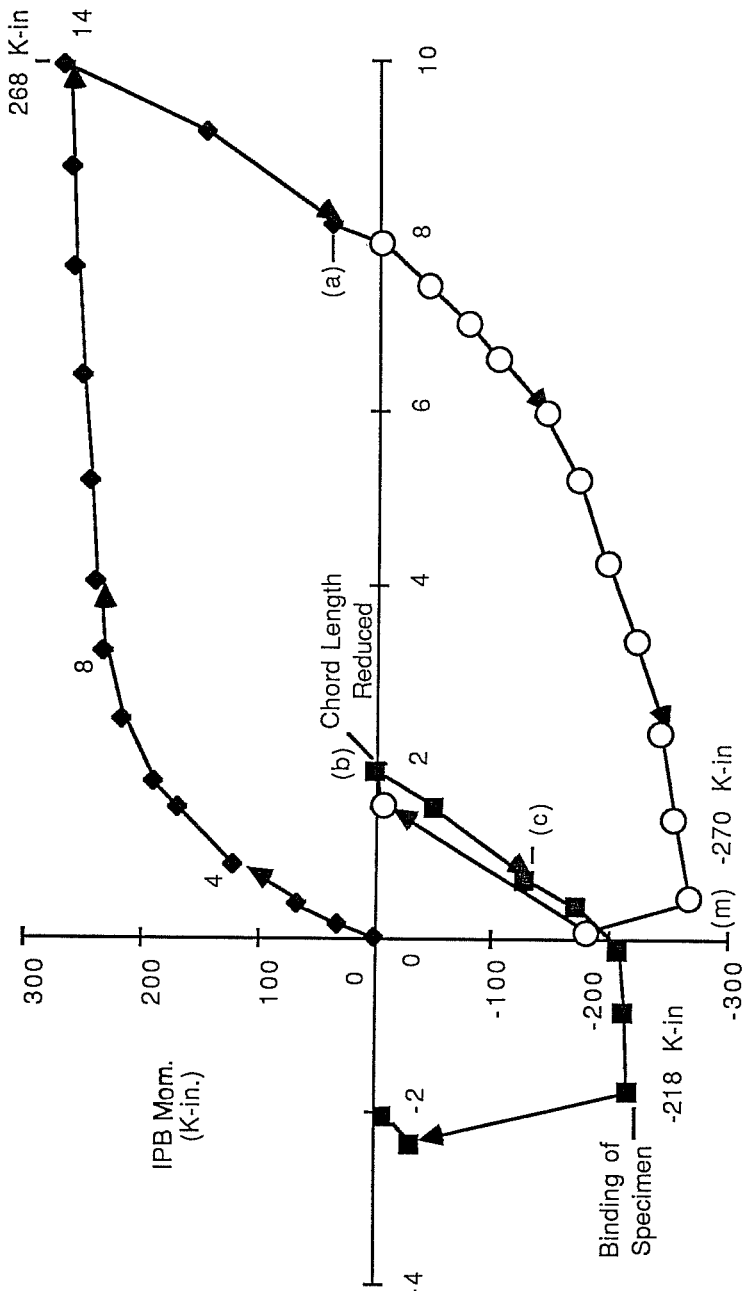

Fig. 3.23 Moment Rotation Curve for Additional Loading in Test I43

and bind the testing equipment. The maximum moment for the cracked specimen was 218 kip-in.

3.3 Axial Load with Out-of-Plane Bending

3.3.1 β=1.0

3.3.1.1 Test A031. In this test, approximately 25% of the ultimate axial load was applied and then the joint was loaded in OPB until failure. The OPB moment-rotation curve is plotted in Fig. 3.24. First yielding was noted at Load Stage 6, with a moment of 614 k-in, along the bottom saddle point on the compression side of the joint. Failure is defined by the deformation limit of 6.42° between Load Stages 16 and 17 at a moment of 1085 kip-in. After the initial yielding, yielding continued around the saddle points on the compression side until failure. The yield band was contained within a 45° arc along the weld on either side of the saddle. Failure occurred by buckling of the chord wall between the saddle points on the compression side of the joint; yielding on the tension side of the joint was not observed until after failure.

3.3.1.2 Test A032. In Test A032, approximately 50% of the ultimate axial load was applied then the joint was loaded in OPB. The moment-rotation curve is shown in Fig. 3.25. First yielding on the joint occurred at the compression side saddle points at a moment of 620 kip-in. during Load Stage 8. Failure of the specimen occurred at Load Stage 10 with an ultimate moment of

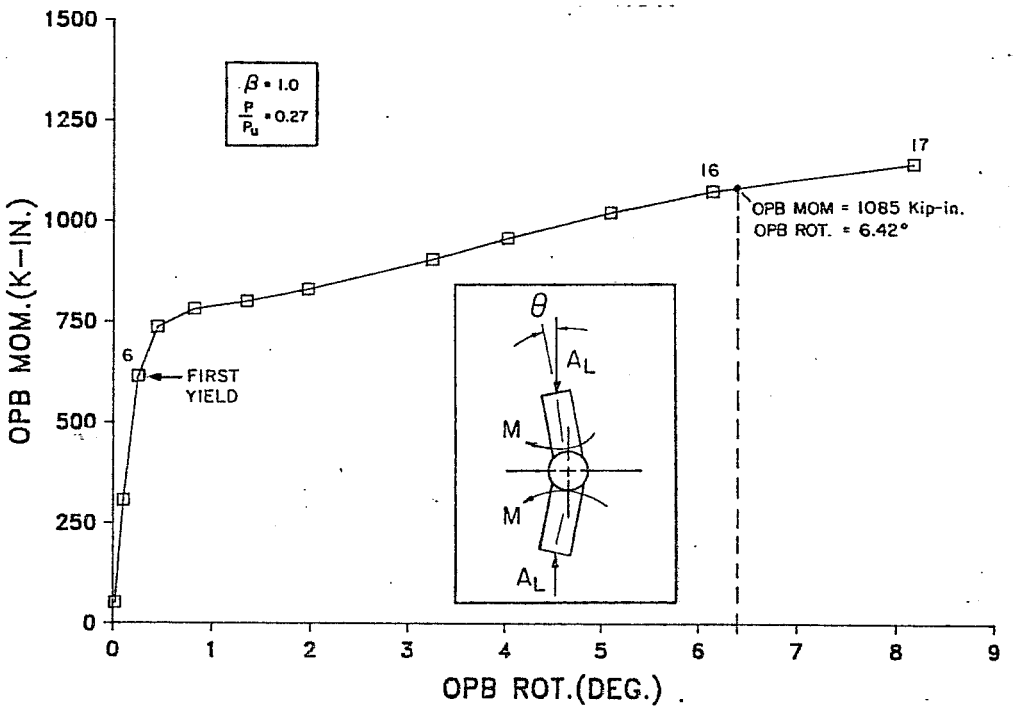

Fig. 3.24 OPB Moment-Rotation Curve for Test A031

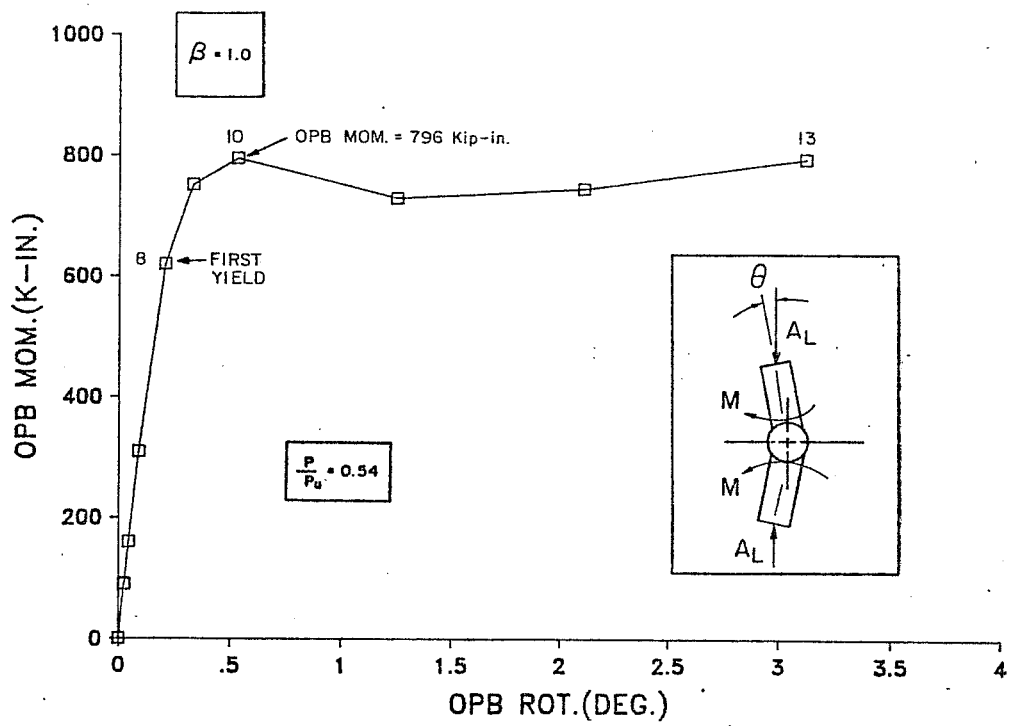

Fig. 3.25 OPB Moment-Rotation Curve for Test A032

796 kip-in. at a rotation of only 0.53°. From this point, the secondary moments began to drive the specimen. By reducing the branch loading, the joint was allowed to deform until a branch rotation of 3.12° and a moment of 796 kip-in was attained at Load Stage 13. Failure occurred by buckling of the chord wall between the saddle points no yielding was apparent on the tension side of the joint.

3.3.1.3 Test A033. To get an interaction point near the axial loading axis, in Test A033 25% of the reference out-of-plane moment was applied and then the joint was failed in axial loading. The lower axial load in the branch vs. the average branch deflection curve is plotted in Fig. 3.26. The average branch deflection is used instead of the lower branch deflection corrected for rigid body motion as in the other phases of this study because it was not possible to accurately measure rigid body rotations while the joint deformed in the out-of-plane direction. First yielding of the joint was noted at the saddle points on the OPB compression side of the joint at an axial load of 87.9 kips during Load Stage 6. The specimen failed suddenly at an axial load of 118.4 kips. Failure occurred when the chord wall between the saddle points on the OPB compression side of the joint buckled.

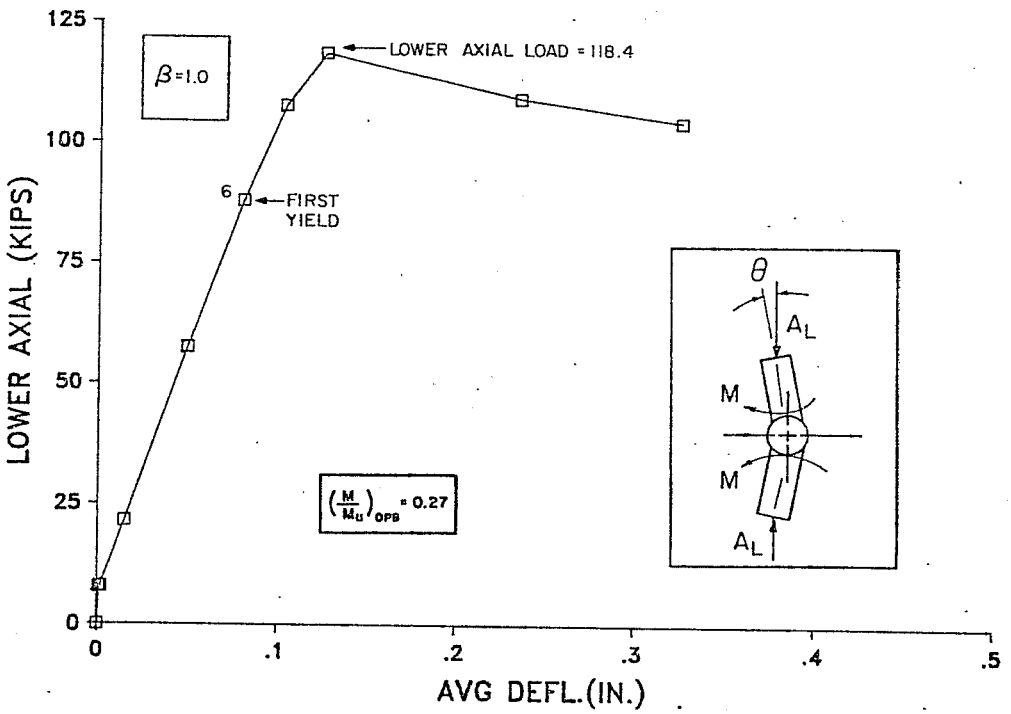

Fig. 3.26 OPB Moment-Rotation Curve for Test A033

3.3.2 β=0.35

3.3.2.1 Test A044. In Test A044 approximately 30% of the axial reference load was applied then the joint was loaded to failure in OPB. The OPB moment-rotation curve is shown in Fig. 3.27. First yielding was noted on the joint at the saddle points on the compression side at a moment of 39 kip-in. Failure of the specimen was defined by the deformation limit at a rotation of 7.73° and a moment of 124 kip-in. between Load Stages 18 and 19. Failure occurred when the compression side of the branch began to punch into the chord and yielding became apparent on the tension side of the joint.

3.3.2.2 Test A045. In this test, approximately 70% of the reference axial load was applied before the specimen was loaded to failure in OPB. The OPB moment-rotation curve is plotted in Fig. 3.28. First yield became apparent during Load Stage 2 before reaching the target axial load. Failure occurred at Load Stage 13 with an ultimate moment of 73 kip-in. Due to the initial out-of-straightness of the specimen of 0.35 in., the moment produced by the initial deflection at the centerline of the chord multiplied by the axial load caused the joint to deflect in the out-of-plane direction. Because this type of loading is very unstable, the flow of oil from the OPB ram was shut off at each load stage to stop the deformation of the joint. The pressure on this line produced a force which caused a moment

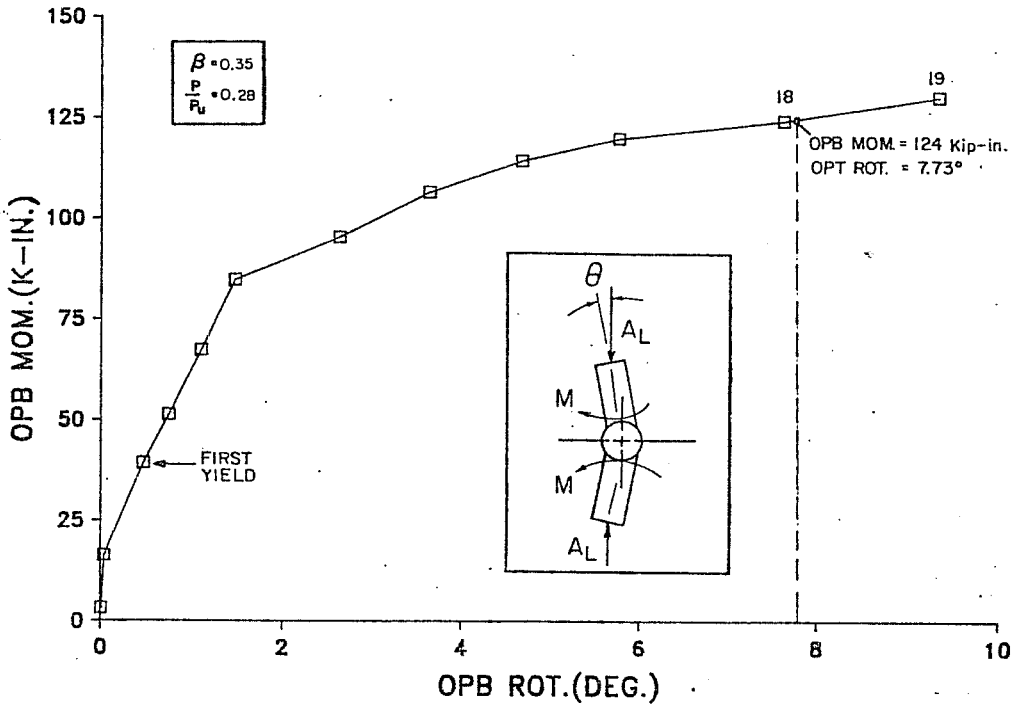

Fig. 3.27 OPB Moment-Rotation Curve for Test A044

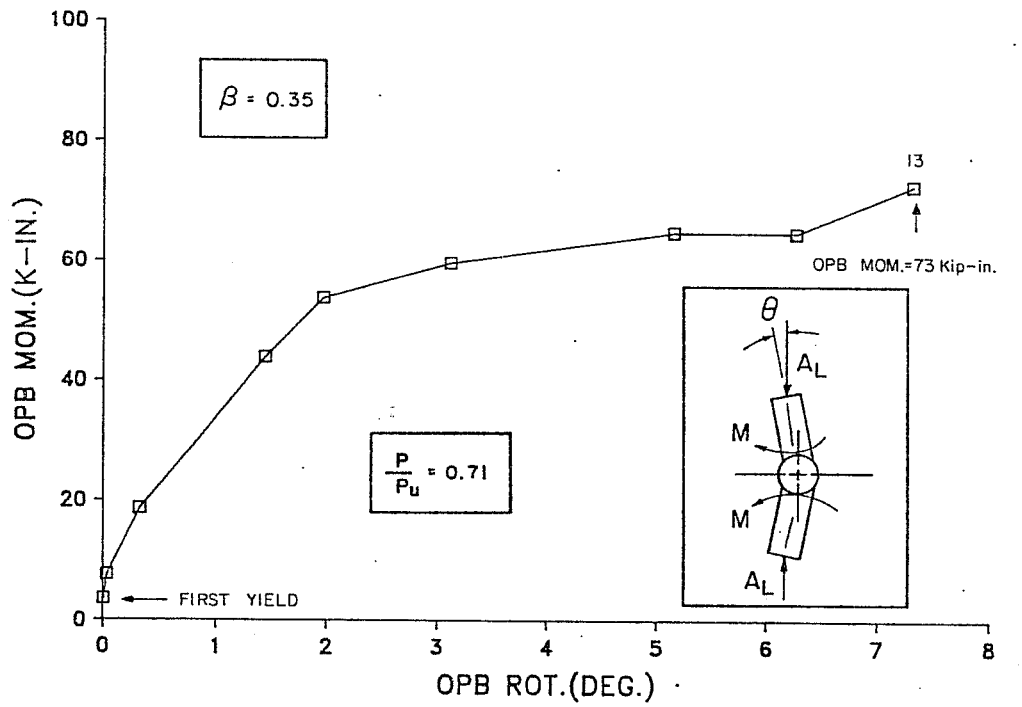

Fig. 3.28 OPB Moment-Rotation Curve for Test A045

in opposition to the secondary bending effects. This resisting moment was calculated and is shown as a negative branch moment in the table of results in Appendix B. Failure was caused by twisting of the chord about its centerline similar to the failure shown in Test A22.

3.4 Axial Load with In-Plane Bending

3.4.1 $\beta=1.0$

3.4.1.1 Test AI34. In Test AI34, approximately 25% of the axial reference load was applied before the joint was loaded to failure in IPB. The IPB moment-rotation curve is shown in Fig. 3.29. First yielding of the joint became apparent at a moment of 1196 kip-in. during Load Stage 5. The yielding began in an arc from the saddle point to 75° toward the crown along the weld on the compression side of the joint. Failure of the specimen occurred at a moment of 2123 kip-in. and 4.16° rotation. After first yield, yielding on the compression side of the joint progressed to the crown. Yielding along the centerline of the chord on the tension side of the joint began at Load Stage 8 indicating an ovalling of the chord. Failure was caused by gross yielding in the chord wall.

3.4.1.2 Test AI35. In this test, 50% of the axial reference load was applied and then the specimen was loaded to failure in IPB. The moment-rotation curve for Test AI35 is shown

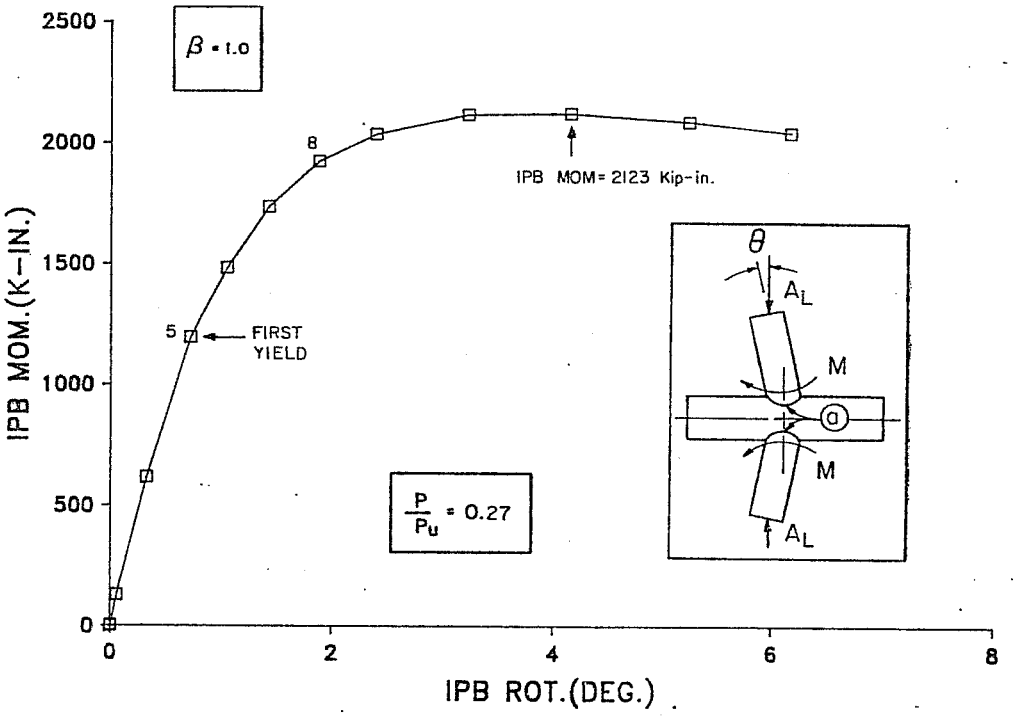

Fig. 3.29 IPB Moment-Rotation Curve for Test AI34

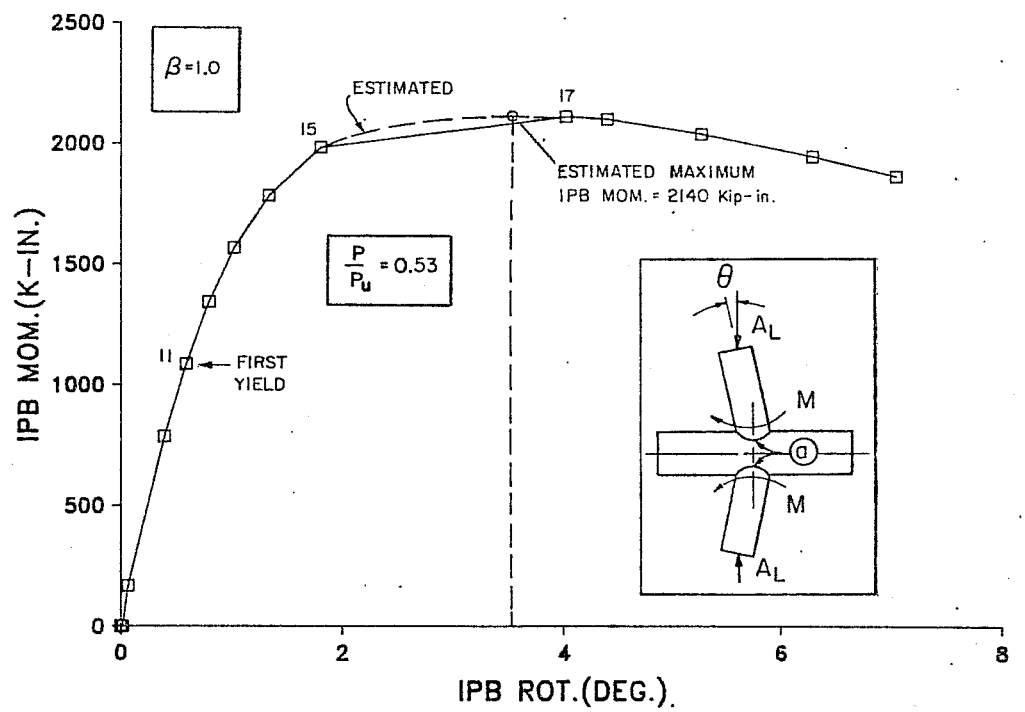

Fig. 3.30 IPB Moment-Rotation Curve for Test AI35

in Fig. 3.30. First yielding of the joint occurred at a moment of 1085 kip-in. during Load Stage 11. The initial yielding of the joint occurred in a band from the saddle point to 35° toward the crown on the compression side of the joint. During Load Stage 16 a malfunction was found in the LVDT used to determine the in-plane deflection; however, the load readings were found to be accurate. Thus the only error in the determination of the total moment could be in the calculation of the secondary moments. The possible moment varied between 2060 and 2194 kip-in. By assuming several different deflections and comparing the resulting moments with the shape of the rest of the moment rotation curve, it was estimated that failure occurred at a rotation of 3.5° and an ultimate moment of 2140 kip-in. Failure occurred by gross yielding of the chord wall in the vicinity of the joint.

3.4.1.3 Test AI36. The loading path used for this test was first to apply approximately 50% of the reference IPB moment then to fail the specimen under axial loading. The axial load vs. the average branch deflection is plotted in Fig. 3.31. First yielding on the joint was noted at an axial load in the lower ram of 80.0 kips. The yielding occurred from the saddle points to 45° toward the compression side of the joint along the weld toe. Failure occurred at a lower axial ram load of 169.0 kips during Load Stage 11. After initial yielding, yielding progressed from the saddle points on only one side of the joint. This

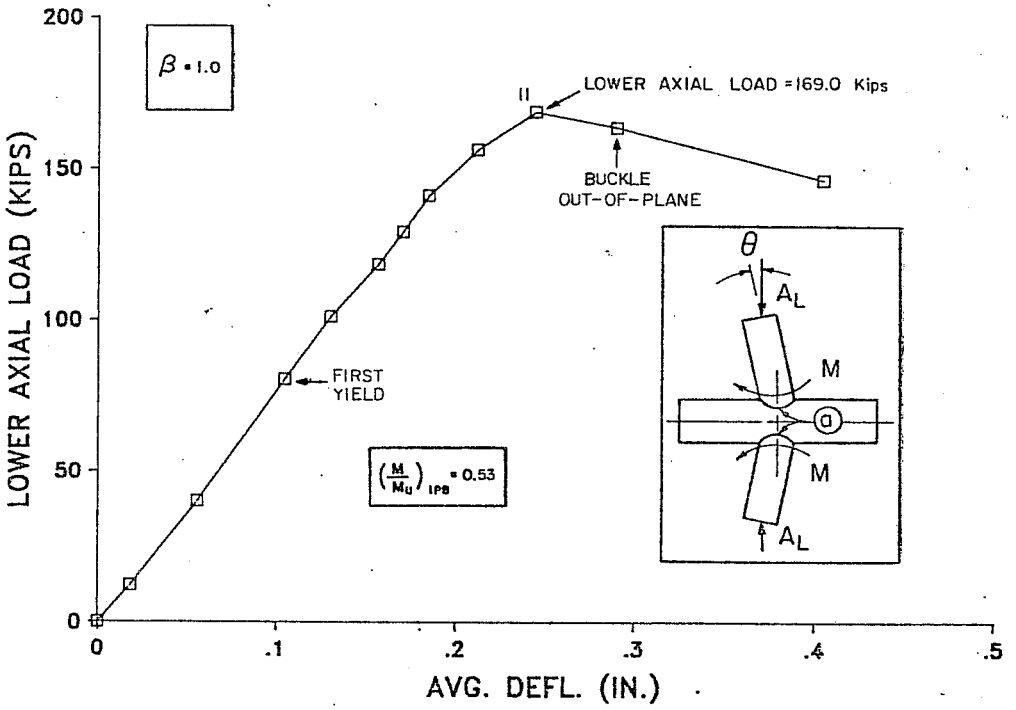

Fig. 3.31 IPB Moment-Rotation Curve for Test AI36

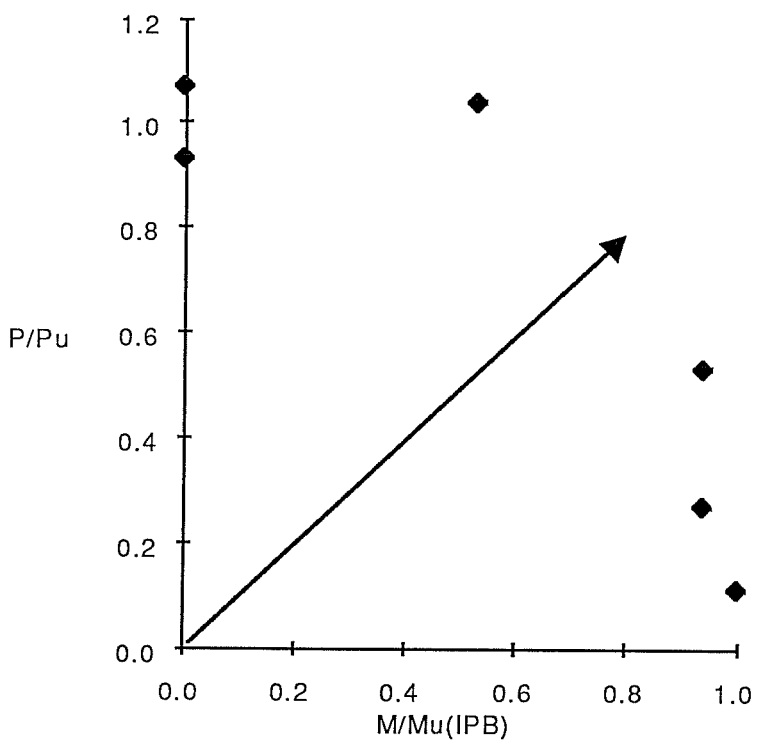

Fig. 3.32 Example Load Path for Proportional Loading

unsymmetrical yielding caused the specimen to buckle in the out-of-plane direction soon after reaching the ultimate load. Failure was a result of buckling of the chord wall between the saddle points on one side of the joint.

3.4.1.4 Test AI50. Because the results of the previous three axial load with IPB tests displayed very little interaction as shown in Fig. 3.32 a proportional load path was chosen which would follow a 45° line on the interaction diagram also shown in Fig. 3.32. This was done to gain as much information about the middle portion of the interaction equation as possible. In this test, the axial load and IPB moment were applied simultaneously at the predetermined ratio. The lower axial ram vs. average branch deflection is plotted in Fig. 3.33a, while the IPB moment-rotation curve is plotted in Fig. 3.33b. The actual load path for Test AI50 is shown in Fig. 3.34. Initial yielding began in a band from the saddle point to 45° toward the crown on the compression side of the joint at Load Stage 3 with an axial load of 84.9 kips and an IPB moment of 1099 kip-in. At Load Stage 4, the yield band continued from the saddle point on one side of the joint to the other on the compression side of the joint. Failure of the joint occurred at an axial load of 129.0 kips and an IPB moment of 1600 kip-in. The failure mode was mainly controlled by an axial type failure with a sudden buckling of the chord wall between the two saddle points.

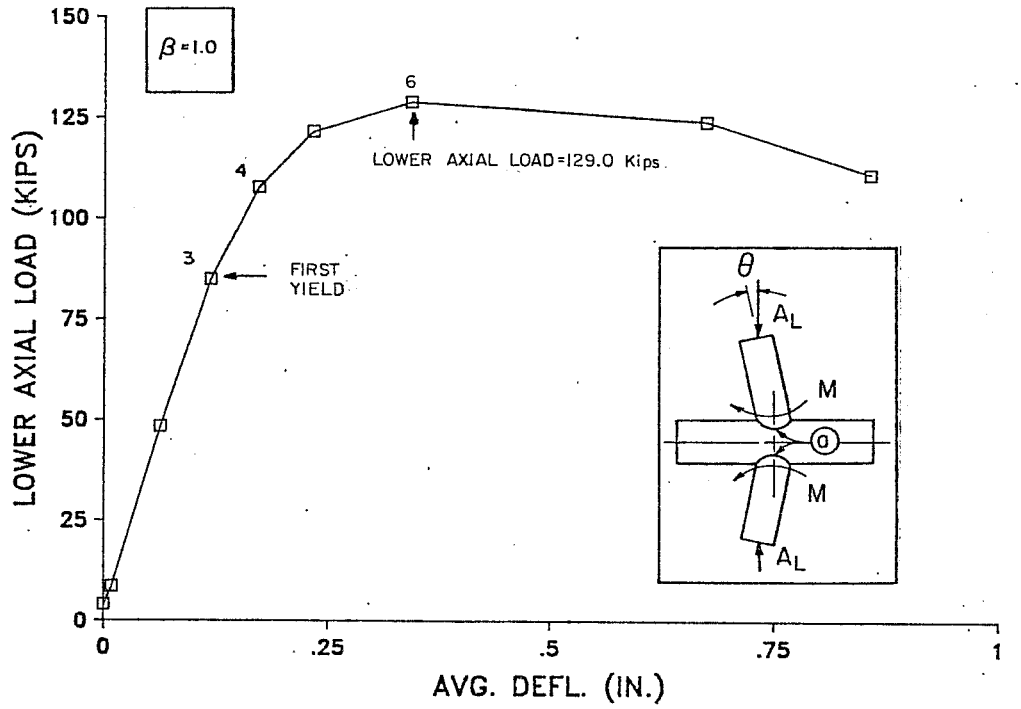

a.) Axial

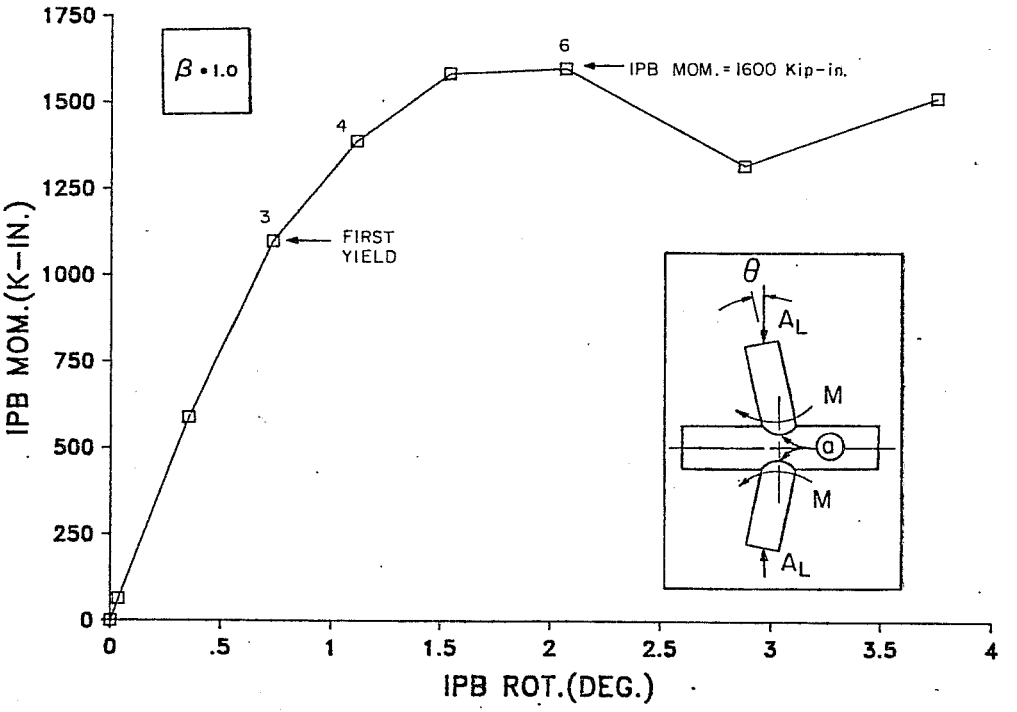

b.) IPB

Fig. 3.33 Load-Displacement and IPB Moment-Rotation Curves for Test AI50

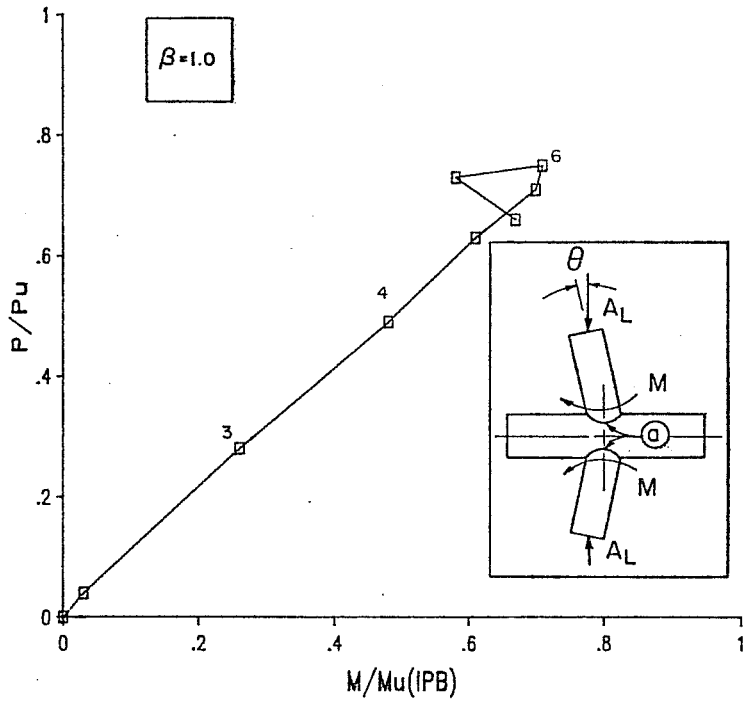

Fig. 3.34 Actual Load Path of Test AI50

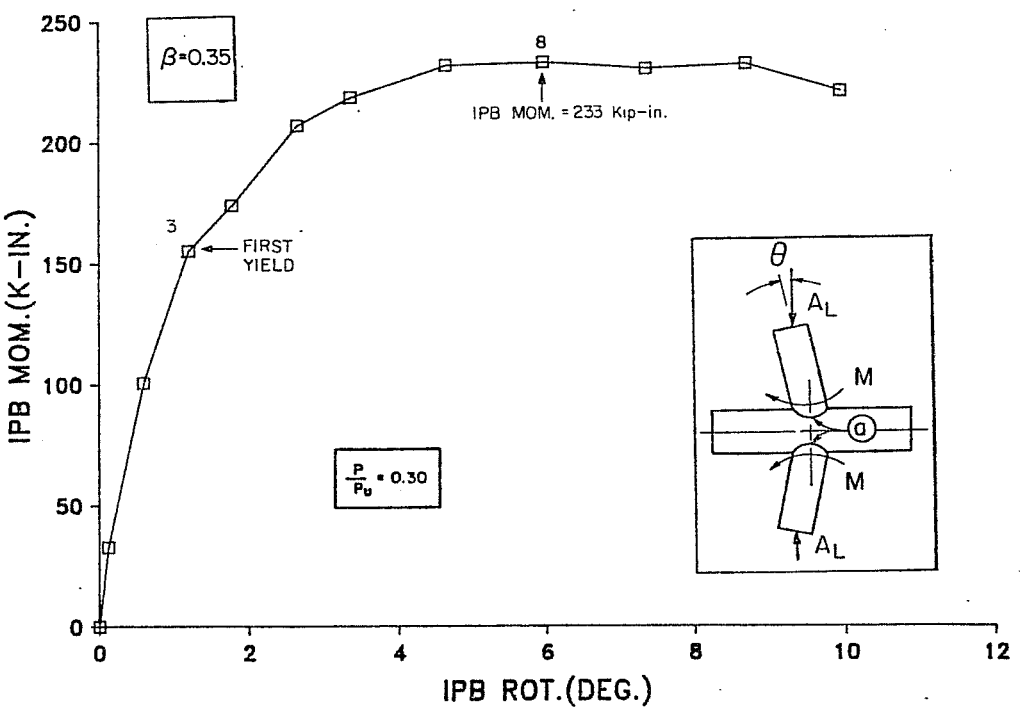

Fig. 3.35 IPB Moment-Rotation Curve for Test AI46

3.4.2 β=0.35

3.4.2.1 Test AI46. In Test AI46 approximately 30% of the reference axial load was applied before the joint was loaded to failure in IPB. The IPB moment-rotation curve is plotted in Fig. 3.35. Yielding was first noted at a moment of 155 kip-in. during Load Stage 3. The initial yield band stretched from saddle point to crown to the other saddle point on the compression side of the joint. The maximum moment, 233 kip-in., was attained at a rotation of 5.96° in Load Stage 8. The specimen maintained this moment to a rotation of 8.69° illustrating the ductility of this joint geometry. Failure was a result of gross yielding of the chord wall in the vicinity of the crowns. Yielding extended almost 4.5 in. away from the joint along the crown on the compression side of the joint as shown in Fig. 3.36.

3.4.2.2 Test AI47. In this test, approximately 70% of reference axial load was applied and then the joint was loaded in IPB until failure occurred. The IPB moment-rotation curve is plotted in Fig. 3.37. First yielding was noted at the saddle points of the joint at an axial load of 24.3 kips, before the target axial load was reached. Due to an initial in-plane out-of-straightness in the specimen, the application of the axial load resulted in a negative secondary moment in the joint before the branch bending moment was applied. This moment, 7 kip-in, is about 3.5% of the maximum moment of the joint. Failure of the

Fig. 3.36 Picture of Joint AI46 at Failure

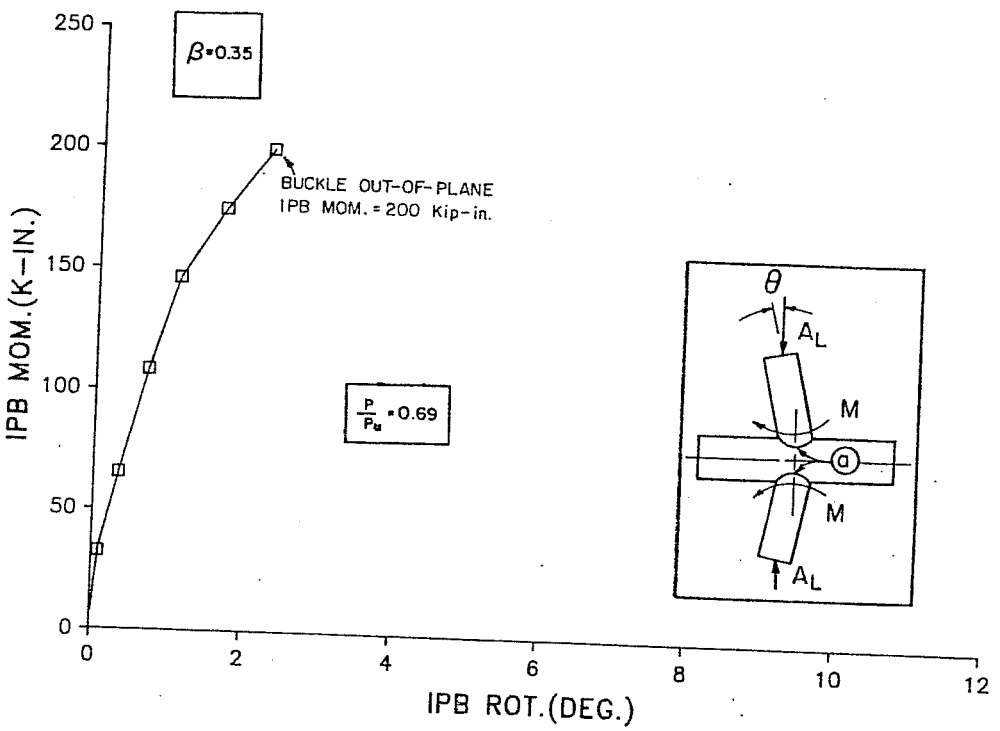

Fig. 3.37 IPB Moment-Rotation Curve for Test AI47

joint was defined by the stability criterion when the chord buckled approximately 6 in. in the out-of-plane direction at a moment of 200 kip-in.

3.5 In-Plane Bending with Out-of-Plane Bending

3.5.1 $\beta=1.0$

3.5.1.1. Test I037. In this test approximately 25% of the IPB reference moment was applied before the joint was loaded in OPB. The OPB moment-rotation curve is plotted in Fig. 3.38. First yielding occurred in a band from the compression saddle point 45° toward the IPB compression crown during Load Stage 7 at an OPB moment of 313 kip-in.. Failure was defined by gross distortion of the joint at an out-of-plane rotation of 5.96° and an OPB moment of 1419 kip-in. At the point of failure, the chord wall between the saddle points on the OPB compression side of the joint had buckled and yielding around the weld had spread into the branch because the toes of the branches were bent as shown in Fig. 3.39.

3.5.1.2 Test I038. In Test I038 approximately 50% of the IPB reference moment was applied and then the joint was loaded to failure in OPB. The OPB moment-rotation curve is shown in Fig. 3.40. First yielding was noted during Load Stage 7 at an OPB moment of 314 kip-in. The yielding occurred in two bands, one in the compression quadrant (compression from both IPB and OPB)

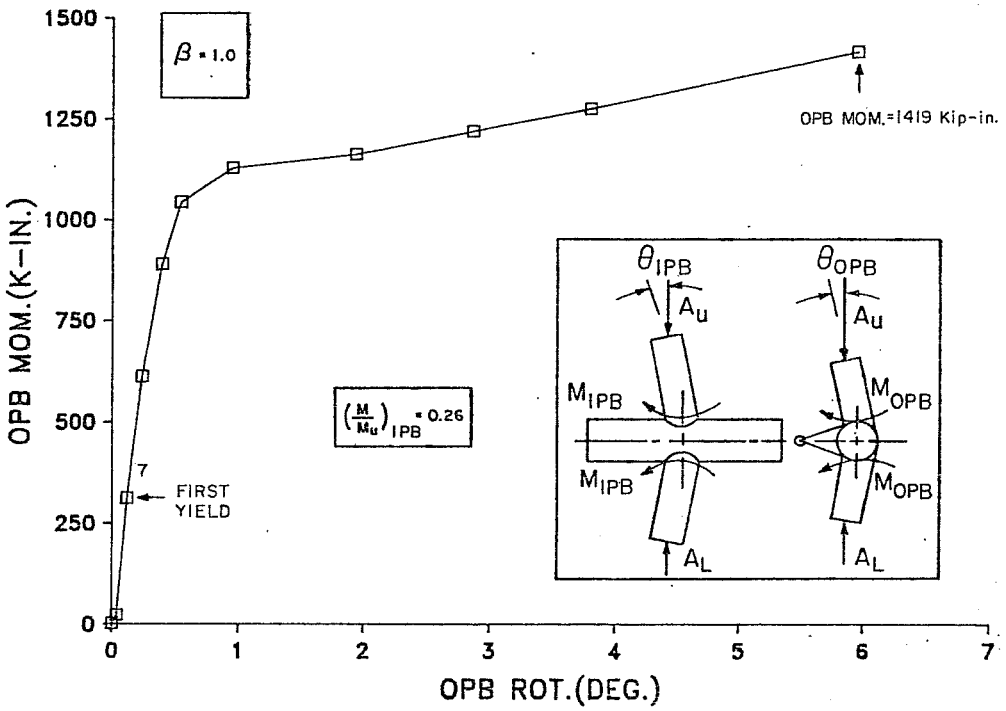

Fig. 3.38 OPB Moment-Rotation Curve for Test I037

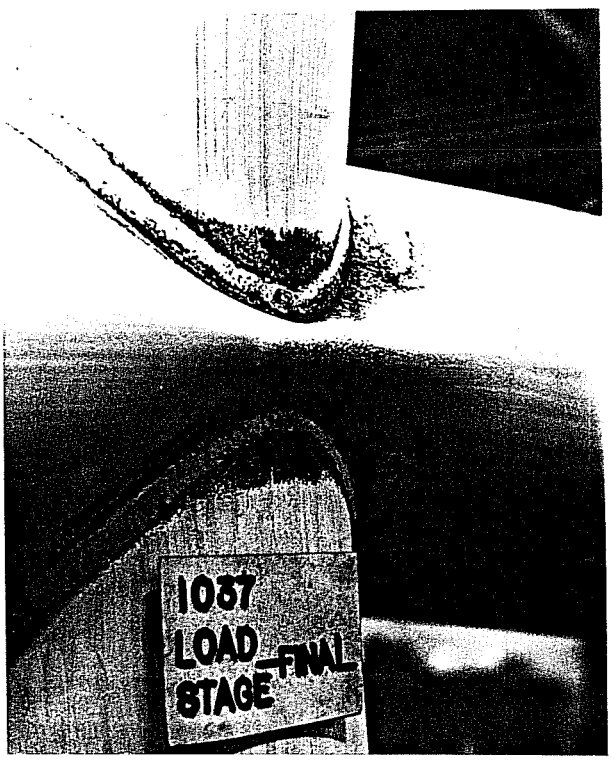

Fig. 3.39 Picture of Yielding in Branch in Test I037

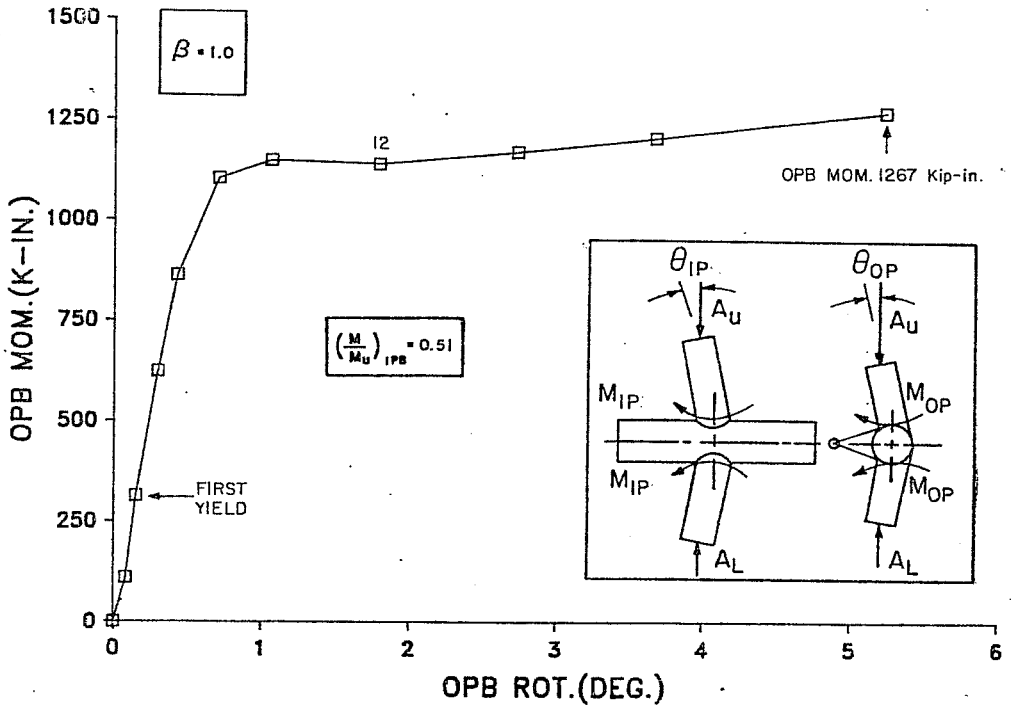

Fig. 3.40 OPB Moment-Rotation Curve for Test IO38

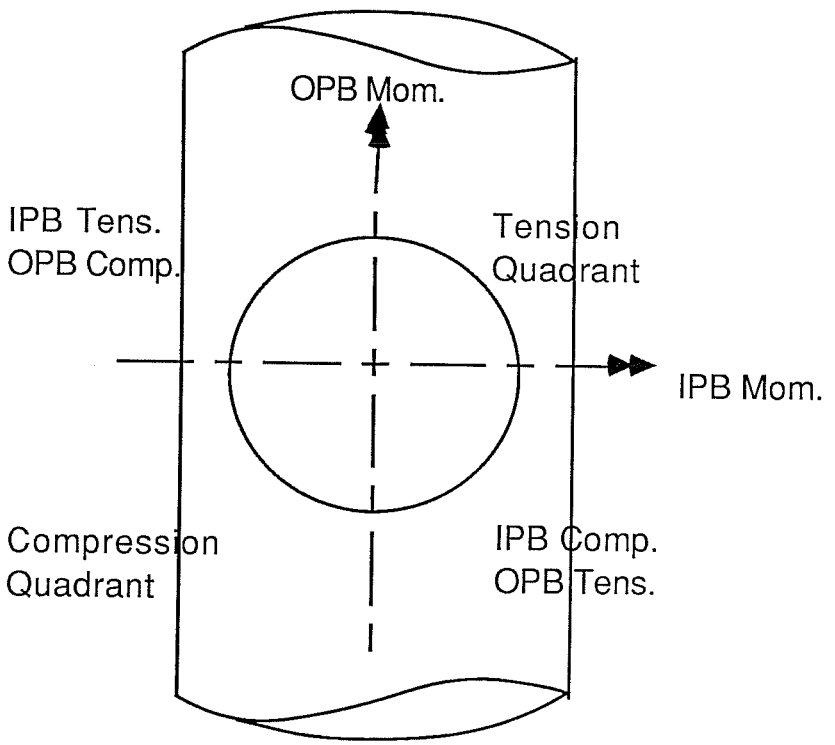

Fig.3.41 Schematic of Tension and Compression Quadrants

from the saddle point to 45° toward the IPB compression crown, the other occurred in the tension quadrant (tension from both IPB and OPB) from the saddle point to 45° toward the IPB tension crown. The quadrants are shown in Fig. 3.41. Failure was defined by gross distortion of the joint at an OPB moment of 1267 kip-in. and an OPB rotation of 5.26°. The increase in stiffness of the joint apparent after Load Stage 12 was accompanied by a significant increase in the amount of yielding in the tension quadrant of the joint. The yielding pattern on the joint was a combination of the yielding patterns seen on OPB and IPB specimen. On the OPB compression side of the joint the chord wall buckled between the two saddle points while on the IPB tension side of the joint, yielding was noted along the chord centerline indicating an ovalling of the chord. Pictures of the joint at failure are presented in Fig. 3.42.

3.5.1.3 Test I039. In this test approximately 50% of the reference OPB moment was applied before the joint was loaded to failure in IPB. The IPB moment-rotation curve for Test I039 is plotted in Fig. 3.43. First yielding was noted during Load Stage 6 at an IPB moment of 599 kip-in. The initial yielding occurred in the compression quadrant of the joint from the saddle to 45°. The joint failed at an IPB moment of 2173 kip-in. and an IPB rotation of 4.64° during Load Stage 11. After initial yielding, the yielding pattern was very similar to the yielding shown in

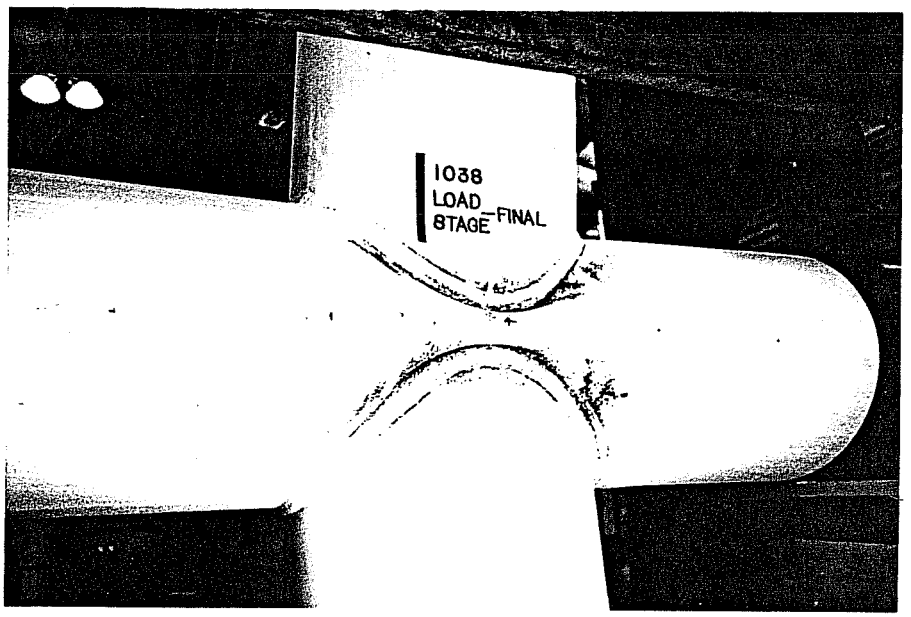

a.) OPB Compression Side

b.) OPB Tension Side

Fig. 3.42 Picture of Specimen I038 at Failure

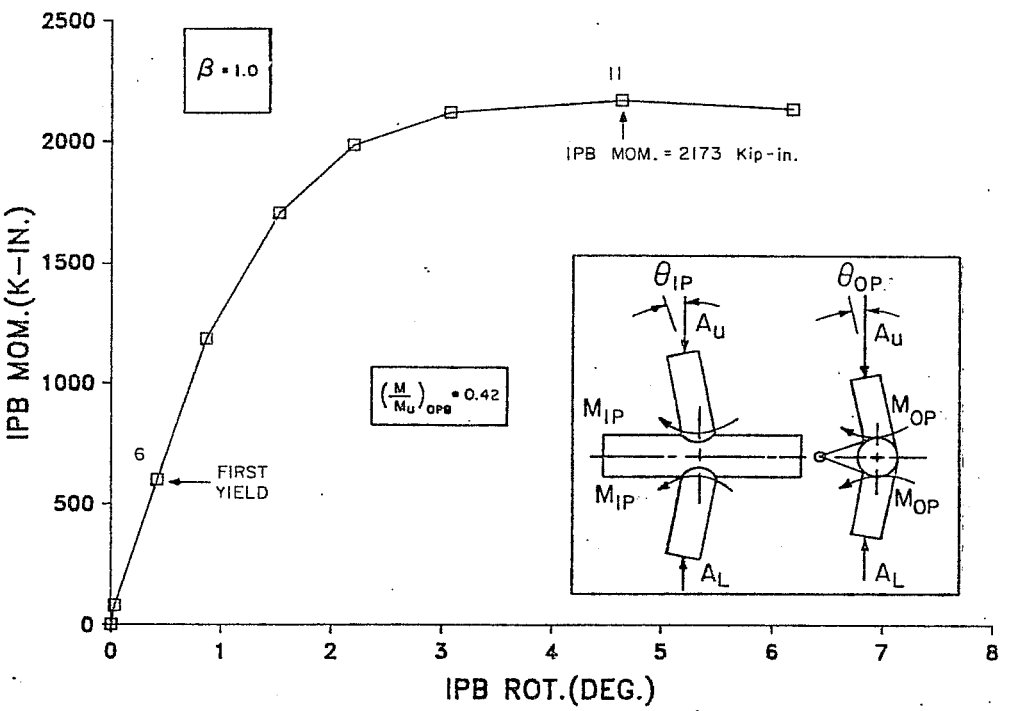

Fig. 3.43 IPB Moment-Rotation Curve for Test I039

the IPB reference test with a yield band from saddle to saddle point on the IPB compression side of the joint and a section of yielding in the chord wall along the chord centerline on the IPB tension side of the joint. The only difference in the pattern was that the yielding on the OPB compression side of the joint was less significant than on the OPB tension side of the joint. Failure was caused by gross yielding of the chord wall in the vicinity of the joint.

3.5.1.4 Test I026. Because the results of previous IPB with OPB interaction tests placed points only on the fringes of the interaction diagram, a proportional load path was chosen which would follow a 45° line as in Test AI50. In that test, the axial load and IPB moment were applied simultaneously at the predetermined ratio. The moment-rotation curves for IPB and OPB are plotted in Figs. 3.44a and b respectively. The actual loading path for Test I026 is plotted in Fig. 3.45. First yielding was noted during Load Stage 6, with IPB and OPB moments of 1073 kip-in. and 556 kip-in. respectively, in a band from the saddle to 45° in the compression quadrant of the joint. Following initial yielding, the yielding pattern progressed much like the one seen in Test I039. After Load Stage 10, the moment-rotation curve of the joint in both directions reached a plateau and the joint could not carry more moment, but continued to deflect with no significant loss in capacity. Failure of the joint was defined by

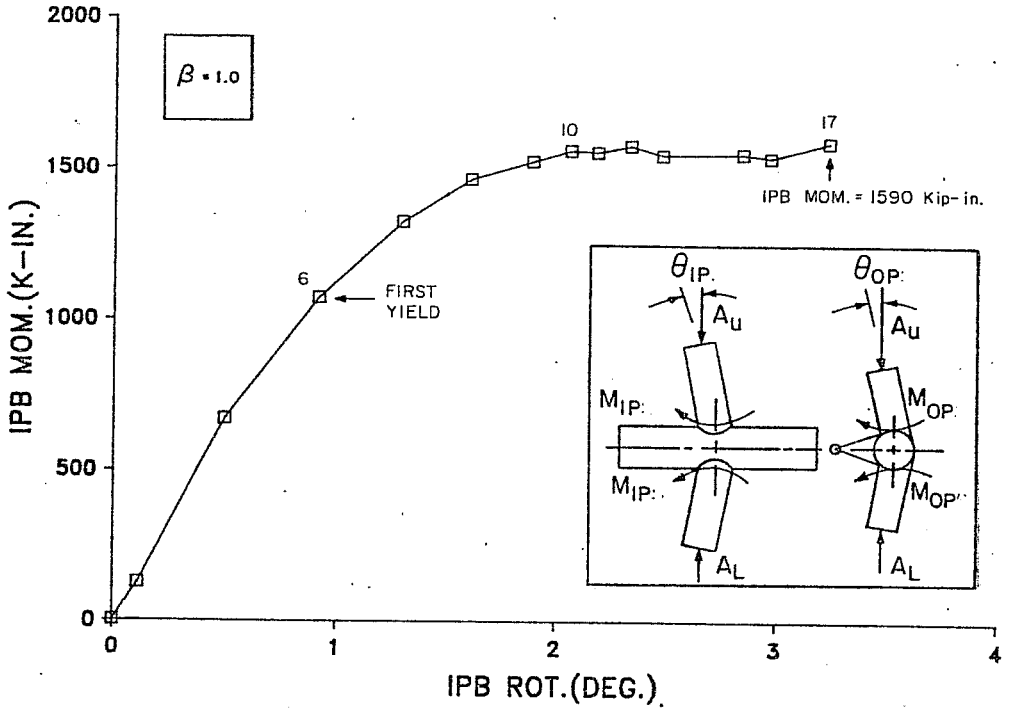

a.) IPB

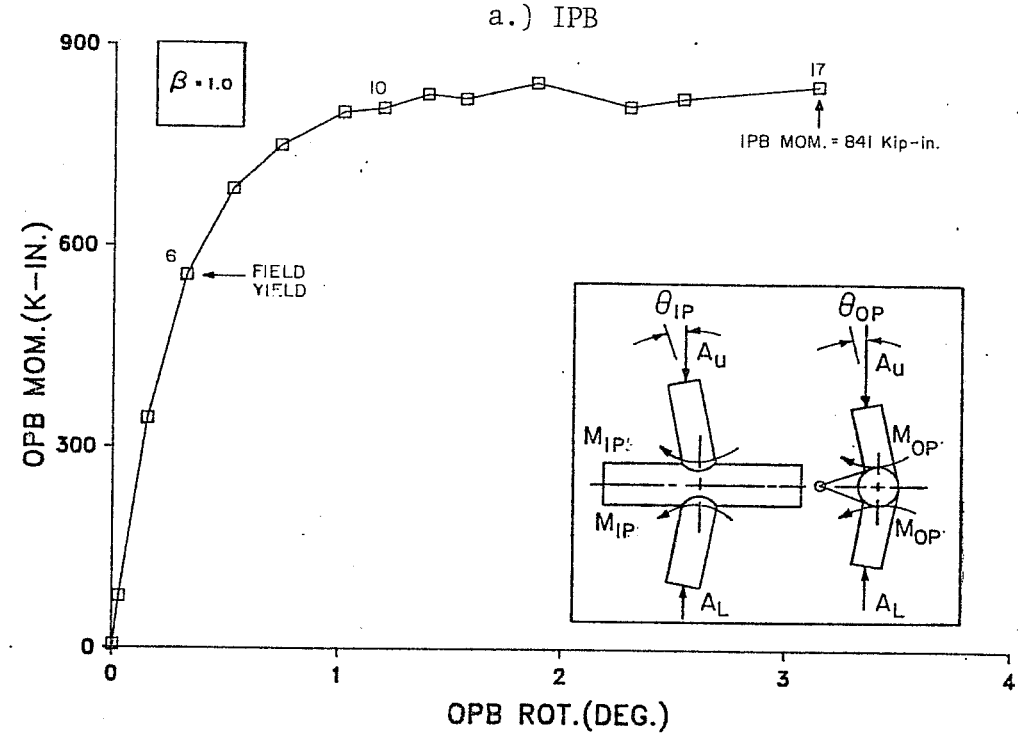

b.) OPB

Fig. 3.44 IPB and OPB Moment-Rotation Curves for Test I026

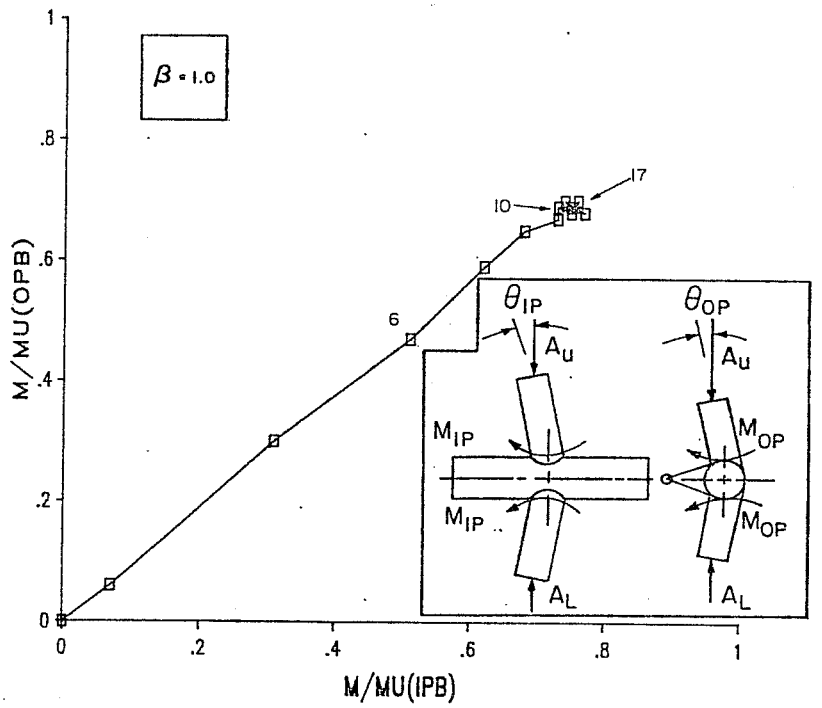

Fig. 3.45 Actual Loading Path for Test I026

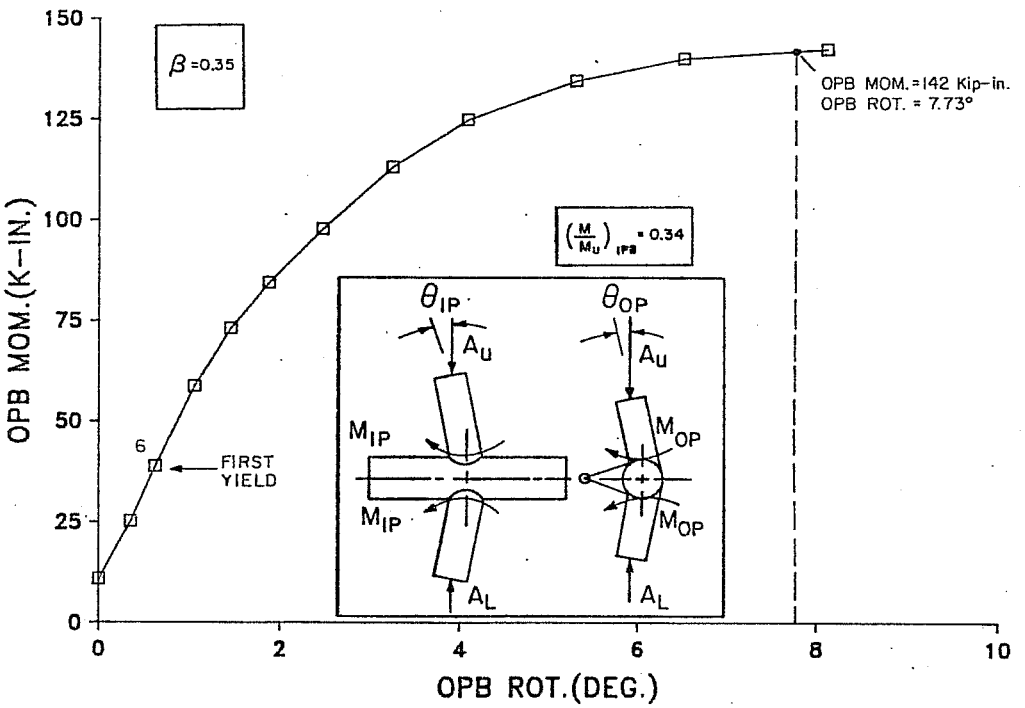

Fig. 3.46 OPB Moment-Rotation Curve for Test I048

gross deformations in the vicinity of the joint. From observation of the load path shown in Fig. 3.45 it seems irrelevant which point after Load Stage 10 is chosen as failure because the moments are very similar. The farthest point from the origin is taken from Load Stage 17, therefore this Load Stage was chosen to define the ultimate moments of 1590 and 841 kip-in. for IPB and OPB respectively.

3.5.2 β=0.35

3.5.2.1 Test I048. In Test I048, approximately 30% of the reference IPB moment was applied before the joint was loaded to failure in OPB. The OPB moment-rotation curve is plotted in Fig. 3.46. First yielding of the joint occurred around the saddle points of the OPB compression side of the joint during Load Stage 6 at an OPB moment of 39 kip-in. Failure of the specimen as defined by the deformation limit of 7.73° at an OPB moment of 142 kip-in. The specimen continued to carry moment until the test was stopped at an OPB rotation of 8.13°. After initial yielding, the yield pattern progressed from the saddle point on the OPB side of the joint first toward the IPB compression crown and then toward the tension crown. Just before reaching the deformation limit, the OPB compression toe of the branch began to punch into the chord wall and small cracks formed at the saddle point on the tension side.

3.5.2.2 Test I049. In Test I049, approximately 70% of the reference IPB moment was applied and then the joint was loaded in OPB until the specimen failed. The OPB moment-rotation curve is shown in Fig. 3.47. First yielding on the joint was noted during Load Stage 5, with an OPB moment of 21 kip-in., in a band around the weld toe in the compression quadrant of the joint. After initial yielding, the pattern of yielding progressed from the compression quadrant around toward the OPB tension saddle point on the IPB compression side of the joint and small surface cracks formed in the tension quadrant of the joint. At 6.18° OPB rotation the yield band was almost completely around the branch-chord intersection. Failure of the specimen was defined by the deformation limit at an OPB moment of 125 kip-in.

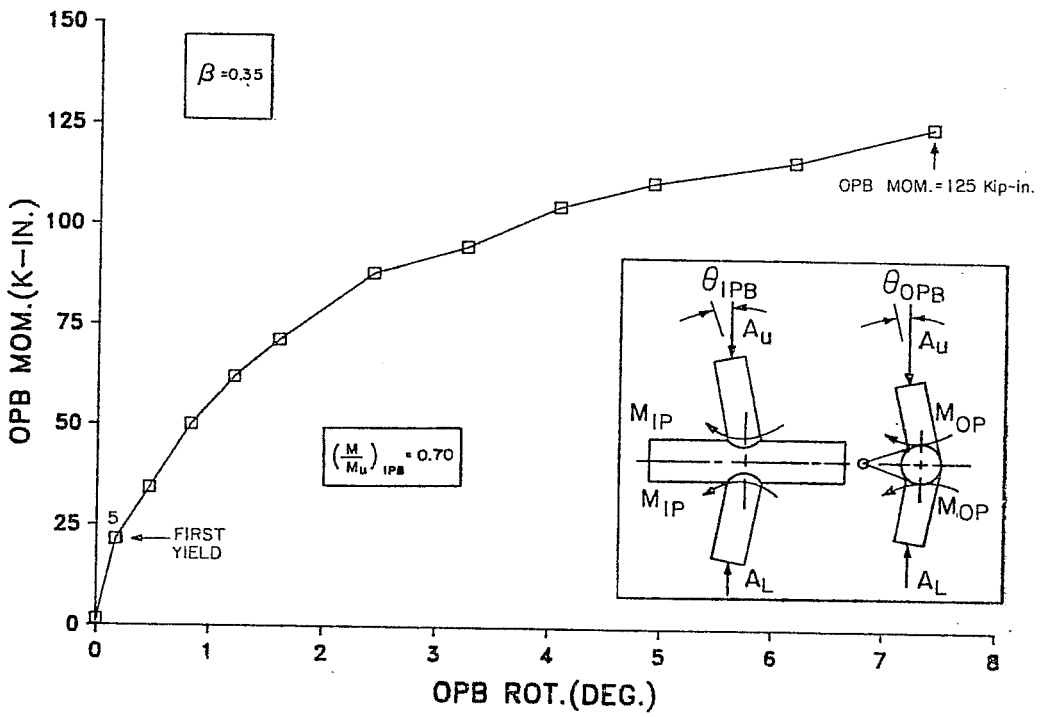

Fig. 3.47 OPB Moment-Rotation Curve for Test IO49

CHAPTER 4

DISCUSSION OF TUBULAR JOINT BEHAVIOR

The previous chapter was dedicated to presenting the results of the testing program; in this chapter several areas concerning the general behavior of the joints will be discussed. First, the failure mode of β=1.0 joints in compression and OPB, which is different than joints with smaller β ratios, will be discussed. Second, the effects of the β ratio on the interaction of branch loadings based on the results of the interaction tests (from both Phase 2 and 3) will be addressed. In addition, the test results will be compared to ultimate strength predictions based on the arcsine interaction equation in the 15th edition of the API specification [1]. Third, the DT data is compared to the results of a recent test program on T joints [30, 31] to investigate the effect of the geometry on the interaction of branch loadings.

A DT tubular joint's strength is determined by the ability of the chord wall to resist the applied branch loads. Around the periphery of the joint the chord resists the branch load in two ways as shown in Fig. 4.1; by plate action and by membrane action. Plate action occurs when the chord wall resists branch loads similar to a flat plate; as a combination of shear and bending in the chord wall. This action dominates as the

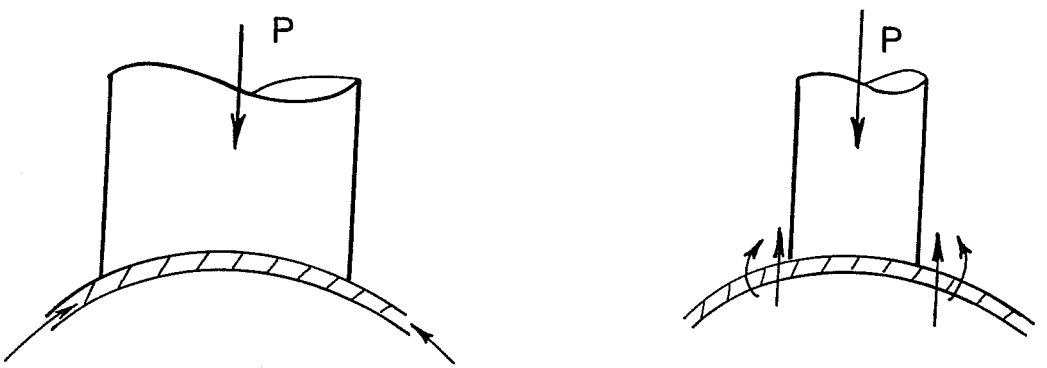

Fig. 4.1 Diagram of Plate and Membrane Action in Chord Wall

intersection of branch and chord walls approaches a right angle, as in the crown region or when β is small. Membrane action occurs when the branch loads are resisted by "axial", or membrane, forces in the chord wall. This action dominates in regions where the branch wall becomes tangent to the chord wall, as in the saddle region of a β=1.0 joint. In the elastic range, the chord wall is much stiffer in membrane action than in plate action, so the stiffness of the chord wall varies around the joint. This variation in stiffness is the cause of the stress concentrations which occur in tubular joints. In addition, the two actions have different failure modes. The failure of the chord wall in membrane action is an instability or buckling failure while the failure of the chord wall in plate action is a ductile or bending type failure.

At a β close to unity, most of the branch load is resisted in membrane action in the saddle region. Therefore, the failure of this type of joint under compression is an instability or buckling failure. As β decreases, the stiffness of the chord wall at the saddle approaches that of the crown and the branch loads are more evenly distributed around the joint. Since the branch loads are resisted primarily by plate action in the chord wall, the failure of this type of joint is a ductile or bending failure.

4.1 Influence of Gap on β=1.0 Joints in Compression

Comparison of the load-deflection curves of the reference tests for axial compression and OPB of the β=1.0 joint geometry shown in Figs.4.2 and 4.3 indicates significant differences in ultimate loads as well as behavior because the failure is controlled by instability of the chord wall between the saddle weld toes, or membrane action. The joints being compared are nominally identical, therefore there is some difference between the joints which would not be accounted for in design which has a significant effect on the strength and behavior of the joint. This difference was found to be in the distance between the weld toes at the saddle points which are loaded in compression. This parameter, which is shown in Fig. 4.4, will be referred to as the gap, G, and was measured on each β=1.0 specimen before testing. The gap dimension varied from 2.75 to 4.25 in. for the β-1.00 specimens with an average of 3.6 in. The gap dimensions for each specimen is given in Appendix C with other specimen dimensions.

Several procedures are involved in the fabrication of a tubular joint and some imperfections must be expected. Since the alignment of all of the joints was measured before each test (see Appendix C), and all were within a 1/3" in 5', alignment of the branches does not seem to be the reason for the variation in the gap. The variation in the gap sizes can be explained by an unsymmetric setting of the branch on the chord, as shown in Fig

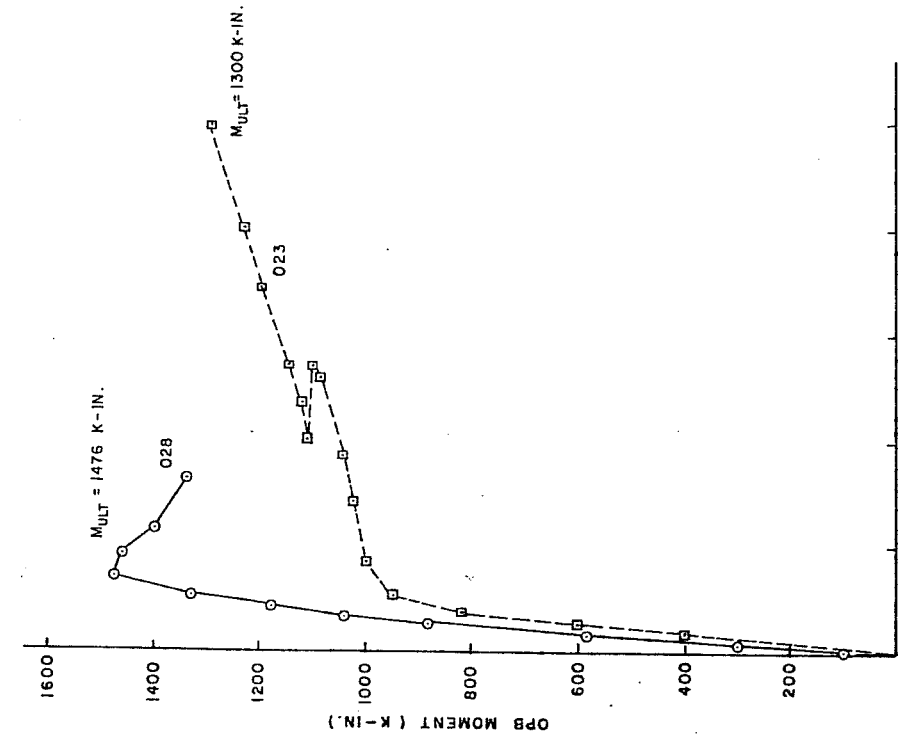

Fig. 4.3 Comparison of Tests 023 and 028

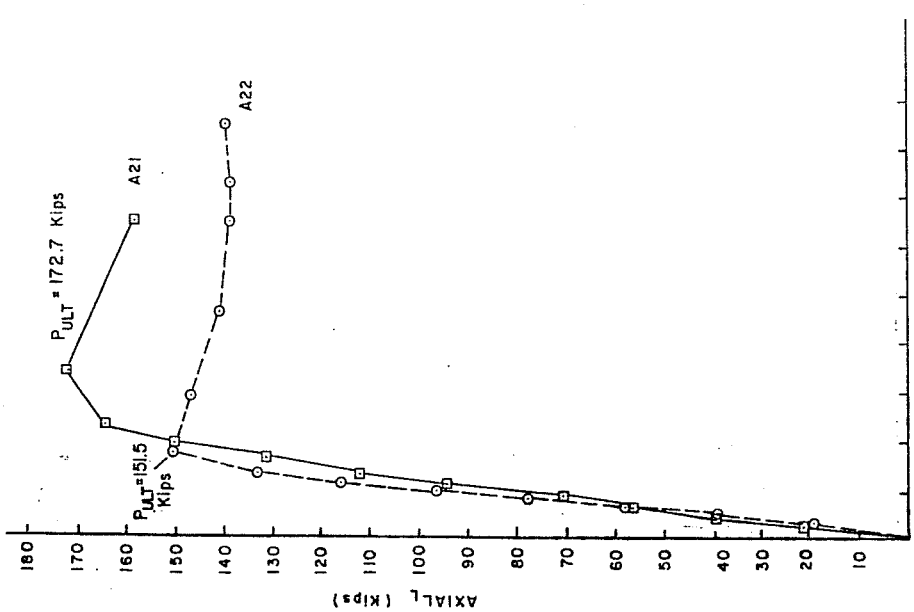

Fig. 4.2 Comparison of Tests A21 and A22

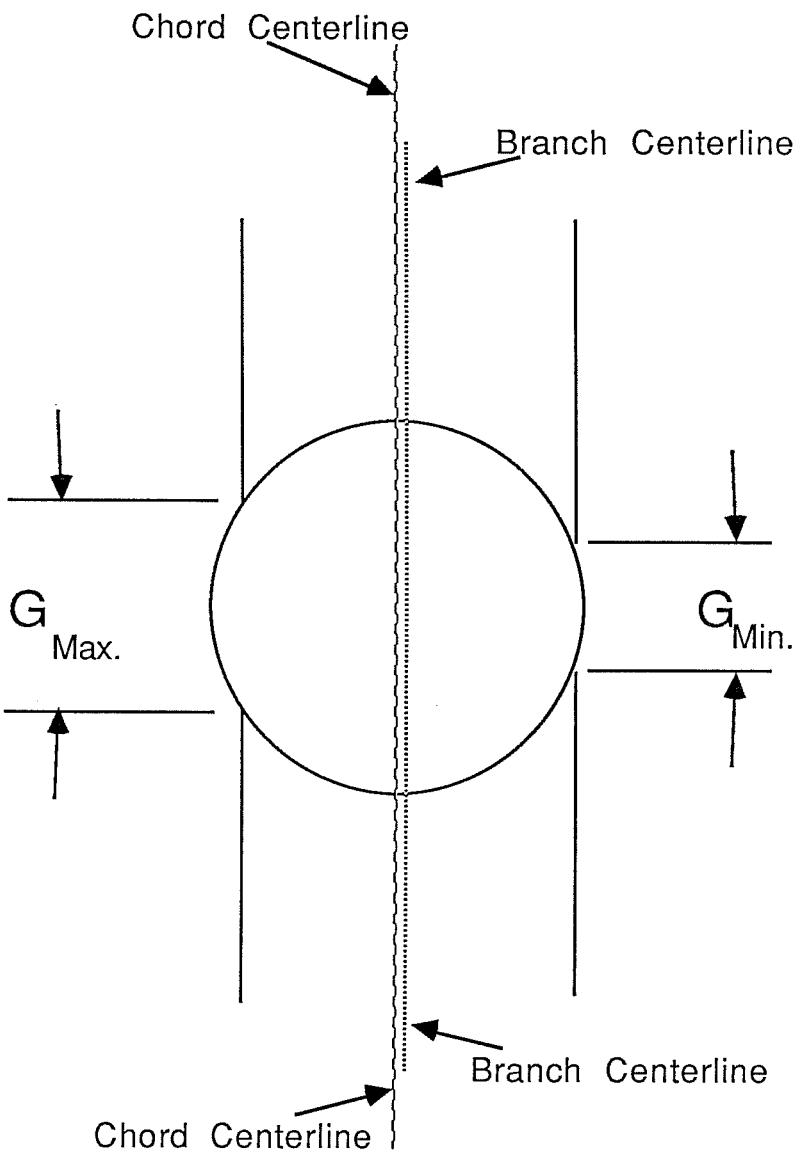

Fig. 4.4 Definition of Gap Parameter

4.4, due to a slightly off-center cut or a branch which is not perfectly round. Because the length of the saddle portion of the branch is very sensitive to the cut in a β=1.0 joint, a small eccentricity in the cut can result in a large variation in the gap dimensions.

The influence of the gap arises from the fact that the compression forces from the branch are resisted by a very small area of the joint. Tests in tension on β=1.0 joints recently completed at the University of Texas [28] support this conclusion because there was no significant loss of strength when the chord outside of the weld region was removed. In Ref. 28 the weld region is defined as the region of the chord between the welds of the joint. In addition, measurements from strain gages placed along the chord during Test A22 indicate that the chord outside of the weld region is not involved in resisting the branch loads until after the ultimate load is attained and large deformations are applied. Therefore, the branch loads are resisted mainly by the material between the weld toes. It follows that when compression is applied thru the branch, the chord wall between the weld toes behaves as a column with a length equal to the gap size. Thus, an analysis which treats the chord wall between the gaps as a column should yield an approximate prediction of the strength of the joint.

By Euler's equation, the strength of a column is a function of the slenderness ratio, (L/r). Thus, the strength of the joint should be a function of the ratio of the gap, G, to the radius of gyration, r. It is assumed that the chord wall at the weld toes is past yield so the effective length factor will be taken as 1.0. The respective values of the maximum compression gaps, slenderness ratios, and experimental load for tests A22, A21, 023, and 028 are given in Table 4.1. The experimental load for the axial tests is calculated by dividing the ultimate load by 2, since two gaps resist the load. The experimental load for the bending tests is calculated by taking the ultimate moment and dividing by a moment arm equal to the chord diameter.

Fig. 4.5 is a plot of the experimental loads vs. G/r, as given in Table 4.1, along with a portion of the SSRC inelastic buckling curve calibrated to Test 028. The experimental load was calculated from the critical stress inelastic buckling curve by assuming an effective area of 2.00 sq. in. which made the curve match the results of Test 028. An E of 29,000 ksi was assumed, and Fy was taken as 48.9 ksi from Table 2.2. Fig. 4.5 shows that the the results of Tests A21 and 023 fall along the calibrated inelastic buckling curve indicating that the correlation between joint failure and the buckling of the gap as a column is reasonably valid. The experimental load from Test A22 falls somewhat outside of the other data, but is well within the

TABLE 4.1 GAP INFORMATION FOR TESTS A21, A22, O23 AND O28

TEST	G (in.)	G/r	EXP. LOAD (kips)
O28	2.75	37.16	92.25
A21	3.63	49.05	86.4
A22	3.88	52.43	75.8
O23	4.25	57.43	81.3

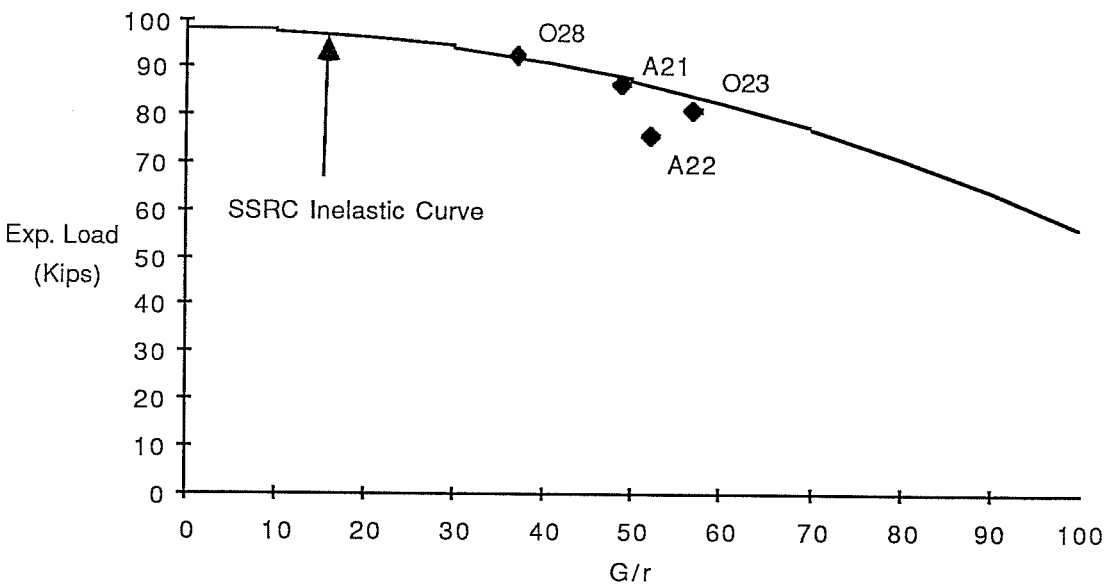

Fig. 4.5 Plot of Experimental Load vs. G/r

scatter typical of inelastic column buckling data for similar L/r values [33]. In Chapter 6, this behavior will be investigated analytically to determine the validity of the theory in the absence of experimental scatter.

Another gap parameter, the difference in the gaps, influences the mode of failure of the joint in axial compression. If the difference between the gaps is large, then one side of the joint will buckle and the chord will twist as in Test A22. This type of failure is ductile as the remaining side of the joint continues to resist load. However, if the gap difference is small, both sides of the joint will fail simultaneously with little reserve capacity; in other words, the joint will exhibit buckling type failure.

Because the gap parameter has a significant effect on the capacity of a β=1.0 joint in axial compression and OPB, the variation in this parameter should be accounted for in the factor of safety used in the design of the β=1.0 joint if mean equations are used.

4.2 Two-Dimensional Interactions

The nondimensionalized values used to develop the following interaction figures were calculated by dividing the experimental ultimate strength for each loading type in the interaction tests (Axial, IPB, or OPB) by the experimentally

TABLE 4.2 ULTIMATE STRENGTH AND INTERACTION VALUES: TEXAS TESTS

	TEST	AXIAL (kips)	MOM. (OPB) (kips)	MOM. (IPB) (K-IN)	P/PU (K-IN)	M/MU (OPB)	M/MU (IPB)
β=0.35	A40	42.0	0	0	0.95	0.00	0.00
	A41-P	46.2	0	0	1.05	0.00	0.00
	O42-P	3.1	118	0	0.07	1.00	0.00
	I43-P	4.8	0	257	0.11	0.00	1.00
	AO44-D	12.4	124	0	0.28	1.05	0.00
	AO45-D	31.2	73	0	0.71	0.62	0.00
	AI46-P	13.2	0	233	0.30	0.00	0.91
	AI47-B	30.2	0	200	0.69	0.00	0.78
	IO48-D	4.1	142	87	0.09	1.20	0.34
	IO49-D	3.3	125	179	0.08	1.06	0.70
	Reference	44.1	118	257			
β=0.67	A1-P	78.8	0	0	1.05	0.00	0.00
	A51-P	71.0	0	0	0.95	0.00	0.00
	O8-P	3.5	400	0	0.05	1.00	0.00
	I7-P	8.8	0	1056	0.12	0.00	1.00
	AO4-P	19.7	319	0	0.26	0.80	0.00
	AO13-P	52.6	177	0	0.70	0.44	0.00
	AI20-P	25.2	0	885	0.34	0.00	0.84
	AI17-B	52.7	0	687	0.70	0.00	0.65
	IO15-P	5.5	377	347	0.07	0.94	0.33
	IO14-P	5.0	268	678	0.07	0.67	0.64
	AIO16-D	19.8	335	328	0.26	0.84	0.31
	AIO18-P	49.6	153	410	0.66	0.38	0.39
	AIO19-D	49.3	140	352	0.66	0.35	0.33
	Reference	73.9	400	1056			
β=1.00	A21-P	172.7	0	0	1.07	0.00	0.00
	A22-P	151.5	0	0	0.93	0.00	0.00
	O23-D	13.5	1302	0	0.08	0.94	0.00
	O28-P	12.3	1476	0	0.08	1.06	0.00
	I24-P	18.6	0	2265	0.11	0.00	1.00
	AO31-D	44.4	1085	0	0.27	0.78	0.00
	AO32-P	88.1	796	0	0.54	0.57	0.00
	AO33-P	118.4	379	0	0.73	0.27	0.00
	AI34-P	43.8	0	2123	0.27	0.00	0.94
	AI35-P	86.6	0	2140	0.53	0.00	0.94
	AI36-P	169.0	0	1208	1.04	0.00	0.53
	AI50-P	129.0	0	1600	0.80	0.00	0.71
	IO37-D	15.2	1419	582	0.09	1.02	0.26
	IO38-D	17.2	1267	1160	0.11	0.91	0.51
	IO39-P	16.2	584	2173	0.10	0.42	0.96
	IO26-P	14.6	841	1590	0.09	0.61	0.70
	Reference	162.1	1389	2265			

NOTE: P = Peak load failure
D = Deformation limit failure
B = Buckling failure

determined average reference value. For example, the axial reference value of 44.1 kips for β=0.35 is the average of Tests A40 and A41. The experimental ultimate strengths, experimental reference values, as well as the nondimensionalized interaction values are given in Table 4.2.

4.2.1 Axial Compression with OPB: The interaction between axial compression and OPB for all three β ratios used in this project are shown in Fig. 4.6 along with the recommended API interaction curve for comparison. The axial and bending terms are normalized by experimental values given in Table 4.2. In the OPB reference tests, a small axial load was required to hold the specimens in the test frame, therefore the data points from Tests 023, 028, 08,and 042 do not fall directly on the bending axis. All points represent peak load failures except as noted. A "D" next to a data point denotes failure by the deformation limit. Comparison of the data to the arcsine equation indicates that several points fall below the arcsine equation. But, it should be noted that no replicate tests were run for the interaction data and the reference tests for axial load show a scatter band of approximately 15%. Most of the points seem to fall within this band so the arcsine equation may represent a reasonable mean equation but it is not a lower bound.

From the distribution of data points in Fig. 4.6 it seems that the β ratio influences the AO interaction. Test A033,

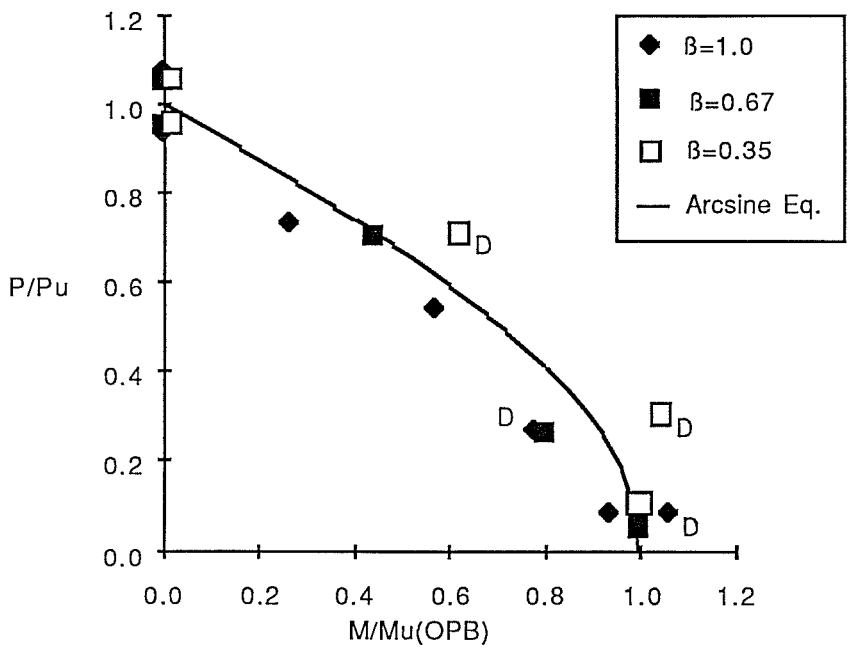

Fig. 4.6 AO Interaction Texas Tests

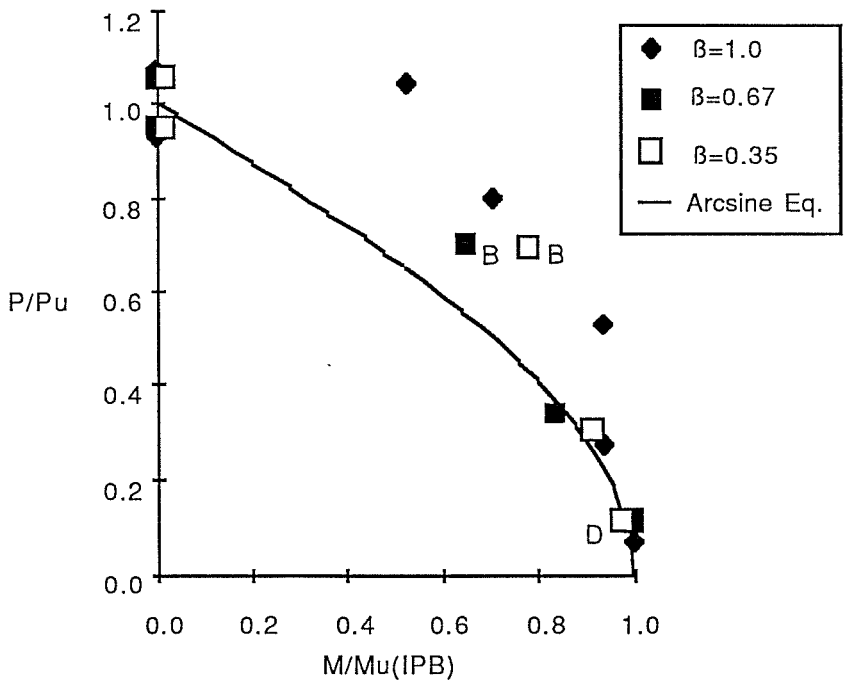

Fig. 4.7 AI Interaction Texas Tests

β=1.0, serves as a lower bound to the data with a linear interaction while the other two β=1.0 joints showed less interaction much like the β=0.67 joints. The β=0.35 joints produce an upper bound to the interaction with a more circular interaction.

The variation in interaction with β is not surprising considering the variation in the behavior of a tubular joint with β. For the β=1.0 joints, both axial and OPB loads are resisted almost exclusively in the saddle region so a linear interaction seems reasonable. This observation is supported by the fact that yielding in these specimens was confined to the saddle region. As β decreases from 1.0, the stiffness of the saddle region decreases with respect to the rest of the joint so the axial and OPB loads can be more evenly distributed around the joint. The OPB loads are mainly resisted at the saddle region because of the linear variation of stresses in the branch; however, the axial loads can be resisted by other portions of the joint. Thus, there is less direct interaction of the two loadings as β decreases.

4.2.2 Axial Compression with IPB: The interaction between axial compression and IPB for β=1.0, 0.67, and 0.35 is shown in Fig. 4.7 along with the recommended API interaction curve for comparison. The axial and IPB terms are normalized by the experimental values shown in Table 4.2. In the IPB reference tests, a small axial load was required to hold the specimens in

the test frame; therefore, the data points from Tests I24, I7, and I43 do not fall directly on the bending axis. All data in Fig. 4.7 represent failure defined by peak load except as noted. A "D" next to a point denotes failure defined by the deformation limit, "B" next to a point denotes failure by buckling. Comparison of the test data to the arcsine equation shows that the arcsine equation is conservative in most cases, but it does not fit the data very well. The arcsine equation is accurate for low values of P/P_u but is rather conservative for values of P/P_u larger than 0.5.

As in the AO interaction, β seems to influence the interaction. The results of the tests on joints with β=0.67 produce a lower bound to the data while the joints with β=0.35 and 1.0 fall along an upper bound. This distribution of data can be explained by the manner in which the load is transferred to the chord wall in each joint. The branch axial load for a β=1.0 specimen is resisted primarily in the saddle region; however, the linear stress distribution in the branch due to IPB requires the IPB loads to be resisted in the crown regions. Because the loads are resisted by two different portions of the joint, it follows that little interaction should be expected. As β decreases, the stiffness of the joint becomes more uniform and more of the joint is used to resist the branch loads; therefore, it is expected

that the interaction should increase as the β ratio decreases. But, the data shown in Fig. 4.7 shows less interaction in the β=0.35 joint than in the β=0.67 joint. This can be explained by redistribution of loads around the joint after first yielding in the β=0.35 joint since plate bending action is the primary mode of resistance for both IPB and axial load. In the β=0.35 joint all of the joint was utilized in resisting the branch loads while in the β=0.67 joint only the regions around the crown and saddle were utilized. This theory is supported by the yielding which was observed on the joints. On the β=0.67 joints, yielding before failure occurred at the saddle or crown region but not all around the joint. On the β=0.35 joints, yielding before failure occurred all across the IPB compression side of the joint as well as at the saddle positions, so almost all of the joint was utilized in resisting the branch loads.

4.2.3 IPB with OPB: The results of interaction tests between IPB and OPB are plotted in Fig. 4.8 along with the recommended API interaction curve for comparison. In all of the bending tests a small axial load was applied to hold the specimen in place, but for clarity these loads are ignored in Fig. 4.8. As before, all points on Fig. 4.8 represent failure defined by peak load, except for points marked with a "D: in which large deformations defined failure. A comparison of the test data to the arcsine curve shows that the curve fits the data fairly well

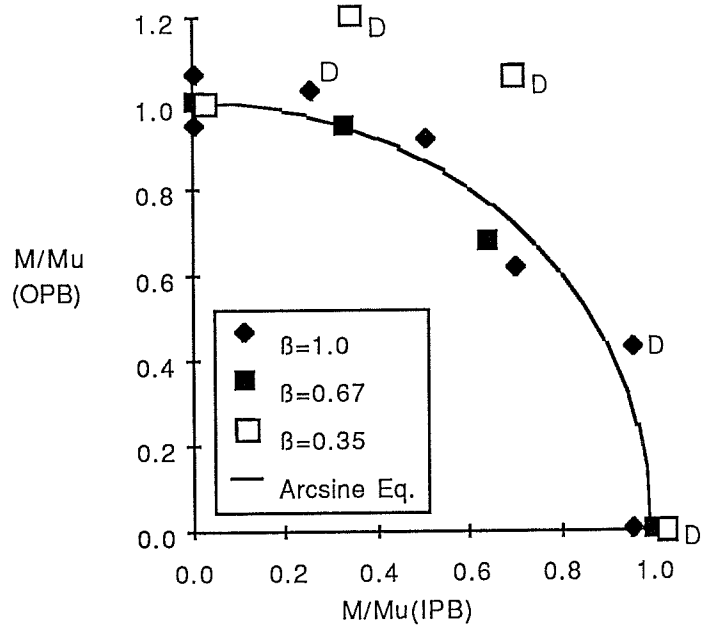

Fig. 4.8 IO Interaction Texas Tests

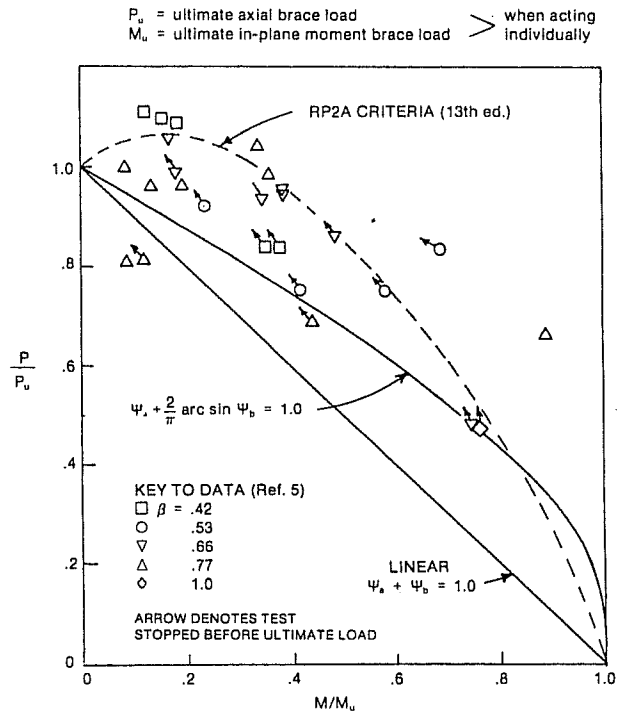

Fig. 4.9 AI Interaction from Stamenkovic Research: Ref.1

but 2 test results fall slightly on the unconservative side of the curve.

The data in Fig. 4.8 indicate that the IO interaction is different than the AI, or AO interaction. First, unlike the previous two interactions the effect of β on the interaction is not very distinct. For example, the result of Test I026 (β=1.0) falls along a lower band with the β=0.67 data, but the point from Test I039 (β=1.0) falls along an upper bound with the β=0.35 data. This may be the result of the difference in failure mechanisms. Tests I026, I037,and I038 all failed by buckling of the chord wall typical of OPB failure which is also prone to large amounts of scatter, but Test I039 failed by IPB which is a more ductile type of failure.

Second, the two IO interaction test results for joints with β=0.35 indicate that there is an increase in OPB strength with the addition of IPB moment. The question which must be answered is whether or not this increase can be depended on in design. A similar increase was shown by Stamenkovic's AI interaction tests on T joints for small β's and low values of $(M/M_u)_{IPB}$ [23]. This data is reproduced in Fig. 4.9 as presented in the commentary to the API-RP 2A Specification. Even though Stamenkovic's work did not include IO interactions, the fact that both axial and OPB loads are resisted primarily at the saddle point of the joint provides some basis for comparison. However,

recent testing on T joints at Delft University in the Netherlands [30 & 31], which will be discussed later, includes one test on a β=0.36 T joint at an $(M/M_u)_{IPB}$ of 0.39 which shows a reduction in OPB strength.

It might be argued that the experimental results indicate a false increase in OPB strength because of a low reference value in OPB or IPB which would tend to skew the interaction results. To check this theory it is reasonable to refer to the scatter present in past work on similar joints in IPB and OPB. A review of published data shows that the only tests on β = 0.35 DT joints in bending were completed as a part of this study; however, several sets of replicate bending tests on T joints are reported in Ref. 34. Since the branches are far removed in the β=0.35 DT joint, the behaviors of T and DT joints should not be too dissimilar; thus, the results should give some insight into the expected scatter. Two sets of identical T joints with β=0.38 and 0.33, and γ=20.0 and 32.2 respectively loaded in IPB show a difference of only 2.4% and 2.7%. In addition, both the Texas and Delft reference values for IPB fall very close to the mean of the available β=0.35-0.36 data as shown in Fig. 4.10 [39]. From these results it is not likely that the IPB reference data skews the interaction.

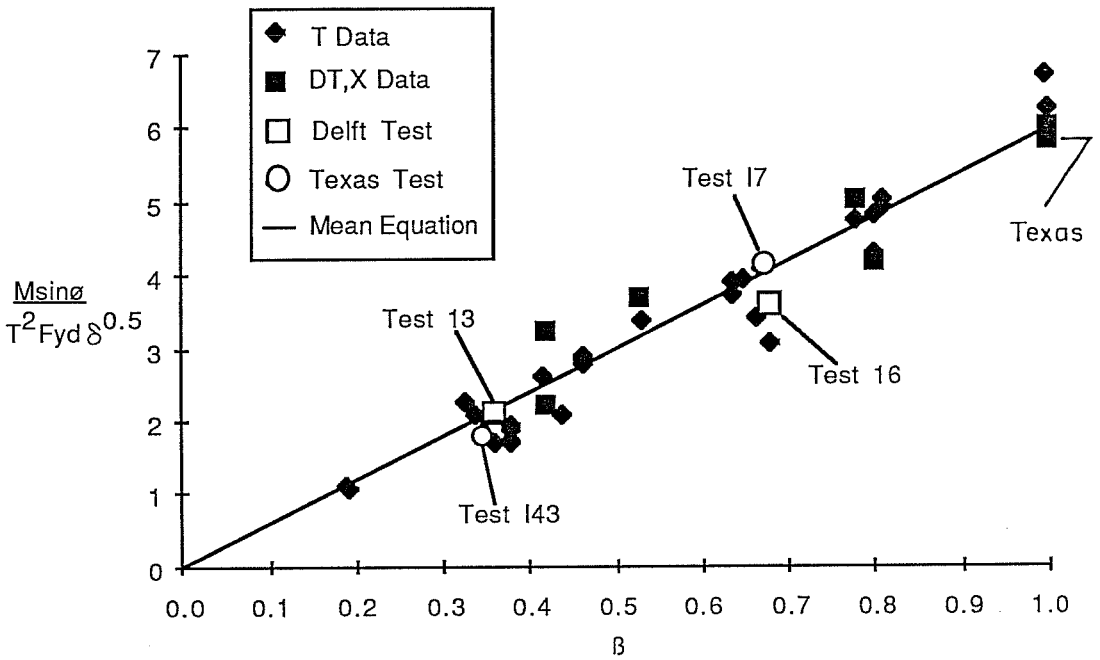

Fig. 4.10 IPB Ultimate Strength T and DT Data: Ref. 39

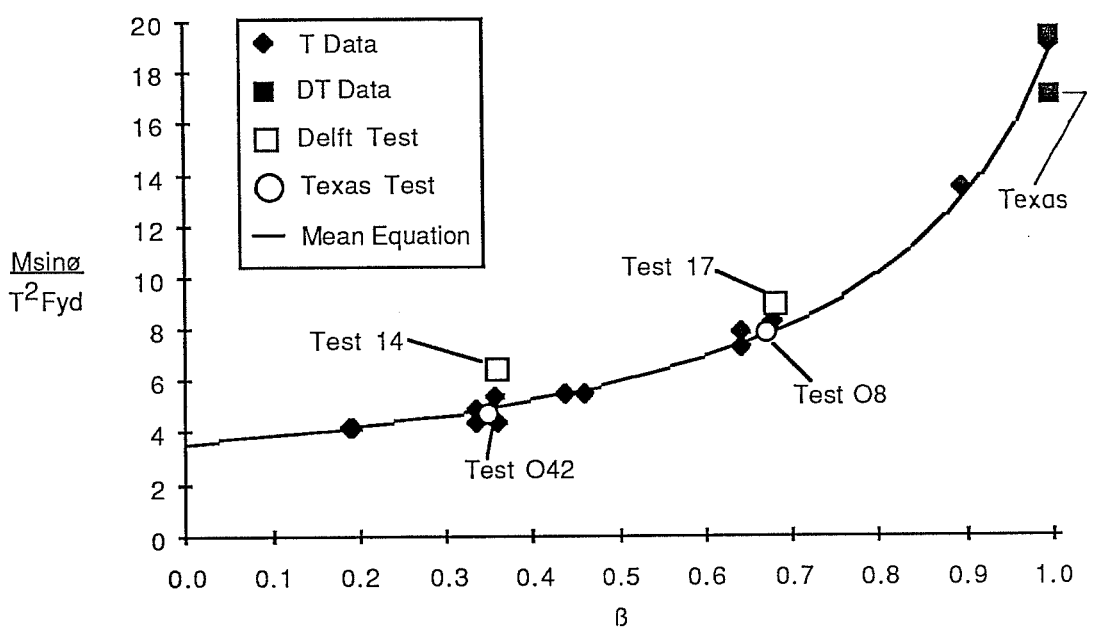

Fig. 4.11 OPB Ultimate Strength T and DT Data: Ref. 39

One set of T joints with β=0.34 and γ=22.8 loaded in OPB shows a difference of 9.6%. But, when compared to other OPB test results with similar β's, shown in Fig. 4.11 [39], the Delft reference test is approximately 40% higher than two test results with similar β and γ (β=0.34 and γ=22.8) while the Texas DT result falls almost on the mean of these two test results. This indicates that the Delft reference test is on the high side of the experimental results, thus reducing the relative strength of the IO interaction results in the OPB direction and supporting the idea that there is an increase in OPB strength with small IPB moments. But due to the small amount of experimental data, no definitive conclusions can be made.

In Chapter 6, an analytical study of this interaction showed a decrease in OPB strength with IPB load as shown in Delft's experiment. Therefore, further study is required and this increase should be used in design.

4.3 Comparison of DT and T Interactions

Two other research programs involving the interaction of branch loadings have been published. Stamenkovic and Sparrow conducted 105 tests on T joints under branch axial and IPB loads [29]. A chord diameter of 4.5 in. was used for all specimens which is very close to the minimum size of 4.33 in. recommended by the UEG [34], and less than the limit of 5.5 in. recommended

by Yura [40]. In addition, Hoadley [15] and Marshall [23] have shown that the definition of failure used for the combined load tests does not represent the ultimate capacity of the joint. For these two reasons the Stamenkovic data will not be used for comparison.

A more recent series of tests was completed at the Institute TNO for Building Materials and Building Structures in Delft in The Netherlands [30 & 31]. This research included a total of 77 tests on T joints with three different β ratios (0.36, 0.68, and 1.0) and three different γ ratios (8, 15, and 24). The loading conditions included axial brace compression, IPB, and OPB and four different loading combinations; AO, AI, IO, and AIO. All loadings, except two which were used for comparison, were applied in a proportional fashion similar to the loading of specimens AI50, and IO26. Due to plasticity in the chord or brace wall adjacent to the joint, only the following three series of tests yielded reliable interaction data [31];

1. β=0.68, γ=15
2. β=0.68, γ=24
3. β=0.36, γ=24

The failure loads from these three test series were defined for use in this report from load-deformation curves and information concerning material properties and specimen dimensions provided by TNO. The deformation limits discussed in

Chapter 3 were also used in the determination of failure loads. The three dimensional tests, AIO interaction, are not included because the location of a singular failure point was impossible from the load-deformation curves because not all loads decreased simultaneously.

The experimental ultimate strengths, experimental reference values, as well as the nondimensionalized interaction values are given in Table 4.3. The two dimensional interaction data from the Delft and Texas tests are plotted for comparison in Figs. 4.12-4.17. A set of curves, which are developed in Appendix A to fit thru the Texas data, is also included in Figs.4.12-4.17 to aid in comparison of the data. Series 1 data from the Delft tests are not included in the β=0.67 figures because the γ of 15 does not compare with the γ of approximately 25 for the other two test series. These figures show that the β=0.67 interactions for the T and DT joints are very similar except for the IO interaction where the T tests are an upper bound. The interactions of the T and DT joints for a β ratio of 0.35 are different with the T joints in general representing a lower bound.

Some insight into the difference between the DT and T interactions for β=0.35 may be gained by comparing the nondimensionalized reference values. The nondimensionalized

TABLE 4.3 ULTIMATE STRENGTH AND INTERACTION VALUES: DELFT TESTS

	TEST	AXIAL (kips)	MOM. (OPB) (kips-in.)	MOM. (IPB) (kips-in.)	P/PU	M/MU (OPB)	M/MU (IPB)
β=0.35	12	9.4	0	0	1.00	0.00	0.00
γ=24	13	0	0	19.5	0.00	0.00	1.00
	14	0	12.0	0	0.00	1.00	0.00
	34	8.3	0	8.1	0.88	0.00	0.42
	35	3.9	0	15.9	0.41	0.00	0.82
	36	7.4	5.8	0	0.79	0.48	0.00
	37	2.9	9.2	0	0.31	0.77	0.00
	38	0	11.0	7.6	0.00	0.91	0.39
	Reference	9.4	12.0	19.5			
β=0.68	15	18.0	0	0	1.00	0.00	0.00
γ=24	16	0	0	64.6	0.00	0.00	1.00
	17	0	32.8	0	0.00	1.00	0.00
	39	7.3	0	51.3	0.41	0.00	0.79
	40	14.8	0	27.4	0.83	0.00	0.42
	41	5.4	27.4	0	0.30	0.84	0.00
	42	12.3	15.6	0	0.68	0.48	0.00
	43	0	33.6	25.2	0.00	1.03	0.39
	44	0	18.4	54.0	0.00	0.56	0.84
	Reference	18.0	32.8	64.6			
β=0.68	9	38.2	0	0	1.00	0.00	0.00
γ=15	10	0	0	131.0	0.00	0.00	1.00
	11	0	70.8	0	0.00	1.00	0.00
	28	28.6	0	52.2	0.75	0.00	0.40
	29	15.7	0	109.8	0.41	0.00	0.84
	30	28.3	29.2	0	0.74	0.41	0.00
	31	13.9	54.9	0	0.36	0.78	0.00
	32	0	33.6	124.8	0.00	0.48	0.95
	33	0	67.3	63.7	0.00	0.95	0.49
	Reference	38.2	70.8	131.0			

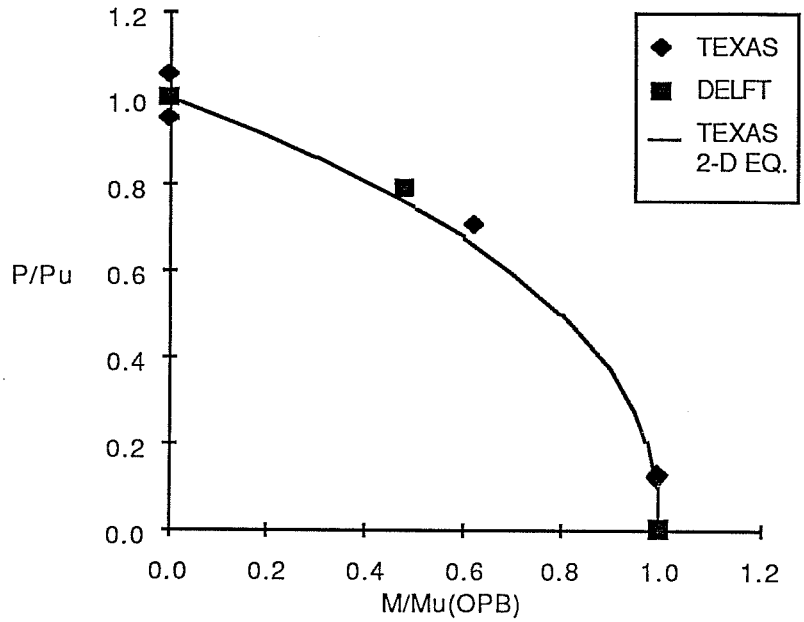

Fig. 4.12 Comparison of Texas and Delft Data- AO Interaction: ß=0.35

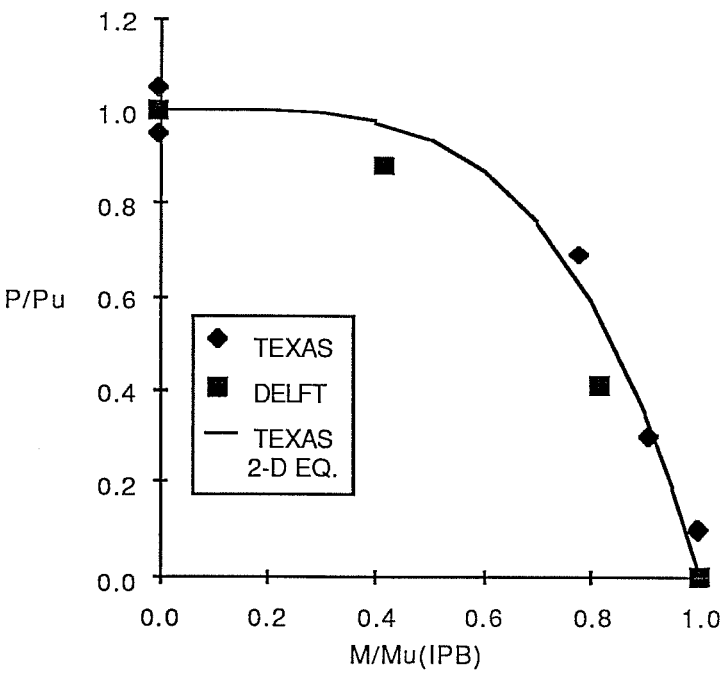

Fig. 4.13 Comparison of Texas and Delft Data- AI interaction: ß=0.35

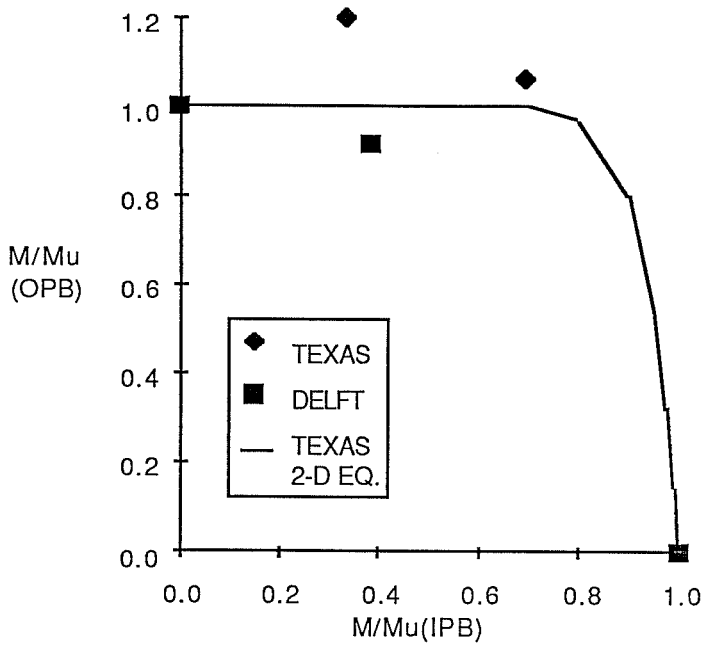

Fig. 4.14 Comparison of Texas and Delft Data- IO Interaction: ß=0.35

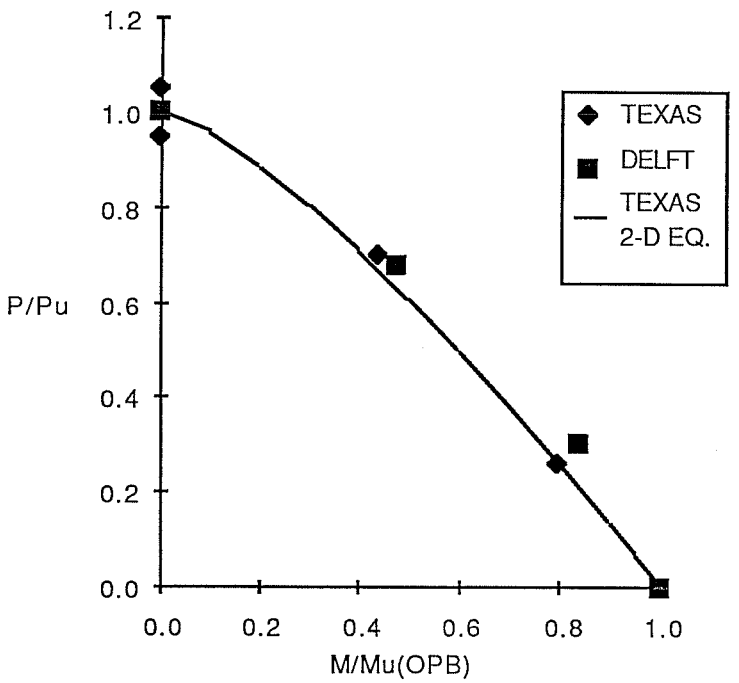

Fig. 4.15 Comparison of Texas and Delft Data- AO Interaction: ß=0.67

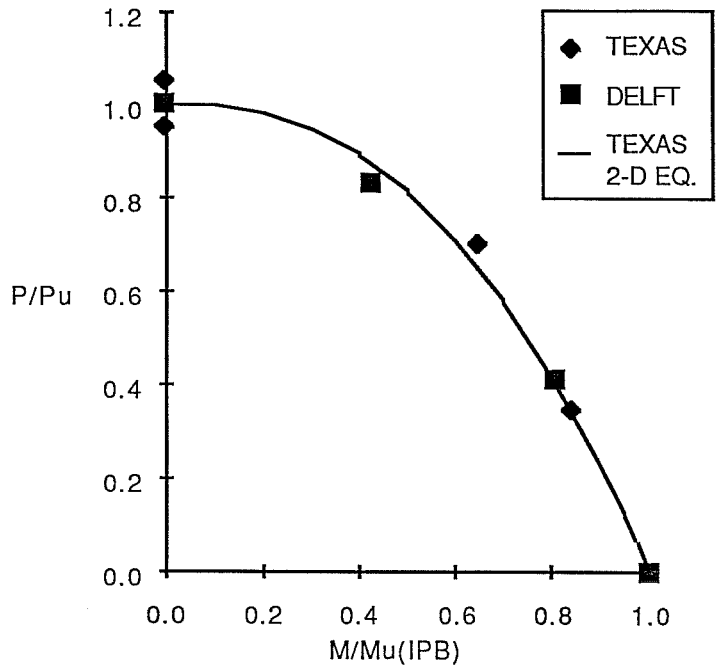

Fig. 4.16 Comparison of Texas and Delft Data- AI Interaction: ß=0.67

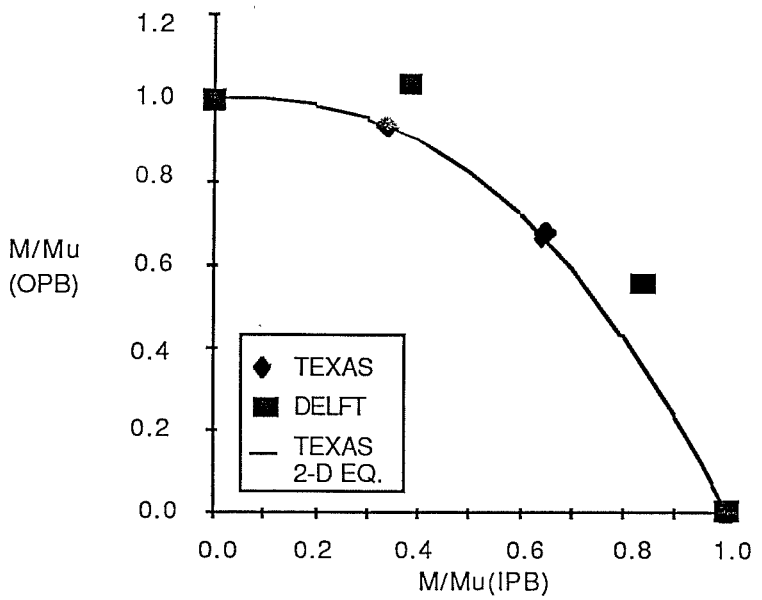

Fig. 4.17 Comparison of Texas and Delft Data- IO interaction: ß=0.67

reference test results for IPB and OPB are plotted along with other data in Figs. 4.10 and 4.11. From these figures it can be seen that the T and DT data fall within the same band and thus may be treated together as is done in the present API specifications. The data plotted in Fig. 4.10 shows that the Texas and Delft IPB reference values fall very close together and are near the mean of the data for the β=0.35 case, but for the β=0.67 case the Delft reference point falls below the Texas reference point which is on the high side of the data. This could explain the difference between the T and DT data for the β=0.67 IO interaction. Fig. 4.11 shows that the β=0.67 OPB reference points fall close together while the Texas β=0.35 OPB reference point falls below the Delft point which is on the high side of the data. This could explain the difference between the T and DT β=0.35 interaction data.

It may also be argued that the difference between the T and DT joint data is a result of the different load paths used in the testing because the T joints were loaded proportionally while the DT joints were not. In the published report containing the T joint data [30], Stol et al. stated that the proportional loadings appeared to give a lower bound to the ultimate loads when compared to nonproportional loading and that the nonproportional loadings significantly overestimate ultimate loads. This phenomenon may explain the differences for the β=0.35

interactions, but the argument does not hold for the $\beta=0.67$ interactions. In addition, the results of the DT tests do not indicate any significant difference between the proportional and nonproportional data.

C H A P T E R 5

INTERACTION EQUATIONS

Comparison of the test results and the recommendation in the 15th edition of API RP 2A show that the recommended interaction formula is unconservative in many cases, and very conservative in others. Therefore, a new lower bound interaction equation will be developed based on the experimental results of the present phase and of the phase 2 research. The equation will be evaluated using both the Texas DT interaction data and the Delft T interaction data and compared with the current API recommendation [1] and with an equation proposed by Hoadley [14] which was recommended for use by the recent UEG Design Guide [34]. To determine the interaction equations' usefulness in design, the interaction data will be nondimensionalized by reference values predicted from API strength equations as well as the experimental reference values.

The interaction equations will be evaluated using the parameter C, which was developed by Hoadley. C is the ratio of the distance from the origin to the interaction curve to the distance from the origin to the data point in question, and is calculated as follows:

$$C=L1/L2$$

where, L1= distance from origin to the data point and L2=distance

from the origin to the interaction curve. An example of the distances L1 and L2 are shown in Fig. 5.1. From this definition, a ultimate strength prediction is conservative if C is larger than 1.0. The C parameter is especially useful because it can be used in both two and three dimensions and is not a function of the exponents X, Y, or Z of Eq (5.1). In addition, it can be used to determine the amount of conservatism in an equation when the experimental parameters are outside the range of the equation, as with the arcsine equation when the moment parameter is larger than 1.

5.1 Proposed Interaction Equation

From a preliminary analysis of the experimental data in the two dimensional form, which is shown in Appendix A, it was found that a general equation of the following form provided a satisfactory fit to the data;

$$P/P_u{}^X + (M/M_u)_{OPB}{}^Y + (M/M_u)_{IPB}{}^Z = 1.0 \qquad (5.1)$$

A very accurate three dimensional interaction could be developed by replacing the exponents with those derived for the two-dimensional interactions. However, the exponents vary with both the type of interaction (AI, AO, or IO) and the β ratio, so the exponents X, Y, and Z would have to be written as functions of both the type of interaction and the β ratio. This formulation is very cumbersome and the accuracy is not warranted given the

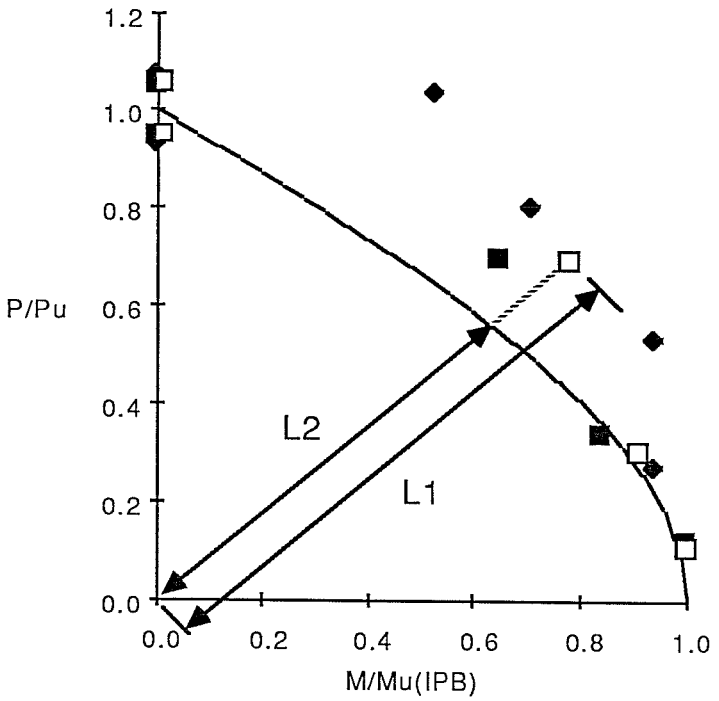

Fig. 5.1 Definition of L1, and L2

scatter shown in the reference tests. A more approximate but much simpler equation can be developed by making X, Y, and Z functions of β only. This method requires a reformulation of the two dimensional interaction equations so that there is only one value of X, Y, and Z for each β.

In the reformulation of the two dimensional interaction equations, the values of X, Y, and Z, were varied to find a lower bound to the data for each β ratio with the lowest standard deviation. In determining a lower bound to the data, a slightly unconservative value of C was accepted if there was a significant reduction in the standard deviation by accepting the set of coefficients. The lowest value of C accepted was 0.98, which is well within a scatter band set by the reference tests of 0.93 to 1.07. In the three dimensional interaction the axial load present in the bending tests is not ignored in Eq. 5.1, but the experimental reference values given in Table 4.2 remain unchanged. The resulting values of X, Y, and Z are given in Table 5.1. In order to obtain a continuous value of the exponents X, Y, and Z, the following functions of β were developed;

$$X=1.0 \tag{5.1X}$$

$$Y=2.35 - 1.35(\beta)^{0.63} \tag{5.1Y}$$

$$Z=3.44(\beta) + 0.01(\beta)^{-5.60} \tag{5.1Z}$$

A plot of the X, Y, and Z vs. β is shown in Fig. 5.2. The axial term remains linear for all β ratios as recommended in

TABLE 5.1 EXPONENTS FOR THREE DIMENSIONAL INTERACTION

β	X	Y	Z
1.0	1.00	1.00	3.45
0.67	1.00	1.30	2.40
0.35	1.00	1.65	4.78

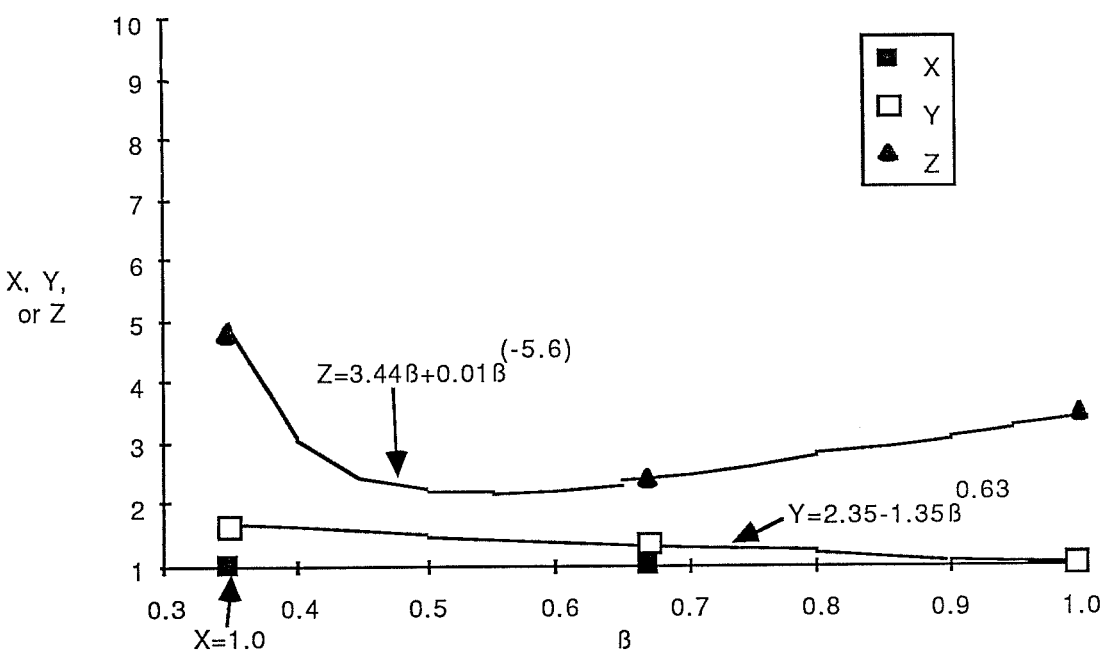

Fig. 5.2 Variation of Exponenets X,Y, and Z with ß

Hoadley's interaction equation. The OPB term decreases with β showing the decreasing interaction between axial and OPB with increasing β. The IPB exponent shows more of a parabolic variation with β.

5.2 Other Interaction Equations

Several interaction equations have been suggested for use in the design of tubular joints. A linear interaction was proposed by Stamenkovic [29]. The 15th Ed. of API recommendations use the arcsine equation which is based on the plastic section strength of the branch member. Hoadley developed a polynomial type interaction equation based on DT interaction tests. Most recently Stol, Puthli, and Bijlaard, have presented an equation of the same form as Eq. 5.1 (Hoadley) with exponents that vary with β and γ. This report will deal only with the two formulations which are most widely recommended for use in design. These are the equations proposed by Hoadley and the arcsine equation.

5.2.1 Hoadley Equation: Equation 5.2 shown below was developed by Hoadley based on nine interaction tests on DT joints with β=0.67 [14] and was recommended for use in design by the recent UEG Design Guide [34]. The same interaction data was included in the development of the proposed equation; however, the axial reference for β=0.67 was altered based on the results

of Test A51.

$$(P/P_u) + (M/M_u)^{1.2}_{OPB} + (M/M_u)^{2.1}_{IPB} = 1.0 \qquad (5.2)$$

5.2.2 Arcsine Equation: The arcsine interaction equation, given below, is recommended for use in design in the 15th edition of API RP 2A.

$$P/P_u + (2/\pi)\ \text{Arcsine}[(M/M_u)^{2}_{OPB} + (M/M_u)^{2.1}_{IPB}]^{1/2} = 1.0 \qquad (5.3)$$

The arcsine interaction is based on the plastic section strength of a hollow circular cross section assuming that plane sections remain plane. Thus Eq. 5.3 really predicts the failure of the branch member and not necessarily the strength of the joint, because the strength of the joint is a function of the ability of the chord wall to resist the branch loads.

5.3 Evaluation of Interaction Equations: Experimental Reference

Table 5.2 contains the C values for the two dimensional (given in Appendix A), the proposed (Eq. 5.1), Hoadley's (Eq. 5.2), and the API (Eq. 5.3) interaction equations applied to the Texas Tests where ultimate strength is taken from experimental reference values given in Table 4.2. Table 5.3 contains the same information except that the interaction equations are applied to the results of the Delft tests and reference values are taken from Table 4.3 The C values from Tables 5.2 and 5.3 are

TABLE 5.2 C VALUES FOR INTERACTION EQUATIONS - TEXAS TESTS: EXPERIMENTAL REFERENCE

	TEST	P/PU	M/MU (OPB)	M/MU (IPB)	2-D	EQ. 5.1 PROPOSED	EQ. 5.2 HOADLEY	EQ. 5.3 API
β=0.35	A40	0.95	0.00	0.00	0.95	0.95	0.95	0.95
	A41	1.05	0.00	0.00	1.05	1.05	1.05	1.05
	O42	0.07	1.00	0.00	0.99	1.04	1.03	1.01
	I43	0.11	0.00	1.00	1.03	1.02	1.05	1.01
	AO44	0.28	1.05	0.00	1.10	1.23	1.28	1.13
	AO45	0.71	0.62	0.00	1.04	1.12	1.24	1.12
	AI46	0.30	0.00	0.91	0.99	0.98	1.06	1.01
	AI47	0.69	0.00	0.78	1.02	0.99	1.18	1.22
	IO48	0.09	1.20	0.34	1.20	1.26	1.34	1.26
	IO49	0.08	1.06	0.70	1.04	1.16	1.40	1.28
β=0.67	A1	1.05	0.00	0.00	1.05	1.05	1.05	1.05
	A51	0.95	0.00	0.00	0.95	0.95	0.95	0.95
	O8	0.05	1.00	0.00	1.02	1.02	1.02	1.00
	I7	0.12	0.00	1.00	1.05	1.04	1.05	1.02
	AO4	0.26	0.80	0.00	1.00	1.00	1.02	0.89
	AO13	0.70	0.44	0.00	1.03	1.04	1.07	0.99
	AI20	0.34	0.00	0.84	0.99	0.99	1.01	0.98
	AI17	0.70	0.00	0.65	1.04	1.04	1.07	1.14
	IO15	0.07	0.94	0.33	1.01	1.05	1.05	1.00
	IO14	0.07	0.67	0.64	1.00	0.98	1.04	0.91
	AIO16	0.26	0.84	0.31	-.—	1.08	1.12	0.98
	AIO18	0.66	0.38	0.39	-.—	1.04	1.10	1.03
	AIO19	0.66	0.35	0.33	-.—	0.99	1.03	0.98
β=1.00	A21	1.07	0.00	0.00	1.07	1.07	1.07	1.07
	A22	0.93	0.00	0.00	0.93	0.93	0.93	0.93
	O23	0.08	0.94	0.00	1.02	1.02	0.99	0.95
	O28	0.08	1.06	0.00	1.08	1.08	1.12	1.07
	I24	0.11	0.00	1.00	1.02	1.03	1.04	1.01
	AO31	0.27	0.78	0.00	1.06	1.06	1.01	0.88
	AO32	0.54	0.57	0.00	1.12	1.12	1.05	0.94
	AO33	0.73	0.27	0.00	1.00	1.00	0.94	0.75
	AI34	0.27	0.00	0.94	1.00	1.02	1.07	1.02
	AI35	0.53	0.00	0.94	1.09	1.13	1.24	1.22
	AI36	1.04	0.00	0.53	1.08	1.13	1.25	1.39
	AI50	0.80	0.00	0.71	1.00	1.06	1.19	1.27
	IO37	0.09	1.02	0.26	1.05	1.11	1.13	1.06
	IO38	0.11	0.91	0.51	1.07	1.10	1.17	1.06
	IO39	0.10	0.42	0.96	1.13	1.14	1.19	1.07
	IO26	0.09	0.61	0.70	1.00	0.99	1.05	0.94
			Average		1.03	1.05	1.09	1.04
			St. Dev.		0.05	0.07	0.11	0.13
			Coef. of Var.		4.77	6.81	9.10	12.08

TABLE 5.3 C VALUES FOR INTERACTION EQUATIONS - DELFT TESTS: EXPERIMENTAL REFERENCE

	TEST	P/PU	M/MU (OPB)	M/MU (IPB)	EQ. 5.1 PROPOSED	EQ. 5.2 HOADLEY	EQ. 5.3 API
β=0.36 γ=24	12	1.00	0.00	0.00	1.00	1.00	1.00
	13	0.00	0.00	1.00	1.00	1.00	1.00
	14	0.00	1.00	0.00	1.00	1.00	1.00
	34	0.88	0.00	0.42	0.90	1.04	1.15
	35	0.41	0.00	0.82	0.92	1.04	1.02
	36	0.79	0.48	0.00	1.07	1.18	1.10
	37	0.31	0.77	0.00	0.96	1.02	0.89
	38	0.00	0.91	0.39	0.92	1.03	0.99
β=0.68 γ=24	15	1.00	0.00	0.00	1.00	1.00	1.00
	16	0.00	0.00	1.00	1.00	1.00	1.00
	17	0.00	1.00	0.00	1.00	1.00	1.00
	39	0.41	0.00	0.80	0.99	1.01	0.99
	40	0.83	0.00	0.43	0.96	0.99	1.10
	41	0.30	0.84	0.00	1.08	1.09	0.95
	42	0.68	0.48	0.00	1.05	1.08	0.99
	43	0.00	1.03	0.39	1.09	1.13	1.10
	44	0.00	0.56	0.84	1.06	1.10	1.01
β=0.68 γ=15	9	1.00	0.00	0.00	1.00	1.00	1.00
	10	0.00	0.00	1.00	1.00	1.00	1.00
	11	0.00	1.00	0.00	1.00	1.00	1.00
	28	0.75	0.00	0.40	0.88	0.90	1.01
	29	0.41	0.00	0.84	1.03	1.06	1.03
	30	0.74	0.41	0.00	1.05	1.08	1.01
	31	0.37	0.78	0.00	1.07	1.09	0.94
	32	0.00	0.48	0.95	1.12	1.16	1.06
	33	0.00	0.95	0.49	1.07	1.12	1.07
				Average =	1.01	1.05	1.02
				St. Dev. =	0.07	0.07	0.06
				Coef. of Var. =	6.78	6.86	5.78

presented graphically in Fig. 5.3 where the C values for each interaction equation are plotted for each β ratio. In Tables 5.4 and 5.5 the average, standard deviation, and the coefficient of variation of C are presented for each interaction equation for each series of testing in the Texas and Delft research respectively. The average, standard deviation, and the coefficient of variation of C for all of the data and for each interaction equation is given in Table 5.6.

Comparison of the average values, standard deviations, and the coefficient of variations for the 2-D and proposed interaction equation (Eq. 5.1) given in Tables 5.2 and 5.4 shows that the 3-D approximation has little effect on the accuracy of the predictions of the interaction formula for the Texas data. C values could not be calculated for the 2-D interaction formula applied to tests AI016, AI018, and AI019 because these were three dimensional interactions in which the axial load was too high to be ignored. This fact shows why the 2-D equation is not applicable to design and why it will not be evaluated for other than the Texas data.

The average values, standard deviations, and the coefficients of variation given at the bottom of Table 5.2 indicate that in general, of the three-dimensional interaction equations, the proposed interaction is the most applicable to the Texas data, which is expected because this is the data base used

TABLE 5.4 SUMMARY OF C VALUES FOR INTERACTION EQUATIONS - TEXAS TESTS: EXPERIMENTAL REF.

	β=1.0			β=0.67			β=0.35		
Eq.	Avg.	S.D.	C. of V.	Avg.	S.D.	C. of V.	Avg.	S.D.	C. of V.
2 - D	1.05	0.05	4.99	1.01	0.03	3.13	1.04	0.07	6.68
Eq. 5.1	1.06	0.06	5.64	1.02	0.04	3.54	1.08	0.11	9.95
Eq. 5.2	1.09	0.10	9.11	1.04	0.04	4.07	1.16	0.15	13.08
Eq. 5.3	1.04	0.16	14.96	0.99	0.06	6.29	1.10	0.12	10.58

Eq. 5.1 - Proposed
Eq. 5.2 - Hoadley
Eq. 5.3 - Arcsine

TABLE 5.5 SUMMARY OF C VALUES FOR INTERACTION EQUATIONS - DELFT TESTS: EXPERIMENTAL REF.

	β=.68 γ=24			β=0.68 γ=15			β=0.35 γ=24		
Eq.	Avg.	S.D.	C. of V.	Avg.	S.D.	C. of V.	Avg.	S.D.	C. of V.
Eq. 5.1	1.03	0.05	4.42	1.02	0.07	6.60	0.97	0.06	5.86
Eq. 5.2	1.04	0.05	5.22	1.05	0.08	7.52	1.04	0.06	5.74
Eq. 5.3	1.02	0.05	5.00	1.01	0.04	3.76	1.02	0.08	7.63

Eq. 5.1 - Proposed
Eq. 5.2 - Hoadley
Eq. 5.3 - Arcsine

TABLE 5.6 SUMMARY OF C VALUES FOR ALL DATA: EXPERIMENTAL REFERENCE

β	Num. of Tests	Eq. No.	Average C	Standard Deviation	Coef. of Var.
0.35	18	5.1	1.03	0.103	9.95
		5.2	1.11	0.132	11.91
		5.3	1.07	0.108	10.11
0.67	31	5.1	1.02	0.048	4.68
		5.2	1.04	0.056	5.39
		5.3	1.01	0.052	5.21
1.00	16	5.1	1.06	0.060	5.64
		5.2	1.09	0.099	9.11
		5.3	1.04	0.155	14.96
Total	65	5.1	1.04	0.070	6.81
		5.2	1.07	0.096	8.91
		5.3	1.03	0.103	10.04

Eq. 1 - Proposed
Eq. 2 - Hoadley
Eq. 3 - Arcsine

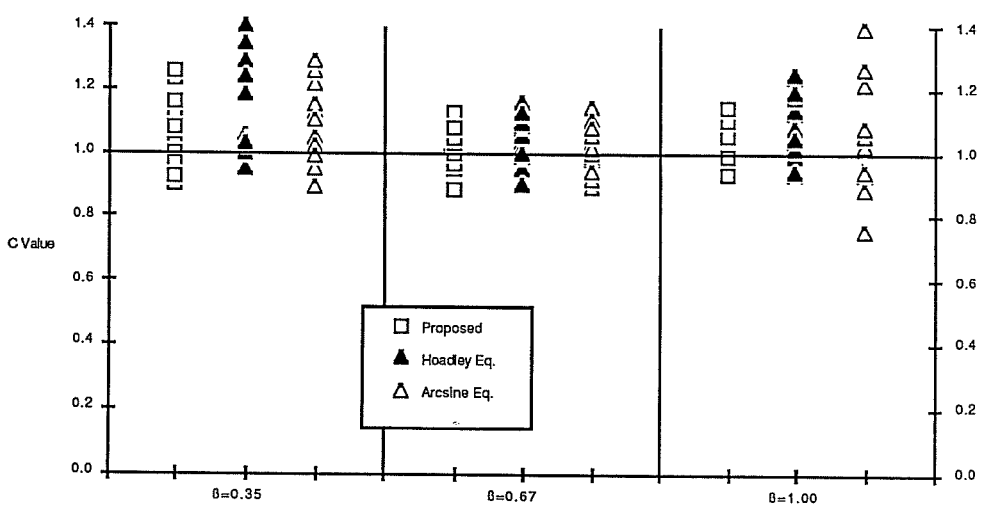

Fig. 5.3 C Values vs. β : Exp. Reference

to generate the equation. In addition, the average C values, standard deviations, and the coefficients of variation given in Table 5.4 show that the proposed equation is the most accurate for all β's tested. The importance of varying the interaction equation with β is shown by the relatively large standard deviations and coefficients of variation produced by Hoadley's and the arcsine equation for β=0.35 and 1.00 shown in Table 5.4

Comparison of the average values, standard deviations, and the coefficients of variation given at the bottom of Table 5.3 indicate that the arcsine equation (Eq. 5.3) best fits the Delft interaction data although there is little difference among the three interaction equations. The information presented in Table 5.5 reveals that the proposed equation is just as accurate as the arcsine equation for β=0.68 and γ=24, and Hoadley's equation is the most accurate for β=0.36 and γ=24. The arcsine equation provides a significantly better fit to the data for only the β=0.68 and γ=15 series of tests.

Comparison of the coefficient of variation of C for all of the data, as shown in Table 5.6, indicates that the proposed equation fits the data better than the other equations for all β ratios. Of the 65 tests included in the data base, 39, or 60% of the total, were performed on DT joints while the other 26, or 40% of the total, are from the TNO research on T joints, so

coefficients of variation are not severely skewed toward the DT results.

The results of the Texas and Delft tests along with the three interaction curves are plotted in Figs. 5.4 -5.12. Because of the two dimensional nature of the interactions, and the variation in the forms and powers used in the three interaction equations, the results are shown graphically in two dimensions (AO, AI, and IO). In addition, each β ratio is presented in a different graph. The plots for AO, AI, and IO for β=0.35, 0.67 and 1.0 are presented in Figs. 5.4-5.6, 5.7-5.9, and 5.10-5.12 respectively. In the figures, the Delft data is referred to as series 1 (β=0.68, γ=15), series 2 (β=0.68, γ=24), and series 3 (β=0.36, γ=24).

For β=0.35, the proposed equation does not always represent a lower bound to the data. In the AI and IO interactions, Figs. 5.5 and 5.6 respectively, the proposed equation is unconservative when compared to the T joint results from Delft. Hoadley's equation provides a lower bound to all of the β=0.35 data, but is very conservative for much of the Texas test results. The β=0.67 data as well as the interaction curves fall within a relatively tight band in the interaction figures. The arcsine equation is unconservative in several cases for the AO interaction, but in general the predictions of three equations are comparable. Comparison of the arcsine curve with the β=1.0

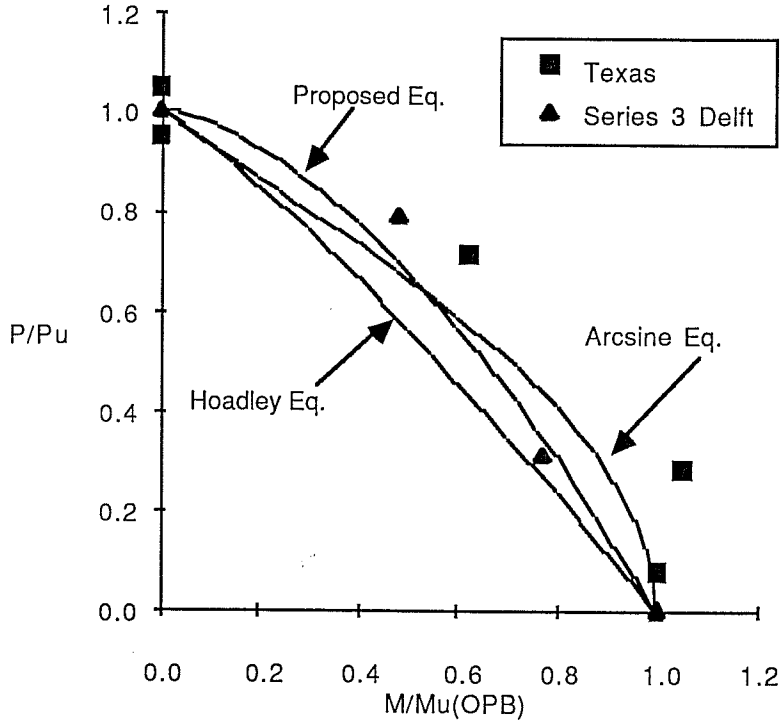

Fig. 5.4 AO Interaction ß=0.35-Test Data and Interaction Curves: Exp. Reference

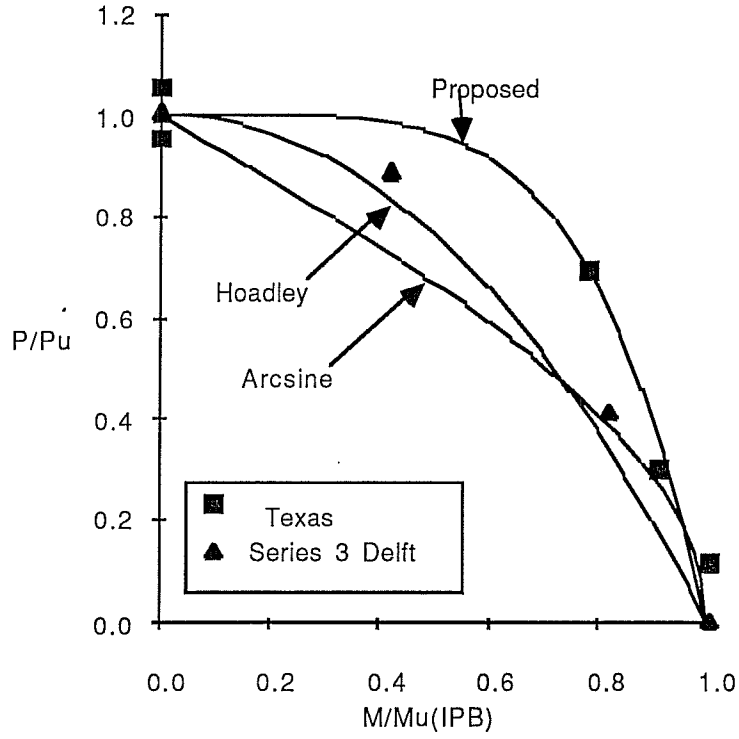

Fig. 5.5 AI Interaction ß=0.35-Test Data and Interaction Curves: Exp. Reference

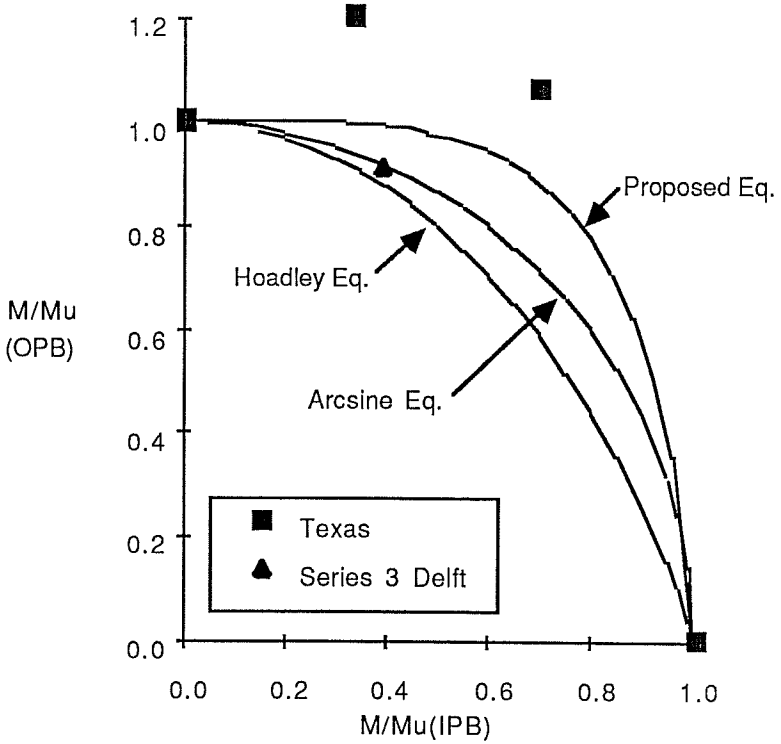

Fig. 5.6 IO Interaction ß=0.35-Test Data and Interaction Curves: Exp. Reference

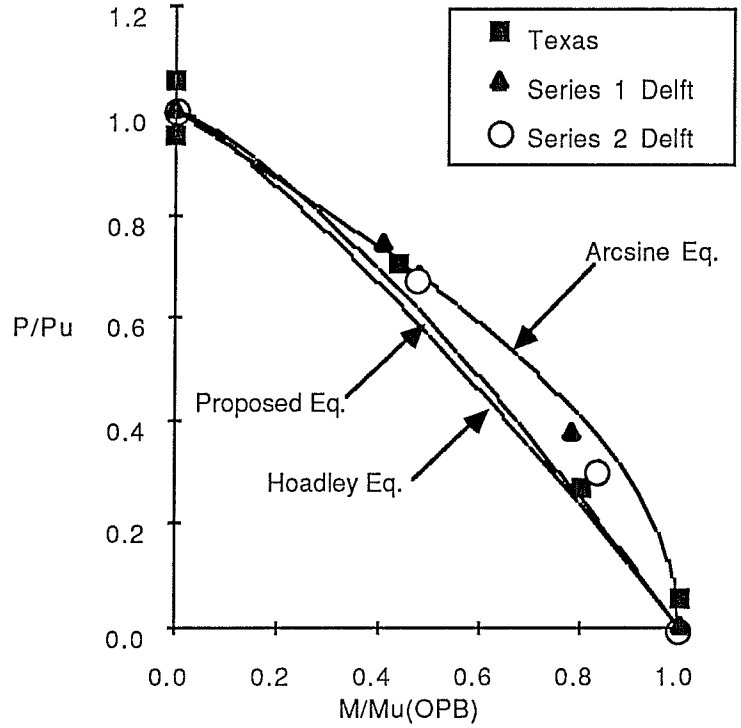

Fig. 5.7 AO Interaction ß=0.67-Test Data and Interaction Curves: Exp. Reference

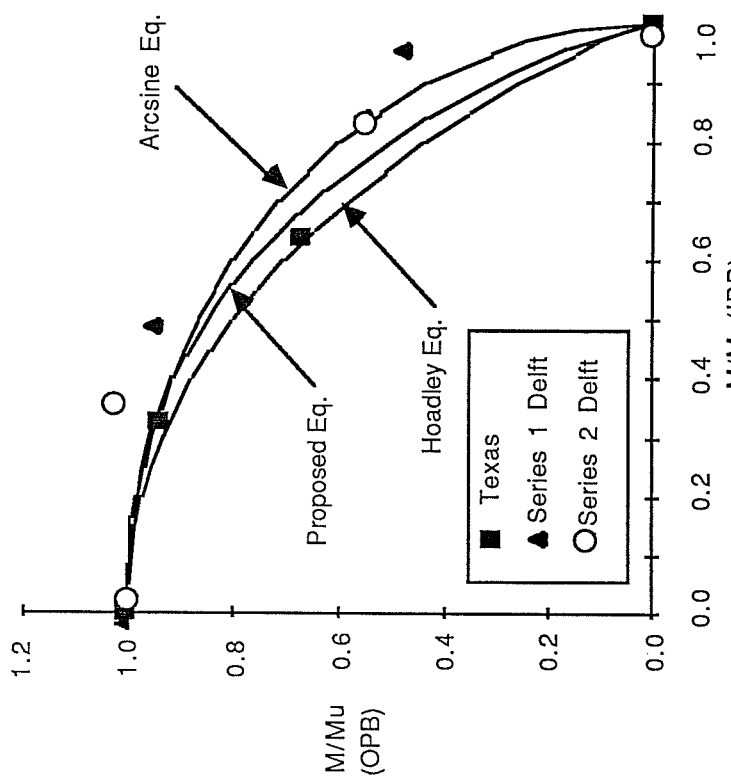

Fig. 5.9 IO Interaction β=0.67-Test Data and Interaction Curves: Exp. Reference

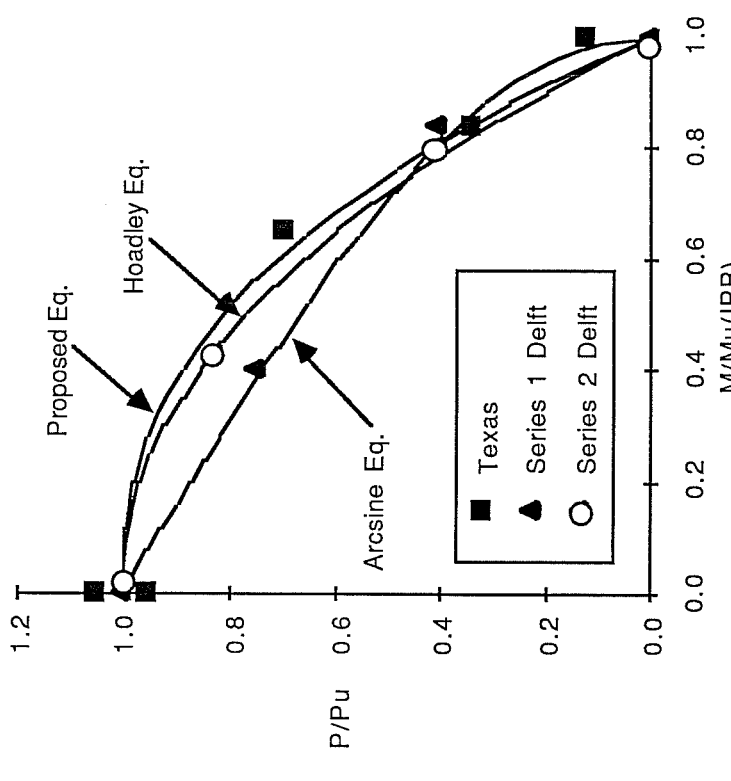

Fig. 5.8 AI Interaction β=0.67-Test Data and Interaction Curves: Exp. Reference

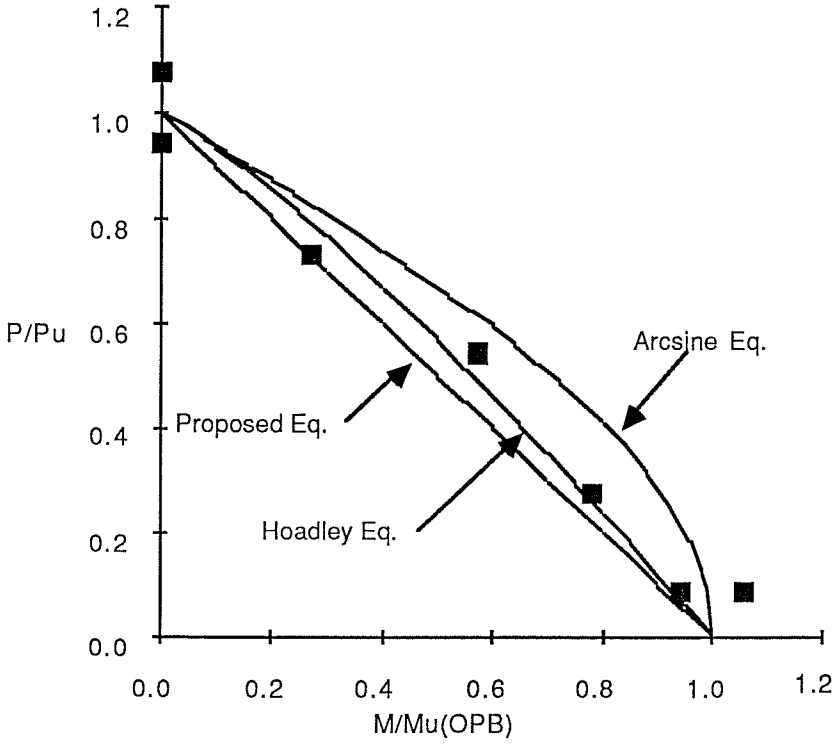

Fig 5.10 AO Interaction ß=1.00-Test Data and Interaction Curves: Exp. Reference

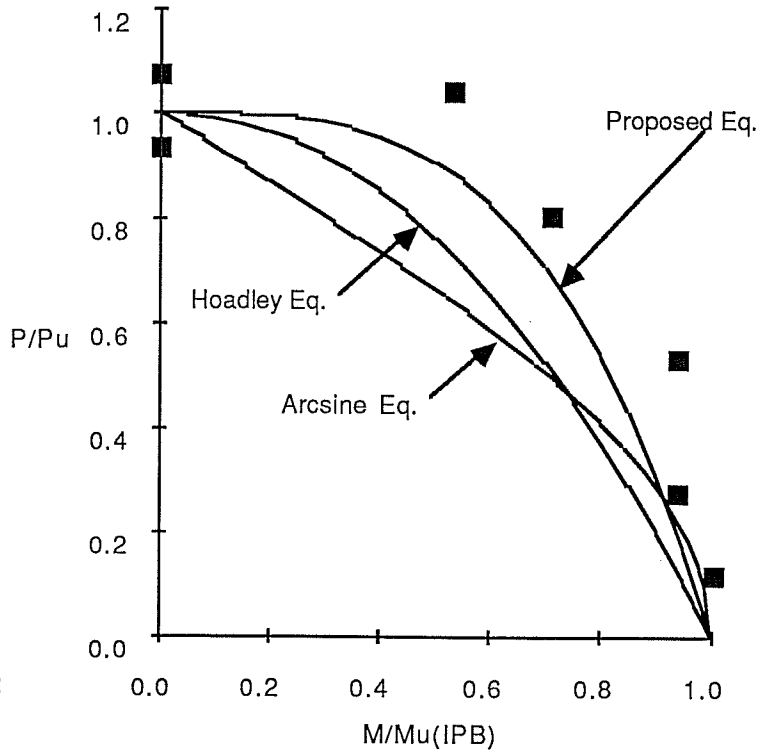

Fig 5.11 AI Interaction ß=1.00-Test Data and Interaction Curves: Exp. Reference

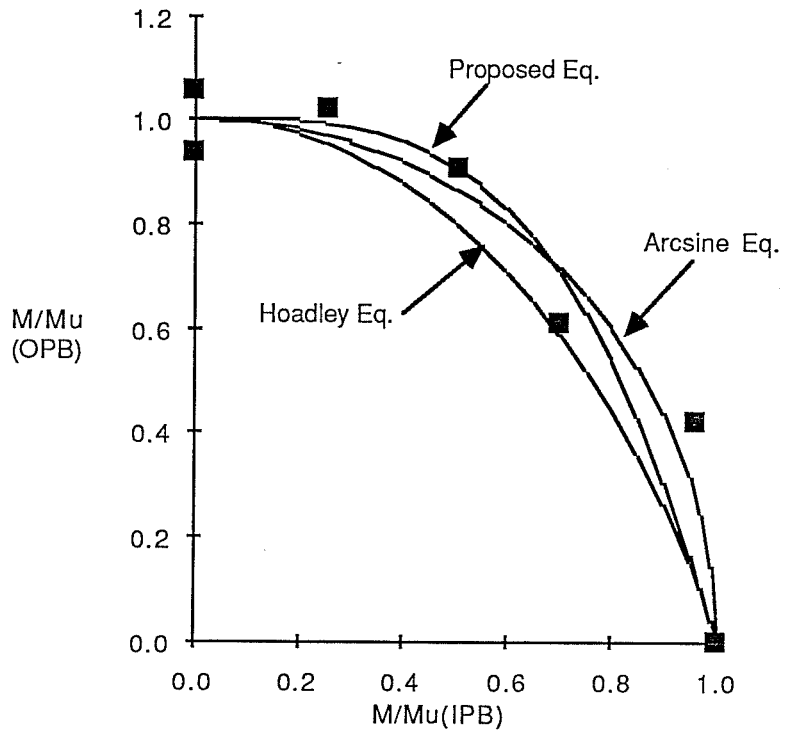

Fig. 5.12 IO Interaction ß=1.00-Test Data and Interaction Curves: Exp. Reference

data shows that it does not follow the trend of the data in either the AO or AI interactions. The proposed and Hoadley's curves follow the trend of the data well with Hoadley's predictions on the conservative side in the AI and IO interactions.

5.4 Evaluation of Interaction Equations: API RP 2A Reference

In the evaluation of interaction equations to be used in design, it is important to note that the designer does not have access to the experimental values of ultimate axial load and moment by which to normalize design loads. The designer must use the ultimate loads calculated from code equations which in most cases are not equivalent to the experimental values. The difference between the experimental and code predicted reference values can have a significant impact on the accuracy of the interaction equation used. Therefore, the various interaction equations will be compared using values of P_u and M_u predicted by the predominant code used in design, the 15th edition of API RP 2A. Since the accuracy of the interaction equations is to be determined, the safety factors will be removed from the code ultimate load equations.

In the 15th edition of API RP 2A, P_u and M_u are calculated with the following equations:

$$P_u = Q_u F_y T^2$$

$$M_u = Q_u F_y T^2 (0.8d)$$

The factor Q_u is a function of the type of load and the geometry of the joint. For the DT and T joint the following equations are used to define Q_u:

$$\text{Axial DT} - Q_u = (3.4 + 13\beta) Q_\beta$$

$$\text{T} - Q_u = (3.4 + 19\beta) Q_\beta$$

$$\text{OPB} \quad Q_u = (3.4 + 7\beta) Q_\beta$$

$$\text{IPB} \quad Q_u = (3.4 + 19\beta)$$

$$\text{For } \beta \geq 0.6, \; Q_\beta = 0.3 \; / \; [\beta(1 - 0.833\beta)]$$

$$\text{For } \beta < 0.6, \; Q_\beta = 1.0$$

The values of P_u and M_u computed for both the Texas and Delft specimens are given along with the experimental values for comparison, in Tables 5.7 and 5.8 respectively . The ultimate axial loads and bending moments from the Texas and Delft tests normalized by P_u and M_u computed using the API recommendations are presented in Tables 5.9 and 5.10 respectively. Tables 5.9 and 5.10 also include the C values for the proposed (Eq. 5.1), Hoadley's (Eq. 5.2), and the arcsine (Eq. 5.3) interaction equations. The C values are presented graphically in Fig. 5.13 where C is plotted for each β ratio and for each interaction equation. The averages, standard deviations, and coefficients of variation of C for each test series of the Texas and Delft research are given in Tables 5.11 and 5.12 respectively. The averages, standard deviations, and coefficients of variation of C

TABLE 5.7 EXPERIMENTAL AND API PREDICTED REFERENCE VALUES: TEXAS TESTS

β	Axial (kips) Test	Axial (kips) API	OPB (kip-in.) Test	OPB (kip-in.) API	IPB (kip-in.) Test	IPB (kip-in.) API
1.00	162.1**	141.1	1389**	1148	2265*	1373
0.67	73.9**	57.1	400*	330	1056*	650
0.35	44.1**	38.1	118*	126	257*	216

* Result of one test
** Average of two test results

TABLE 5.8 EXPERIMENTAL AND API PREDICTED REFERENCE VALUES: DELFT TESTS

β	γ	Axial (kips) Test	Axial (kips) API	OPB (kip-in.) Test	OPB (kip-in.) API	IPB (kip-in.) Test	IPB (kip-in.) API
0.68	15	38.2	36.7	70.8	78.0	131.0	153.5
0.68	24	18.0	13.0	32.8	23.9	64.6	47.8
0.36	24	9.4	8.2	12.0	9.1	19.5	15.7

All test values represent the result of one test.

TABLE 5.9 C VALUES FOR INTERACTION EQUATIONS - TEXAS TESTS: API RP 2A 15TH ED. REFERENCE

	TEST	P/PU	M/MU (OPB)	M/MU (IPB)	EQ. 5.1 PROPOSED	EQ. 5.2 HOADLEY	EQ. 5.3 API
β=0.35	A40	1.10	0.00	0.00	1.10	1.10	1.10
	A41	1.21	0.00	0.00	1.21	1.21	1.21
	O42	0.08	0.94	0.00	0.97	0.99	0.95
	I43	0.13	0.00	1.16	1.22	1.25	1.21
	AO44	0.33	0.96	0.00	1.19	1.26	1.10
	AO45	0.82	0.52	0.00	1.18	1.31	1.20
	AI46	0.35	0.00	1.08	1.15	1.26	1.20
	AI47	0.79	0.00	0.93	1.17	1.39	1.43
	IO48	0.11	1.10	0.40	1.20	1.30	1.21
	IO49	0.09	0.93	0.81	1.18	1.46	1.30
β=0.67	A1	1.38	0.00	0.00	1.38	1.38	1.38
	A51	1.24	0.00	0.00	1.24	1.24	1.24
	O8	0.06	1.21	0.00	1.23	1.23	1.21
	I7	0.15	0.00	0.62	1.68	1.68	1.63
	AO4	0.35	0.97	0.00	1.24	1.26	1.10
	AO13	0.92	0.54	0.00	1.33	1.36	1.27
	AI20	0.44	0.00	1.36	1.57	1.59	1.51
	AI17	0.92	0.00	1.06	1.49	1.60	1.65
	IO15	0.10	1.14	0.53	1.30	1.38	1.27
	IO14	0.09	0.81	1.04	1.41	1.46	1.29
	AIO16	0.35	1.02	0.50	1.39	1.44	1.25
	AIO18	0.87	0.46	0.63	1.41	1.48	1.39
	AIO19	0.86	0.42	0.54	1.32	1.39	1.32
β=1.00	A21	1.22	0.00	0.00	1.22	1.22	1.22
	A22	1.07	0.00	0.00	1.07	1.07	1.07
	O23	0.10	1.13	0.00	1.23	1.20	1.14
	O28	0.09	1.29	0.00	1.37	1.32	1.30
	I24	0.13	0.00	1.65	1.65	1.69	1.66
	AO31	0.31	0.95	0.00	1.26	1.21	1.06
	AO32	0.62	0.69	0.00	1.32	1.24	1.10
	AO33	0.84	0.33	0.00	1.17	1.09	1.05
	AI34	0.31	0.00	1.55	1.63	1.69	1.62
	AI35	0.61	0.00	1.56	1.76	1.87	1.81
	AI36	1.20	0.00	0.88	1.45	1.64	1.78
	AI50	0.91	0.00	1.17	1.51	1.68	1.73
	IO37	0.11	1.24	0.42	1.32	1.41	1.32
	IO38	0.12	1.10	0.84	1.41	1.53	1.41
	IO39	0.11	0.51	1.58	1.79	1.79	1.69
	IO26	0.10	0.73	1.16	1.45	1.55	1.36
				Average =	1.34	1.39	1.33
				St. Dev. =	0.19	0.21	0.22
				Coef. of Var. =	14.23	15.12	16.87

TABLE 5.10 C VALUES FOR INTERACTION EQUATIONS - DELFT TESTS: API RP 2A 15TH ED. REFERENCE

	TEST	P/PU	M/MJ (OPB)	M/MJ (IPB)	EQ. 5.1 PROPOSED	EQ. 5.2 HOADLEY	EQ. 5.3 API
β=0.36 γ=24	12	1.15	0.00	0.00	1.15	1.15	1.15
	13	0.00	0.00	1.24	1.24	1.24	1.24
	14	0.00	1.32	0.00	1.32	1.32	1.32
	34	1.02	0.00	0.52	1.05	1.22	1.35
	35	0.48	0.00	1.02	1.14	1.27	1.24
	36	0.91	0.63	0.00	1.30	1.44	1.32
	37	0.35	1.01	0.00	1.23	1.31	1.14
	38	0.00	1.20	0.49	1.21	1.33	1.30
β=0.68 γ=24	15	1.38	0.00	0.00	1.38	1.38	1.38
	16	0.00	0.00	1.35	1.35	1.35	1.35
	17	0.00	1.37	0.00	1.37	1.37	1.37
	39	0.56	0.00	1.07	1.22	1.38	1.35
	40	1.14	0.00	0.57	1.32	1.36	1.51
	41	0.42	1.15	0.00	1.48	1.50	1.31
	42	0.93	0.65	0.00	1.45	1.44	1.37
	43	0.00	1.41	0.53	1.50	1.54	1.50
	44	0.00	0.77	1.13	1.44	1.50	1.37
β=0.68 γ=15	9	1.04	0.00	0.00	1.04	1.04	1.04
	10	0.00	0.00	0.86	0.86	0.86	0.86
	11	0.00	0.91	0.00	0.91	0.91	0.91
	28	0.78	0.00	0.34	0.87	0.89	1.00
	29	0.43	0.00	0.72	0.93	0.95	0.95
	30	0.77	0.38	0.00	1.05	1.07	1.01
	31	0.38	0.70	0.00	1.01	1.03	0.89
	32	0.00	0.43	0.82	0.97	1.01	0.92
	33	0.00	0.86	0.42	0.96	0.99	0.96
				Average =	1.18	1.23	1.20
				St. Dev. =	0.20	0.21	0.20
				Coef. of Var. =	17.07	17.12	17.02

TABLE 5.11 SUMMARY OF C VALUES FOR INTERACTION EQUATIONS - TEXAS TESTS: API REF.

	β=1.0			β=0.67			β=0.35		
Eq.	Avg.	S.D.	C. of V.	Avg.	S.D.	C. of V.	Avg.	S.D.	C. of V.
Eq. 5.1	1.41	0.21	14.93	1.38	0.13	9.65	1.16	0.07	6.39
Eq. 5.2	1.45	0.26	18.00	1.42	0.14	9.86	1.25	0.13	10.69
Eq. 5.3	1.40	0.28	20.07	1.35	0.16	12.08	1.19	0.13	10.65

Eq. 5.1 - Proposed
Eq. 5.2 - Hoadley
Eq. 5.3 - Arcsine

TABLE 5.12 SUMMARY OF C VALUES FOR INTERACTION EQUATIONS - DELFT TESTS: API REF.

	β=0.68 γ=24			β=0.68 γ=15			β=0.35 γ=24		
Eq.	Avg.	S.D.	C. of V.	Avg.	S.D.	C. of V.	Avg.	S.D.	C. of V.
Eq. 5.1	1.39	0.09	6.30	0.95	0.07	7.33	1.21	0.09	7.38
Eq. 5.2	1.43	0.07	5.05	0.97	0.07	7.65	1.29	0.09	6.70
Eq. 5.3	1.39	0.07	5.05	0.95	0.06	6.33	1.26	0.08	6.34

Eq. 5.1 - Proposed
Eq. 5.2 - Hoadley
Eq. 5.3 - Arcsine

for each β ratio and for all of the data are presented in Table 5.13.

It is interesting to note the difference in the average C's, the standard deviations, and the coefficients of variation obtained when the data is normalized by the experimental references (Tables 5.2-5.3) and those obtained when the predicted reference values are used for normalization (Tables 5.9-5.10). For all three equations there is a significant increase in the standard deviations. This increase means that there is a significant increase in the size of the band of the data, and is a result of the fact that the accuracy of the predicted ultimate strengths varies. For example, the average P/P_u of the reference tests for $\beta=0.67$, A1 and A51, is 1.31 but the M/M_u for the IPB reference test, I7, is 1.62. This same situation occurs for the $\beta=1.0$ test series. The predictions for the $\beta=0.68$ $\gamma=15$ bending reference tests are unconservative resulting in unconservative predictions for the interaction results. Thus, when the experimental ultimate strengths are normalized by the predicted values, the interactions will change from the interactions given when the ultimate strengths are normalized by the experimental values.

The coefficients of variation presented at the bottom of Table 5.9 show that the proposed interaction equation provides the most accurate predictions for all the Texas data. The results

shown in Table 5.11 indicate that the proposed equation also provides the best fit to the interaction data for each individual β ratio. The most significant improvements over Hoadley's and the arcsine equation occur for β's of 0.35 and 1.0. The arcsine equation produces the lowest coefficient of variation of C for the Delft T joint interaction results as shown in Table 5.10, but the difference among the three equations is not significant The arcsine equation also provides the best fit to the data for each individual test series, as shown by the coefficients of variation presented in Table 5.12. When all of the data is considered, as shown in Table 5.13, the proposed equation provides the most accurate predictions as indicated by the coefficients of variation, but the improvement in accuracy is not significant. The proposed equation does provide a significant increase in accuracy for the β=1.0 DT interaction test series.

The results of the Texas and Delft tests normalized by the API RP 2A predicted reference values along with the three interaction curves are plotted in Figs. 5.14-5.22. As before, the results are shown graphically in two dimensions (AO, AI, and IO) for clarity. In addition, each β ratio is presented in a different graph. The plots for AO, AI, and IO for β=0.35, 0.67 and 1.0 are presented in Figs. 5.14-5.16, 5.17-5.19, and 5.20-5.22 respectively. In the figures, the Delft data is referred to

TABLE 5.13 SUMMARY OF C VALUES FOR ALL DATA: API REFERENCE

β	Num. of Tests	Eq. No.	Average C	Standard Deviation	Coef. of Var.
0.35	18	5.1	1.18	0.082	6.99
		5.2	1.27	0.113	8.94
		5.3	1.22	0.111	9.10
0.67	31	5.1	1.26	0.226	17.90
		5.2	1.29	0.231	17.88
		5.3	1.24	0.224	18.00
1.00	16	5.1	1.41	0.211	14.93
		5.2	1.45	0.261	18.00
		5.3	1.40	0.280	20.07
Total	65	5.1	1.28	0.200	16.26
		5.2	1.32	0.223	16.85
		5.3	1.27	0.224	17.55

Eq. 1 - Proposed
Eq. 2 - Hoadley
Eq. 3 - Arcsine

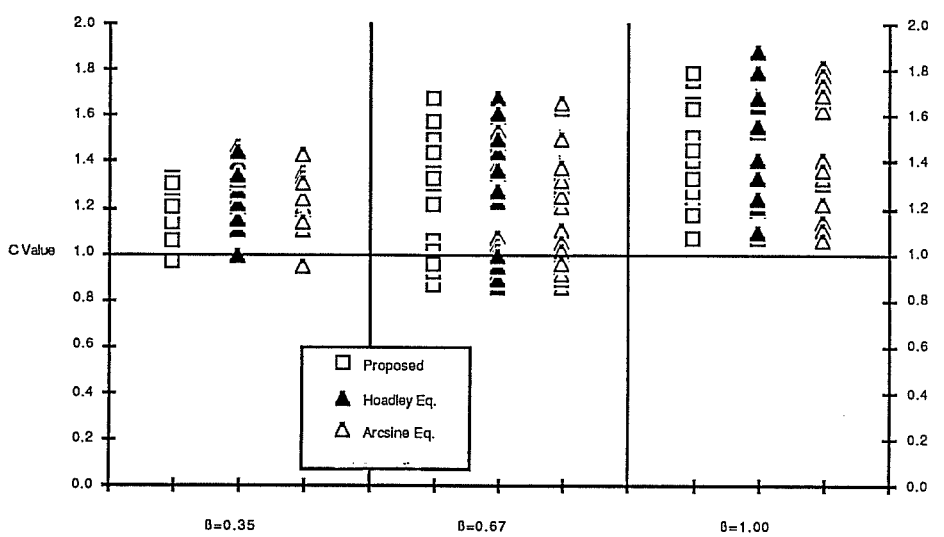

Fig. 5.13 C Values vs. β : API Reference

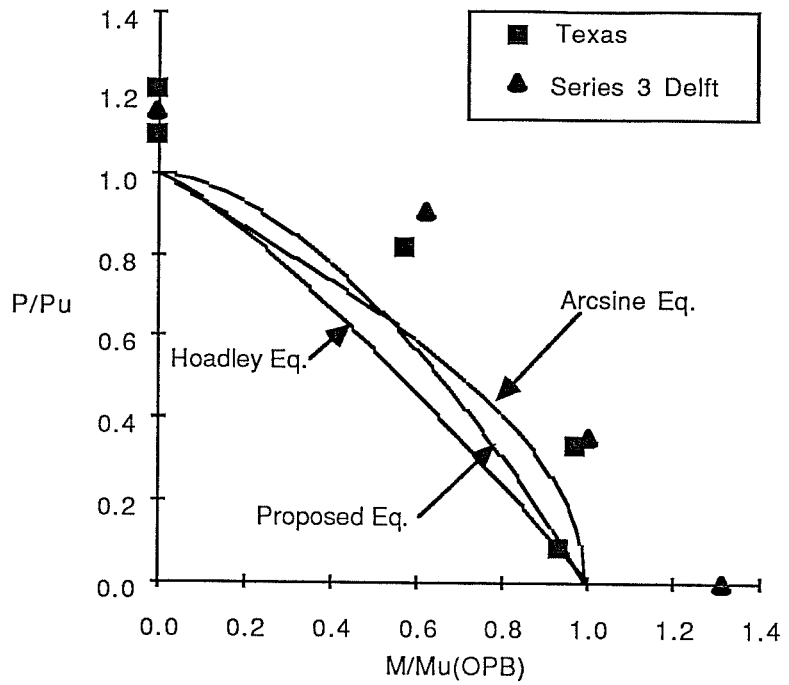

Fig. 5.14 AO Interaction ß=0.35-Test Data and Interaction Curves: API Reference

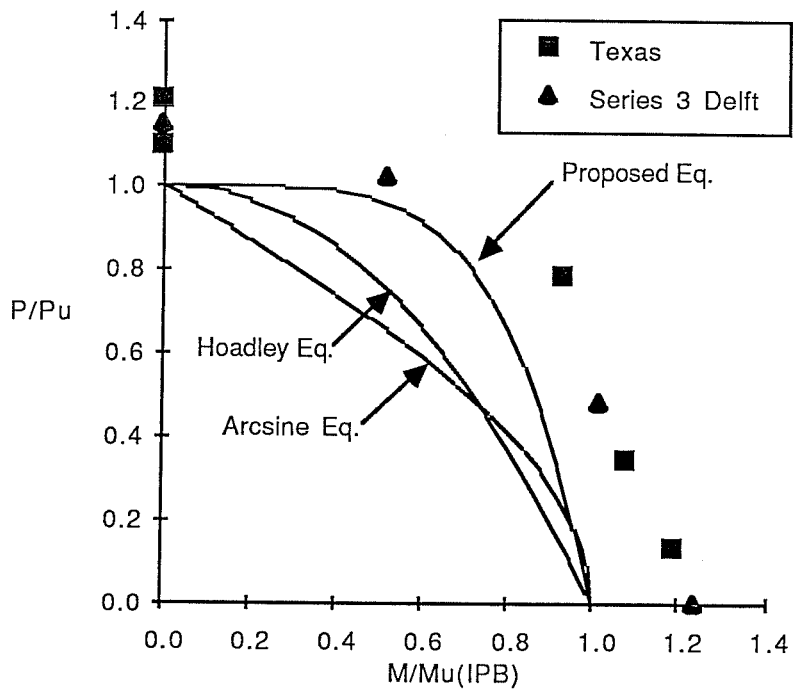

Fig. 5.15 AI Interaction ß=0.35-Test Data and Interaction Curves: API Reference

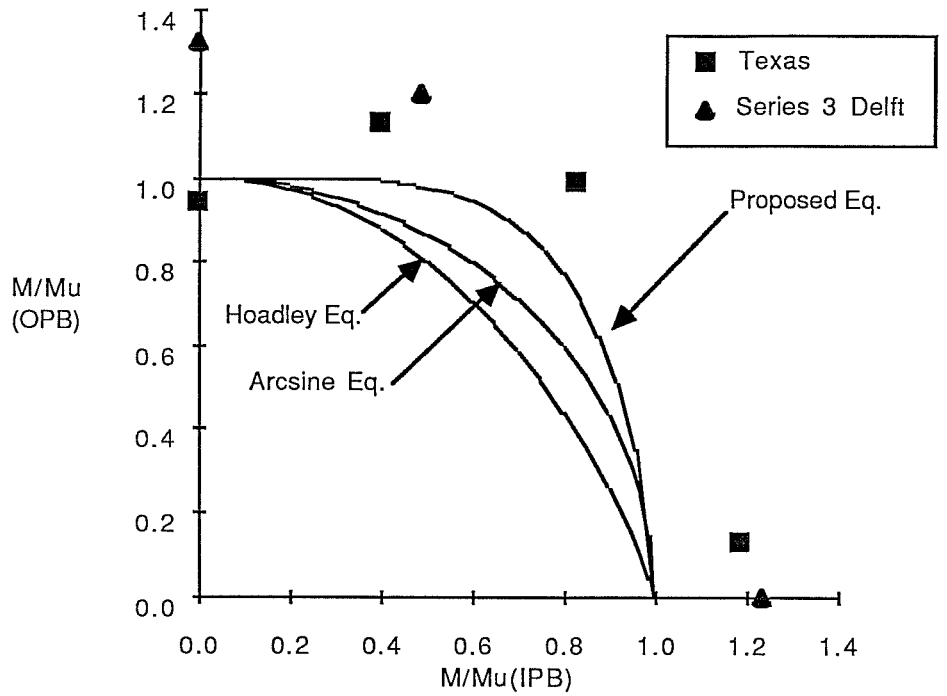

Fig. 5.16 IO Interaction ß=0.35-Test Data and Interaction Curves: API Reference

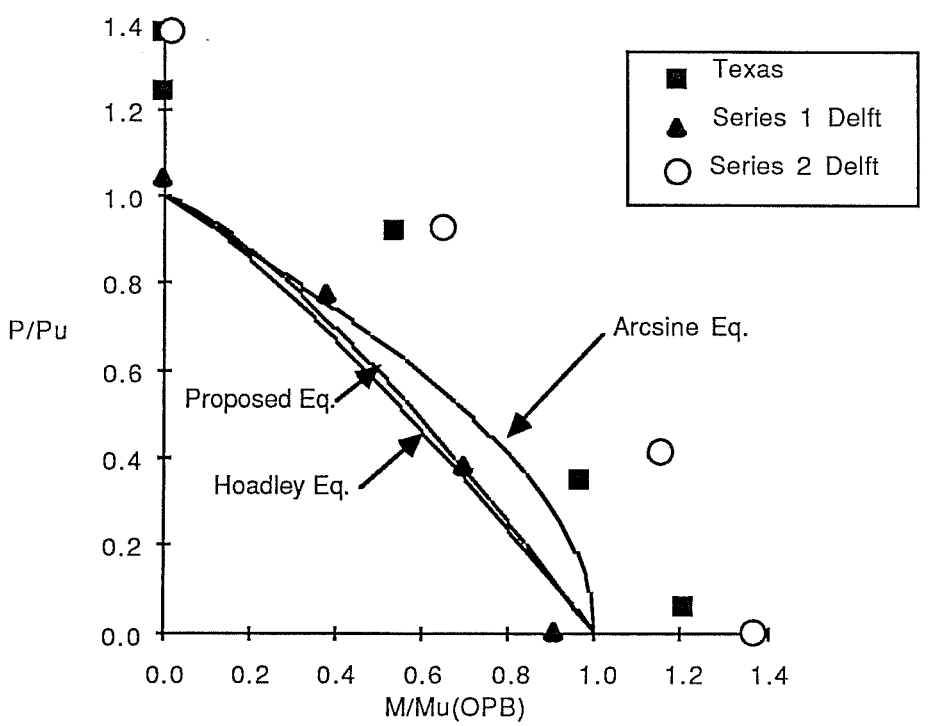

Fig. 5.17 AO Interaction ß=0.67-Test Data and Interaction Curves: API Reference

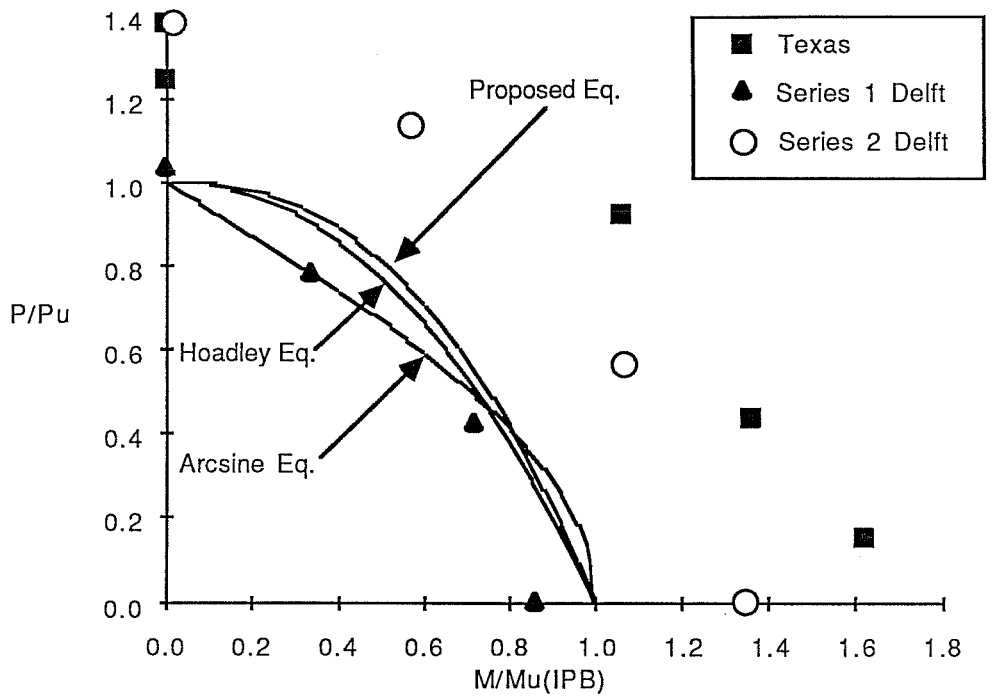

Fig. 5.18 AI Interaction ß=0.67-Test Data and Interaction Curves: API Reference

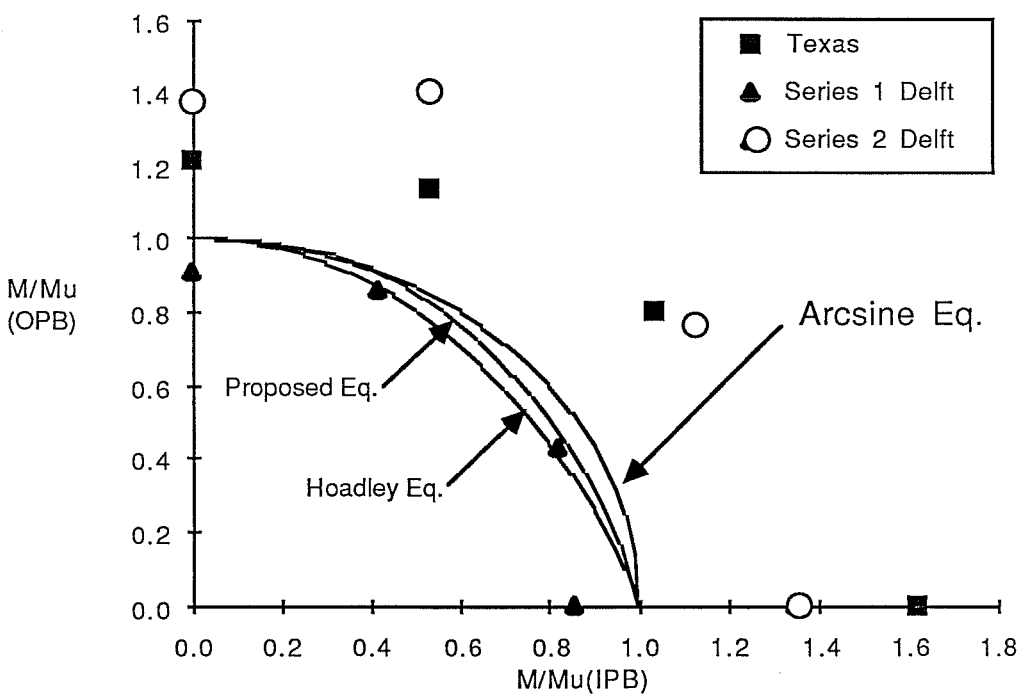

Fig. 5.19 IO Interaction ß=0.67-Test Data and Interaction Curves: API Reference

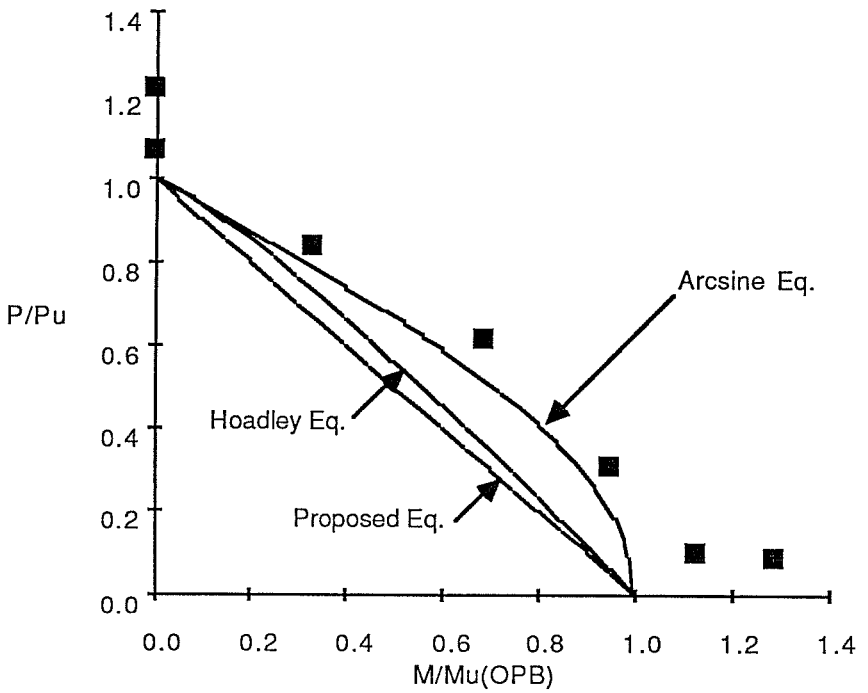

Fig. 5.20 AO Interaction ß=1.00-Test Data and Interaction Curves: API Reference

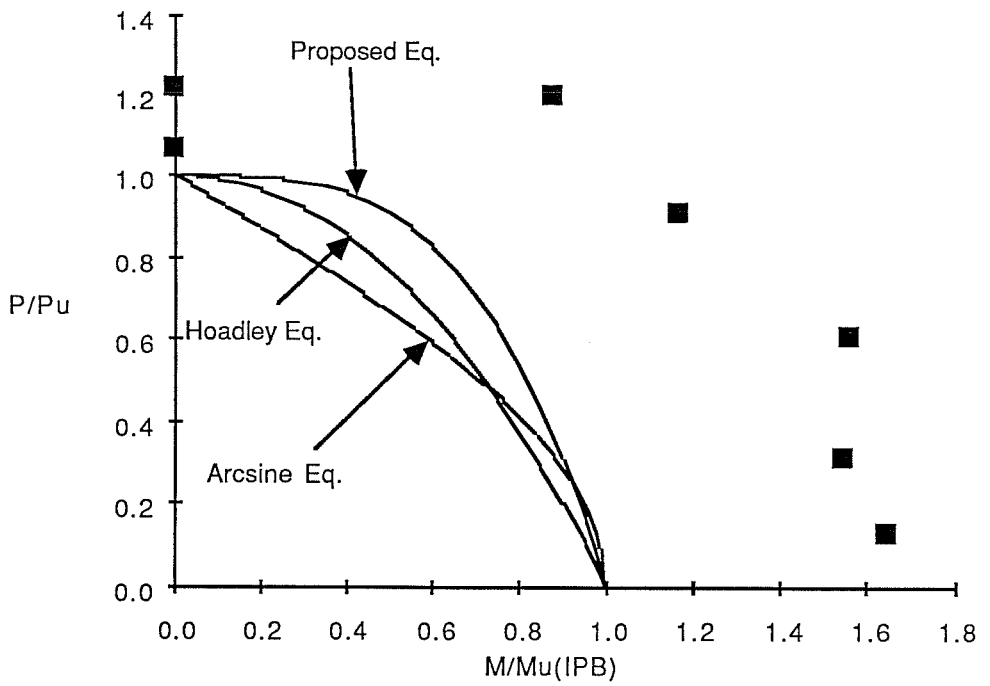

Fig. 5.21 AI Interaction ß=1.00-Test Data and Interaction Curves: API Reference

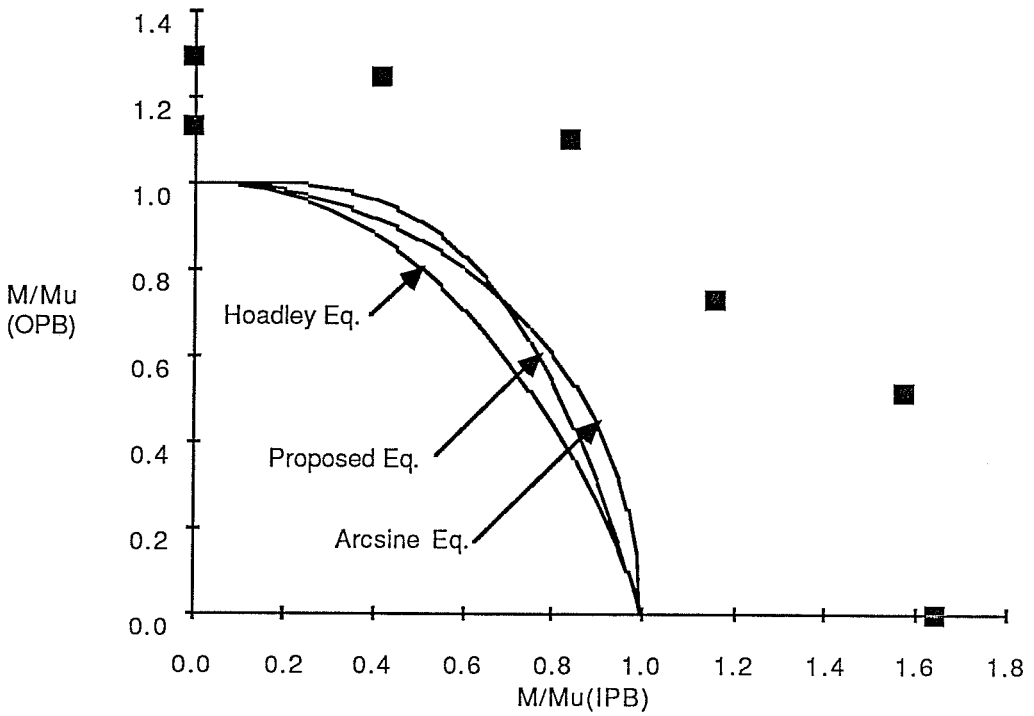

Fig. 5.22 IO Interaction ß=1.00-Test Data and Interaction Curves: API Reference

as series 1 (β=0.68, γ=15), series 2 (β=0.68, γ=24), and series 3 (β=0.36 γ=24).

In general for the β=0.35 data shown in Figs. 5.14-5.16, the proposed equation seems to follow the trends of the data better than the other interaction equations. In addition, there is a reasonable amount of conservatism provided by equations due to the conservatism of the API recommendations. The only unconservative point is the β=0.35 OPB reference test shown in Figs. 5.14 and 5.16. The main trend to observe in the β=0.67 data shown in Figs. 5.17-5.19 is the wide band in which the data falls. The results of series 1 of the Delft research fall among the interaction curves and in some cases below the curves, while the results of the series 2 and Texas testing are far outside of the interaction curves. Assuming that the Delft experimental results are valid, this disparity is a result of the variation in the accuracy of the ultimate strength predictions of the API RP 2A. The differences between the accuracy of the interaction equations are small compared to the width of the band of results; in other words better predictors of ultimate strength in tubular joints must be developed before the interaction equations can be made significantly more accurate. This situation is again illustrated in the β=1.0 data shown in Figs. 5.20-5.22. The AO interaction (Fig. 5.20) indicates that the arcsine equation follows the shape of the interaction results very well, and that

the predictions from API RP 2A are reasonable accurate for the axial and OPB cases. However, Figs. 5.21 and 5.22 show that the data falls far outside of the predicted interaction curves. More specifically, the data is skewed in the in-plane-bending axis which indicates that the predicted IPB ultimate strength is overconservative. As was seen in the β=0.67 interaction figures, the best way to significantly increase the accuracy of the interaction predictions is to increase the accuracy of the ultimate strength predictions.

5.5 Limit State Analyses

Because of the several codes and recommendations available, the designer uses different methods to achieve a satisfactory design; i.e. load factors, factors of safety, lower bound or mean equations; therefore, it is difficult to recommend a design equation without specifying the particulars of the code being used. However, there seems to be a trend in the field toward limit states or load and resistance factor type design. Therefore, the following limit states type of design criterion will be used to choose an interaction equation recommended for use in design:

$$\phi R_n \geq \sum \gamma Q_m \tag{5.4}$$

where ϕ is the "resistance factor", R_n is the "nominal

resistance", γ is the "load factor", and Q_m is the "mean load effect" for a certain limit state. The left side of the equation represents the resistance or capacity of the structure while the right side represents the loads acting on the structure [9]. The resistance factor is affected by the accuracy of the interaction equations, so the equations can be evaluated by the determination of ϕ for each equation.

Since there are many statistical methods available to describe the relationship between an equation and a population of data, a characteristic value type analysis as used in the recent UEG Design Guide [34] as well as an LRFD type analysis as used in the development of the proposed AISC specification for steel building design [9] will be utilized in the evaluation of the interaction equations for use in design. In addition, a relative chord thickness term which is a function of ϕ is used to give the designer some indication of how the ϕ factor effects the amount of material required by a design equation. The development of this relationship between ϕ and T is given in Appendix D.

5.5.1 Characteristic Value Analysis: The characteristic value of the ultimate limit state is defined as the 95 percentile of the resistance of the joint. Thus, if the design equation yields the characteristic value of the resistance as given by experimentation, 95 % of the experimental results will be conservative. A more detailed development of the characteristic

value is given in Ref. 34. The characteristic value was used in the UEG design recommendations as a factor which was applied to a basic equation to make the equation yield the characteristic value of the experimental data. We can call this factor the resistance factor, ϕ. The characteristic value of the resistance factor is given by the following equation:

$$\phi = P_m (1 - ZV_P) \tag{5.5}$$

where P_m is the mean value of the ratio of test to prediction for each interaction equation and V_P is the coefficient of variation of the ratio of test to prediction for each interaction equation, and Z is a constant based on the population size.

Table 5.14 contains the P_m, V_P, and ϕ values for each interaction equation. The Z values were approximated as 1.65 for all data (65 tests), 1.67 for the β=0.35 data (18 tests), 1.66 for the β=0.67 data (31 tests), and 1.67 for the β=1.00 data (16 tests). Also included in Table 5.14 are the ϕ_{EFF} and T/TArc values. ϕ_{EFF} is defined as ϕ / P_m and is developed in Appendix D. T/TArc is the ratio of the thickness required by a design based on an interaction equation (Hoadley's or the proposed) to that required by the arcsine equation given that all other variables were equal. The experimental data nondimensionalized by both the experimental reference values and those calculated by API are included for comparison, but because the API ultimate

TABLE 5.14 CHARACTERISTIC ϕ VALUES AND RELATIVE THICKNESSES FOR INTERACTION EQUATIONS

β	Equation	P_m	V_P	ϕ	ϕ_{EFF}	T/T_{Arc}
Experimental Reference						
All	Arcsine	1.03	0.100	0.859	0.833	1.000
	Hoadley	1.07	0.089	0.912	0.853	0.989
	Proposed	1.04	0.068	0.923	0.887	0.969
0.35	Arcsine	1.07	0.101	0.889	0.831	1.000
	Hoadley	1.11	0.119	0.889	0.801	1.019
	Proposed	1.03	0.100	0.859	0.834	0.998
0.67	Arcsine	1.01	0.052	0.923	0.914	1.000
	Hoadley	1.04	0.054	0.947	0.911	1.002
	Proposed	1.02	0.047	0.941	0.922	0.995
1.00	Arcsine	1.04	0.150	0.781	0.750	1.000
	Hoadley	1.09	0.091	0.924	0.848	0.941
	Proposed	1.04	0.056	0.942	0.906	0.910
API Reference						
All	Arcsine	1.27	0.176	0.901	0.710	1.000
	Hoadley	1.32	0.169	0.952	0.721	0.992
	Proposed	1.28	0.164	0.934	0.729	0.986
0.35	Arcsine	1.22	0.091	1.035	0.848	1.000
	Hoadley	1.27	0.089	1.080	0.851	0.998
	Proposed	1.18	0.070	1.042	0.883	0.980
0.67	Arcsine	1.24	0.180	0.869	0.701	1.000
	Hoadley	1.29	0.179	0.907	0.703	0.999
	Proposed	1.26	0.179	0.886	0.703	0.999
1.00	Arcsine	1.40	0.201	0.931	0.665	1.000
	Hoadley	1.45	0.180	1.014	0.699	0.975
	Proposed	1.41	0.149	1.058	0.751	0.941

strength values will vary with time,the data using the experimental reference will be used for the recommendation of a design equation.

The T/T_{Arc} values presented in Table 5.14 show that overall the required thickness of a joint is not very sensitive to the interaction equation recommended. The proposed equation requires the least amount of material, but there is only a 3% reduction. However, when the data base is divided by β ratio, the T/T_{Arc} values show that the proposed equation will yield a 9% savings in material for β=1.0. When the API predicted reference values are used, the reductions are slightly smaller.

5.5.2 LRFD Analysis: This analysis is taken mostly from the development of the proposed AISC specification [8, 9, 10, 11]. The LRFD method is more rigorous than the characteristic value method because it accounts for a specific level of safety. The basic equation of LRFD is given in Eq. 5.4. The resistance factor, ϕ, can be calculated using the following equations [9]:

$$\phi = (R_m / R_n) \exp(-0.55\, \eta\, V_R) \tag{5.6}$$

$$R_m / R_n = P_m\, M_m\, F_m \tag{5.7}$$

$$V_R^2 = V_P^2 + V_M^2 + V_F^2 \tag{5.8}$$

where (R_m / R_n) is the ratio of mean to nominal strength and is given by Eq. 5.7, η is the safety index which is selected to give a predetermined level of safety in the design, and V_R is the coefficient of variation of the resistance which is given by Eq.

5.8. The coefficients P_m and V_P are the mean and standard deviation of the professional factor. The professional factor is basically the accuracy of the design equation, thus P_m is the mean value of the ratio of test to prediction for each interaction equation and V_P is the coefficient of variation of the ratio of test to prediction for each interaction equation. The coefficients M_m and V_M represent the mean and coefficient of variation of the ratio of the actual to the minimum yield stress. Since the actual measured yield stresses are used in the calculations, M_m will be taken as 1.0. From Ref. 11, V_M =0.11 will be used. The variables F_m and V_F are the mean and coefficient of variation of the fabrication factor which represents the geometric accuracy of the fabrication of the element under consideration. From Ref. 9, F_m = 1.00 and V_F = 0.05.

The safety index is only a relative measure of reliability, but for the range of common probability distributions of interest, the safety index can be used in the following equation to determine an approximate probability of failure, P_F [10]:

$$P_F = 460 \times 10^{-1.869\eta} \qquad (5.9)$$

Equation 5.9 is not presented as a method to calculate an actual

probability of failure of a tubular joint in an offshore structure, it can only give an approximate measure for the sensitivity of the probability of failure or reliability to the safety index. For steel buildings η of approximately 3.0 is a good estimate of the reliability provided for main members in current design. Since it is desirable that connections have a higher degree of reliability than the members that they join, a higher η seems appropriate [8]. Thus, for this analysis, the safety index will be taken as 3.0 and 4.0 to investigate the differences in the calculated resistance factors. The safety indexes of 3.0 and 4.0 translate into probabilities of failure of 1.1 x 10-3 and 1.5 x 10-5 over the life of the structure using Eq. 5.9. These probabilities of failure compare with the generally accepted maximum probability of failure for buildings of 1.0 x 10-5 in any one year [21] or 2.5 x 10-4 over the 25 year life of an offshore structure.

The ϕ values calculated with Eqs. 5.6-5.8 with P_m and V_P obtained for each interaction equation are presented in Table 5.15 along with ϕ_{EFF} values and the ratio of the chord thickness to that required by the arcsine equation. The ϕ, ϕ_{EFF} values, and relative thicknesses are given for η values of 3.0 and 4.0.

The values of T/T_{Arc} given in Table 5.15 show that the choice of interaction equation has very little effect on the required thickness of the joint as was found in the

TABLE 5.15 ϕ VALUES AND RELATIVE THICKNESSES FOR INTERACTION EQUATIONS

β	Equation	P_m	V_P	V_R	$\eta = 3.0$ ϕ	$\eta = 3.0$ ϕ_{EFF}	$\eta = 3.0$ T/T_{Arc}	$\eta = 4.0$ ϕ	$\eta = 4.0$ ϕ_{EFF}	$\eta = 4.0$ T/T_{Arc}
Experimental Reference										
All	Arcsine	1.03	0.104	0.157	0.795	0.772	1.000	0.729	0.708	1.000
	Hoadley	1.07	0.089	0.150	0.835	0.781	0.994	0.769	0.719	0.992
	Proposed	1.04	0.068	0.139	0.827	0.795	0.985	0.767	0.737	0.980
0.35	Arcsine	1.07	0.101	0.158	0.825	0.771	1.000	0.757	0.707	1.000
	Hoadley	1.11	0.119	0.170	0.839	0.756	1.010	0.764	0.688	1.013
	Proposed	1.03	0.100	0.157	0.796	0.772	0.999	0.730	0.709	0.999
0.67	Arcsine	1.01	0.052	0.132	0.813	0.805	1.000	0.756	0.749	1.000
	Hoadley	1.04	0.053	0.132	0.836	0.804	1.001	0.777	0.747	1.001
	Proposed	1.02	0.047	0.130	0.824	0.808	0.998	0.767	0.752	0.998
1.00	Arcsine	1.04	0.150	0.192	0.757	0.728	1.000	0.681	0.655	1.000
	Hoadley	1.09	0.091	0.151	0.849	0.779	0.967	0.781	0.717	0.956
	Proposed	1.04	0.056	0.133	0.835	0.803	0.953	0.776	0.746	0.937
API Reference										
All	Arcsine	1.27	0.176	0.213	0.894	0.704	1.000	0.795	0.626	1.000
	Hoadley	1.32	0.169	0.207	0.938	0.710	0.995	0.836	0.634	0.994
	Proposed	1.28	0.164	0.203	0.915	0.715	0.992	0.818	0.639	0.989
0.35	Arcsine	1.22	0.091	0.151	0.951	0.779	1.000	0.875	0.717	1.000
	Hoadley	1.27	0.089	0.150	0.991	0.780	0.999	0.912	0.718	0.999
	Proposed	1.18	0.070	0.140	0.937	0.794	0.990	0.868	0.736	0.987
0.67	Arcsine	1.24	0.180	0.217	0.867	0.699	1.000	0.770	0.621	1.000
	Hoadley	1.29	0.179	0.216	0.904	0.700	0.999	0.802	0.622	0.999
	Proposed	1.26	0.179	0.216	0.882	0.700	0.999	0.783	0.622	0.999
1.00	Arcsine	1.40	0.201	0.234	0.951	0.679	1.000	0.836	0.597	1.000
	Hoadley	1.45	0.180	0.217	1.014	0.699	0.986	0.900	0.621	0.981
	Proposed	1.41	0.149	0.192	1.027	0.728	0.966	0.924	0.655	0.955

characteristic value analysis. In general, the proposed equation yields the most economical joint. The proposed interaction equation provides for the largest savings for β=1.00 joints with an approximately 5% reduction in T when the experimental reference is used and an approximately 3% reduction in T when the API reference is used. When the safety index is increased to 4.0, the savings produced by the proposed equation increase slightly.

5.6 Recommendations

Both the characteristic value and the LRFD type analysis showed that the proposed equation will produce the most economical design. However, the proposed equation is also the most complicated of the three discussed. Thus, it must be decided if the savings provided by the equation offsets its complexity. If the database is divided by the β ratio, it is shown that the only significant savings provided by the proposed equation occur in the β=1.00 joints. A survey of the joints found in actual offshore structures published in the UEG design guide showed that of the DT joints found only 19% had β ratios of 0.8 or above. Therefore, it seems questionable that the actual savings in the design of the structure as a whole would be significant. Because there is no real difference in the final designs based on these three equations, it seems logical that the simplest equation

should be used. The simplest of the three equations due to its polynomial form, and constant exponents is the equation proposed by Hoadley. The polynomial format eliminates the extra check of the bending terms required by the arcsine equation. Thus, the Hoadley equation is recommended for design. It should be noted that because of the additional capacity of DT joints in tension compared to compression, the recommended interaction equation can be applied in cases where axial tension is present.

Table 5.16 compares the ϕ_{EFF} values and the relative thickness of the chord when the interaction data is nondimensionalized by the experimental reference values and the calculated reference values. The ratios of the thickness given by the experimental or "exact" reference and the thickness given by the API reference indicate that making the ultimate strength equations more accurate will result in a savings of approximately 5% for η=3 and approximately 6% for η=4.

For β=0.35, an increase in thickness is shown because the present API ultimate strength equations are unconservative, however; for β=0.67 and 1.00 significant savings are shown. The comparison of the relative designs when based on the experimental and API reference values indicates that the more significant savings in joints designed for combined branch loads can be realized by increasing the accuracy of the ultimate strength equations than by altering the interaction equations.

TABLE 5.16 COMPARISON OF RELATIVE CHORD THICKNESSES FOR EXPERIMENTAL AND API REFERENCE VALUES

β	Equation	Exp. Ref. ϕ_{EFF}	API Ref. ϕ_{EFF}	T/T_{API}
$\eta = 3$				
All	Arcsine	0.772	0.704	0.955
	Hoadley	0.781	0.710	0.954
	Proposed	0.795	0.715	0.948
$\beta = 0.35$	Arcsine	0.771	0.779	1.005
	Hoadley	0.756	0.780	1.016
	Proposed	0.772	0.794	1.014
$\beta = 0.67$	Arcsine	0.805	0.699	0.932
	Hoadley	0.804	0.700	0.933
	Proposed	0.808	0.700	0.931
$\beta = 1.00$	Arcsine	0.728	0.679	0.966
	Hoadley	0.779	0.699	0.947
	Proposed	0.803	0.728	0.953
$\eta = 4$				
All	Arcsine	0.708	0.626	0.940
	Hoadley	0.719	0.634	0.939
	Proposed	0.737	0.639	0.931
$\beta = 0.35$	Arcsine	0.707	0.717	1.007
	Hoadley	0.688	0.718	1.022
	Proposed	0.709	0.736	1.019
$\beta = 0.67$	Arcsine	0.749	0.621	0.911
	Hoadley	0.747	0.622	0.912
	Proposed	0.752	0.622	0.909
$\beta = 1.00$	Arcsine	0.655	0.597	0.955
	Hoadley	0.717	0.621	0.931
	Proposed	0.746	0.655	0.937

CHAPTER 6

ANALYTICAL PREDICTION OF ULTIMATE STRENGTH

During the investigation of interaction behavior in tubular joints, several questions were raised but remained unanswered by the the experimental data available. These questions, which were discussed in Chapter 4, include the gap effect on behavior in joints with β's close to 1.0, the interaction of IPB and OPB in joints with β=0.35, and the effect of the loading sequence on the interaction behavior. In addition, the results of the IPB reference tests did not agree with the API IPB strength equation. There exists experimental data on these topics; however, the paucity of the data and the scatter inherent in experimental results makes a confident conclusion difficult. This situation illustrates one of the problems with a dependence on experimental results for the investigation of structural behavior. A balance between analytical and experimental methods is needed.

Since normalized strength values are used to describe interaction behavior, the interaction is very dependent on the reference values used for normalization. Thus if not accounted for, experimental scatter could have a significant effect on the apparent interaction behavior. For example, the AO interaction for β=1.00 depends on the reference tests used for

nondimensionalization. Fig. 6.1 shows the interaction results when nondimensionalized by Tests 023 and A22, Tests 028 and A21, and average reference values along with the interaction curve derived in Chapter 4. Comparison of the data points in Fig. 6.1 shows that the scatter in the reference data can have a significant effect on the interaction results. In this program of work replicate tests were performed as often as possible; but many of the curves are based on the result of only one reference test. This does not lead to a great deal of confidence in the results of research.

The amount of experimental work required to investigate these topics fully would take years and a considerable amount of money. For example, to completely describe an interaction curve in two dimensions for one β ratio and one γ ratio would require approximately 10 tests with just one replicate at each loading. If this is multiplied by several β ratios, and γ ratios and then by the type of joint (T, DT, K) the number of experiments becomes considerable. Therefore, it would be advantageous to have an analytical model which could be used to investigate these topics. The purpose of this chapter is to find an acceptable analytical model (for developing interaction data and apply it to the questions raised above).

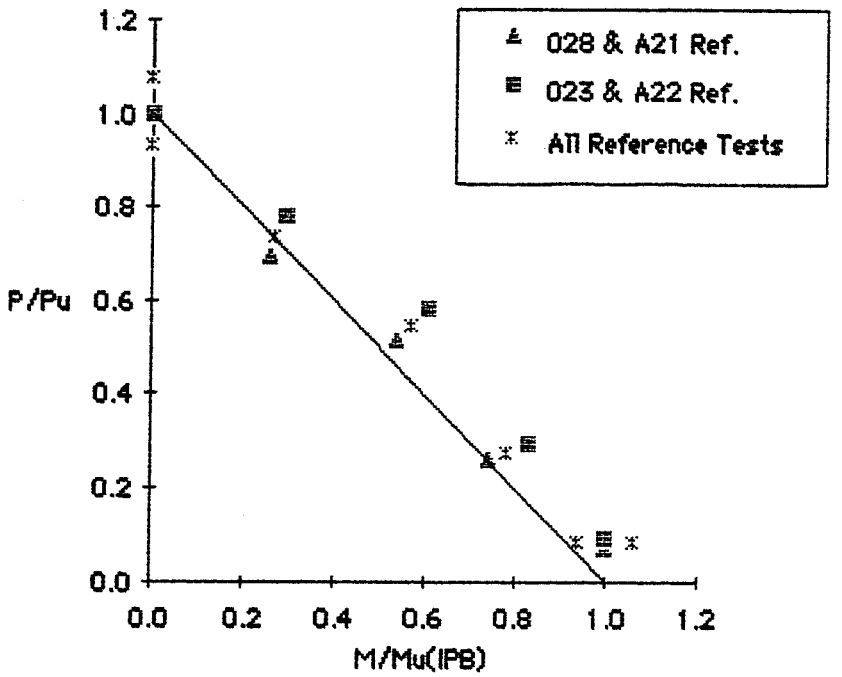

Fig. 6.1 Experimental Scatter in ß=0.67 AO Interaction

6.1 Program of Analysis

The cases which will be analyzed by the chosen analytical model are shown in Table 6.1. The verification cases were chosen for two reasons. First there are replicate data in all cases, and second the loadings and various β ratios check the model's ability to simulate both membrane and plate action.

The gap effect will be investigated by determining the ultimate strength of specimens A21 and A22. If the gap effect influences the ultimate strength as theorized in Chapter 4, the analytical model should show a difference in the ultimate strength of two specimens with different measured gap sizes.

Since the empirical formula recommended by the API does not predict IPB ultimate strength adequately, the analytical model will be used to predict the IPB ultimate strength of the specimen tested in this study. The API recommended design formula shown below, was derived from T data but, in the absence of any DT data, was also applied to DT joints.

$$M_u = (F_y T^2/\sin\theta)(0.8d)(3.4 + 19\beta) \quad \{\text{lower bound eq.}\} \qquad (6.1)$$

It is important to note the absence of the chord thickness ratio, γ, in this equation. In Chapter 1, it was stated that the radial flexibility of the joint, accounted for by γ, would probably have an effect on the IPB strength of tubular joints. In fact several other recommended equations do contain γ [34, 6,39]. All of these

Table 6.1 Program of Analysis

1. Verification of Model - Axial compression: β=0.35 and 0.67
   Axial tension: β=0.35 and 1.00

2. Problems to Investigate

   A. Effect of Gap on β=1.00 Compression Strength

      - Test A21
      - Test A22

   B. Prediction of IPB Strength

      - IPB: β=0.35, 0.67, 1.00; γ=25
      - IPB: β=0.67, γ=15

   C. Interaction

      1. AI Interaction β=0.67

         - IPB to failure, P/P_u= 25, 50, and 75%
         - IPB to failure, P/P_u= 50%, Proportional loading

      2. IO Interaction β=0.35

         - OPB to failure
         - OPB to failure, $M/M_{u(IPB)}$=35%

equations use the following general format to predict IPB strength in T joints;

$$M_u = (F_y T^2) 6 \beta \gamma^{0.5} \quad \{\text{mean eq.}\} \qquad (6.2)$$

except that Yura adds a $\sin\theta$ term in the denominator [39]. Billington and UEG [6, 34] recommendations reduce the IPB strength given by Eq. 6.2 by 0.75 for DT joints based on the relation between compressive strength of T and DT joints. The present IPB data indicates that this factor is not required, and the reduction is eliminated in Yura's recommendations [39]. Yura's equation fits the experimental data rather well as shown in Fig. 6.2 but there is very little experimental data to verify the magnitude of the effect of γ on the DT IPB strength. Thus, the effect of γ will be investigated by analyzing a DT joint with β=0.67, and chord thickness ratios of 25 and 15 subjected to IPB. Comparison of the resulting ultimate strengths will give a measure of the γ effect without the questions raised by experimental scatter

The AI interaction cases with β=0.67 will be compared to the experimental data to see if the proposed analytical method provides a useful tool for the study of interaction behavior. In addition, the influence of the load path on the interaction ultimate strength will be investigated by comparing the results of two interaction solutions one using proportional loading and

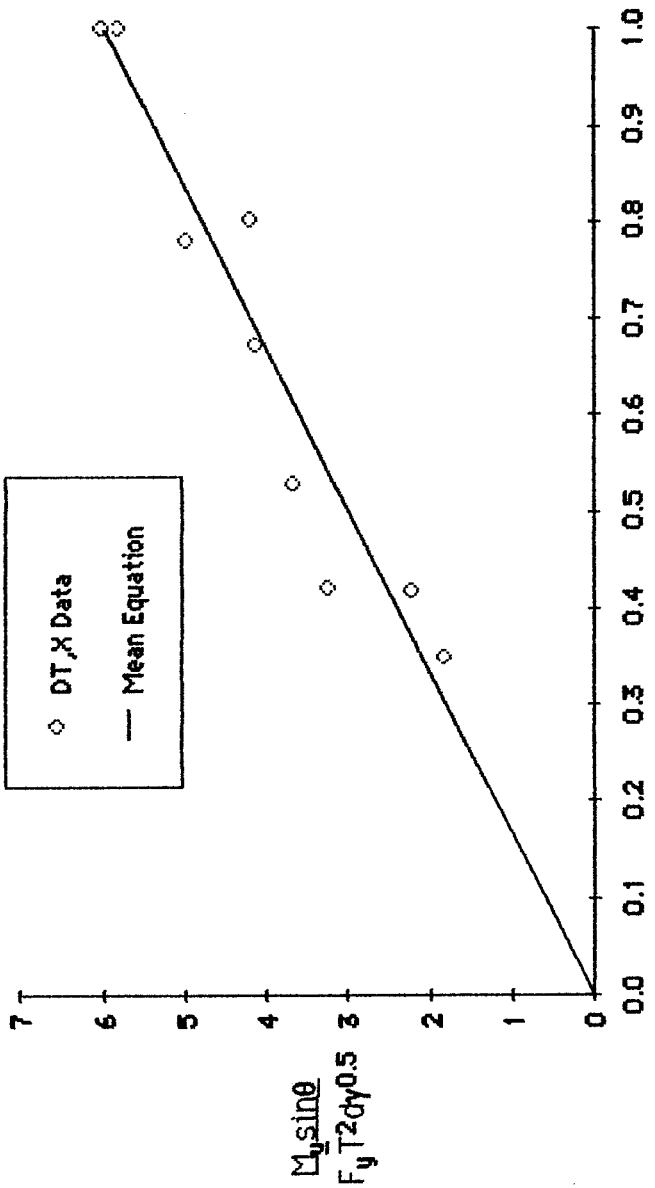

Fig. 6.2 DT IPB Strength Data

one using nonproportional loading. If the load path influences the interaction strength, there should be a significant difference between the results. Finally, the IO interaction for β=0.35 will be investigated with the analytical model to determine whether the increase in OPB strength as IPB is added as shown by the experimental data in Fig. 4.8 is just a result of experimental scatter or a predictable phenomenon. The OPB case for β=0.35 is required to give a reference value for use in the IO interaction case, and provides another loading case for comparison of the analytical and experimental results.

The results of each analytical solution are presented in a tabular form in Appendix G.

6.2 Selection of an Analytical Model

An acceptable analytical solution must produce reasonable predictions of ultimate strength, be applicable to interaction type problems, and be economical. Of the analytical tools available, the finite element method (FEM) has proven to be the most promising in predicting the ultimate strength of tubular joints. In fact, the work by Stamenkovic and Holsgrove [16] presented in Chapter 1 was intended to lead to an application of the model to the prediction of interaction behavior. The ring model developed by Hoadley yielded some good predictions of ultimate strength under simple loadings; however, the model

cannot be used to investigate interaction behavior because the lengths of the transition zone changes from axial to OPB, and the IPB model was unsuccessful. Therefore, it seems that the only practical analytical model acceptable for this investigation is the FEM. However, the present high cost of FEM computations for the number of runs needed makes the FEM with the models presently available [16, 25] unacceptable. Therefore, a new model was developed for this investigation.

Because of its simplicity and its ability to predict the OPB strength of a DT tubular joint, the development of a new finite element model began with the results of Hoadley's work with ABAQUS discussed in Chapter 1. Hoadley suggested that the reason for the poor prediction of IPB strength was that an incorrect load distribution was used. To test this theory, Hoadley's model was recreated except that five concentrated loads were applied assuming a uniform distribution of stresses from a maximum at the crown to a minimum at the saddle instead of three equal concentrated loads at 7.75 in. from the saddle. This new mesh and loading are given in Fig. 6.3. The new analysis predicted the IPB strength of the joint very well as shown in Fig. 6.4. The predicted ultimate strength of 1009 K-in. is within 5% of the experimental value, 1056 K-in.. In addition, the analysis only required 203 sec. computation (cpu) time.

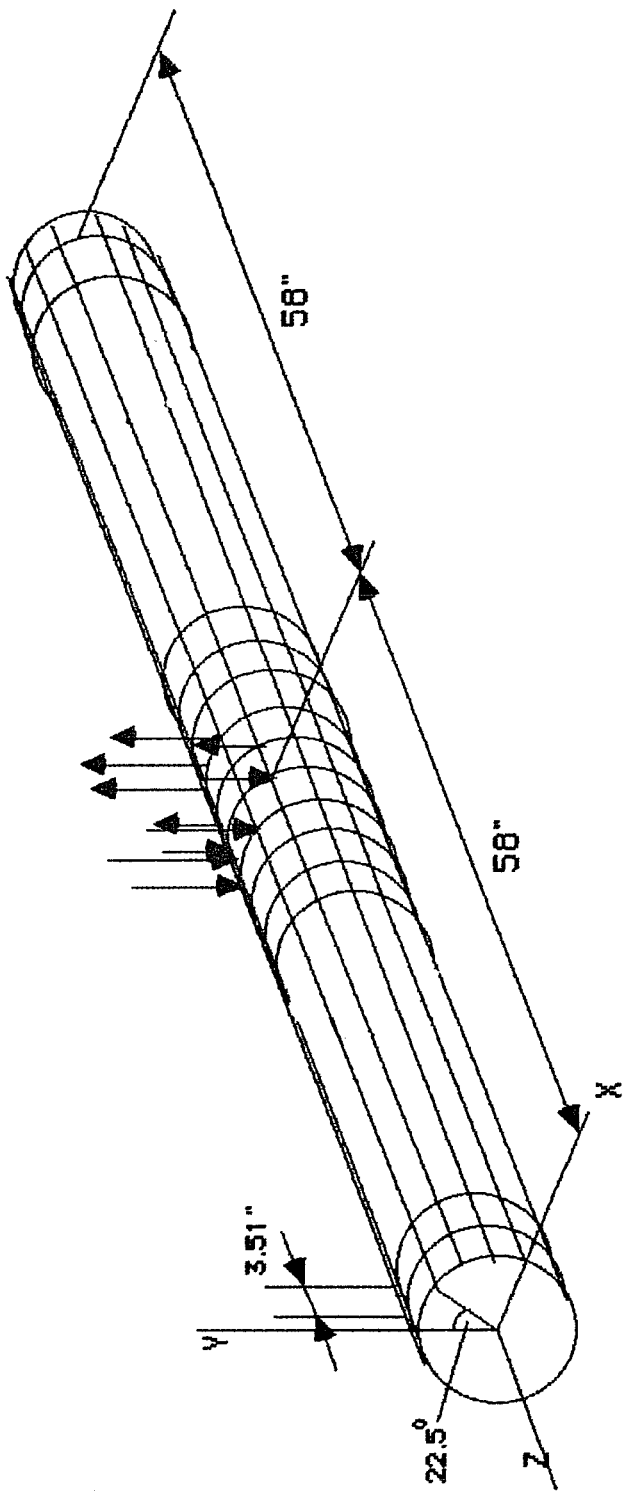

Fig. 6.3 Revised Hoadley FEM Model - IPB

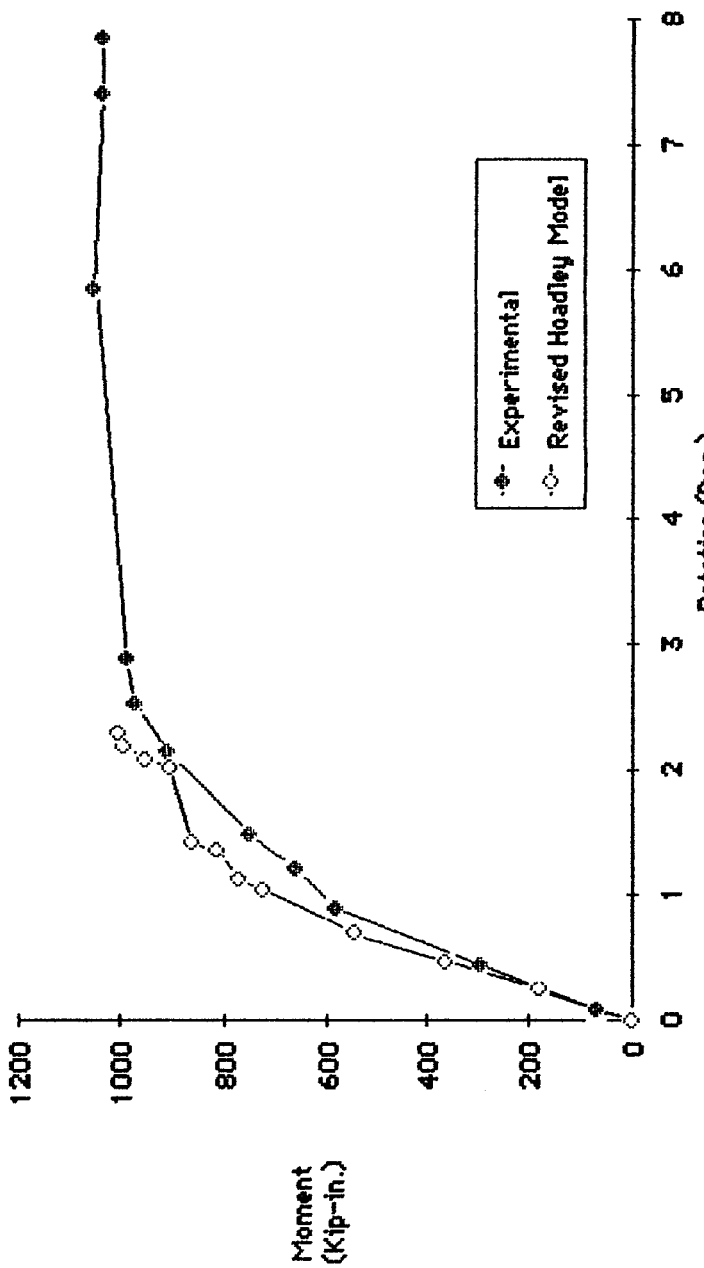

Fig. 6.4 IPB Moment vs. Rotation Curve Predicted by Revised Hoadley Finite Elment Model

From the results of the IPB run it seemed that this finite element model could be applied to this investigation. But, the stair-stepped shape of the moment rotation curve raised some questions about the model. In addition, since the model is sensitive to the distributions of loads, the distribution would effectively be determined by matching the analytical results to the experimental results. Thus, the model becomes semi-empirical.

The stair-stepped shape of the moment-rotation curve is a result of the large tolerance limits set on the equilibrium check used by the solution routine in ABAQUS. The model applied forces to the structure by controlling the magnitude of the concentrated loads. This resulted in significant problems with obtaining a convergent solution after significant yielding had occurred [15]. Therefore, the magnitude of the tolerances on the equilibrium check were increased to achieve a convergent solution. The ABAQUS user's manual recommends the use of displacement control as a first attempt to remedy a convergence problem [13]; however, the displacements are not known at the branch-chord intersection. Thus, a branch member was needed in the model.

The branch member served two purposes: (1) it allowed for the use of displacement control, and (2) it eliminated the guesswork involved in the application of branch forces mentioned by Hoadley. The finite element model proposed for use in this

study is based on Hoadley's model with a branch member and a refined mesh around the joint.

6.3 Finite Element Model

6.3.1 General Information on ABAQUS. ABAQUS is a generally applicable finite element program developed by Hibbit, Karlsson, and Sorensen, Inc. of Providence, Rhode Island. The version used in this research is prerelease version 4-5-134 and is available for internal use at the University of Texas College of Engineering for academic purposes only. ABAQUS is an established program which has been used for several years at the University of Texas to investigate many different types of problems; therefore, a verification of the coding is not deemed necessary.

6.3.2 Element Type. The only shell elements available in the ABAQUS element library suitable for this application are general reduced integration doubly curved shell elements. These elements follow Kirchoff's assumptions which means that the transverse shear is assumed to be zero. Since this application deals with fairly thin shells, it is assumed that the shear components are negligible, thus the use of these elements is acceptable.

The ABAQUS library of elements includes 4 and 8 noded shell elements. Due to the low number of integrations required by

4 noded elements and the success shown in Hoadley's analysis, the 4 noded elements were utilized in the proposed model. This element contains one middle surface integration point, 6 active degrees of freedom at each node, and stress/strain components in the two directions tangent to the shell surface. An additional option allows integration through the thickness of the shell. This option was used to place 7 integration points through the thickness of the chord wall and 5 integration points through the thickness of the branch.

6.3.3 Material Properties. The material properties used in the model were determined by tensile coupon tests using ASTM A370-71 Specifications for the testing of steel products [2]. The material was assumed to be isotropic. The elastic portion of the stress-strain curve is described by a Youngs modulus of 29,000 ksi and a Poisson's ratio of 0.3.

The finite element work by Pan discussed in Chapter 1 showed that the effect of nonlinear material calculations on the predictions of the FEM are significant [25]. Therefore, nonlinear material behavior is included in the finite element model in all cases. The plastic portion of the curve is described by a series of points with yield stress and plastic strain coordinates as shown in Figs. 6.5a and b. Fig. 6.5a shows the complete curve, while Fig. 6.5b shows the curve up to a strain of 0.08 to give a better indication of the shape of the curve. The values of yield

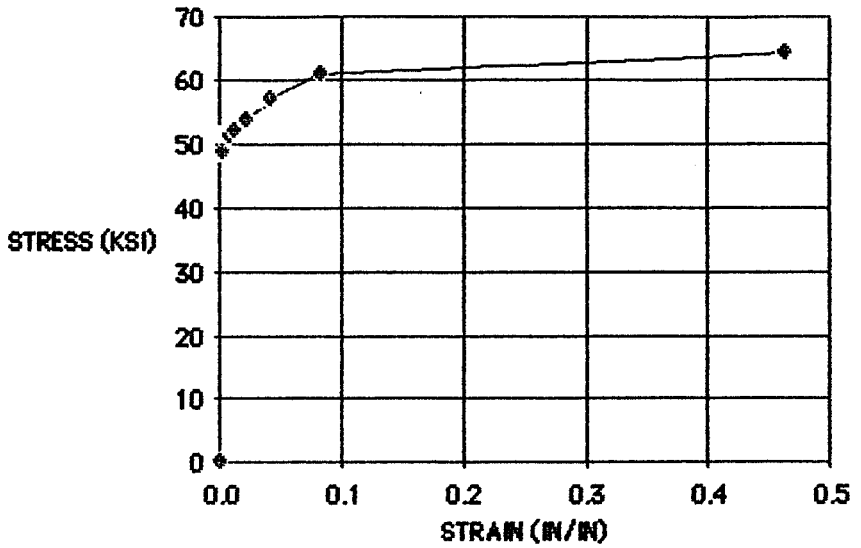

a.) Full Stress-Strain Curve

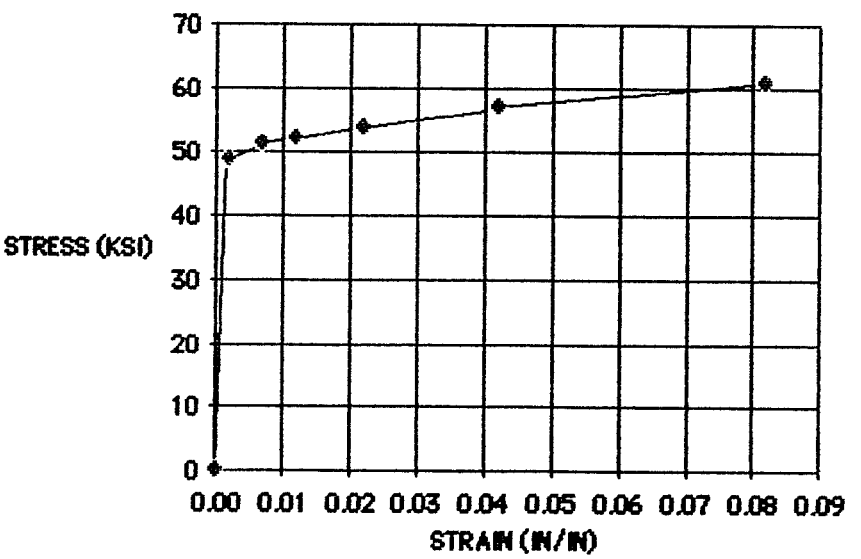

b.) Partial Stress-Strain Curve

Fig. 6.5 Example Stress vs. Strain Curve used in Analytical Model

stress and plastic strain were calculated by first digitizing the experimental stress-strain curves and interpolating to determine the yield stress at several values of plastic strain (0.0, 0.005, 0.01, 0.02, 0.04, 0.08 and at ultimate). Then yield stresses interpolated from the experimental tests were averaged at each value of plastic strain. The actual values of each experimental stress strain curve and the curves used in the model are presented in Appendix E. Plasticity of the material is simulated using a rate independent plasticity theory with a von Mises yield function, a flow rule which satisfies the normality condition, and an isotropic hardening rule.

6.3.4 Solution Technique. Solution of the problem is achieved through a load increment and iteration technique. The size of the loading increment can be input directly or set by the program and the basic nodal variables are assumed to vary linearly over each loading increment. ABAQUS uses a quasi-Newtonian iteration technique. Convergence is checked by comparing the maximum nodal force and moment residuals with tolerances set by the user. The user's manual suggests that the tolerances be set to a small fraction of the typical actual forces (1% to 0.01%). This basic tolerance measure is checked at all nodes except those with prescribed displacements.

The selection of a tolerance level was a difficult process, and was mostly made by trial and error. Some

experimentation with the tolerance level using Hoadley's simple model showed that the tolerance level had a large effect on the cost of each run, put not on the ultimate strength prediction. However, a large tolerance level causes the program to produce the stair-stepped type curve shown in Fig. 6.4 and overpredicts the stiffness of the joint. When displacement control is used, the effect of the tolerance limit on the finite element solution is significantly reduced because convergence is not checked at the points of force application since these are given prescribed displacements. Thus, the tolerances used in this investigation varied from 1% to 5% of the expected nodal forces. The exact effect of the tolerances will be discussed as the results of the investigation are presented.

6.3.5. Loading. The ABAQUS program allows the user several methods of applying force to a structure. The two methods used in this study are load control and displacement control. After a few preliminary runs it became evident that the displacement control method required less computation time than the load control method. In addition, while use of the load control method resulted in problems with convergence, the displacement control method produced convergent solutions well into the inelastic portion of the loading curve and in some cases to unloading. Thus, displacement control was used in all cases

except when applying loads in the interaction cases. Since the movement of the joint does not always follow the line of action of the resultant force, deflection control could only be used in the direction loaded to failure. The force in the second direction was applied using load control. Because the force in the second direction is usually below the yielding load of the joint, using load control did not cause any problem with convergence.

In the ABAQUS program the user has the option to set the size of the loading increments or to let the program determine them automatically within a range set by the user. Because little was known about convergence of each case, the program was allowed to set the increment automatically. Since this investigation is interested in ultimate strength of the joint, the limits input for the increment size were chosen so that the first increment (elastic portion of the loading curve) was as large as possible. This allowed for smaller loading increments, and thus better convergence, near the ultimate condition without a significant increase in cost.

6.3.6. Geometric Nonlinearity. ABAQUS has the ability to model both material and geometric nonlinearities. For shell elements the geometric nonlinearities include large rotations and small strains. Pan's study of nonlinear effects on the prediction of tubular joint behavior indicated that the addition of

nonlinear geometry to the model reduced the ultimate load by approximately 30% [25]. Therefore, the nonlinear geometry option was used in all cases.

6.3.7 Meshes. The development of the meshes used in this analysis was primarily trial and error. The main parameters used in the creation of each mesh were, minimum number of elements, simple geometry (since no generation program was available for 4 noded elements), and a refined mesh in the immediate area of the joint.

Since several β ratios were to be investigated while the chord remained a constant diameter and length, the mesh was divided into a chord section on either side of the joint which basically remained the same and a joint section which varied with each β ratio. The flanges at the end of the branch and chord were modeled by thickened shell elements which were given a modulus of 100,000 ksi and assumed to be elastic. In the axial loading cases, only 1/2 of the branch length is modeled (29 in.) while in the bending cases the full branch length is modeled (58 in.). The chord thicknesses were set to match the test being simulated. The meshes used in this research are not necessarily the most efficient for each application as an optimization of the mesh for each case was beyond the scope of this study.

A plan view of one quadrant of the basic mesh for each joint area is shown in Figs. 6.7-6.10. The orientation of the quadrant is shown in Fig. 6.6. Due to symmetry, the mesh in the joint area was produced by replicating the basic mesh about each line of symmetry. Two meshes were developed for the β=0.67 case as the first coarser mesh [Fig. 6.9] did not produce accurate predictions of ultimate strength. The medium mesh [Fig. 6.10] reduced the size of the elements at the branch-chord intersection and added another row of elements in the joint region. The full meshes are shown in Appendix F. To minimize computation costs and take advantage of symmetry 10 different meshes were used for the cases analyzed; three 1/8 joint meshes for the axial load cases (which are not shown), three 1/4 joint meshes for the IPB cases and the AI interaction, two 1/4 joint meshes for the A21 and A22 cases, one1/4 joint for the OPB β=0.35 case, and one 1/2 joint mesh for the IO interaction case. In addition to these, 1/8 and 1/4 joint "medium" meshes were created for β=0.67 when the initial mesh was shown to be unacceptable. The creation of all of these meshes was greatly simplified by the fact that the ABAQUS program does not require sequential numbering of the nodes. Therefore, four "master meshes" (1 for β=0.35 and 1.00, and 2 for β=0.67) which represented 1/2 of a joint were created, then the unnecessary nodes and elements were eliminated from each mesh to create the 1/4 and 1/8 joint meshes.

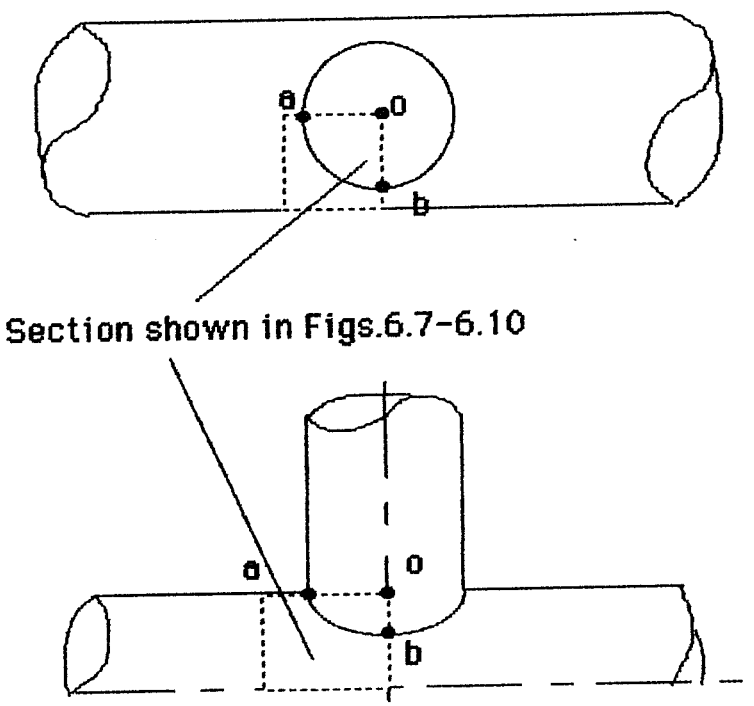

Fig.6.6 Location of Element Meshes shown in Figs.6.7-6.10

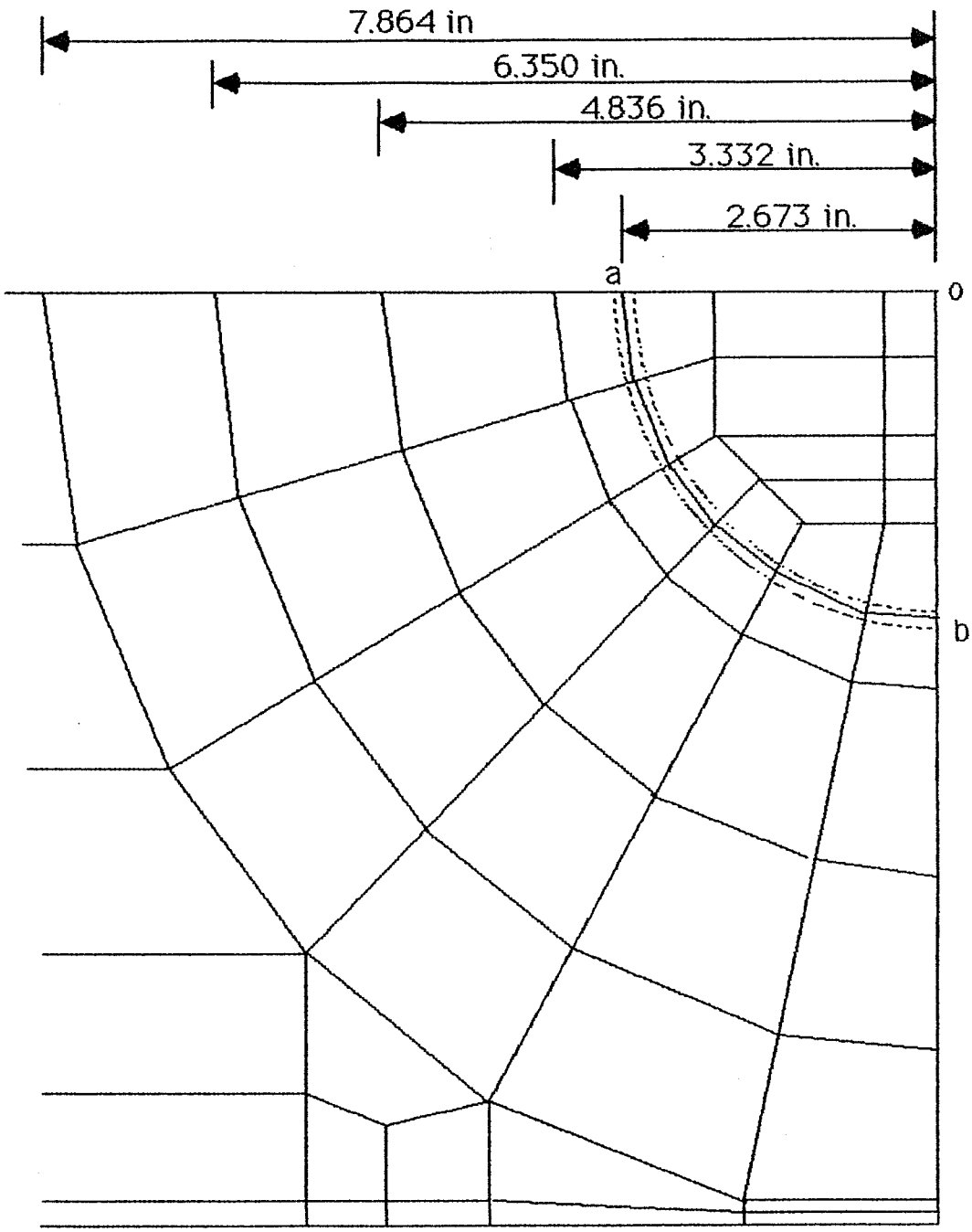

Fig. 6.7 ß=0.35 Mesh in Joint Area

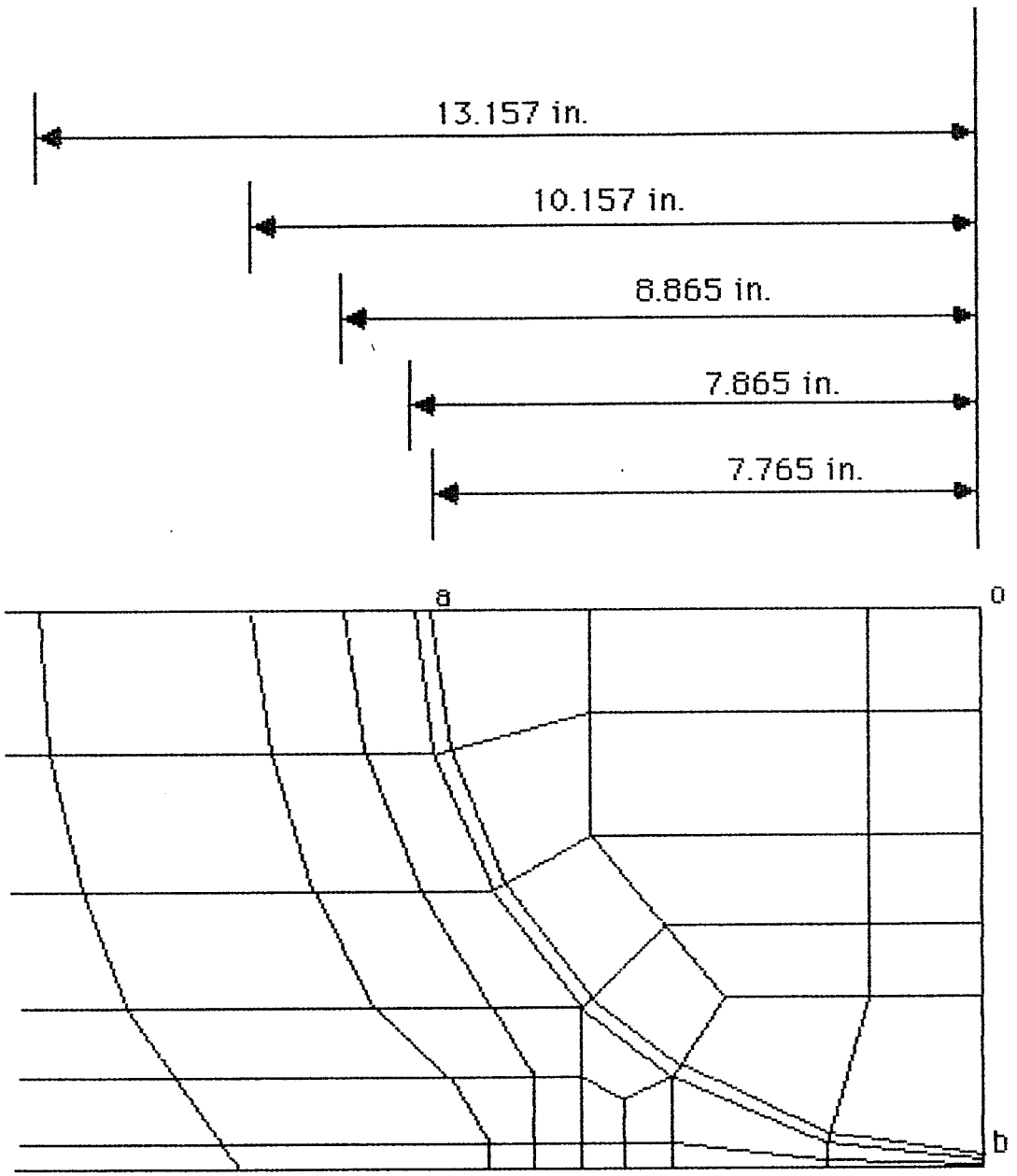

Fig. 6.8 ß=1.00 Joint Mesh

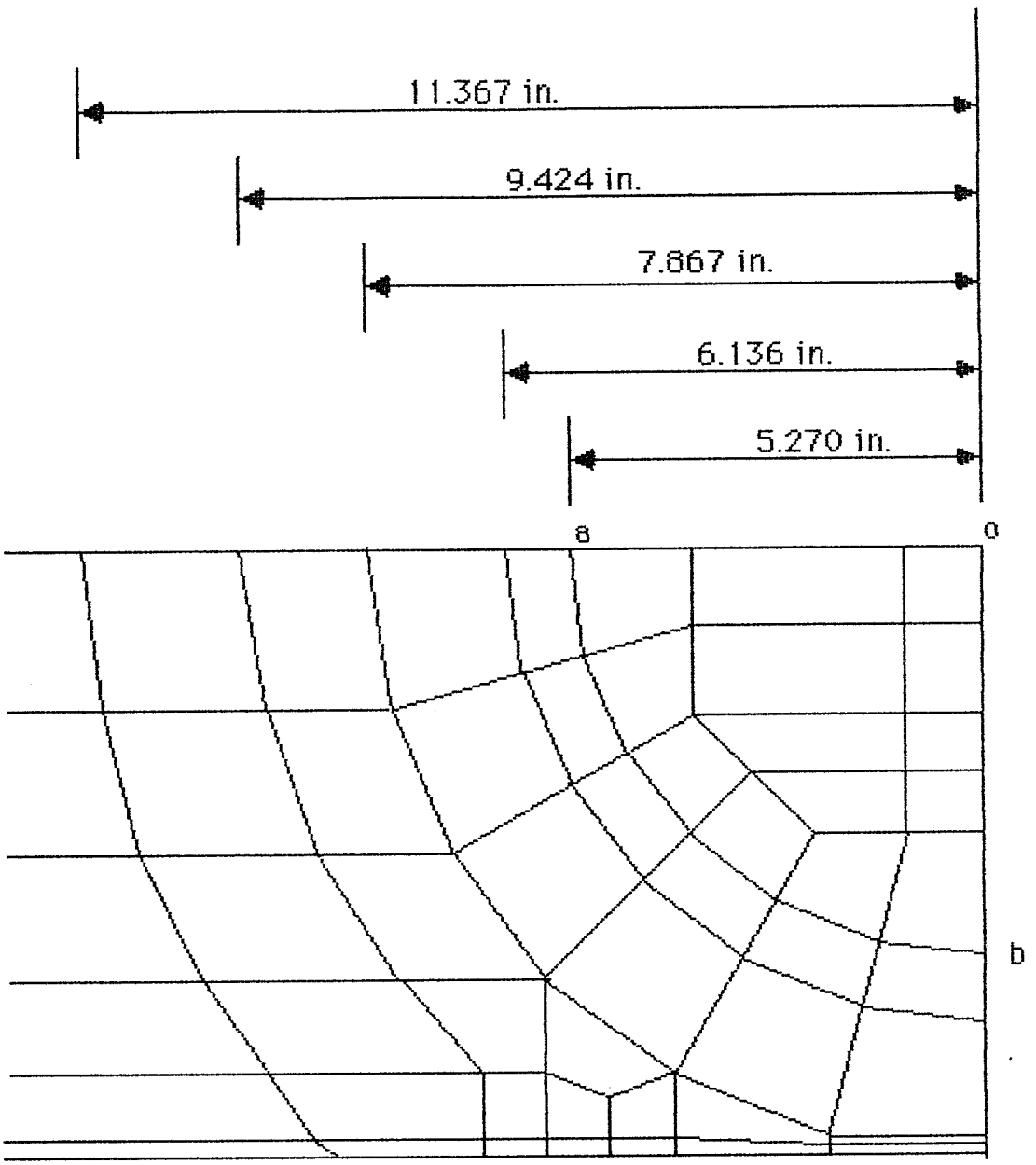

Fig. 6.9 ß=0.67 "Coarse" Mesh in Joint Area

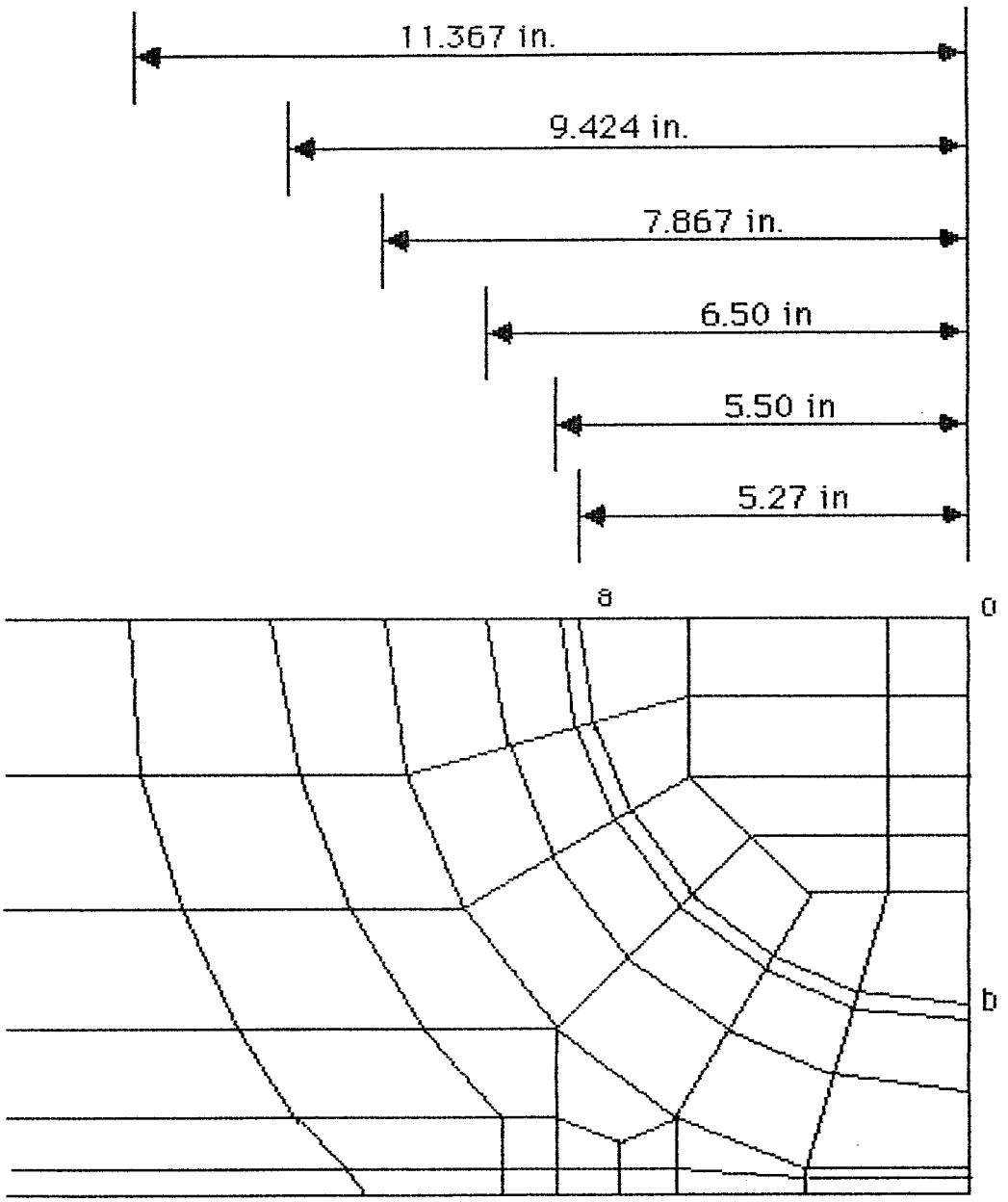

Fig. 6.10 ß=0.67 "Medium" Joint Mesh

6.3.8 Storage, and Computation Time. The number of elements, nodes, and degrees of freedom, and storage required by each case is given in Table 6.2. Also included in Table 6.2, are the cpu, I/O,and total TM times required for each case along with the number of increments, the average number of iterations to convergence, and the tolerance limit used.

6.4 Prediction of Joint Stiffness

Because the finite element method uses discretized degrees of freedom instead of a continuous system, the method typically overestimates the stiffness of a structure. This problem has been alleviated somewhat by the use of reduced integration elements which results in more flexible models. Another method for improving the prediction of structural stiffness is by reducing element sizes. As the element size approaches zero, the discrete DOF comes closer to modeling a continuous system. Using these to methods, the FEM should produce reasonable predictions of joint stiffness. However, it must be noted that the experimental measurements are subject to several variables which are not generally included in the finite element model and may result in a differences between measured and predicted joint stiffnesses.

The finite element analysis of a β=0.67 DT joint in compression performed by Pan overestimated the stiffness of the joint using the reduced integration elements even with a very

Table 6.2 Options, storage and computation times for ABAQUS runs

β	Loading	Tolerance (% of Nodal)	No. Incr.	Avg. No., Iter.	No. Elem.	No. Nodes	No. D.O.F.	Work Space	CPU (sec.)	TIME (I/O) (sec.)	TM (sec.)	Notes
0.35	Comp.	10	8	4.75	125	153	918		288618	1174791	1284143	Load Control
0.35	Comp.	1	4	1.00	125	153	918		157808	711531	750565	Displ. Control
0.35	Tens.	1	17	4.76	95	118	708		543521	1880569	2186095	
0.35	IPB	5	5	4.80	250	289	1734	21598	496065	2110483	2271042	
0.35	IPB	1	8	5.25	250	289	1734	21598	916465	3620531	4000716	
0.35	OPB	5	7	4.43	250	285	1710	21566	586484	2358070	2589023	
0.35	IO	5	12	6.00	504	539	3234	52000	N/A	N/A	N/A	
0.67	IPB	10	12	2.17	132	170	1020	28580	202970	944051	985588	No Branch
0.67	Comp.	1	7	4.57	119	146	876		268656	1098139	1198547	Coarse
0.67	Comp.	1	12	4.58	125	153	918		482382	1813535	2041286	Medium
0.67	IPB	5	9	4.78	238	277	1662	21530	831273	3266247	3616410	Coarse
0.67	IPB	1	8	5.63	250	290	1740	21571	N/A	N?A	N/A	Medium
0.67	IPB	5	9	4.89	238	277	1662	21530	936843	3573851	4000645	Gamma = 15
0.67	A125	5	9	4.89	238	277	1662	21530	929576	3590755	4000850	
0.67	A150	5	9	5.22	238	277	1662	21530	933623	3581480	4000833	
0.67	A175	5	10	4.80	238	277	1662	21530	930928	3587639	4000832	
0.67	A150P	5	9	5.44	238	277	1662	21530	942657	3560827	4000830	Proportional
1.00	Tens.	1	15	5.47	113	139	834		646848	2500516	2785318	
1.00	A21	1	10	5.00	226	259	1554	24354	919374	3613923	4000745	
1.00	A22	1	10	5.00	226	259	1554	24354	921964	3607931	4000694	
1.00	IPB	5	11	4.27	226	264	1584	21498	910207	3635091	4000895	

refined mesh, as shown in Fig. 1.24 [25]. The predicted stiffness is approximately 65% higher than the average of the experimental stiffnesses for several β=0.67 joints loaded in compression. Pan attributes this discrepancy to residual stresses which result from welding at the connection, and approximations inherent in the analytical model. However, the discrepancy can be attributed to the fact that the measured stiffness does not represent the actual specimen stiffness.

The displacement gages used in this research project were placed such that the stiffness of the test frame was included in the displacement measurements as shown in Fig. 6.11a. From the schematic of this configuration shown in Fig. 6.11b, it can readily be seen that the location of the displacement gage will cause an underprediction of the specimen stiffness. The magnitude of the error can be estimated by forming the following relation between the total stiffness measured by the gage, KT [units (force/length], and the individual stiffnesses of the specimen, K1, and the setup, K2;

$$(1/K1) + (1/K2) = (1/KT) \tag{6.3}$$

$$KT = (K1)(K2)/(K1+K2) \tag{6.4}$$

If the specimen is much stiffer than the test setup, i.e. K1>>K2, then from Eq. (6.4), KT would approach the stiffness of the test

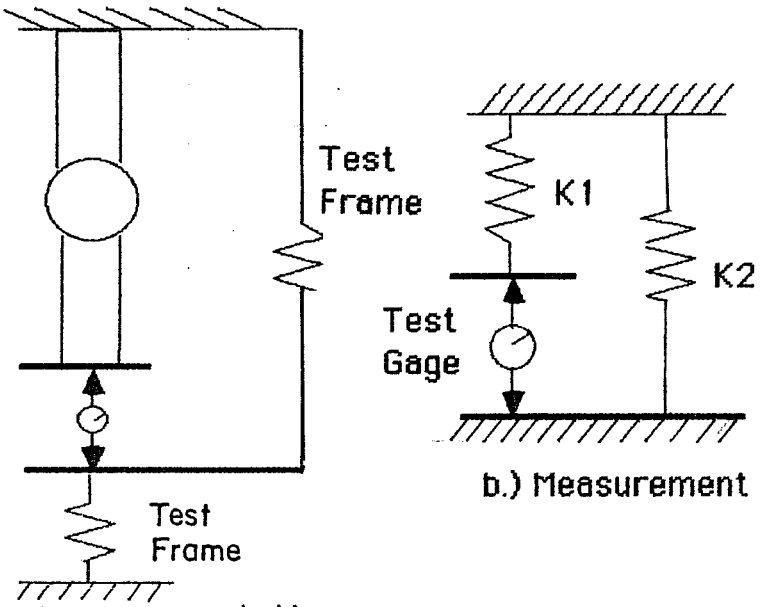

Fig.6.11 Experimental Stiffness Measurements

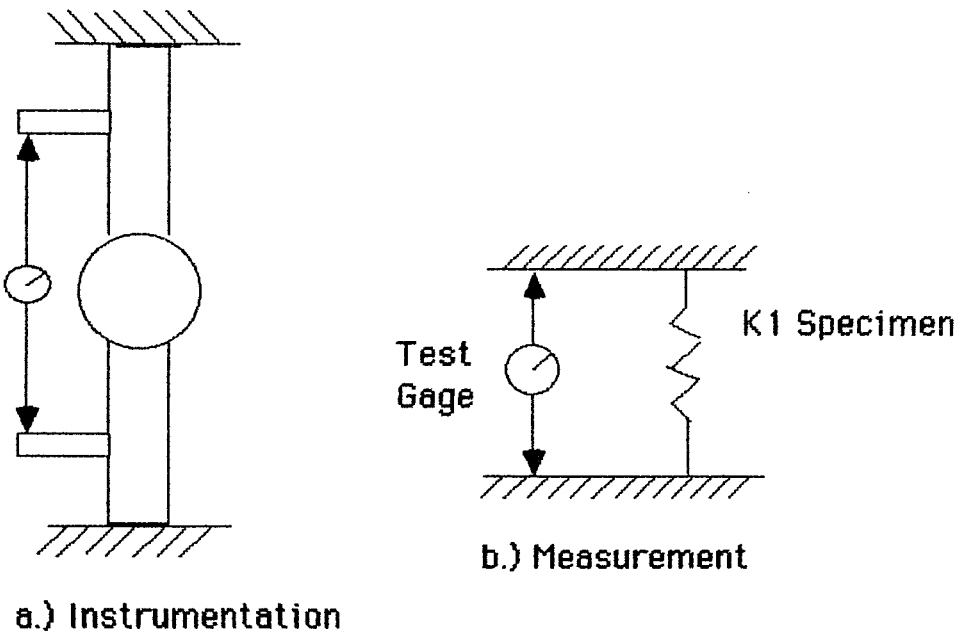

Fig.6.12 Experimental Stiffness Measurements Ref. [SA1]

frame, K2. If the test setup is much stiffer than the specimen, i.e. K2>>K1, then KT would approach the stiffness of the specimen. In order to determine the effect of the flexibility of the test frame using Eq. (6.4), the value of K2 must be determined.

In a series of tests related to this research an elastic test on a β=1.00 DT joint loaded in compression using a very stiff screw type testing machine was performed. The displacement gages were placed as shown in Fig. 6.12a so that the only stiffness measured was that of the specimen as shown in the schematic in Fig. 6.12b. This series of tests was aimed at determining strain concentration factors, and the dimensions and material properties of the specimen were the same as the β=1.00 joints used in the research presented in Chapter 3 [32]. The elastic load-displacement curve produced by the test using the stiff test machine showed an initial stiffness of 2,500 kips/in. The two compression tests on β=1.00 joints presented in Chapter 3, A21 and A22, exhibited elastic stiffnesses of 1108 kips/in. and 1280 kips/in. respectively. If the results of the test in the stiff machine is taken as the specimen stiffness, K1, and the average of the stiffnesses of specimens A21 and A22 (1194 kips/in.) is taken as KT, then the stiffness of the test frame can be determined using Eq. (6.4). The resulting test frame stiffness, K2, is 2279 kips/in. The actual stiffness is

difficult to calculate due to end conditions. However, this stiffness falls between the pinned and fixed conditions.

Using the value of the test frame stiffness, and the total stiffness measured for Test A1, in Eq. (6.4) the actual specimen stiffness can be approximated and compared with Pan's analytical prediction. The total stiffness measured for Test A1 is 320 kips/in. Inserting the stiffness values into Eq. (6.4), the specimen stiffness is calculated to be 373 kips/in. This is still considerably lower than the stiffness of Pan's model, 511 kips/in. Pan points out that five values of stiffness were available for the β=0.67 joint and that the average of these is 309 kips/in. and the standard deviation is 89 kips/in. Using this value of KT, 398 kips/in., in Eq. (6.4) results in a specimen stiffness of 482 kips/in. which compares well with Pan's prediction.

This analysis of the prediction of stiffness by the FEM shows that the method can be used to predict joint stiffness as well as strength. However, the analytical predictions will generally be an upper bound to the actual joint stiffness due to the approximations made by assigning discrete degrees of freedom, the residual stresses present in the joint, and the eccentricities in the joint due to fabrication.

6.5 Validation of Analytical Model

6.5.1 Axial Compression-β=0.67. The load-deflection curves obtained from the finite element model along with load-deflection curve from Test A1 are shown in Fig. 6.13. The results of Test A51 were not included on the graph because the joint did not have the same dimensions and material properties as joint A1 and the analytical models. The analytical model used displacement control and the tolerance was based on 1% of the expected nodal concentrated force which is approximately 0.04% of the total expected load. A uniform displacement was applied to the top of the branch with a maximum value of 0.8 in. The model using the "coarse" mesh yielded an ultimate strength of 92.3 kips, while the model using the "medium" mesh produced an ultimate strength of 85.5 kips. The ultimate strength of Test A1 is 78.8 kip. The analytical ultimate strengths are 17% and 9% higher than the experimental value for the "coarse" and "medium" mesh respectively.

Comparison of the analytical and experimental load-deflection curves shows that as with Pan's model, the stiffness of the joint is apparently overestimated. This overestimation is due mainly to the inclusion of the test frame flexibility in the measured stiffness as discussed previously.

This specific loading case was recently modeled by Pan [25] whose finite element model is described in Chapter 1. A

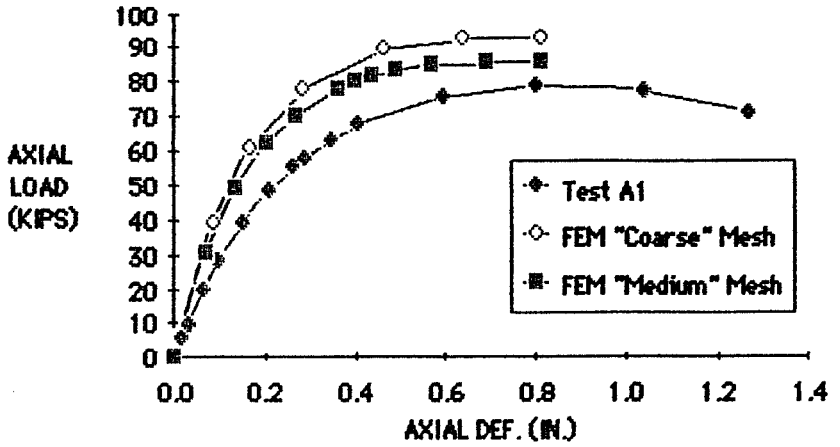

Fig. 6.13 Predicted and Measured Axial Load vs. Deflection Curves for ß=0.67 Joint in Compression

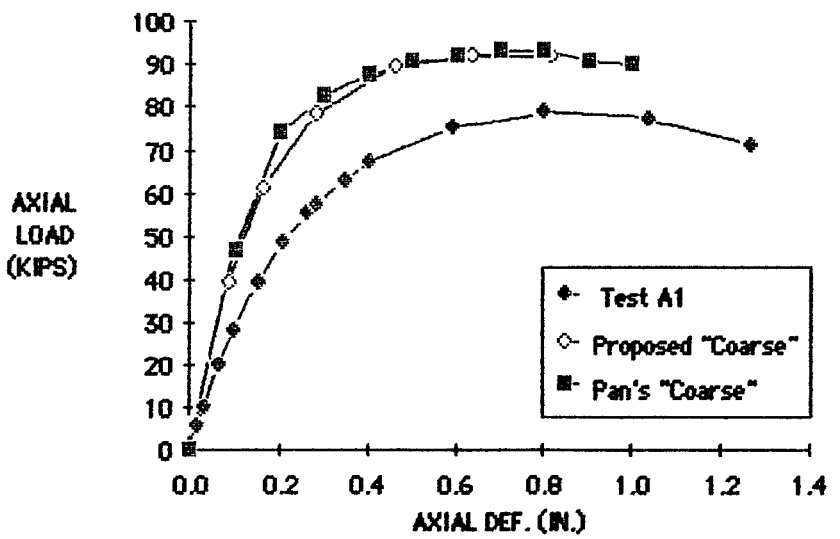

Fig. 6.14 Comparison of Results of Pan's and Proposed "Coarse" Finite Element Meshes

comparison of the results of Pan's model and the proposed model are shown in Fig. 6.14-6.16. Fig. 6.14 compares the results of Pan's "coarse" mesh to the proposed model's "coarse" mesh, and indicates that there is no significant difference between the two loading curves. Fig. 6.15 shows the curves produced by Pan's "medium" mesh with the proposed model's "medium" mesh, again there is no significant difference between the two curves. Finally, Fig. 6.16 compares the curves produced by Pan's "fine" mesh and the proposed model's "medium" mesh, here Pan's "fine" produces a much better prediction of the actual joints behavior; however, the run was stopped prematurely due to the excessive amount of computation time required.

Table 6.3 presents the number of nodes, number of degrees of freedom and the running time required by Pan's model and the proposed model. Comparison of the running times indicates the economy of the proposed model. The proposed model's "coarse" mesh produced the same results as Pan's "coarse" mesh but only required 1/5th of the running time. Comparison of the "medium" meshes from both models shows that the present model required approximately 1/8 as much running time as Pan's model. Because most of the cases to be analyzed in this chapter require 1/4 joint meshes instead of the 1/8th joint meshed used in this case, the savings afforded by the proposed model will be significant in this study.

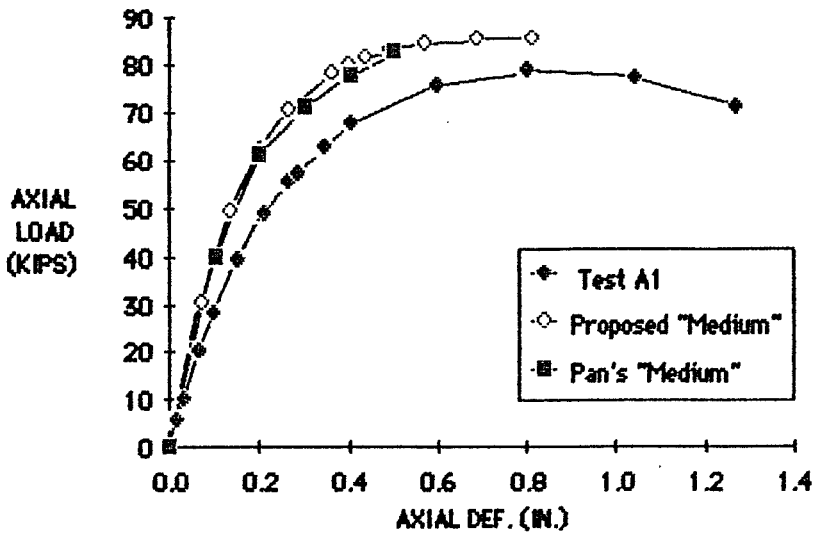

Fig. 6.15 Comparison of Results of Pan's and Proposed "Medium" Finite Element Meshes

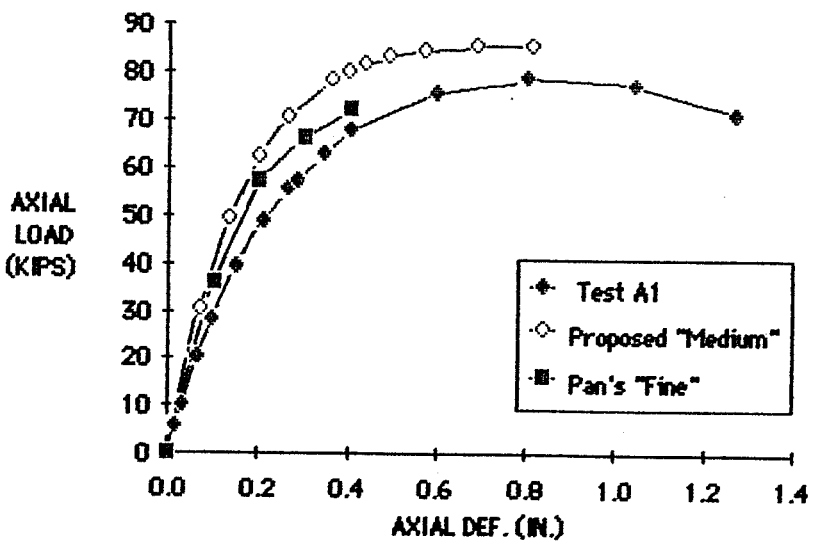

Fig. 6.16 Comparison of Results of Pan's "Fine" and Proposed "Medium" Finite Element Meshes

Table 6.3 Comparison of Running Times for Pan's and Proposed Finite Element Models

Mesh	No. Nodes		No. D.O.F.		Running Time*	
	Pan	Proposed	Pan	Proposed	Pan	Proposed
Coarse	117	146	590	876	6168	1199
Medium	386	153	1939	918	17161	2041
Fine	572		2877		82421	

*TM Time in sec. (0.7 x I/O Time + 1.6 x CPU Time)

Comparison of the running times of the "coarse" and "medium" meshes used in the proposed model shows that the addition of 6 more nodes, and 42 more degrees of freedom almost doubled the computation time. But, the predicted ultimate strength was reduced by only 7%. The significant increase in the computation required by the "medium" mesh over the "coarse" mesh was a result of the smaller elements at the chord-branch intersection. The small elements concentrate the stresses around the branch-chord intersection which leads to yielding at lower loads than in the large elements of the "coarse" mesh which average the stress over a larger area. This resulted in earlier non-linear behavior and required smaller increments to achieve equilibrium. The "coarse" mesh required 7 increments to reach a deformation of 0.8 in. while the "medium" mesh required 12 increments. Because of the smaller elements, the "medium" mesh also produced a lower prediction of the initial stiffness.

6.5.2 Axial Compression - β=0.35. In the simulation of the β=0.35 compression test, the force was applied by both load and displacement control to compare the results of the two loading types. The case using displacement control had a tolerance of 1% of the expected nodal load (0.04% of total) and the load control case used a tolerance of 10% of the expected nodal load (0.4% of total). In the displacement control run a uniform displacement was applied to the top of the branch with a

maximum value of 0.8 in. In the load control run, equal concentrated loads were applied to the top of the branch.

The load-deflection curve produced by the two loading methods are shown in Fig. 6.17. Comparison of the loading curves indicates that there is no difference between the predictions of joint behavior. However, because of the convergence condition, the run using load control required 8 increments compared to the 4 increments required by the displacement control run. The running times were 1284 and 751 secs. for the load and displacement control cases respectively. Thus, it seems that displacement control is a more favorable way to apply force for this application in the ABAQUS finite element system.

The load-deflection curve produced by the displacement control run is shown along with the curves obtained from Tests A40 and A41 in Fig. 6.18. The maximum load achieved by the finite element model is 50.3 kips. The maximum loads attained by Tests A40 and A41 are 46.3 and 42.0 kips respectively with an average of 44.2 kips. The finite element model's ultimate strength prediction is approximately 14% higher than the average of Tests A40 and A41. This overprediction of strength is probably due to the coarseness of the mesh used in the analysis. Since the β=0.67 analyses showed the effect of reducing the mesh size on the ultimate strength prediction, and in order to minimize computation costs, a finer mesh was not used.

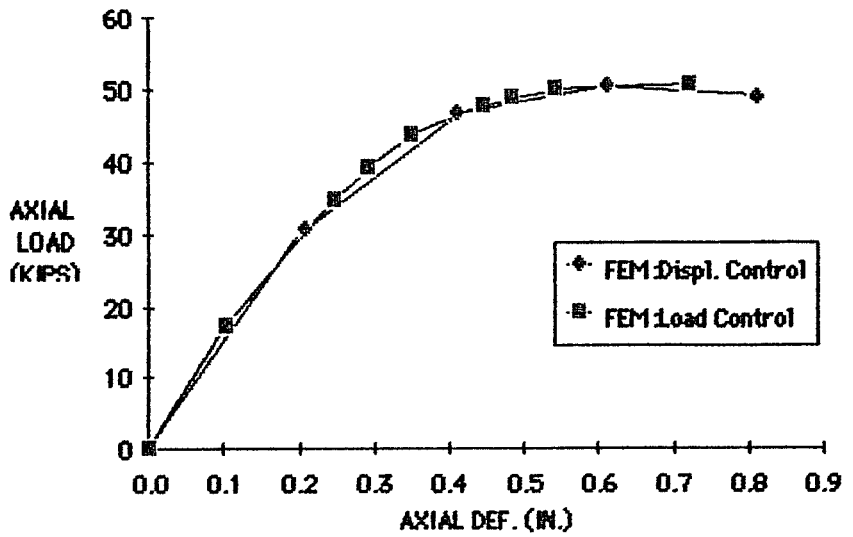

Fig. 6.17 Comparison of Axial Load vs. Deflection Curves Produced using Load and Displacement Control Methods

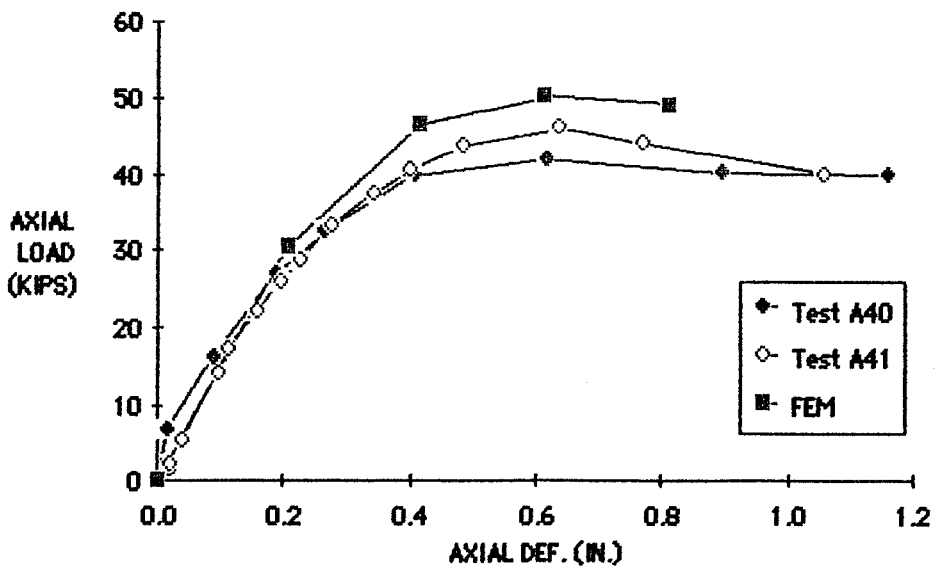

Fig. 6.18 Predicted and Measured Axial Load vs. Deflection Curves for β=0.35 Joint in Compression

Comparison of the analytical and experimental loading curves shown in Fig. 6.18 indicates that the finite element model replicates the measured stiffness rather well. This is because the measured stiffness more closely approximates the actual elastic joint stiffness since the β=0.35 joint is much less stiff than the test frame. Using the measured stiffness,148 kips/in., and the calculated test frame stiffness, 2279 kips/in., in Eq. (6.4), the actual specimen stiffness is 158 kips/in. which is very close to the measured value.

Because of the interest in the contribution of the chord section to the strength of the joint produced by Hoadley's ring model, strain gages were placed along the chord centerline of specimen A40, as shown in Fig. 6.19, to study how strains vary along the chord. As another measure of the applicability of the proposed model, the strains predicted by the model will be compared to the measured strains. The strains in the circumferential direction measured and computed at the ultimate loading condition are plotted in Fig. 6.20. Comparison of the two curves shows that even though the magnitudes are not the same, the finite element model does a good job of following the trend of the experimental strains along the chord. Fig. 6.21 shows the calculated and measured strains for several loading cases illustrate how the strains change with load. Comparison of the two figures indicates that the model does a good job of

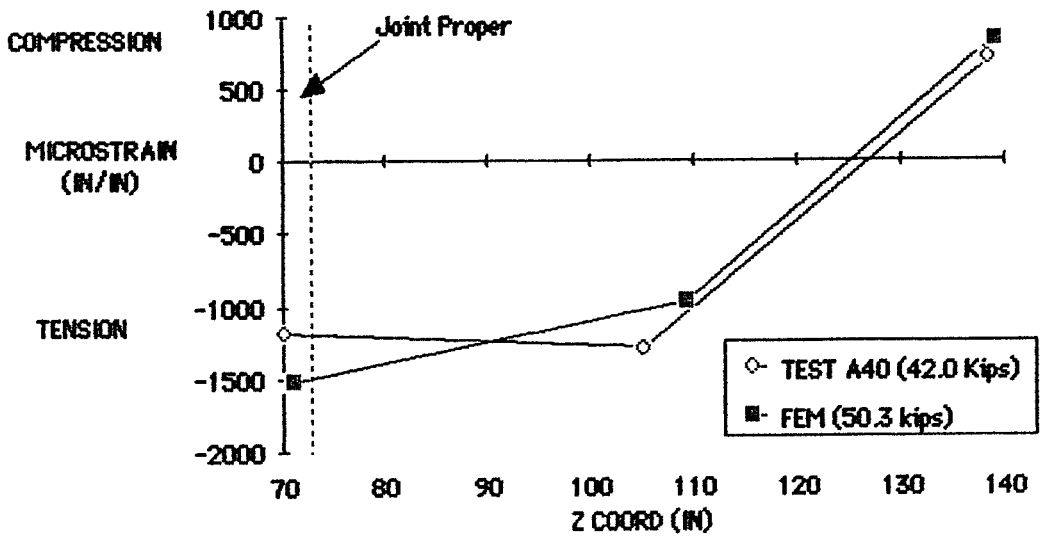

Fig. 6.20 Comaprison of Calculated and Measured Strains Along the Chord Saddle Centerline for Test A40 at Ultimate Load

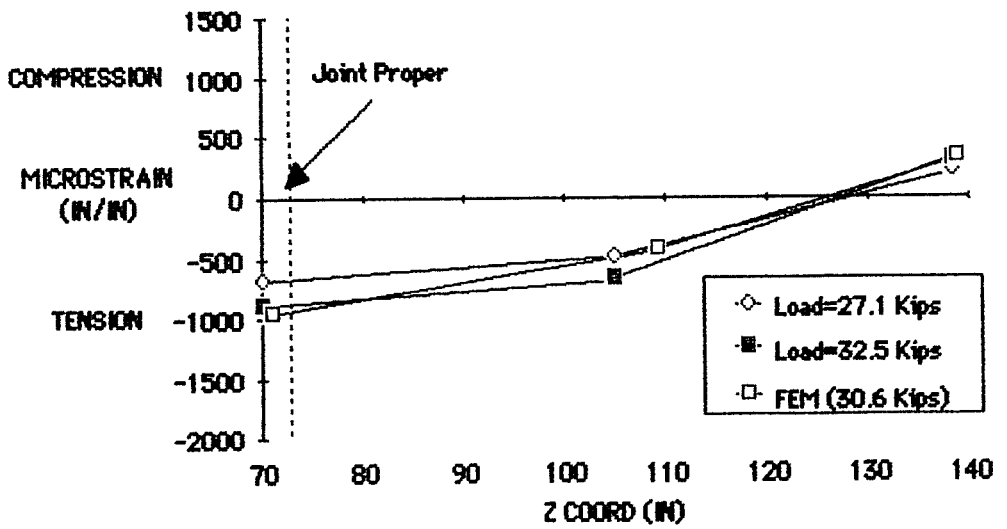

Fig. 6.21 Comaprison of Calculated and Measured Strains Along the Chord Saddle Centerline for Test A40 for Several Loads

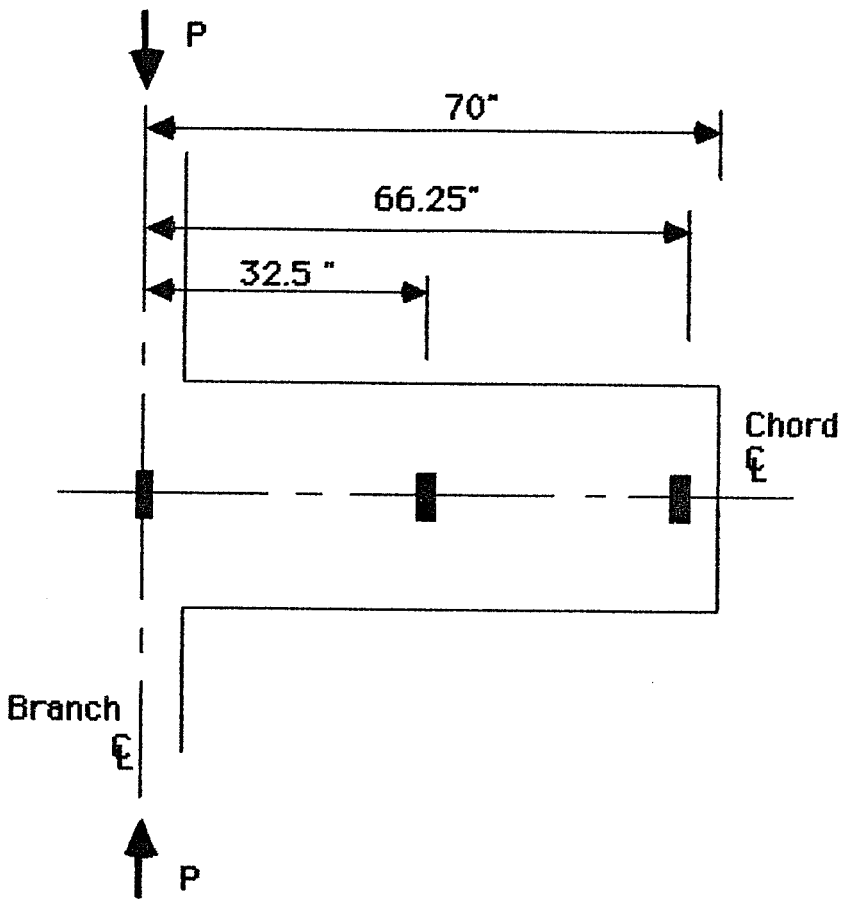

Fig.6.19 Postions of Strain Gages on Specimen A40

replicating the change in strains with load. In addition, the magnitudes of the strains indicate that the chord away from the branch remains elastic throughout the loading.

6.5.3 Axial Tension - β=1.00. As discussed in Chapter 1, the common mode of failure for tubular joints in tension is a fracture along the weld of the branch-chord intersection. This type of failure cannot be simulated by the proposed model because the fracture depends on local conditions at the weld toe which are not included in the model. In addition, the stress-strain curve used to model the material properties does not represent the stress-strain relationship in the heat affected zone around the weld. Therefore, the purpose of the tension runs is not to predict ultimate strength but to see if the model could replicate the shape of the loading curve. As before, a uniform displacement was placed on the top of the branch to apply force and the tolerance was set to 1% of the expected maximum nodal force.

The load-deflection curves produced by the finite element model and by Test T3, taken from Ref. 28, are shown in Fig. 6.22. Several replicates of this test were available; however, because of their similarity only one is included for the sake of clarity. It should be noted that the deflections used in the figure are based on the deformations on both sides of the chord; thus, the deflections given by the finite element run were doubled to match the experimental measurements. In addition, the joint was tested

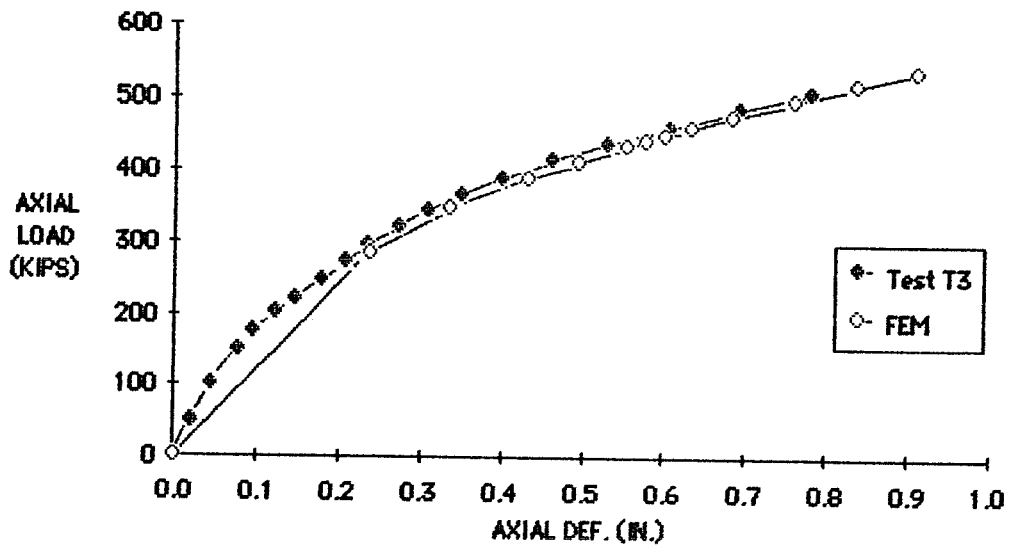

Fig. 6.22 Predicted and Measured Axial Load vs. Deflection Curves for ß=1.00 Joint in Tension

in a screw type machine and joint displacements were measured by gages placed as shown in Fig. 6.12 which eliminates the influence of the test frame flexibility. Because of the automatic incrementation, the first point on the finite element curve occurred at a load of 286 kips and a deflection of 0.236 in. which explains the seeming perfectly elastic behavior in the first load step. Above this first point, the model does a very good job of simulating the loading curve of the joint in tension.

6.5.4 Axial Tension - β=0.35. As before, axial tension was applied by displacement control and the tolerance limit was set at 1% of the expected maximum nodal force. The specimen was tested in the screw type machine and the instrumentation was similar to that used for the β=1.00 joint. For the specimens being simulated, the branch was made of a lower strength steel than the chord and the chord was cut 18" from the center of the joint. In addition, the ends of the chord were reinforced by a two stiffeners constructed of 4"x1/2" plate [28] as shown in Fig. 6.23a. In the finite element mesh, the reduction in the length of the chord was attained by eliminating elements outside of the required length. The stiffening plate was modeled by placing 4" elements at the end of the chord and restricting the deflections in the elements at the crown and saddle centerlines to 0.

The load-displacement curves produced by the proposed model and Tests T8 and T9 are shown in Fig. 6.23b. As with the

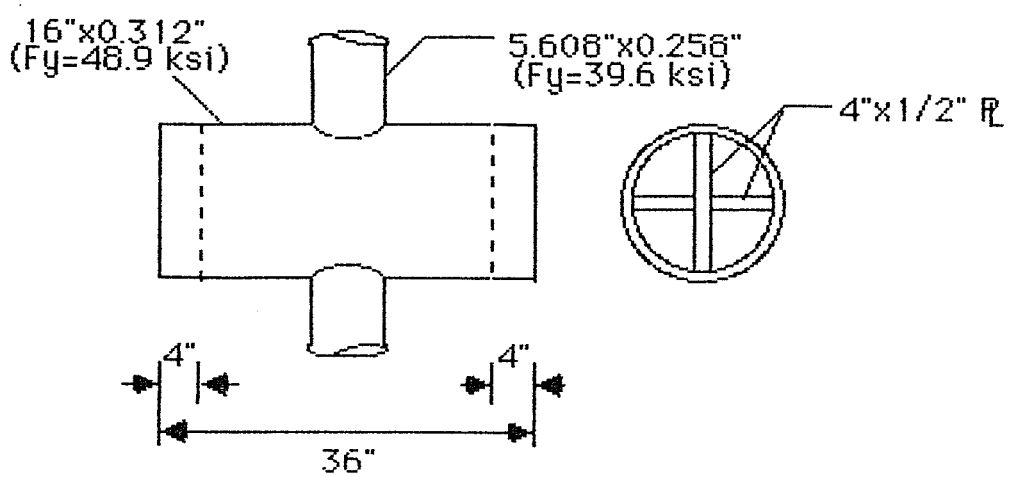

Fig. 6.23a Schematic of ß=0.35 Tension Specimen

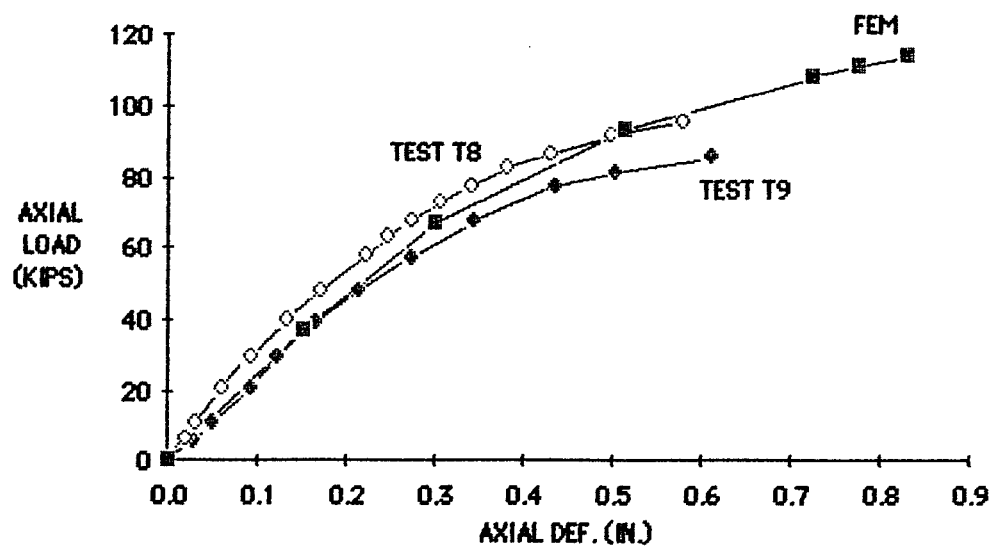

Fig. 6.23b Predicted and Measured Axial Load vs. Deflection Curves for ß=0.35 Joint in Tension

β=1.00 case, displacements yielded by the finite element program were doubled to match the experimental measurements. Comparison of the loading curves, shows that the finite element model falls between the two test results but the model shows very little loss in stiffness at higher loads. This condition is as expected, because the proposed model does not simulate the fracture type behavior which controls the strength of the experimental specimen.

6.5.5 Summary. For the purposes of this study, an acceptable analytical model has been defined as one which is applicable to interaction type problems, produces reasonable predictions of ultimate strength except for axial tension loadings, and is economical. The finite element model is easily applicable to interaction type problems by simply altering the boundary conditions. Comparisons of the predictions of the proposed finite element model and experimental results indicate that the model overestimates the experimental ultimate strength because of the rather coarse meshes used, but the predictions are reasonable. The model also accurately simulates the strains along the chord. Finally, comparisons with the computation times required by Pan's model, indicate that the present model is very economical. Therefore, the proposed model will be accepted and used in this study.

6.6 The Effect of the Gap on Compression Strength of Joints with β=1.00.

The large difference between the ultimate strength and behavior of replicate Tests A21 and A22, and Tests 023 and 028 indicated that the distance between the saddle points, or the gap, influences the behavior of the joints. This effect is discussed in more detail in Chapter 4, and the gap is defined by Fig. 4.4. In short, it was hypothesized that the compression branch forces in a β=1.00 DT joint are resisted almost exclusively by membrane action in the area between the saddle points of the joint. Thus, the compressive strength of the joint could be estimated by treating the gap area as a column. To test this theory, the experimental loads resisted by the specimens were plotted against the SSRC inelastic column curve [Fig. 4.5]. In Fig. 4.5, the results fell close to the SSRC curve except for Test A22 which fell somewhat below the SSRC curve. The result of Test A22 was well within the scatter band typical of this type of failure. But, it would be advantageous to see if the gap effect is also predicted by an analytical model, which is not effected by experimental scatter

To model the geometry of the specimens A21 and A22, the size of the branch member was determined by the average gap of each specimen, thus the β ratio was somewhat less than 1.00 (0.97 for both specimen). The variation in the gaps was attained by

offsetting the branch. Since the symmetry of the axial loading was violated by the variation in gap sizes, a 1/4 joint mesh was used in both cases. Load was applied using displacement control at the centerline of the branch as shown in Fig. 6.24, thus allowing the branch to rotate freely in the out-of-plane direction. The loading point was also prevented from translation in the out-of-plane direction while the chord was free to move in out-of-plane direction. It was determined that this set of boundary conditions best simulated the actual test condition.

The axial load-deflection curves produced by the model and Test A21 are shown in Fig. 6.25a. Specimen A21 had gap dimensions of 3.63 and 3.56 in. The out-of-plane displacement produced by the finite element model is plotted in Fig. 6.25b to give a better indication of the movement of the joint. The finite element model yielded an ultimate strength of 173.0 kips compared to the experimental value of 172.7 kips, thus the model is very accurate for this loading case. The difference between the analytical and measured stiffnesses shown in Fig. 6.25a can be explained by the flexibility of the test setup which is included in the measured stiffness. Comparison of Figs. 6.25a and 6.25b shows that just as the joints reaches maximum load the joint buckles in the out-of-plane direction.

The axial load-deflection curves produced by the model and Test A22 are shown in Fig. 6.26a. Specimen A22 had gap dimensions

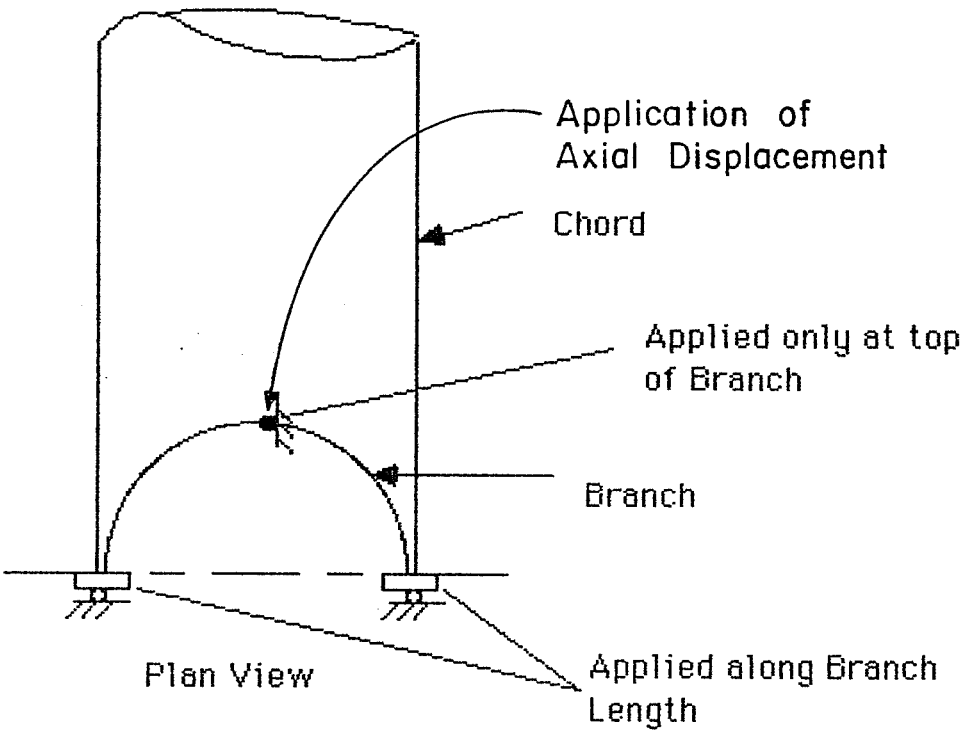

Fig. 6.24 Boundary Conditions for
Models of Tests A21 & A22

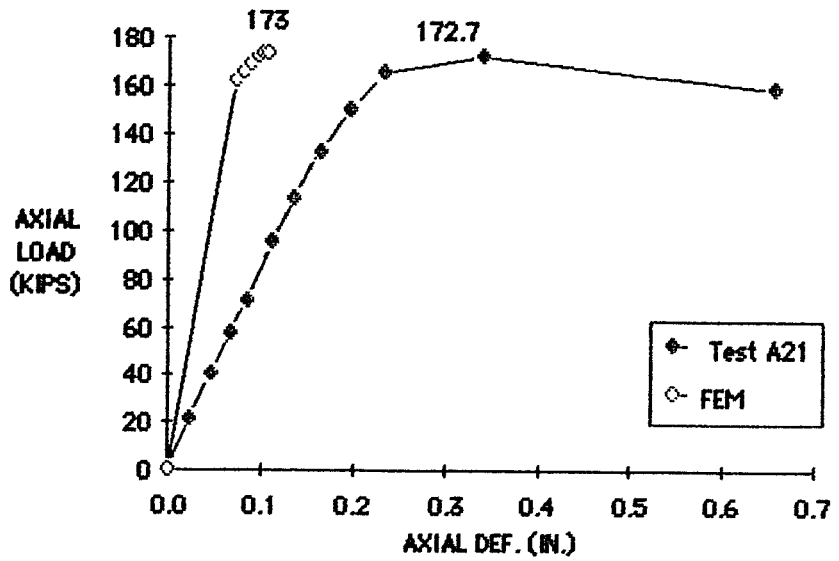

a.) Axial Load vs. Axial Deflection

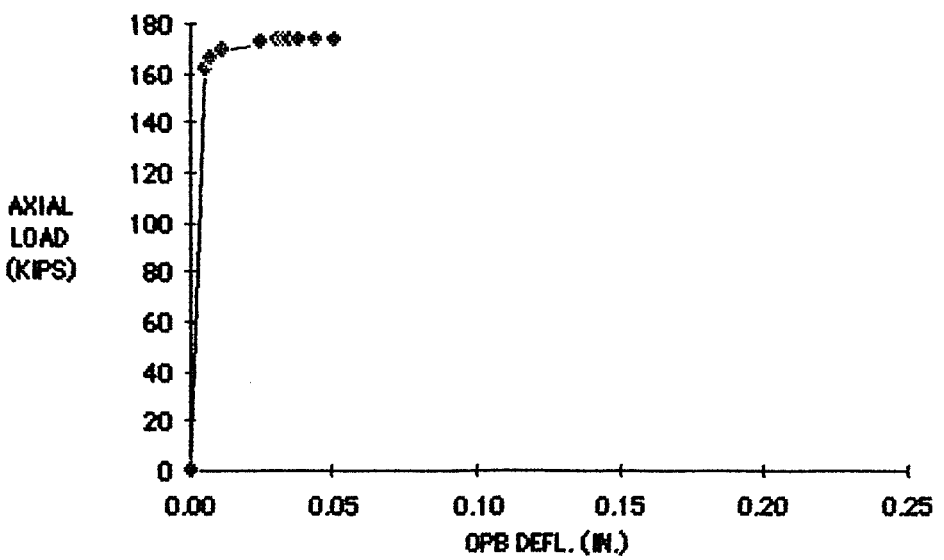

b.) Axial Load vs. OPB Deflection

Fig. 6.25 Predicted and Measured Load vs. Deflection Curves for Test A21

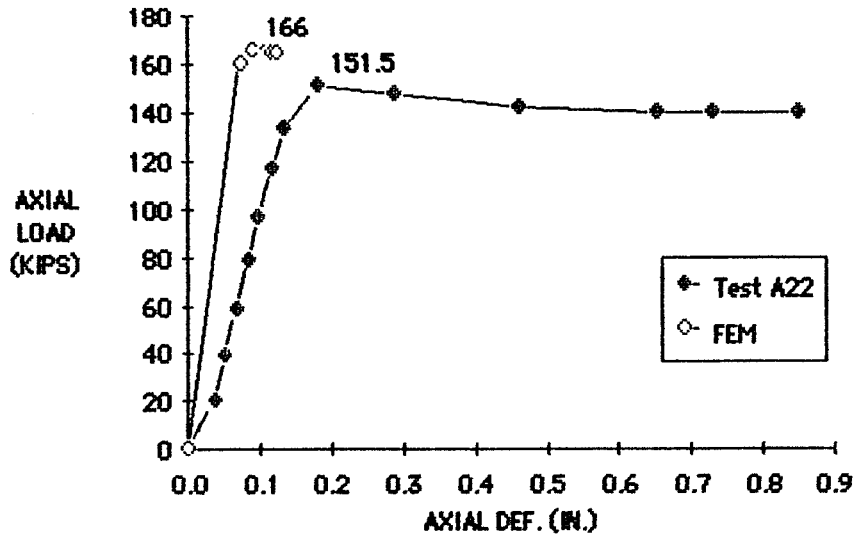

a.) Axial Load vs. Axial Deflection

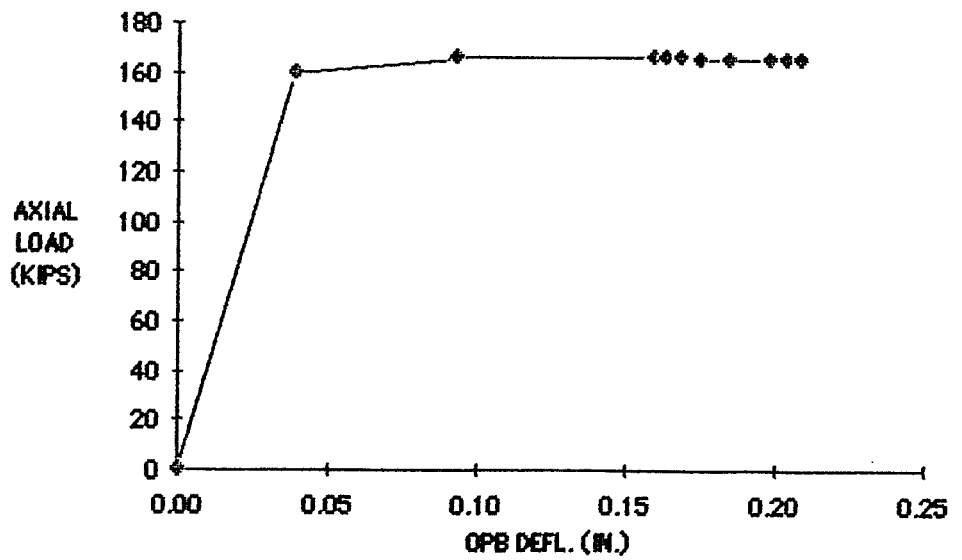

b.) Axial Load vs. OPB Deflection

Fig. 6.26 Predicted and Measured Load vs. Deflection Curves for Test A22

of 3.88 and 3.31 in. The out-of-plane displacement produced by the finite element model is plotted in Fig. 6.26b. The ultimate strengths of the analytical model and Test A22 are 165.8 and 151.5 kips respectively. As in Test A21 comparison of Figs 6.26a and b show that the joint begins to buckle out-of-plane as the joint reaches ultimate load. Again the analytical model exhibits much more stiffness than the experimental results show. Comparison of Figs. 6.25b and 6.26b indicates that the model of Test A22 shows much less stiffness in the out-of-plane direction than the model of Test A21 which is as expected because of the larger eccentricity in specimen A22.

As stated earlier, the difference in the analytical and experimental stiffnesses may be explained by the test frame flexibility included in the measured displacements. Because of the large stiffness of the β=1.00 joint, the stiffness of the specimen approaches the stiffness of the test frame, i.e K1=K2 in Eq. (6.4). The resulting total or measured stiffness should be approximately 1/2 of the actual joint stiffness. The measured stiffnesses of Tests A21 and A22 are 1108 and 1280 respectively which are about 1/2 of the analytical stiffnesses. A true measure of the joint stiffness is given by the elastic compression test performed as part of a strain concentration factor study [32] which was discussed earlier, the elastic stiffness given by this test is 2,500 kips/in. The finite element model produced a

stiffness of 2,220 kips/in. to a load of 162 kips and 2,192 kips/in. to a load of 160 kips for the models of Tests A21 and A22 respectively. Considering the fact that the analytical stiffnesses include an inelastic portion of the load-deflection curve, the analytical stiffnesses match the measured elastic stiffness rather well.

Figure 6.27 is a replication of Fig. 4.5 which plots the experimental load on a gap vs. its G/r along with the SSRC inelastic column curve. The difference is that Fig. 6.27 includes the maximum loads predicted by the analytical method. The experimental load represents the compression load at the branch saddle point and is defined as half of the axial load or the OPB moment divided by the branch diameter. The result of the analytical model of Test A21 falls on top of the experimental result while the result of the model of Test A22 falls much closer to the column curve than the experimental result. Thus, the analytical results support the theory that the gap can be analyzed as an inelastic buckling column. However, the fact that the result of Test A22 is lower than predicted shows that the scatter inherent in buckling failures must still be accounted for in any design.

The membrane forces along the chord centerline at maximum load are plotted against their position on the chord in Figs. 6.28 and 6.29 for the models of Tests A21 and A22 respectively in

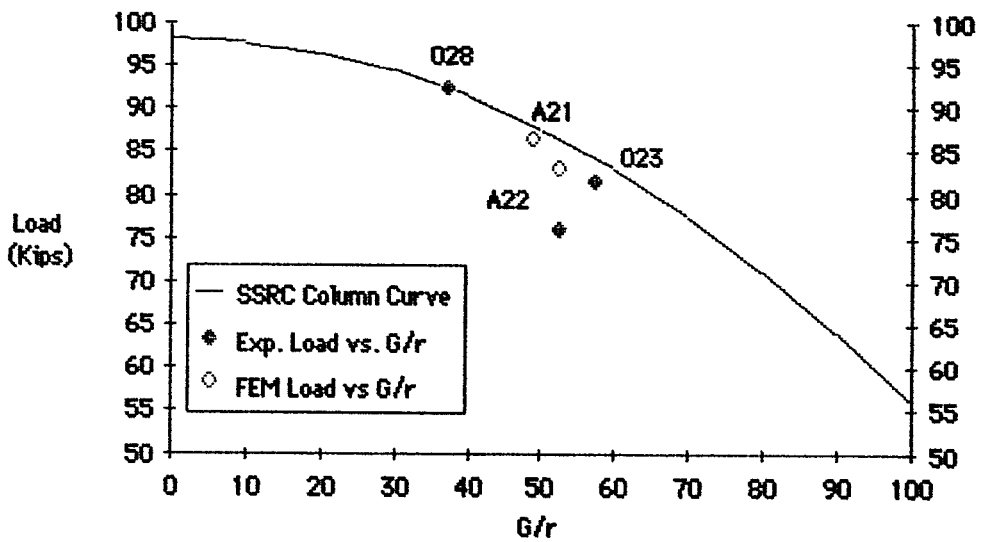

Fig. 6.27 Measured Gap Load vs. G/r

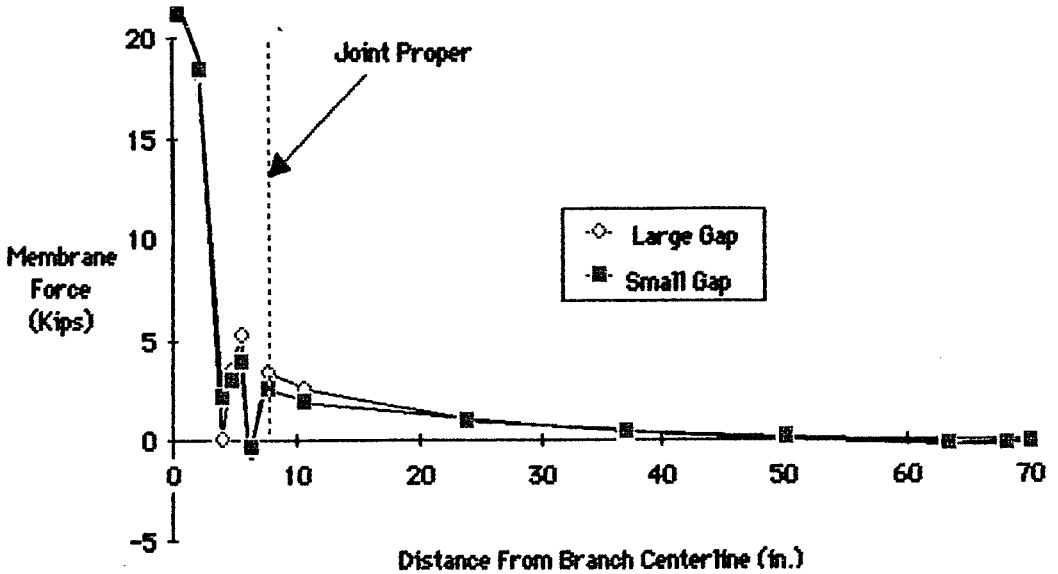

Fig. 6.28 Chord Centerline Membrane Forces from Analysis of Test A21

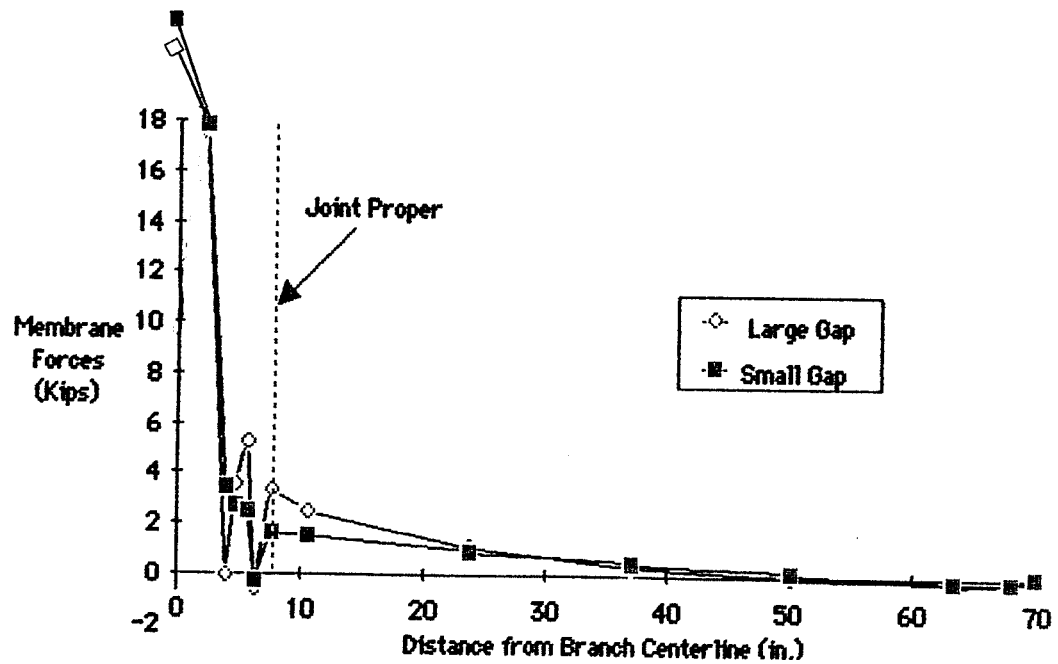

Fig. 6.29 Chord Centerline Membrane Forces from Analysis of Test A22

order to study how the size of the gaps influences the force distribution. These forces are the reactions at the boundary of the finite element model where the displacement of the nodes are restrained. The distribution of the membrane forces shown in the figures indicates that most of the axial load is resisted within the joint proper (area of joint within branch diameter). This distribution is corroborated by the tension tests performed by Sanders which showed that removing the chord outside of the joint proper had no effect on the tension strength of the joint [28]. Comparison of the load distributions of each run show very little difference between the distribution of the membrane forces in the two specimens. For Test A21, Fig. 6.28, in which the gap dimensions are fairly similar the distributions of reactions at either gap are almost identical. For Test A22, Fig. 6.29, in which there was a significant difference between the gaps, there is a small difference in the distribution of reactions on either side of the joint. The reactions on the large gap side of the joint are larger away from the center of the joint indicating that the immediate gap area is buckling and the load is being distributed to the adjacent chord.

As in Test A40, strain gages were placed along the outside surface of the chord for Test A22 to measure the circumferential strains. The layout of the gages is shown in Fig. 6.30. The experimental and calculated strains along the saddle centerline

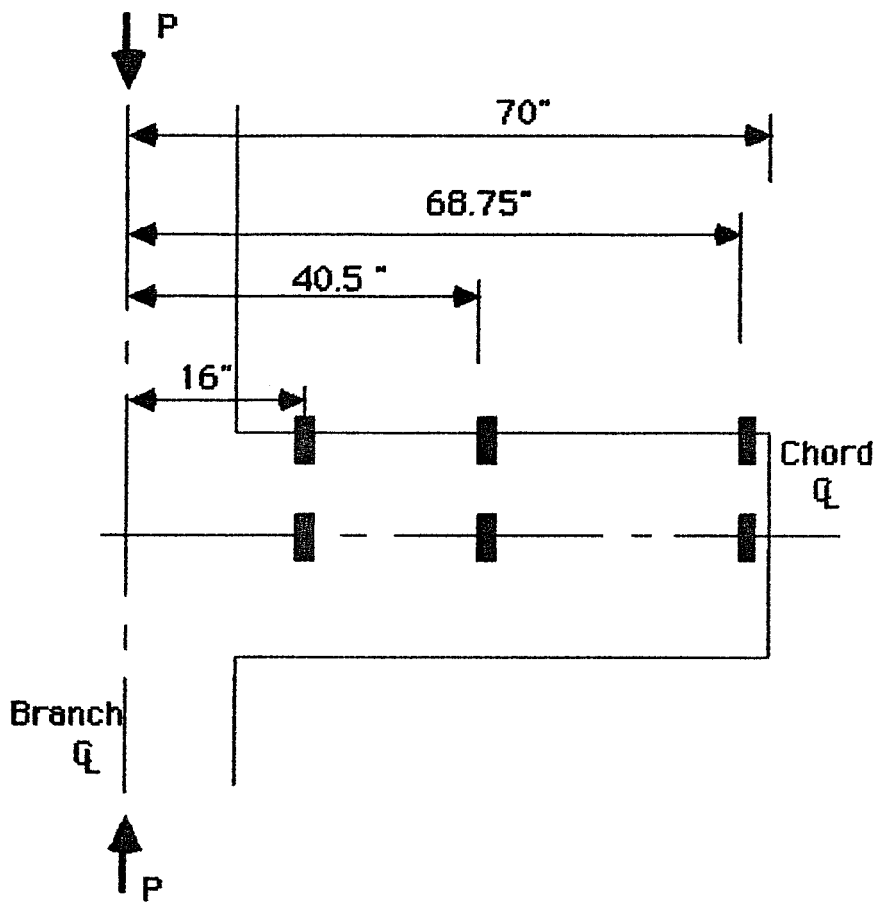

Fig.6.30 Postions of Strain Gages on Specimen A22

and the crown centerline of the chord at the maximum axial loads are plotted in Figs. 6.31 and 6.32. Comparison of the curves shows that, as with the β=0.35 compression case, the model does a very good job of predicting the strains along the chord. The magnitudes of the strains show that the chord outside of the joint proper remains elastic throughout the loading.

Based on the ability of the model to accurately simulate the joint behavior, the proposed model could be used to complete an extensive investigation into the gap effect beyond the scope of this study. Several aspects which might be studied are the effect of the difference between the gaps, a limiting gap dimension beyond which there is no significant effect, the effect of chord thickness, and a formulation for an effective width as shown in Fig. 6.33.

6.7 In-Plane Bending Strength

When the experimental IPB strengths were compared to these predicted by recommended API design equations, it was found that the design equations were overly conservative for the β=0.67 and 1.00 cases. Since the design equation does not predict the IPB case well, the analytical model is used to predict IPB strength. In addition, the analytical results will be compared to another empirical equation developed by Billington [6] and altered for DT

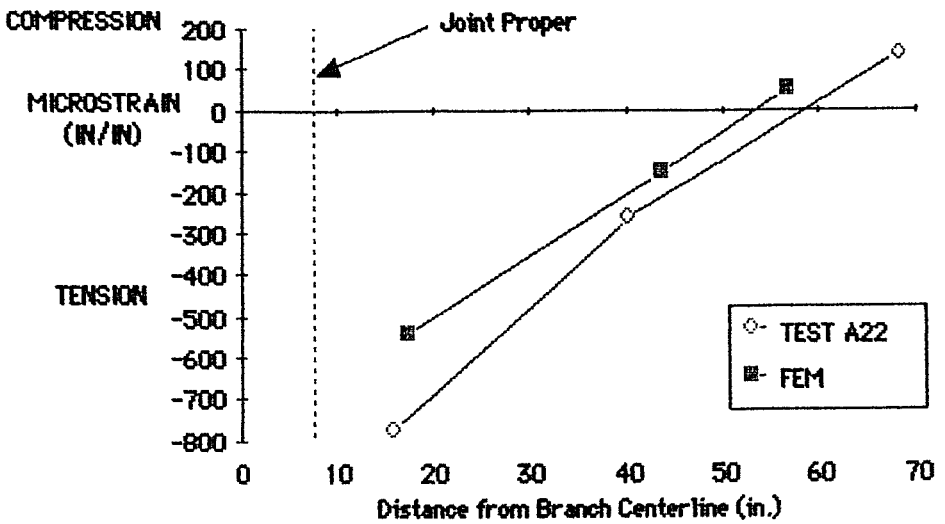

Fig. 6.31 Measured and Calculated Circumferential Strains at Chord Saddle Centerline of Specimen A22

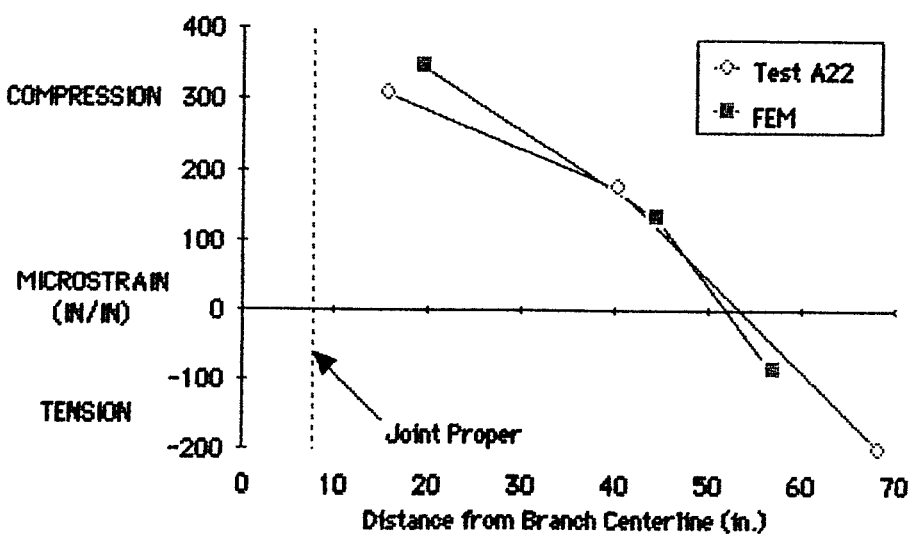

Fig. 6.32 Measured and Calculated Circumferential Strains at Chord Crown Centerline of Specimen A22

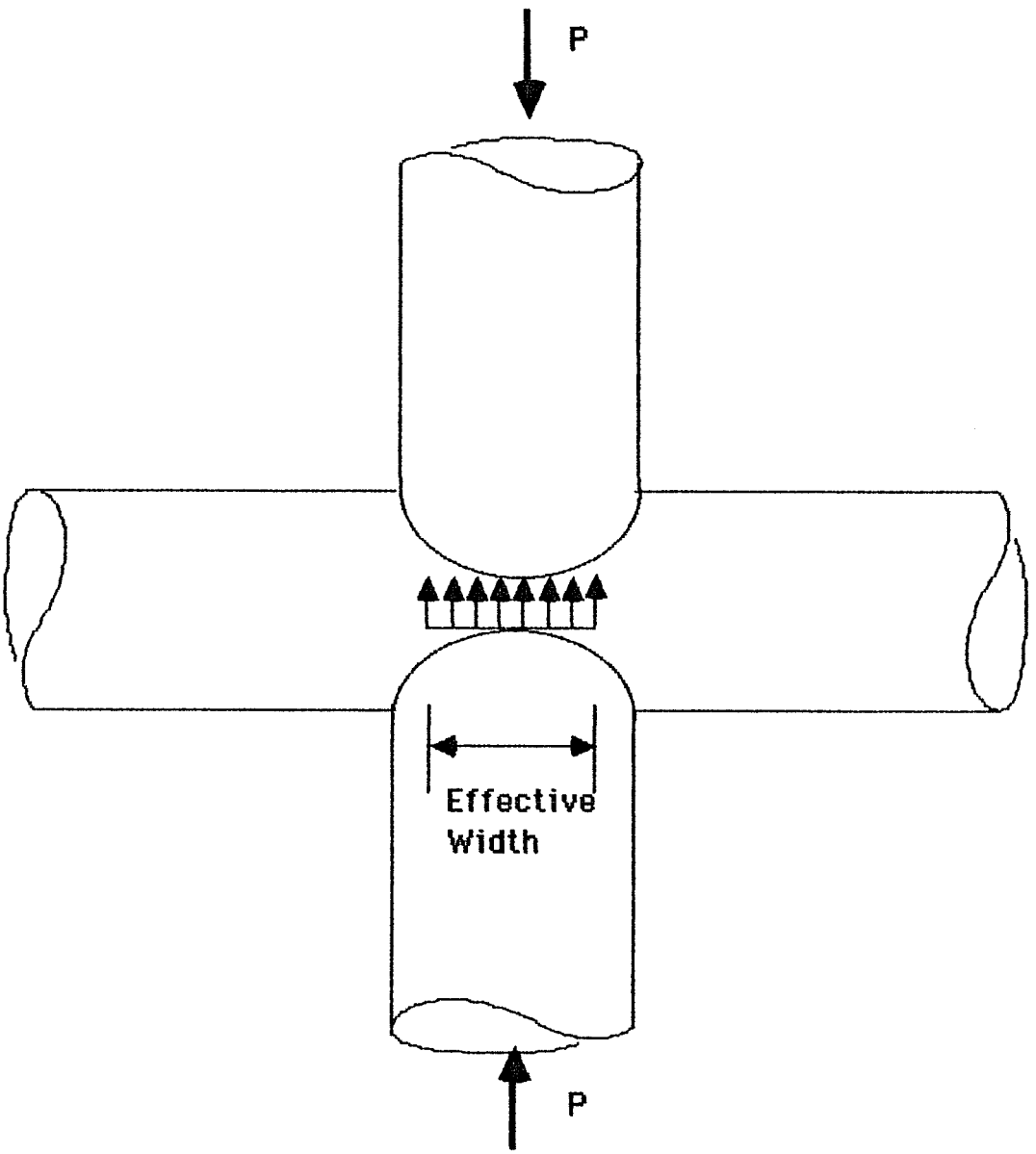

Fig. 6.33 Schematic of Effective Width

joints by Yura [39], and the effect of γ on the IPB strength will be briefly investigated.

In the IPB models, the full branch length (58") is modeled, and force is applied by displacement control. The displacements are applied at one end of the chord which has a thick flange, while the neutral axis at the end of the branch is restrained from in-plane translation. Because the experimental cases contained axial loads, an equal proportion of the axial load predicted by the analytical model was applied to the joint before it was loaded to failure in IPB. Load control was chosen to apply the axial load to allow free rotation of the branch end. The branch moment is calculated by multiplying the reaction at the restrained point on the branch by the branch length. The secondary moment is calculated by multiplying the axial force and the chord displacement. The total moment is the sum of the branch and secondary moments. After a comparison of the results of the β=0.35 IPB model with a tolerance limit of 1% and 5% of the total shear showed no significant difference [Fig. 6.34], the tolerance was set at 5% of the total shear.

6.7.1 β=0.35. The moment-rotation curves produced by the finite element model and Test I43 are presented in Fig. 6.35. The moment achieved at the maximum displacement input by the analytical model is 250 kip-in. Because the model had not reached a maximum moment at the maximum rotation, a maximum moment of 255

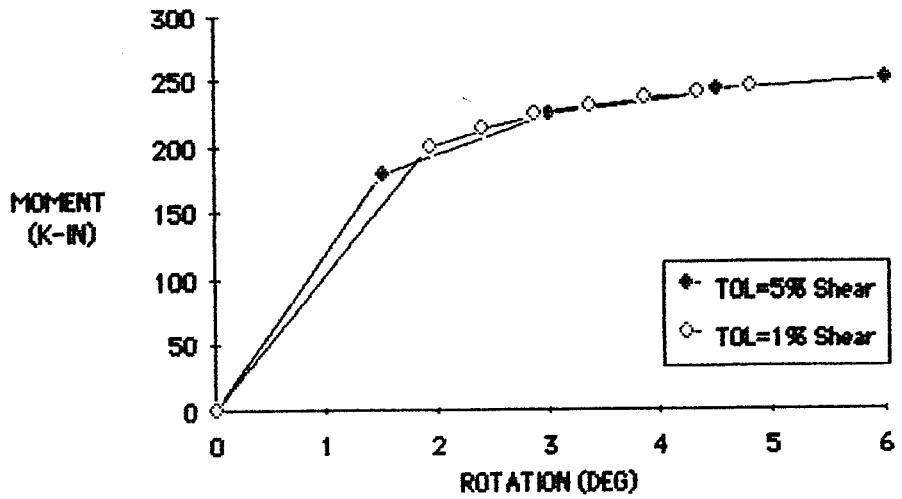

Fig. 6.34 Calculated IPB Moment vs. Rotation Curves for ß=0.35 Joint using 1% and 5% Tolerances

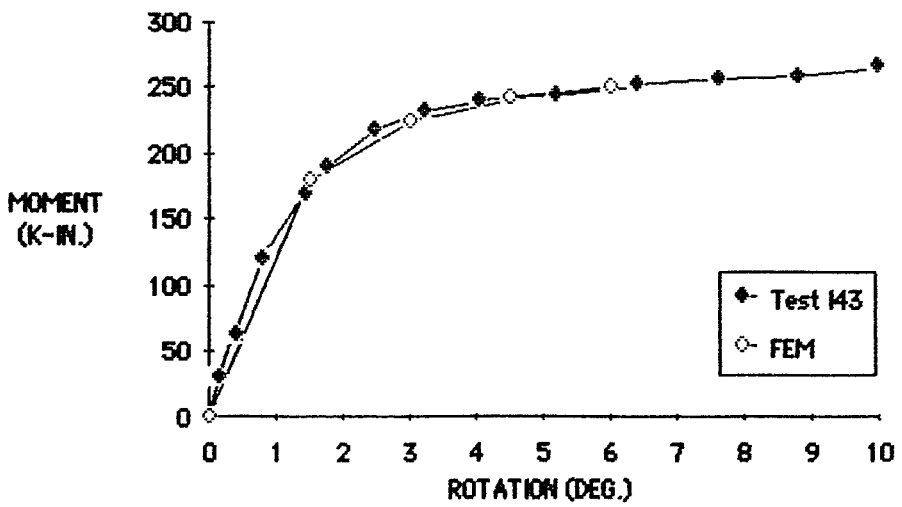

Fig. 6.35 Predicted and Measured IPB Moment vs. Rotation Curves for ß=0.35 Joint

kip-in. was extrapolated to the useful deformation limit from the analytical curve. The maximum moment reached in Test is 267 kip-in. at 9.97° rotation, the useful moment as defined by the deformation limit is 257 kip-in. Comparison of the two curves shows that the analytical model replicates the behavior of the experimental joint almost exactly.

Following-up on the analytical work on IPB by Hoadley, the radial displacements along the saddle and crown centerlines of the chord are presented in Figs. 6.37, and 6.38. The sign conventions for these radial displacements and a definition of the saddle and crown chord centerline are presented in Fig. 6.36. In Hoadley's analysis, the point on the chord where the is no change in diameter along the saddle centerline was taken as the neutral axis of bending [15]. However, Fig. 6.37 shows that the chord diameter increases at the branch centerline. Thus, Hoadley's assumption seems to be too simplistic. Fig. 6.38 shows the deflection of the chord centerline at the crown, and the curve illustrates the variation in the stiffness of the chord loaded in compression and tension which was discussed by Hoadley.

Strain gages were placed along the saddle centerlines of specimen I43 before testing as shown in Fig. 6.39. A comparison of the calculated and measured circumferential strains taken close to the 6° rotation limit of the finite element model is shown in Fig. 6.40. As in other cases, the finite element model

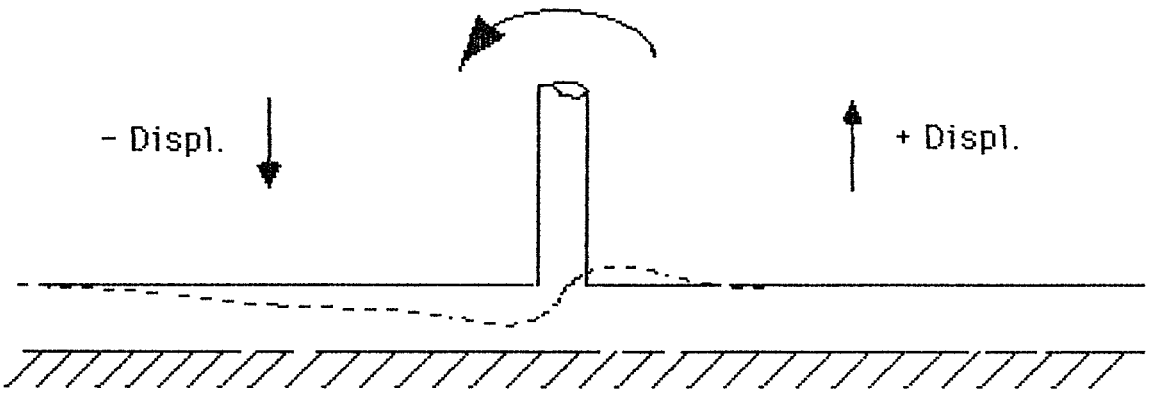

ELEVATION

a.) Vertical Displacements at the chord crown centerline

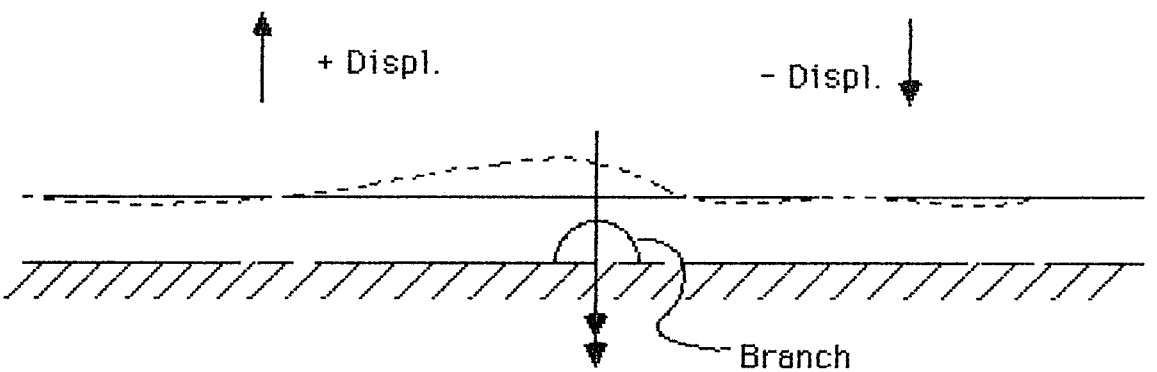

PLAN

b.) Horizontal Displacements at chord saddle centerline

Fig. 6.36 Discription of Radial Displacements

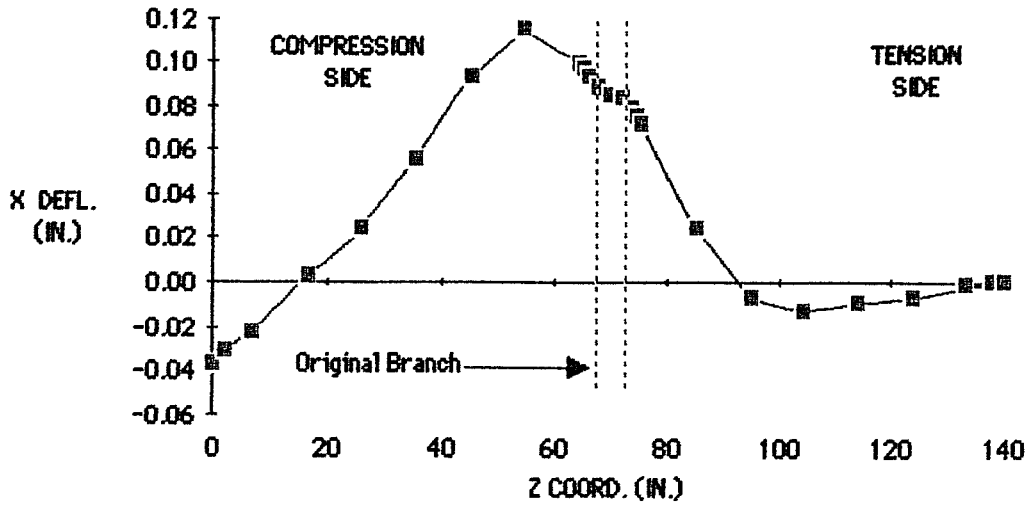

Fig. 6.37 Calculated Displacements of Chord Saddle Centerline for β=0.35 Joint with IPB

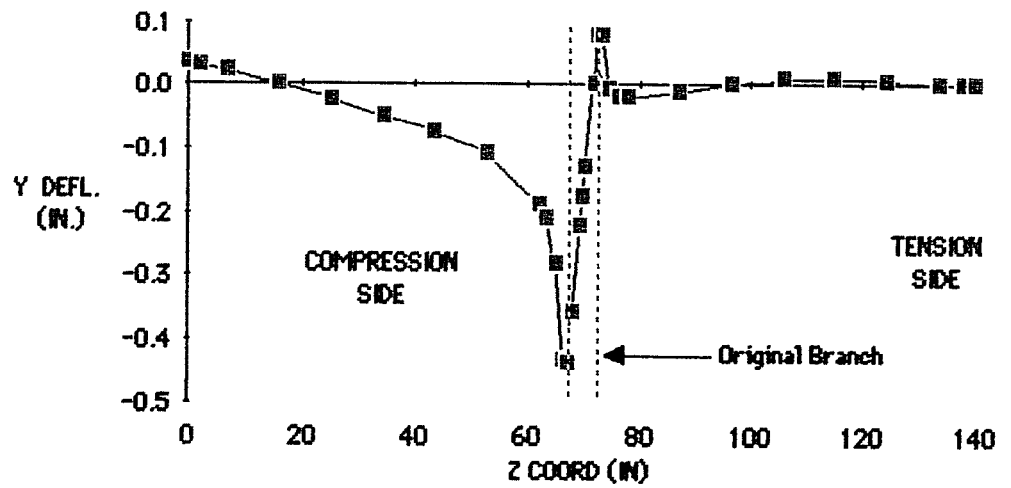

Fig. 6.38 Calculated Displacements of Chord Crown Centerline for β=0.35 Joint with IPB

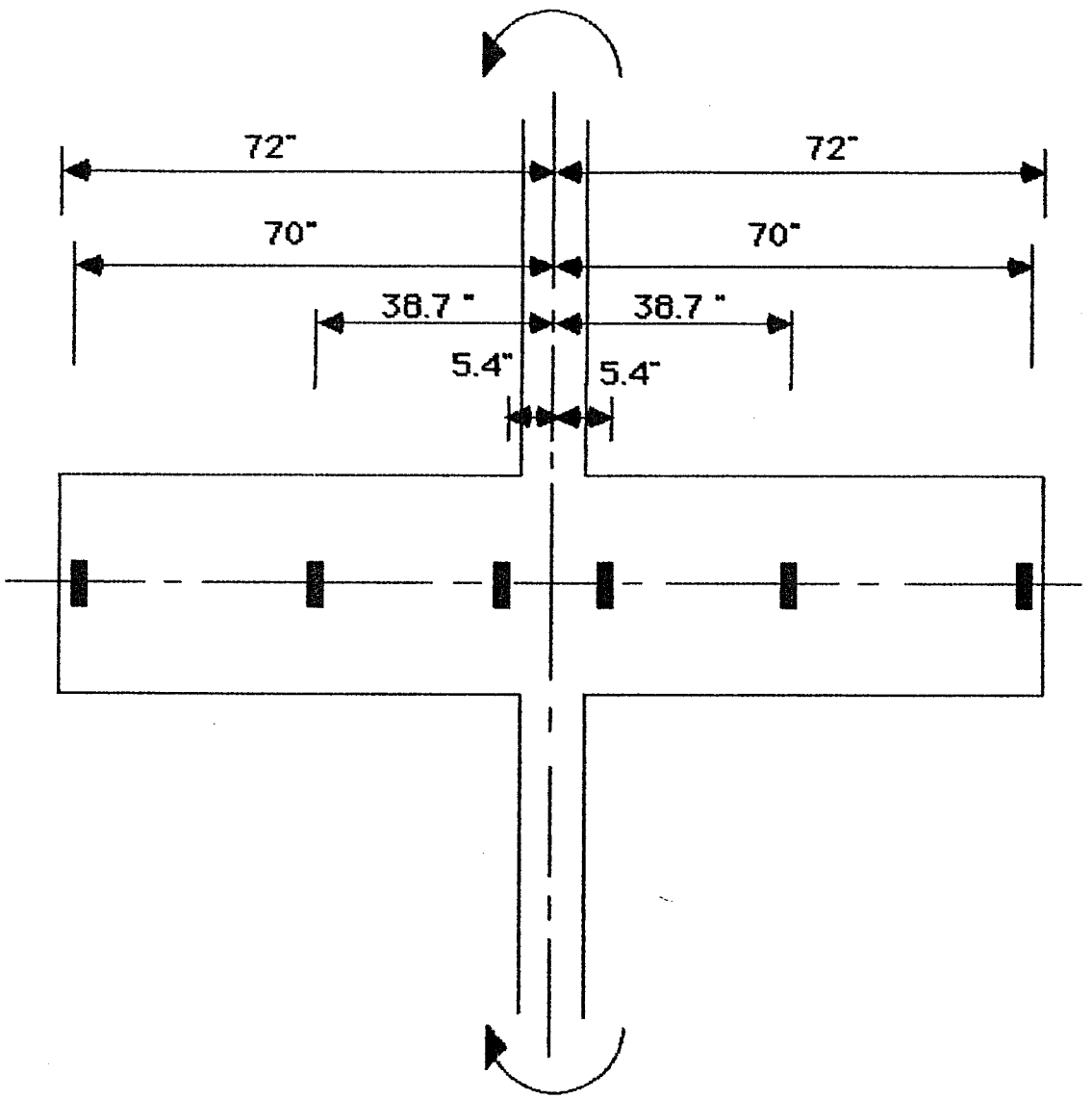

Fig.6.39 Postions of Strain Gages on Specimen 143

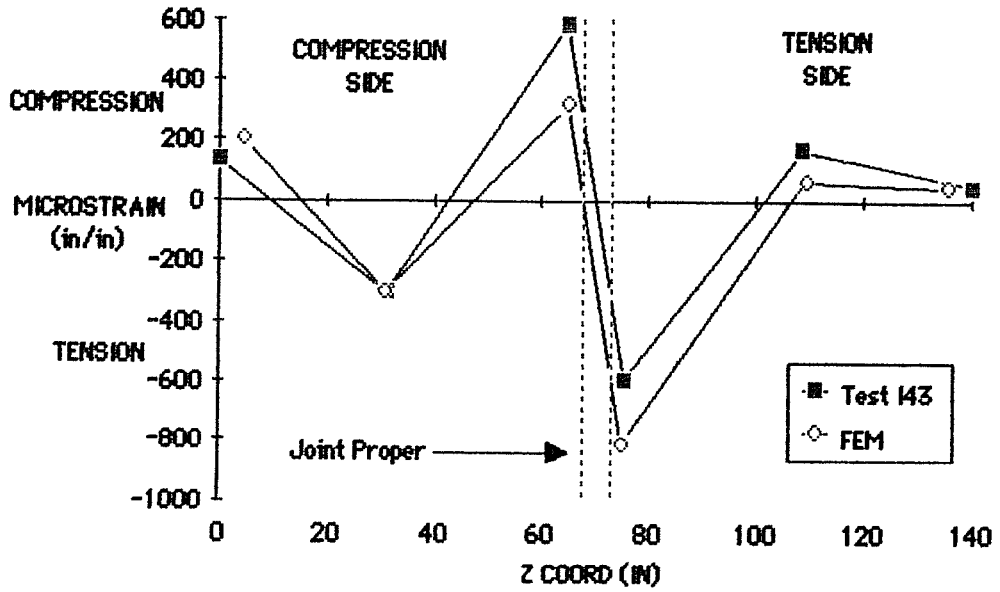

Fig. 6.40 Measured and Calculated Circumferential Strains at Chord Saddle Centerline of Specimen 143

matches the experimental strains very well. The measured strain for three levels of moment are shown in Fig. 6.41; calculated values are given in Fig. 6.42. The strains close to the joint increase rapidly with increasing moment while the strains in the majority of the chord remain mostly unchanged.

6.7.2 β=0.67. The moment-rotation curves produced by Test I7 and the finite element models are shown Fig. 6.43. The two finite element curves are produced by the "coarse" and "medium" meshes similar to those used to analyze the axial cases. From the figure it can be seen that the coarse mesh does not model the experimental behavior very well. This is due to the large elements near the branch-chord intersection in the "coarse" mesh which tend to reduce the softening effects of yielding by spreading the stress over a large area. The reduction in the size of these elements in the "medium" mesh eliminated this problem and does a much better job of simulating the actual joint behavior. The maximum rotation applied to the finite element model was 6°, but the moment-rotation curve was still increasing. However, the difference between the moments in the last 2 loading increments is only 8 kip-in. (0.75% of total moment), which indicates that any further increase in load would be negligible. Thus, the moment at 6° rotation, 1074 kip-in., will be taken as a

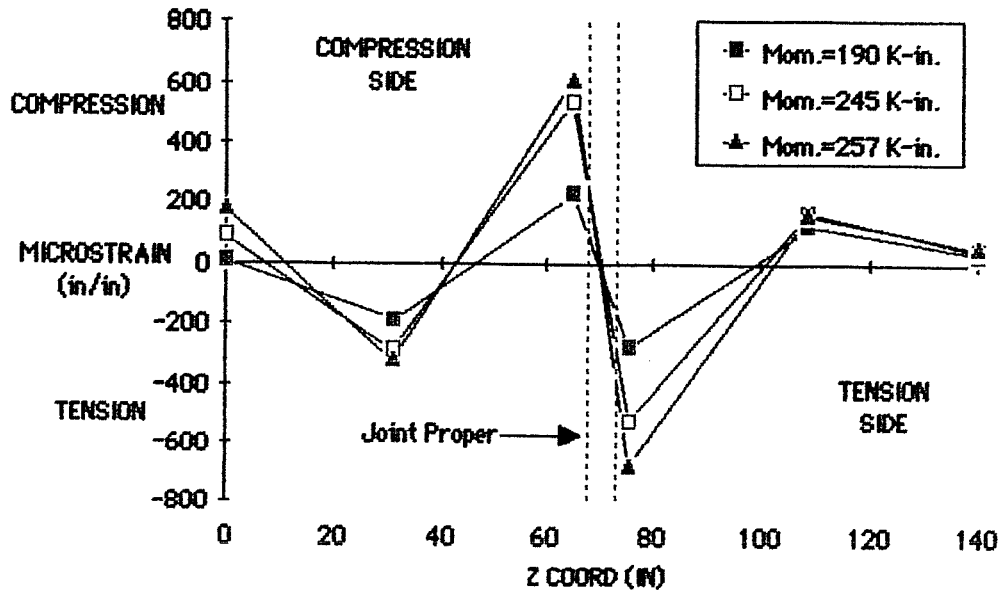

Fig. 6.41 Measured Circumferential Strains at Chord Saddle Centerline of Specimen 143

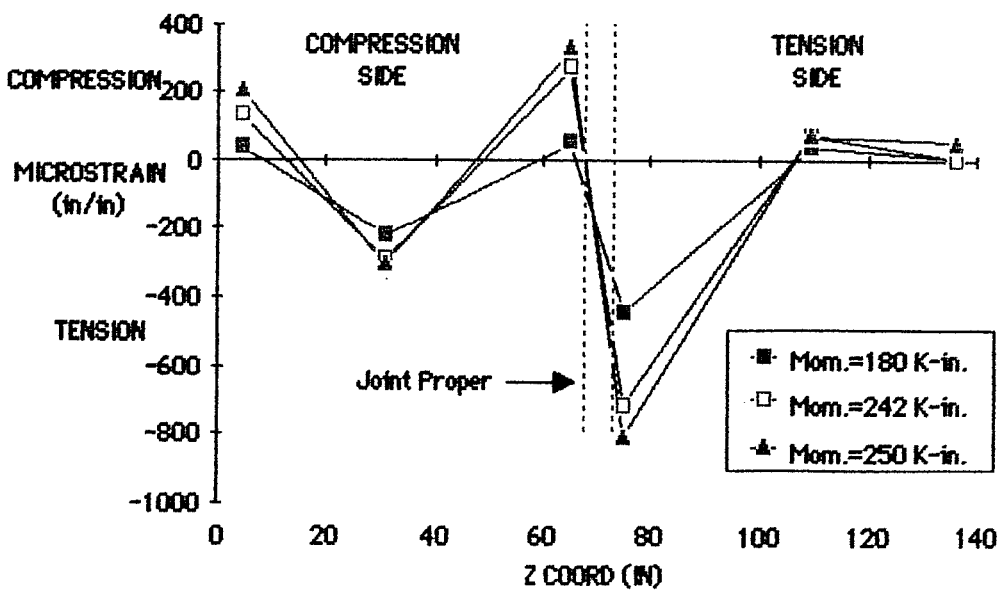

Fig. 6.42 Calculated Circumferential Strains at Chord Saddle Centerline of Specimen 143

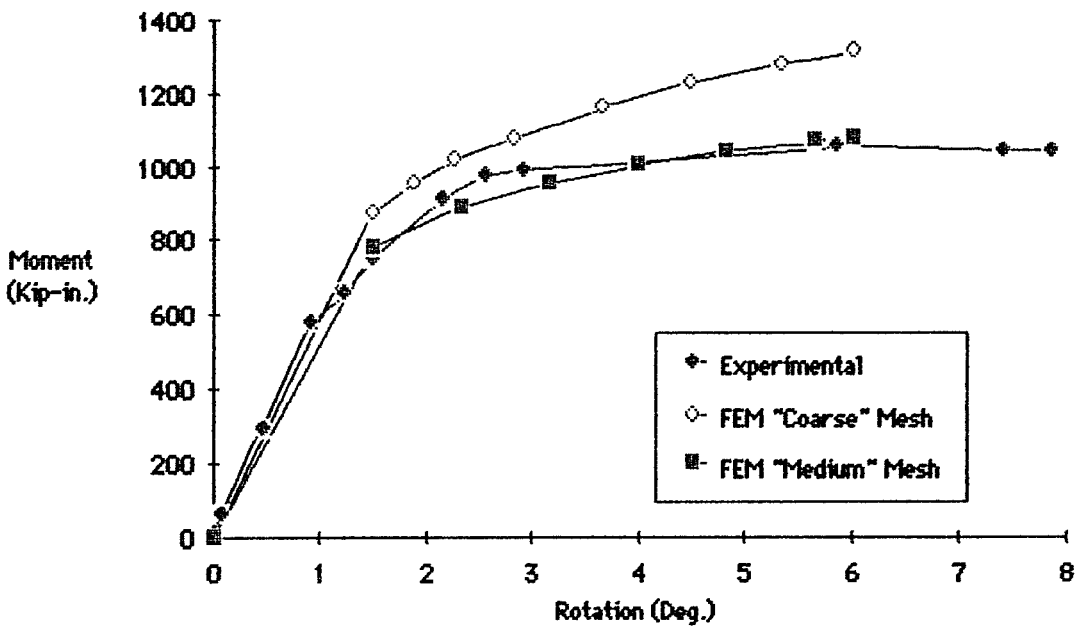

Fig. 6.43 Predicted and Measured IPB Moment vs. Rotation Curves for ß=0.67 Joint

maximum. The maximum moment reached by the model compares well with the experimental maximum of 1056 kip-in.

The radial displacements at the saddle and crown chord centerlines at the maximum moments are shown in Figs. 6.44 and 6.45. The radial displacements at the saddle centerline show the reverse curvature of the chord wall in the vicinity of the joint discussed by Hoadley. The shape of the curve agrees well with the results of Hoadley's simple model; however, the proposed model predicts almost twice the radial deformation. Comparison with the radial deformations calculated for the β=0.35 model [Fig. 6.37], shows that the deformations are much larger in the β=0.67 case and the shape is very different with a definitive change in curvature in the joint region. This indicates that the chord is more involved in the resistance of IPB for the β=0.67 case. The radial displacements along the crown centerline of the chord for β=0.67 are very similar to those shown by Hoadley, but again the magnitudes are larger. Comparison with the β=0.35 curve [Fig. 6.38] shows that the two curves have very similar shapes, with a relatively stiff tension crown and a relatively "soft" compression crown. The difference in the magnitudes of the displacements is a result of the increased movement of the branch tip required by the larger branch of the β=0.67 joint to achieve the same rotation.

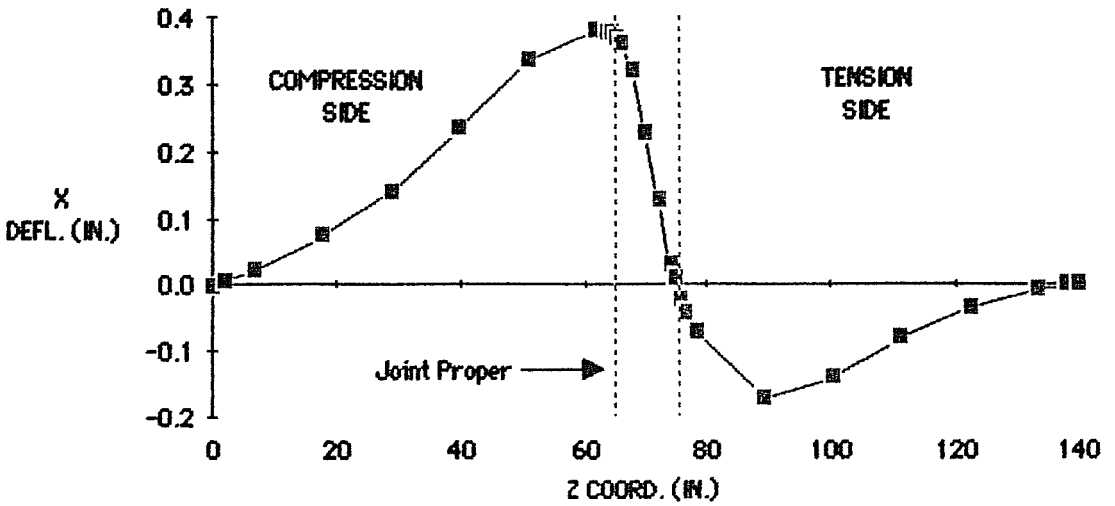

Fig. 6.44 Calculated Displacements of Chord Saddle Centerline for β=0.67 Joint with IPB

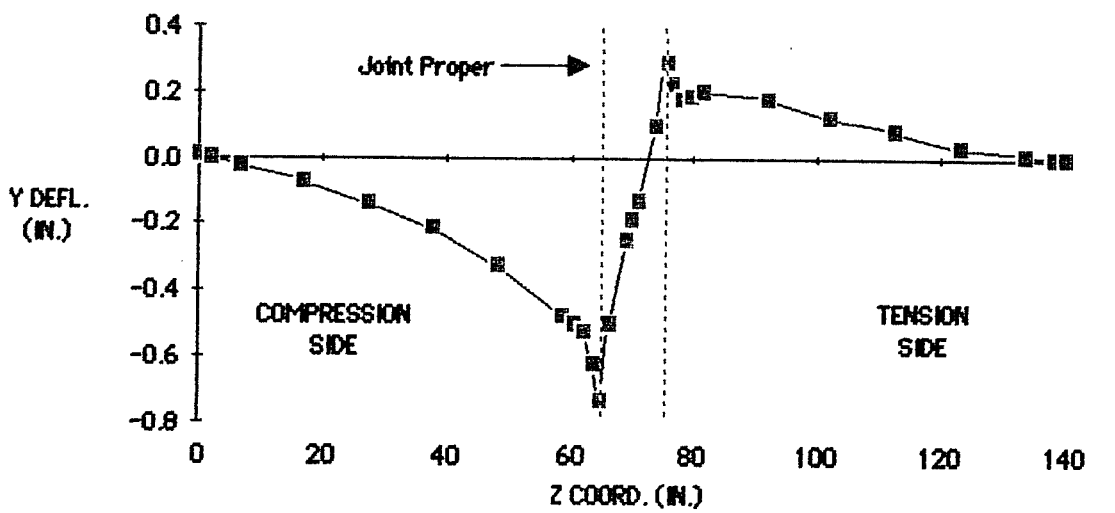

Fig. 6.45 Calculated Displacements of Chord Crown Centerline for β=0.67 Joint with IPB

6.7.3 β=1.00. The moment-rotation curves produced by the finite element model and Test I24 are shown in Fig. 6.46. To account for the gaps on either side of the joint, the actual β ratio used in the finite element mesh is 0.974. As with the β=0.67 loading curve, the β=1.00 analytical curve did not reach a maximum point before the end of the run. However, there was only a 1.4% increase moment in the last load increment. Therefore, it was determined that any further increase in strength would be negligible, and the last point could be used as a maximum. The maximum moment reached by the model, 2426 kip-in., is a reasonable prediction of the experimental maximum of 2267 kip-in. (7.0% high). Other than overestimating the measured stiffness which can be explained by the addition of the test frame flexibility into the displacement measurement, the model simulates the shape of the experimental loading curve very well.

The radial deflections produced by the finite element model at the saddle and crown chord centerlines at the maximum moment are presented in Figs. 6.47 and 6.48. Comparison of the radial deflections at the saddle centerline of the β=0.67 [Fig. 6.44] and the β=1.00 case shows that the displacements on the tension side of the joint in the β=1.00 case are almost 4 times that of the β=0.67 case. In addition the points of maximum deflection are within the joint proper which is not true of the β=0.67 case. This indicates a large change of curvature in the

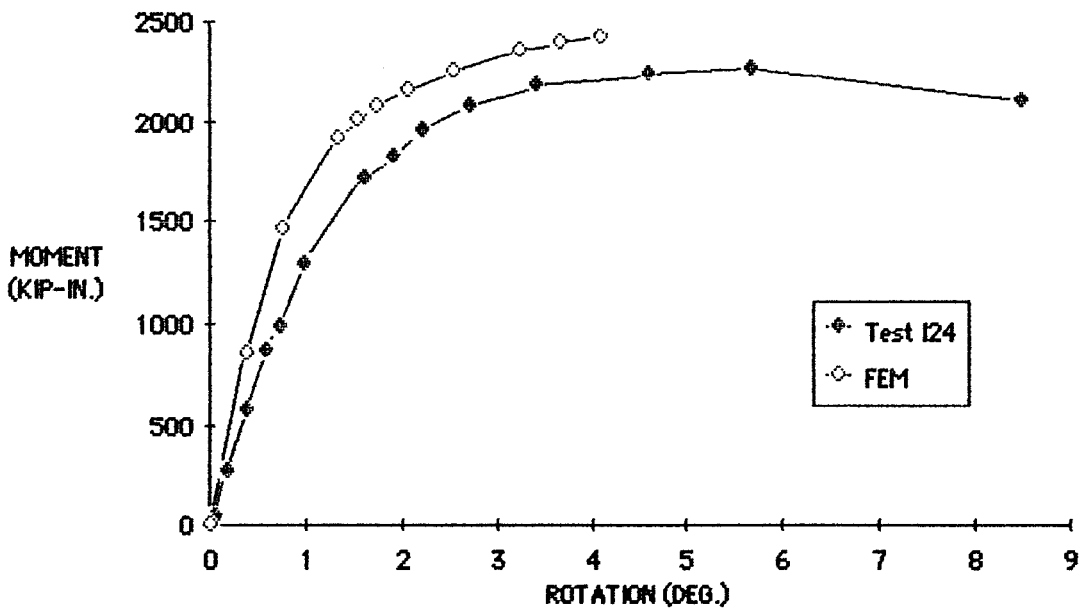

Fig. 6.46 Predicted and Measured IPB Moment vs. Rotation Curves for ß=1.00 Joint

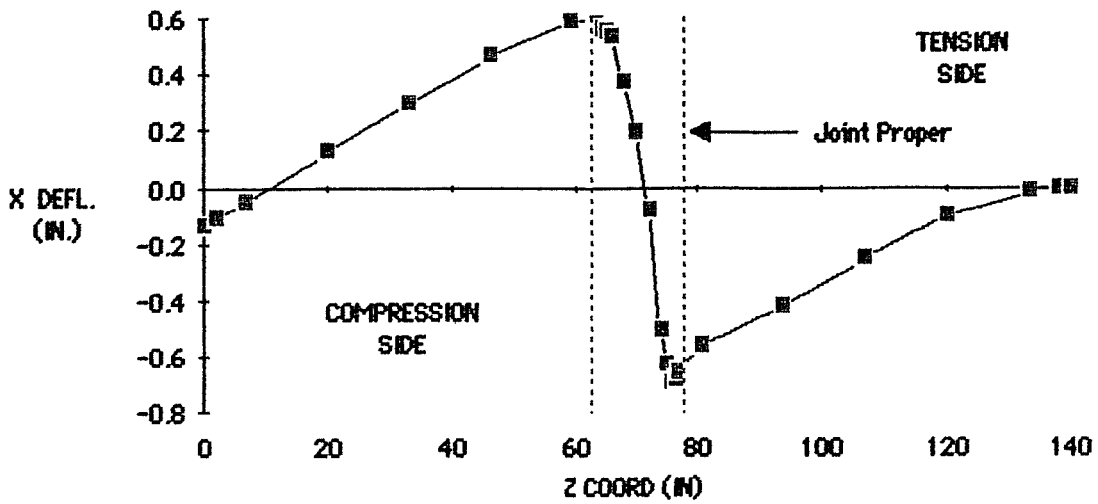

Fig. 6.47 Calculated Displacements of Chord Saddle Centerline for β=1.00 Joint with IPB

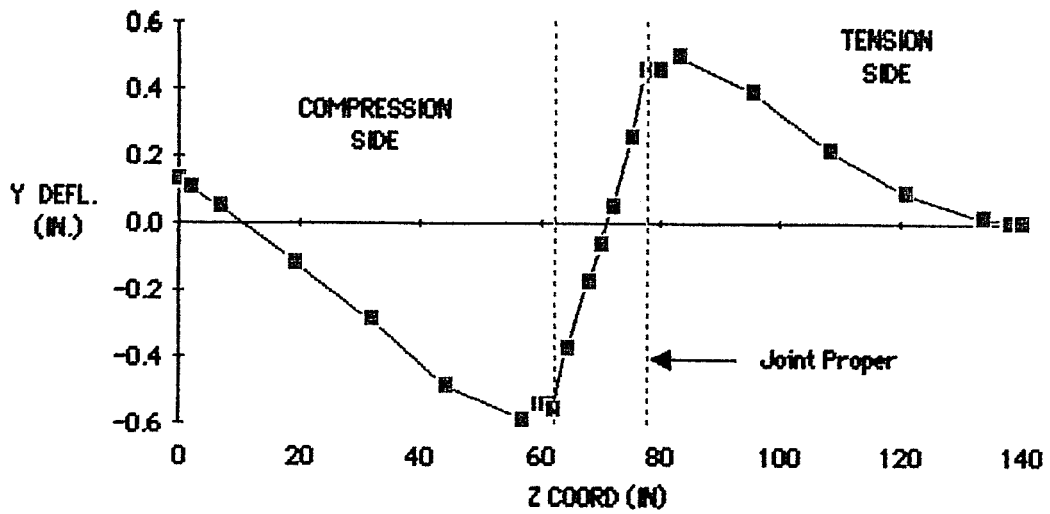

Fig. 6.48 Calculated Displacements of Chord Crown Centerline for β=1.00 Joint with IPB

chord wall and a large influence of stresses along the length of the chord. The radial displacements of the crown centerline of the chord, shown in Fig. 6.48, illustrates a slightly different behavior than the smaller β ratios. The deflections at the tension and compression crowns are of similar magnitudes, which indicates a smaller differential in the stiffness of the compression and tension sides of the joint than with smaller β ratios.

The increase in the stiffness of the compression crown relative to the tension crown may be a result of the increased curvature in the joint region at the saddle centerline. This increase in curvature increases the longitudinal tension stresses in the joint area, which postpones the buckling in the chord wall thus increasing the stiffness of the compression crown.

6.7.4 Prediction of IPB Strength. Comparison of the ultimate strength of Tests I7, I24, and I43 with the values predicted by the strength equations presented in 15th edition of the API Design Recommendations showed that the predicted values were conservative in all cases and very conservative for the Tests I7 and I24 (β=0.67 and 1.00 respectively). The ratios of test to predicted strength taken from Table 5.9 are 1.21, 1.63, and 1.66 for Tests I43, I7, and I24 (β=0.35, 0.67, and 1.00) respectively. Since this empirical formula is not an accurate predictor for the tests run in this research, the analytical

model was used to predict the IPB strength and the ratios of test to predicted strength values are 1.01, 0.98, and 0.93 for the Tests I43, I7, and I24 respectively. Though the predictions are slightly unconservative, they are sufficiently accurate. However, it is difficult to design using a finite element program. Therefore, a new empirical formula is needed to predict IPB strength in DT joints.

As stated earlier, the API recommended design formula was derived from T data but in the absence of any DT data was also applied to DT joints. In addition, the equation does not include the effect of the chord thickness ratio which should have an effect on the IPB strength. The IPB strength equation developed by Billington contains the γ effect but was not fit to DT data. With the IPB DT data recently produced, Yura expanded Billington's equation to DT joints as follows,

$$M_u = (F_y T^2/\sin\theta)6\beta\gamma^{0.5} \quad \{\text{mean eq.}\} \qquad (6.2)$$

Fig. 6.49 shows a plot of the experimental along with the analytical results produced in this study with Yura's proposed equation (6.2). Comparison of the experimental and the analytical data to Yura's equation shows that the equation fits the present data slightly better than the analytical model. However, as the database grows the distribution of points may change.

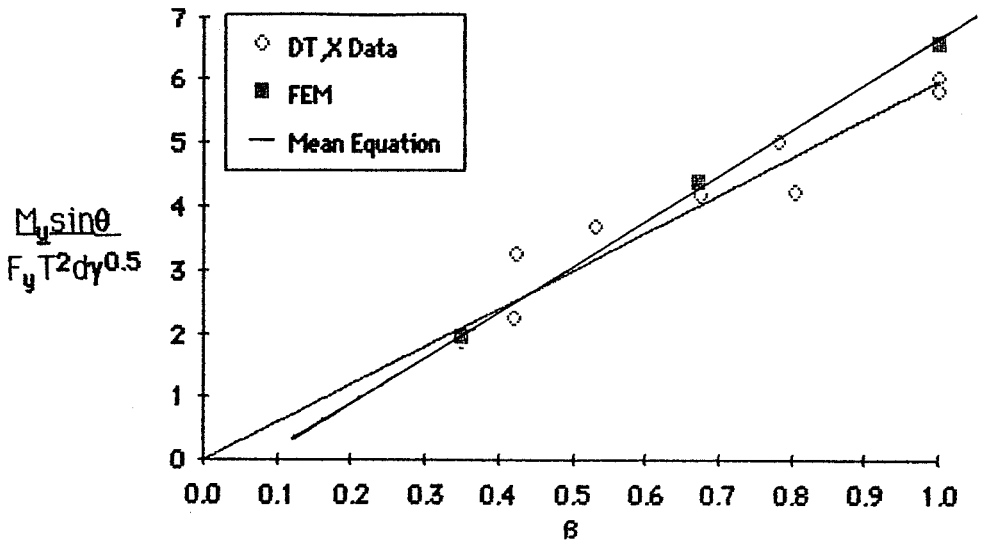

Fig. 6.49 Experimental and Calculated DT IPB Ultimate Strengths

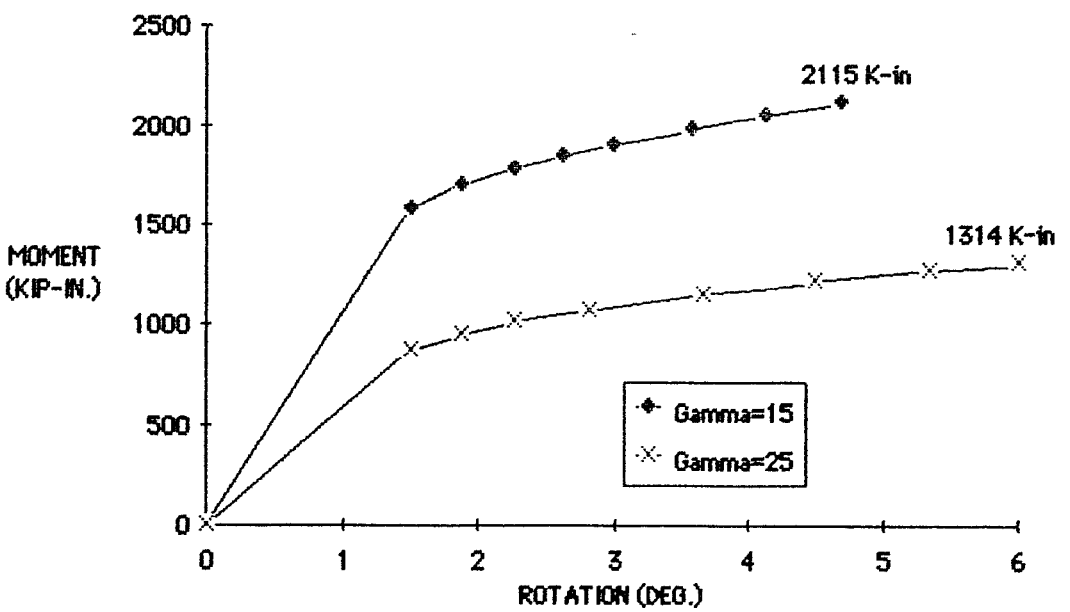

Fig. 6.50 Calculated IPB Moment vs. Rotation Curves for β=0.67 Joint with γ = 15 and 25

6.7.5 γ Effect on IPB Strength. The effect of the chord thickness ratio on the IPB strength was investigated using the finite element model by changing the thickness of the chord on the β = 0.35, 0.67 and 1.00 joint meshes. Failure of the joint section was insured by defining the branch material as elastic only. In the previously run cases the γ ratio was 25 with a chord thickness of approximately 0.32 in. The new cases possessed a chord thickness of 0.535 in. and γ ratio of approximately 15.

The purpose of this analysis was to determine the effect of the chord thickness on the IPB strength. First the results were plotted using the common nondimensionalization of F_yT^2d as shown in Fig. 6.50. This plot indicates a rather significant scatter in the data but more importantly it should be noted that the data point from the analyses on the joints with a γ ratio of 15 (higher thickness) fall below those from the analyses using a γ ratio of 25 (lower thickness). Thus, the use of the chord thickness squared in the IPB strength equation overestimates the effect of the chord thickness. Since the only variable changed in the analyses was the chord thickness, the ratio of the IPB strength. Ratioing the ultimate IPB strengths from the analyses showed that the IPB strength varied with T raised to the 1.5, 1.2, and 1.2 power for β = 0.35, 0.67, and 1.00 respectively. This explains the increase in reliability when the γ ratio is

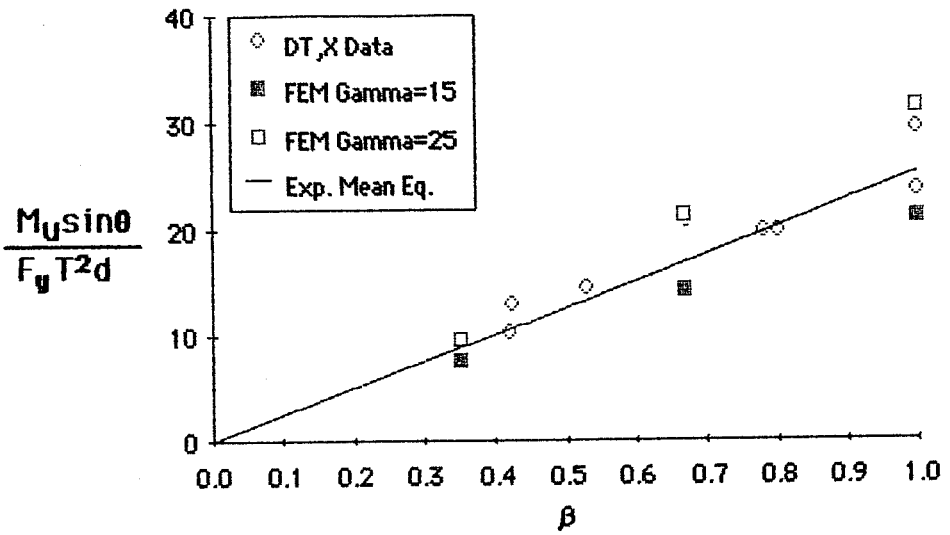

FIG. 6.50 IPB Strength Without γ

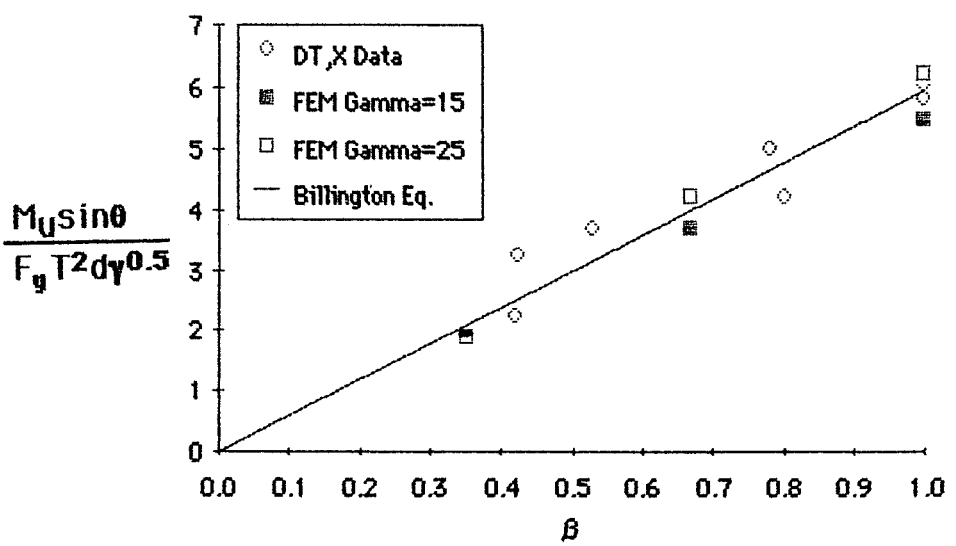

FIG. 6.51 IPB Strength With γ

included in the IPB strength equation, as shown in Fig. 6.51 which is the same as Fig. 6.49 with the three FEM results using a γ ratio of 15. The γ ratio is defined as (D/2T); therefore, the addition of the square root of this term to the strength equation effectively reduces the power of the chord thickness, T, from 2 to 1.5. As a result the strength equation is very accurate for β = 0.35 as shown in Fig. 6.51.

Comparison of the results of the analyses at the three different β ratios indicates that the effect of the chord thickness decreases as β increases. This can be explained by the increasing role of membrane action in the chord wall as β increases. Because plate action is mainly bending of the chord wall then the increase in strength will be a function of T^2; however, membrane action is mainly axial in nature, so the increase in strength will vary as a linear function of T. The use of $\gamma^{0.5}$ which effectively reduces the power of T to 1.5 seems to be a good approximation of actual behavior. In Fig. 6.51, the analyses points fall well within the experimental scatter and Billington's equation falls through the mean of the data so it is recommended for use in IPB strength design. The increase in accuracy that would result from varying the exponent of γ with will not warrant the increase in complexity of the equation.

6.8 Interaction Effects

One of the main purposes for developing an analytical model was to investigate interaction behavior. The model is applied to two cases here. The first is the branch axial compression and IPB interaction (AI) on a β=0.67 joint. In this case, three runs were completed to study the interaction behavior over a range of axial loads. As a part of this case, an additional run is made using a proportional type loading to determine whether the load path has an effect on the interaction behavior. The second case consists of one run on a β=0.35 model subjected to IPB and OPB loads. This run was set to simulate Test I048 which showed a significant increase in OPB strength when approximately 35% of the IPB ultimate strength was applied. As part of the second case, the simple OPB loading case was run to determine a reference OPB ultimate strength.

6.8.1 AI Interaction - β=0.67.

To reduce computation costs, the "coarse" mesh was used for all runs in this case. As in the experiment, the load was applied in two steps, first the axial load was applied and held constant, then the model was loaded to failure in IPB. The axial load was applied using load control so the deflections at the end of the branch would not be restricted. The magnitude of the axial reference load was taken from the result of the "coarse" mesh axial load run (92.3 kips).

The IPB load was applied by displacement control, with the displacements applied to the end of the chord.

6.8.1.1 Prediction of Interaction Strength. In addition to the axial compression and IPB reference cases which have already been documented, three additional runs were performed with constant axial loads set at 25%, 50% and 75% of the axial reference load. For future reference, the runs will be referred to as AI25, AI50, and AI75 respectively. The moment-rotation curves produced by these runs are presented along with the IPB reference curve in Fig. 6.52. The IPB reference run as well as run AI25 did not reach the ultimate capacity of the model. In the IPB reference case, the moment only increased 2.74% in the last 0.66° rotation. Because the tangent slope is relatively small at the last point, the moment at this point will be taken as a maximum. For the AI25 run, the curve did not reach the 6° rotation attained by the reference test; therefore, for comparison, the curve was extrapolated to 6° rotation to determine a maximum moment. The resulting moment is 1267 kip-in. The nondimensional strengths are shown in Table 6.4, and are plotted along with both the Texas DT and Delft T data in Fig. 6.53. The distances from the origin, L1, which is a measure of the interaction strength introduced in Chapter 5, is also included in Table 6.4. Comparison of the analytical and experimental data shows that the analytical data follows the

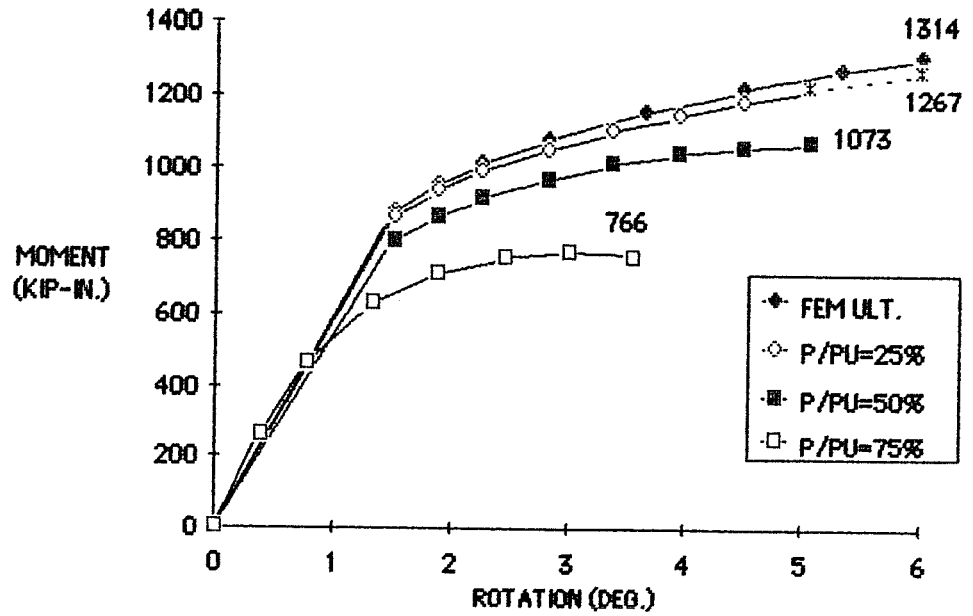

Fig. 6.52 Calculated IPB Moment vs. Rotation Curves for β=0.67 Al Analysis

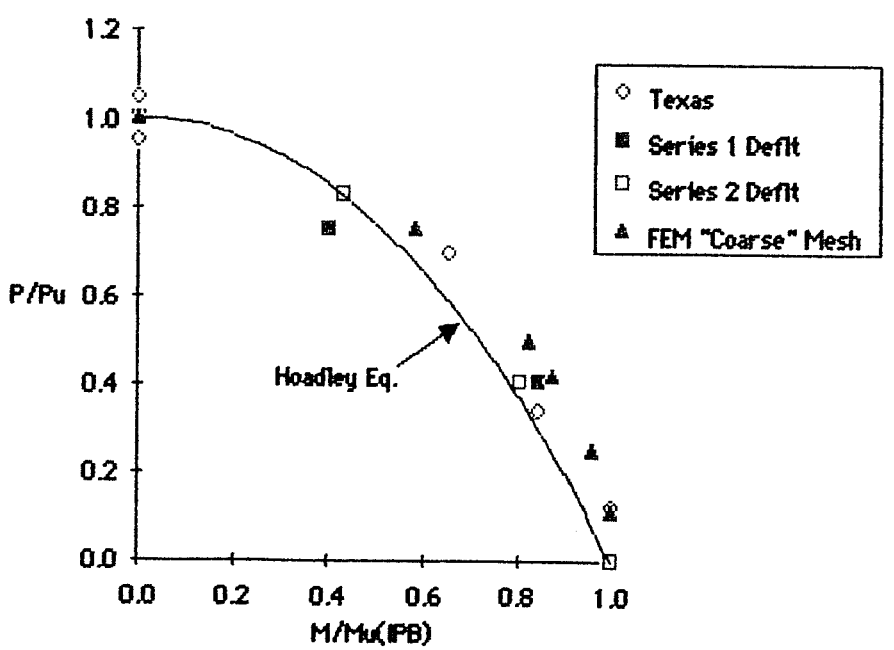

Fig. 6.53 Analytical and Experimental Al Interaction Data for β=0.67

Table 6.4 Nondimensionalized strengths of interaction tests

Run	P (kips)	M(IPB) (kip-in.)	P/P_u	M/M_u	L1
Axial	92.3	0.0	1.00	0.00	1.00
IPB	10.3	1314	0.11	1.00	1.01
A125	23.1	1267	0.25	0.96	1.00
A150	46.2	1073	0.50	0.82	0.96
A150 (Prop.)	38.9	1140	0.42	0.87	0.96
A175	69.3	766	0.75	0.58	0.95

shape of the experimental data. Thus, this analytical model can be used to produce interaction data with confidence.

6.8.1.2 Effect of Loading Path. Stol et al. concluded that tests on tee joints using proportional loadings produced lower ultimate strengths than corresponding tests using non-proportional loadings [30]. In addition, it was stated that tests using nonproportional loadings significantly overestimate ultimate strengths. This is a very serious conclusion considering that almost all of the interaction tests completed in this research used the nonproportional type loadings.

Comparison of the Delft T data (proportional loading) and the Texas DT (nonproportional loading) data in Chapter 4 showed no significant differences. However, it could be argued that this is a result of a combination of joint geometry and loading differences. Hoadley, investigated the influence of the load path by running a three dimensional interaction test using both proportional (AI019) and nonproportional (AI018) loading techniques. The results of the two tests are shown in Fig. 6.54. The distances from the origin, L1, which is a measure of the interaction strength introduced in Chapter 5, are 0.86 and 0.82 for Tests AI018 and AI019 respectively. Hoadley concluded that the similarity of the two L1 values shows that the loading path has no significant influence on the interaction ultimate strength.

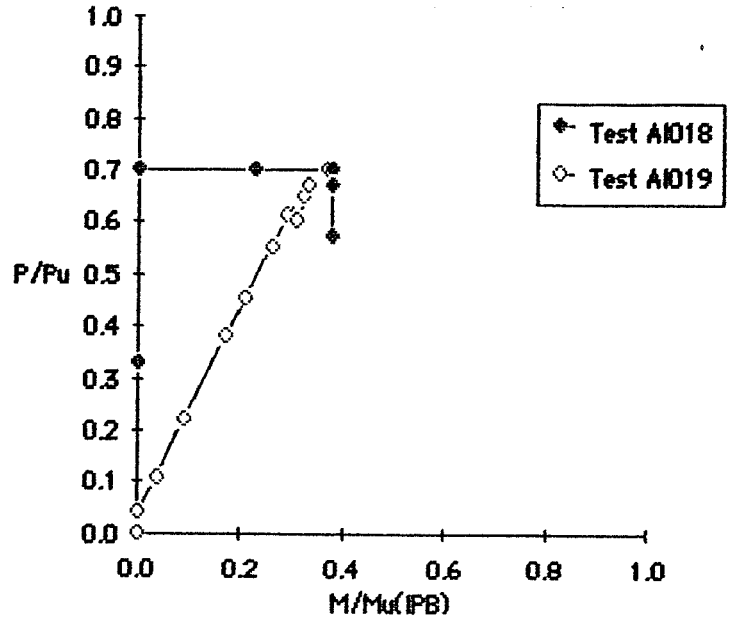

a.) AI Load Path

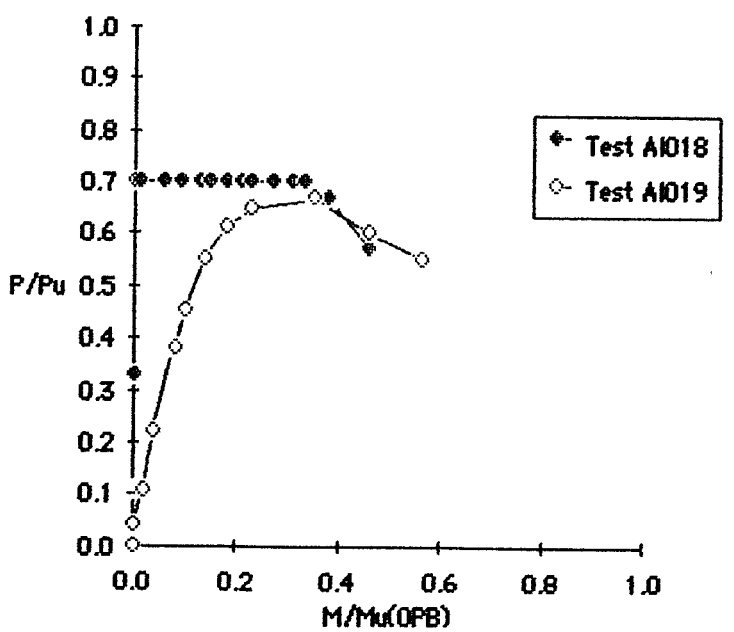

b.) AO Load Path

Fig. 6.54 Load Paths for Tests AI018 and AI019 from Ref. 15

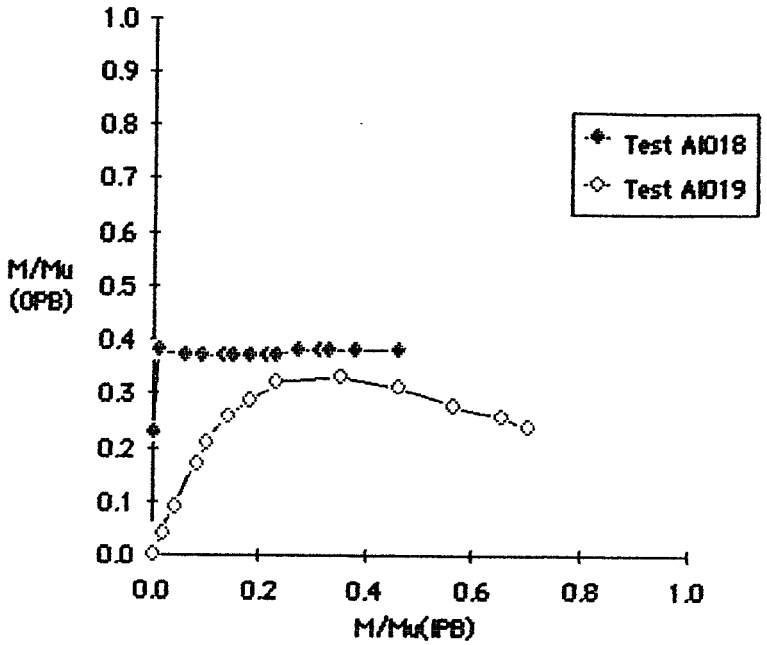

c.) IO Load Path

Fig. 6.54 Load Paths for Tests AI018 and AI019 from Ref.15

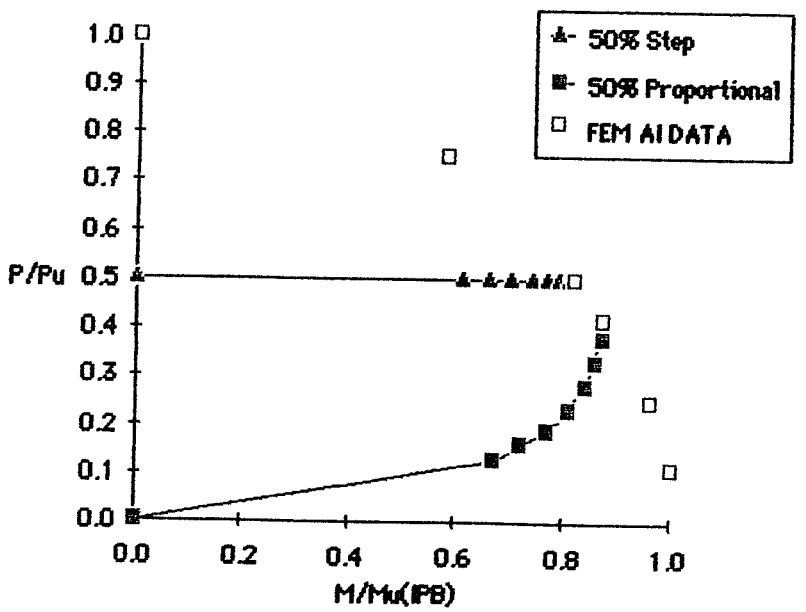

Fig. 6.55 Load Paths from Analysis of Run AI50 using Proportional and Non-proportional Loadings

To check Hoadley's conclusion using an analytical model which eliminates any questions of experimental scatter, the AI50 run was repeated using a proportional type loading. In this run, the load was applied in one step with axial load and IPB moment applied simultaneously instead of in two steps as done previously. As with all other runs, the actual loading increments were automatically chosen by the program. The load paths of the two runs are presented in Fig. 6.55. From the curves shown in Fig. 6.55, it can be seen that the proportional loading was not exactly proportional, as it did not follow a 45° line on the interaction diagram. This is a result of the use of a combination of load and displacement control. However, the loading path does represent quite a different load path to failure than the step wise path; therefore, it is acceptable for the stated purpose. In addition, the use of a combination of load and displacement control resulted in the IPB loading direction reaching ultimate before the axial direction, thus the nondimensional strength values are not identical. But, the proximity of the points to each other and the fact that the distance from the origin to the maximum points, L1, for both points is the same, as shown in Table 6.4, supports Hoadley's conclusion that the load path has no effect on the interaction ultimate strength

6.8.2 IO Interaction - β=0.35.

6.8.2.1 OPB Reference. Before the IO interaction problem could be addressed, an analytical reference value for OPB had to be obtained. This case was set up to simulate the results of Test 042, so the load was applied in two steps. First a small amount of axial load was applied using load control, then the joint was loaded to failure in OPB using displacement control. Applying the OPB displacements was more complicated than the IPB displacements. Since only one end of the chord was modeled, the displacements applied to the other end of the chord had to be transferred to the joint area. The displacements around the chord in the joint area could not be specified because local deformations would effect these values. Therefore, it was assumed that the chord stiffness was large enough to preclude any bending of the chord and the centerline of the chord at the crown would remain straight. Based on this assumption, equal displacements were applied along the end of the chord and at the crown centerline of the chord at the line of symmetry, as shown in Fig. 6.56.

The moment-rotation curves produced by Test 042 and the finite element model are shown in Fig. 6.57. Comparison of the two curves indicates that the finite element model simulates the experimental behavior very well. In this case, the useful deflection limit was reached by the finite element model at a

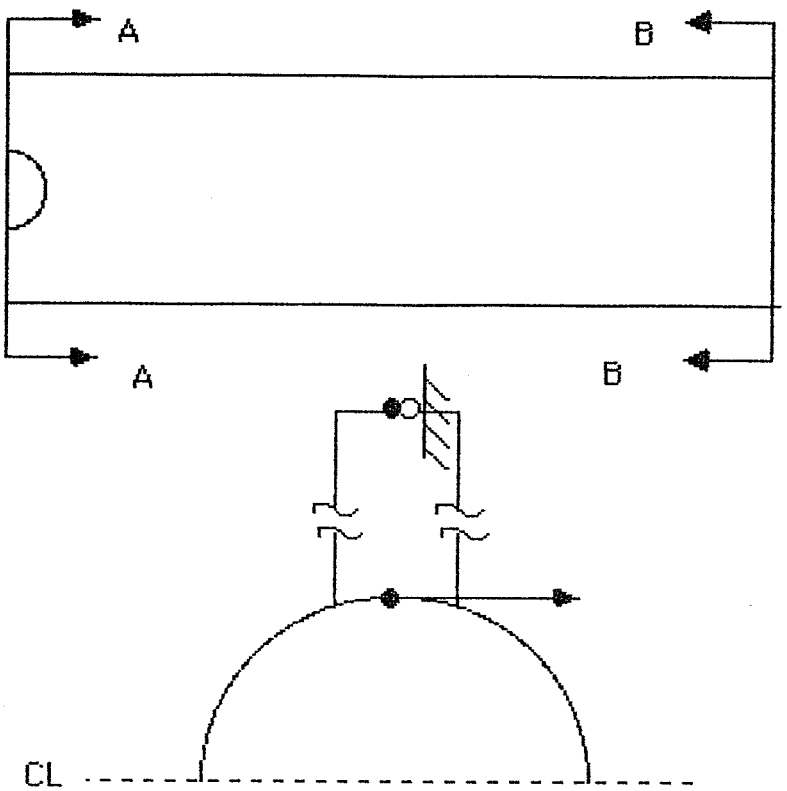

SECTION A-A

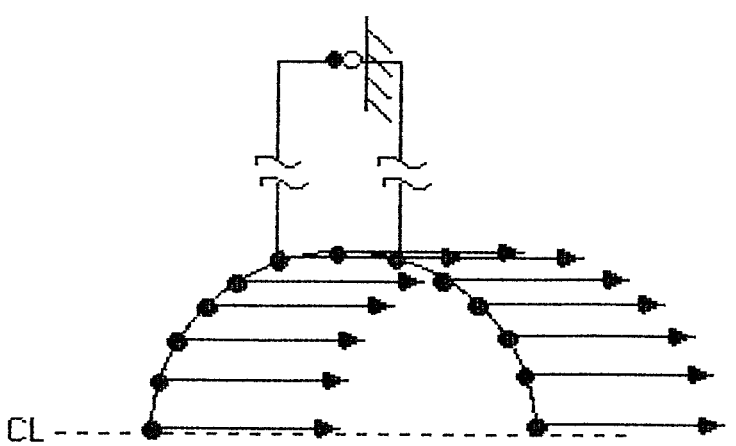

SECTION B-B

FIG.6.56 Applied displacements for OPB Load

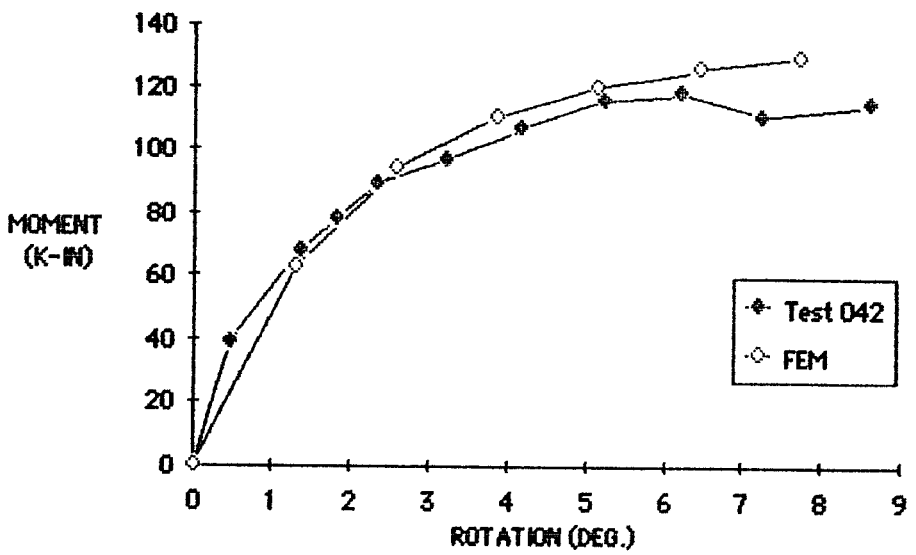

Fig. 6.57 Predicted and Measured OPB Moment vs. Rotation Curves for ß=0.35 Joint

moment of 130 kip-in. This value compares with a maximum experimental value of 118 kip-in.

As with the other β=0.35 tests, strain gages were placed along the outside surface of the chord to measure the circumferential strain at different positions along the chord as shown in Fig. 6.58. A comparison of the strains predicted by the analytical model and measured during Test 042 at the tension and compression saddle chord centerline at the maximum moment point are shown in Fig. 6.59 and 6.60 respectively. These figures show that the finite element model simulates the strains well except near the end of the chord. This discrepancy at the end of the chord is probably due to the presence of a collar used to apply the OPB load in Test 042 which was not included in the finite element model. In addition, the progression of the strains with increasing load both measured and calculated at the tension and compression saddle chord centerlines are shown for comparison in Figs. 6.61 and 6.62.

6.8.2.2 IO Interaction. Because of the lack of symmetry in the IO interaction loading a full 1/2 joint model was required. Due to the size of the model, only one case was run. The case chosen was a replicate of Test I048 which indicated a 20% increase in OPB strength with approximately 34% of the ultimate IPB moment applied. In order to allow for free displacement of the chord, four additional stiff flange elements

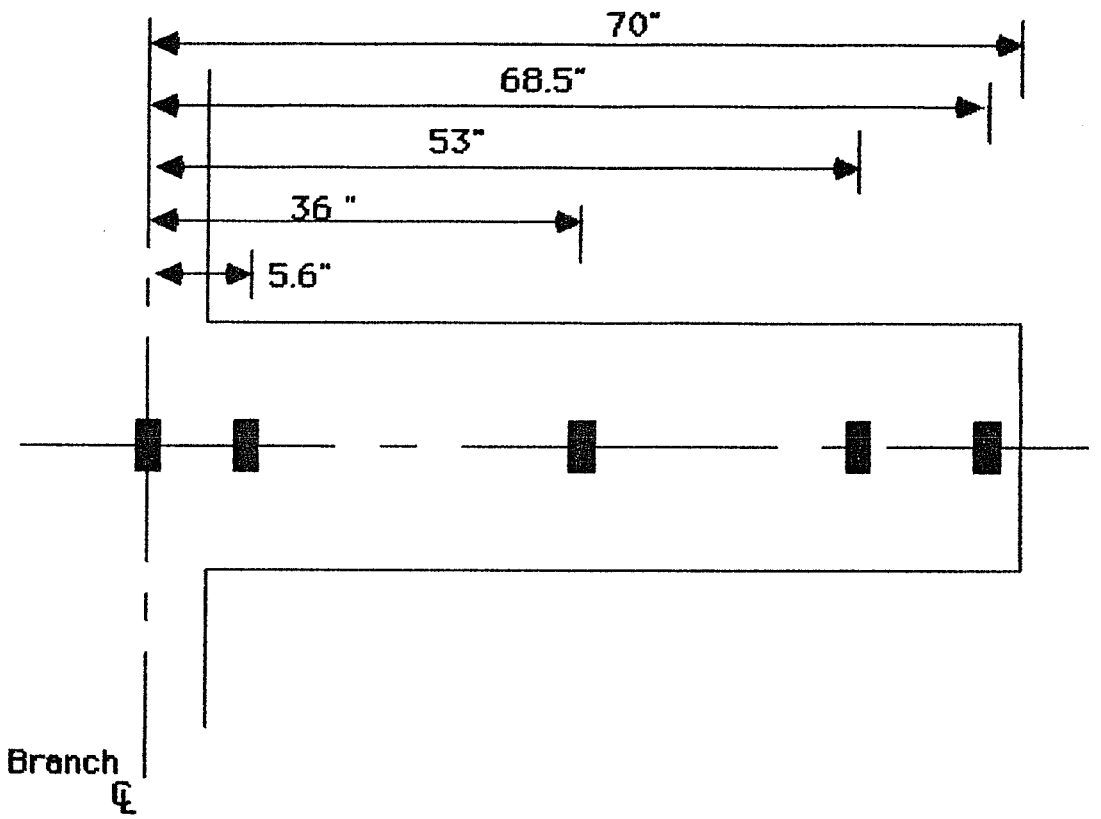

Fig.6.58 Postions of Strain Gages along Tension and Compression Saddle on Specimen 042

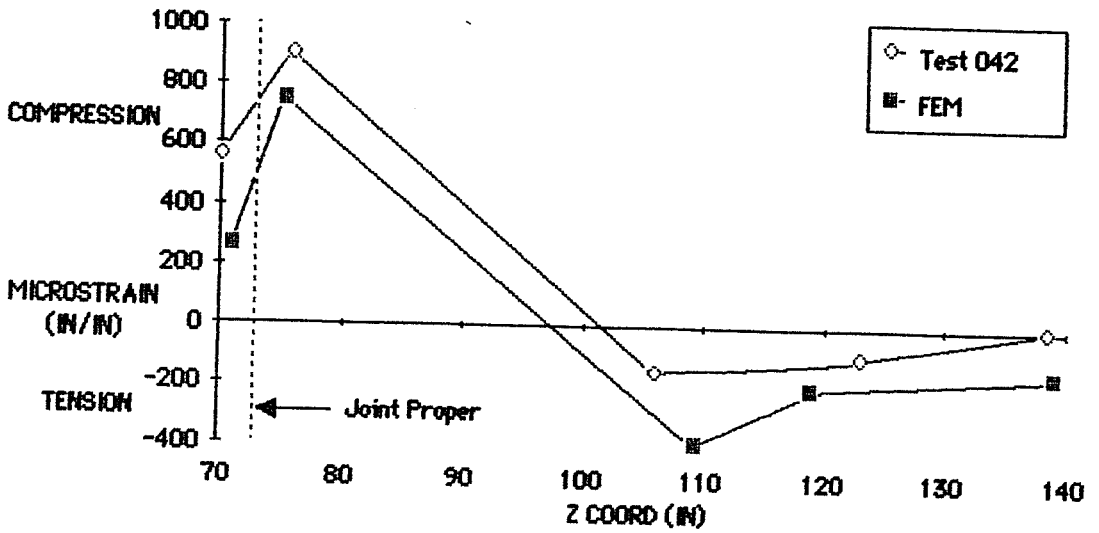

Fig. 6.59 Measured and Calculated Circumferential Strains at the Tension Chord Saddle Centerline for Test 042 at Ultimate Moment

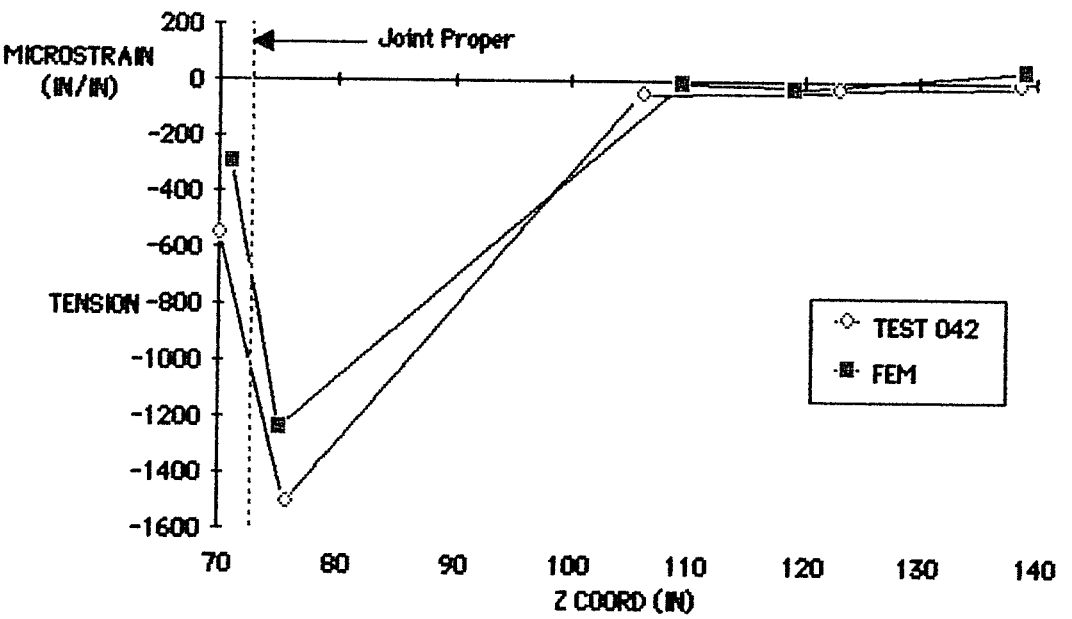

Fig. 6.60 Measured and Calculated Circumferential Strains at the Compression Chord Saddle Centerline for Test 042 at Ultimate Moment

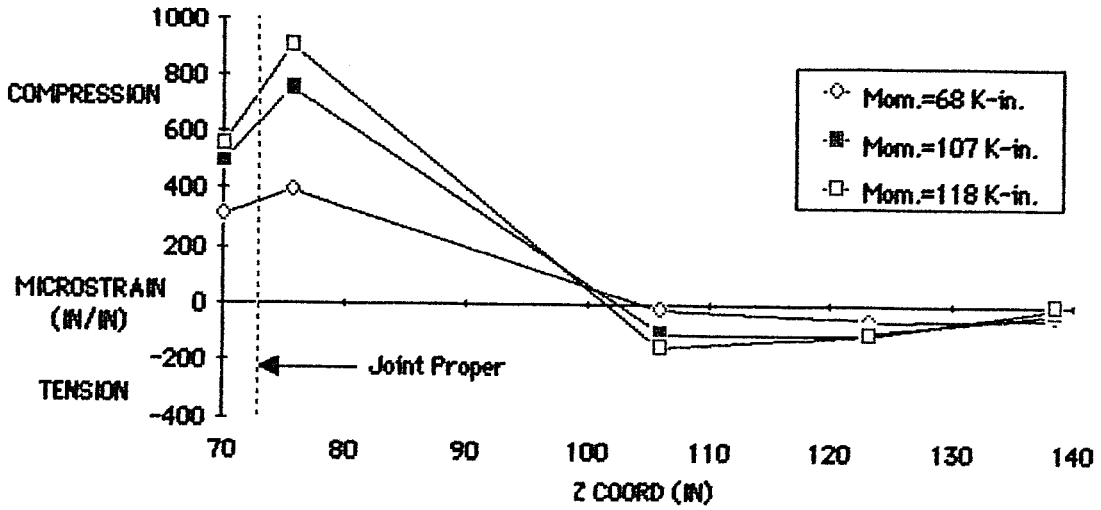

a.) Measured

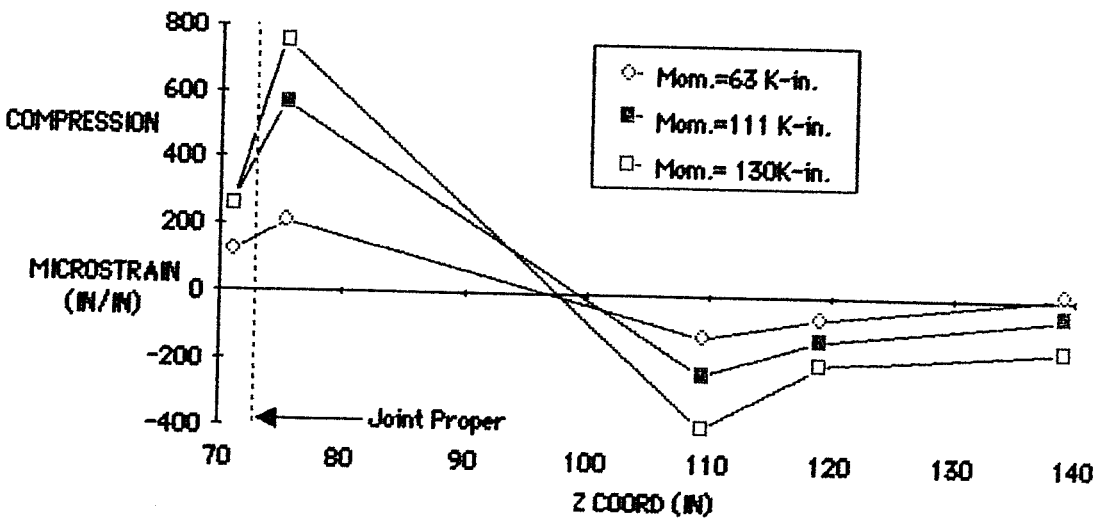

b.) Calculated

Fig. 6.61 Measured and Calculated Circumferential Strains at the Tension Chord Saddle Centerline for Test 042

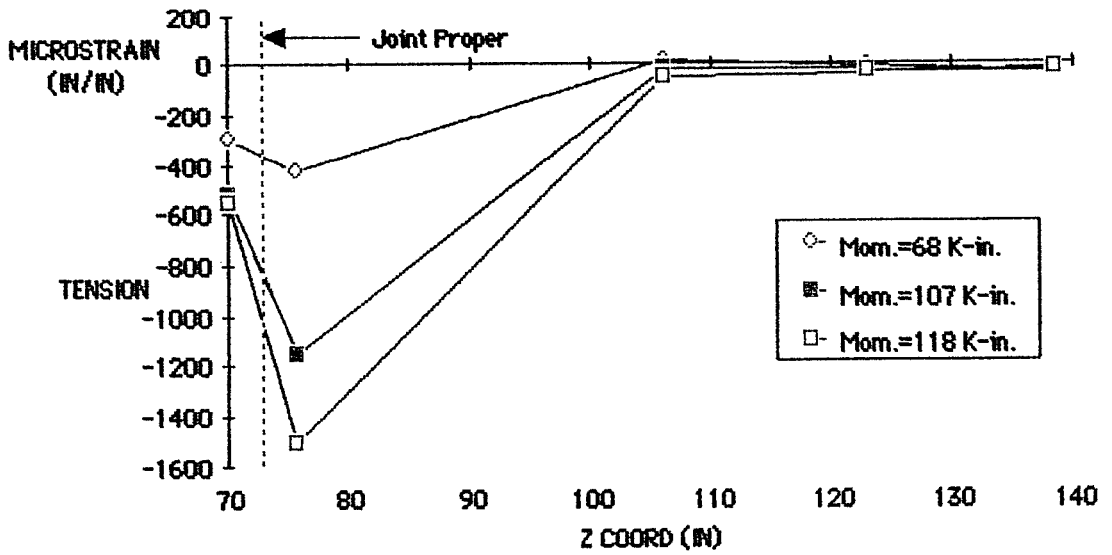

a.) Measured

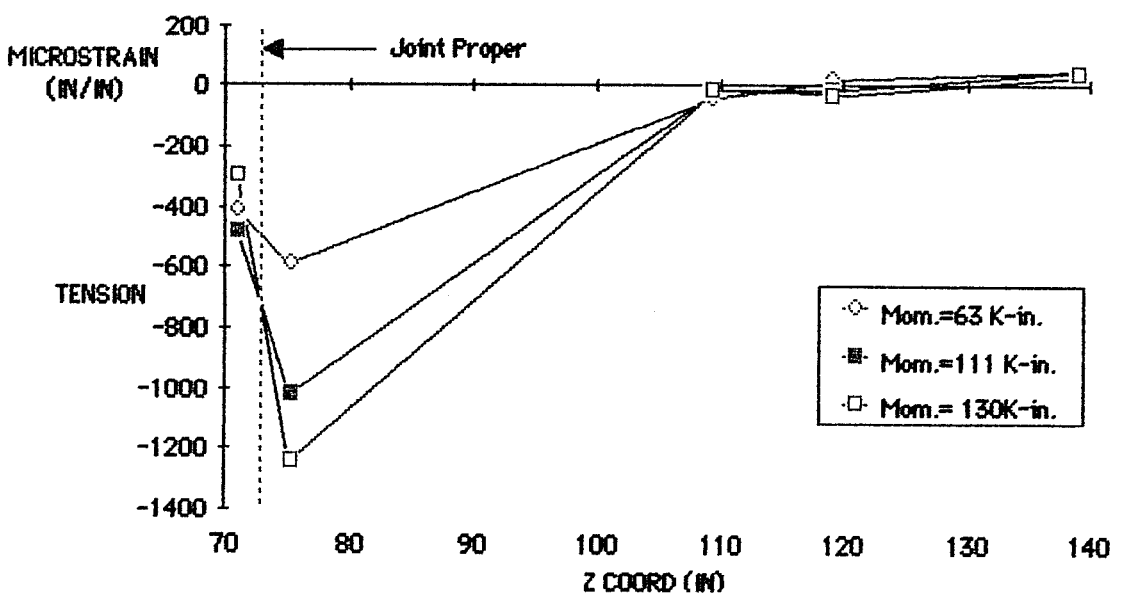

b.) Calculated

Fig. 6.62 Measured and Calculated Circumferential Strains at the Compression Chord Saddle Centerline for Test 042

were added to the model at the top of the branch, as shown in Fig. 6.63 so the branch could pivot about it true center. This is important because the displacement of the chord does not always follow the line of action of the force [15].

As in the actual test, a small axial load was applied to the joint before the joint was loaded in bending and held constant during the analysis. To allow rotation at the end of the chord, the axial load was applied by controlling the magnitude of concentrated loads at the end of the branch. Then the IPB moment was applied using load control with equivalent concentrated loads applied to the end of the chord similar to the loading used in the experiment. Finally, the OPB load was applied using displacement control to failure as in the reference run.

The OPB moment-rotation curves obtained from the reference and the interaction runs are shown in Fig. 6.64. The maximum moment achieved by the interaction model was 117 kip-in. which is 10% less than the reference moment and is 16% less than the ultimate moment achieved by Test I048. Thus,the finite element model shows that there is a small reduction in OPB capacity when a significant (38%) IPB moment is present whereas an increase in OPB strength was observed experimentally.

Since the analytical model has demonstrated good reliability for a wide variety of problems, it appears that the experimental result should be viewed with caution. However, both

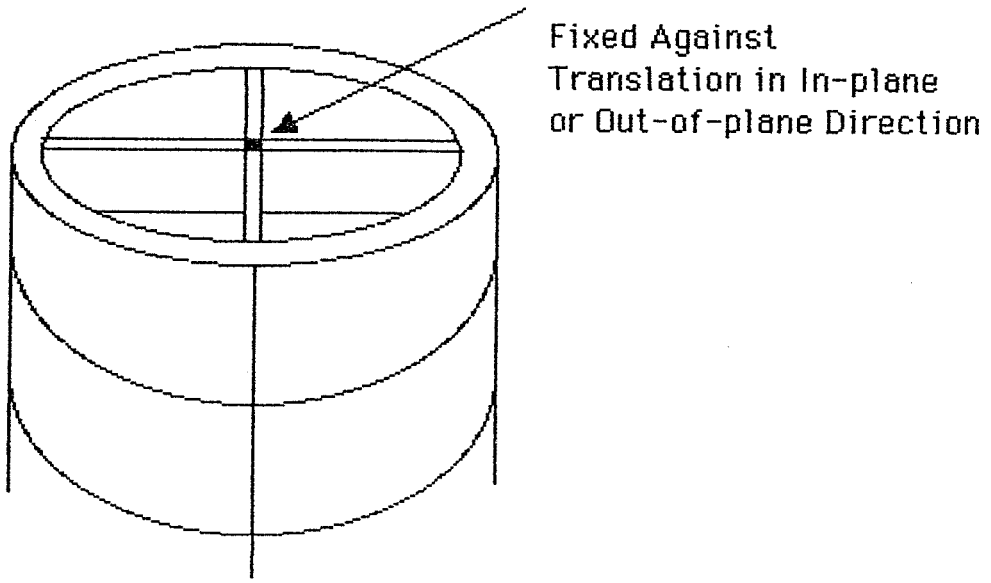

Fig. 6.63 Boundary Condtion at End of Branch
for IO Interaction Model

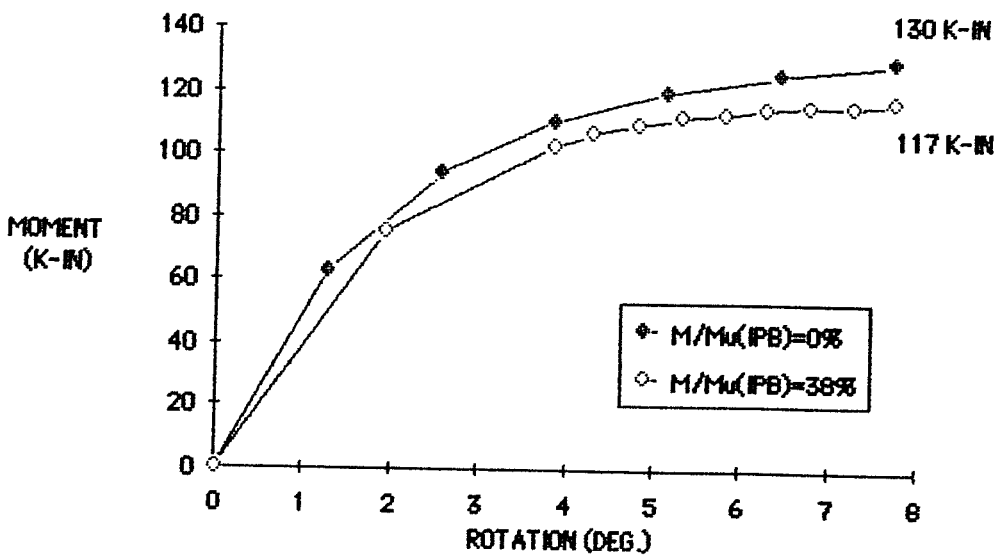

Fig. 6.64 Calculated OPB Moment vs. Rotation Curves for β=0.35 with and without IPB Moment

Tests I048 and I049 showed an increase in OPB strength (20% and 7% respectively), thus some experimental error must be found before the experimental results can be dismissed. This error is most probably a restraint in the system which resists the OPB shear in combination with the specimen resulting in an overestimation of joint strength. In addition, the restraint must have an increased effect when IPB displacements are applied to explain the increased experimental OPB strength with IPB moment. This restraint may be provided by the anti-twist mechanism shown in Fig. 2.4, which is used in the test setup to prevent rotation of the chord about the branch centerline. The restraint of the anti-twist mechanism was demonstrated during a series of elastic loadings to determine strain concentration factors [32]. In addition, since the anti-twist mechanism is constructed of relatively thin steel plate and deflected under it's own weight, any IPB deflection would cause a twisting in the joints of the mechanism and thus increase its restraint as IPB moment is applied. This theory explains the discrepancy between the analytical and experimental results rather well but should be verified by further experimentation.

6.9 Summary

The purpose of this chapter was to find an analytical model which could be used to investigate the ultimate strength

behavior of tubular joints including interaction effects economically, and then to apply this model to several topics raised by experimental results. A finite element model using the ABAQUS finite element program was created and used to predict the ultimate strength behavior of DT joints with β ratios of 0.35, 0.67 and 1.00 subjected to branch tension and compression, IPB, OPB and interaction loadings. The results of preliminary verification runs showed that the proposed model produced reasonable predictions of the ultimate strength of tubular joints, modeled the joint behavior well, and required very little computation time compared to some other finite element models.

When used to investigate the influence of the gap size on the axial compression capacity of a DT joint with a β ratio close to 1.0, the model predicted the ultimate strength of the joints very accurately. The results of the analytical work support the theory that the compression load is resisted almost exclusively by membrane action in the gap area of the joint, and that the ultimate load of the joint could be predicted by treating the gap as a column. However, further work is needed to develop an effective width of the gap and the exact influence of the gap dimensions over a wider range of values.

The proposed finite element model was also used to predict the IPB strength of the DT joints tested in this research. Comparisons of predicted and test ultimate strengths showed that

the model produced good predictions of IPB ultimate strength. An investigation of the effect of the chord thickness ratio was attempted using the analytical model; however, the results were very different than experimental results. The explanation for this discrepancy is that the model assumes no transverse shear in the chord or branch wall. While this assumption may be acceptable for higher γ values, it seems to cause an underestimation of strength for joints with relatively thick chord walls.

The ultimate strength of β=0.67 DT tubular joints subjected to combinations of axial compression and IPB were predicted using the proposed finite element model. The results of the interaction runs compared well with the experimental results. Thus, the model can be used as a tool for investigating interaction behavior. In addition to developing interaction data, two runs were performed to determine what influence, if any, that the loading path has on the interactive ultimate strength of tubular joints. Comparison of two replicate runs with different load paths showed that the load path had no significant effect on the interactive ultimate strength of the joint.

Finally, the finite element model was used to determine if the apparent increase in OPB strength with application of a small IPB moment shown by some of the experimental data on β=0.35 joints was a result of experimental scatter. The OPB reference

run agreed well with the experimental result. But, the IO interaction solution contradicted the results of the experiments, and showed a decrease in OPB strength with the application of IPB moment. The discrepancy between the analytical and experimental results can be explained by an unaccounted for restraint supplied by the anti-twist mechanism. Because the analytical model provided reliable results in a wide variety of applications, and because the analytical result agrees with a series of tests performed at Delft, the increase in OPB strength shown by experimentation should not be accounted for in the interaction equations used for design. Reanalysis of the recommendations of interaction equations for use in design made in Chapter 5 shows that Hoadley's equation which was recommended does not account for this apparent increase and fits the Delft experimental result well. Thus, the analytical result will not effect the recommendation of the interaction equation.

CHAPTER 7

SUMMARY AND CONCLUSIONS

7.1 Experimental Conclusions

7.1.1 β Effect on Interaction. Comparison of the DT interaction data for the β=1.0, 0.35 and the β=0.67 interaction data reported by Hoadley indicates that the β ratio of a joint has a significant effect on its interaction behavior. In addition, the interaction equation recommended in the 15th edition of API RP 2A, the arcsine equation, produced unconservative strength predictions for several of the tests. Hoadley's equation provided a lower bound to the data but does not account for the effect of the β ratio on the interaction. When the DT joint interaction results produced at Texas were compared to the results of a series of interaction tests on T joints published by TNO-IBBC near Delft, the interaction of the T and DT joint were found to be different. However, because of the variations in the nondimensionalized strength of the reference values between the T and DT joints and because the differences in the interactions were not large, it was determined that DT and T joints could be analyzed using one interaction equation. Therefore, a new interaction equation which accounts for the β ratio was developed using the Texas DT interaction data. The following interaction equation was developed as a lower bound to

the data:

$$P/P_u + (M/M_u)_{OPB}^{Y} + (M/M_u)_{IPB}^{Z} = 1.0$$

where, $Y = 2.35 - 1.35\beta^{0.63}$

$Z = 3.44\beta + 0.01\beta^{-5.6}$

7.1.2 Evaluation of Proposed Equation. The proposed interaction equation; Hoadley's equation, which is recommended for design in the UEG design guide [34]; and the arcsine equation, which is recommended for design in API publication RP 2A, were evaluated for accuracy using both the Texas DT joint and Delft T joint interaction data. The data base included 65 test results. When the ultimate strengths in the interaction tests were nondimensionalized by the experimental reference values, the proposed interaction equation predictions proved to be the most accurate of the three. However, the proposed equation produced several unconservative predictions for the β=0.35 T joint test series. The largest improvement in accuracy provided by the proposed equation was for the β=1.00 DT joint test series.

Since the designer does not have access to the experimental reference values and must approximate them with the use of ultimate strength formulas, the ultimate strengths in the interaction tests were also nondimensionalized by the reference values calculated using the recommended ultimate strength formulas given in the 15th edition of the API RP 2A. When the

calculated reference values were used, the proposed equation again provided the most accurate predictions for the test results, but the accuracy of the three equations was very similar. For the Delft T joint tests alone, the arcsine equation provided a slightly better fit to the data than the other equations. The proposed equation provided significantly better predictions of the ultimate strength for the β=1.0 DT joint tests.

In the evaluation of the interaction equations, it was shown that the ultimate strength predictions from API RP 2A for IPB strength of the β=0.67 and β=1.0 DT joints were overconservative compared to the axial and OPB predictions, and all were unconservative for the β=0.68 γ=15 T joints loaded in IPB and OPB. This variation in accuracy of the ultimate strength equations skewed the data and increased the standard deviations of the test-to-prediction values for the interaction data significantly. The scatter band of the data produced by this variation in the ultimate strength predictions was much larger than the variation in the three interaction equations; therefore, the accuracy of the interaction formulations can be most significantly improved by accurate prediction of the reference ultimate strengths.

7.1.3 Design Recommendations. In order to make recommendations for design, resistance factors were calculated

for the three interaction equations based on the tests available. These resistance factors were then used to calculate the relative chord thicknesses which would be required by each equation for a given joint. The results of the evaluation showed that the proposed interaction equation produced the most economical design but the only significant savings occurred in β=1.0 joints. Because β=1.0 joints make up only a small portion of the DT joint population used in practice, use of the proposed interaction equation will not have a significant effect on the overall structure. Therefore, since the three interaction equations produced similar design results, a recommendation for design was made based on the simplicity of the interactive equation. Because of its simplicity, Hoadley's equation is recommended for design at this time. It should be noted that tension loadings were not included in this study. Because the ultimate strength and stiffness of the DT joint is higher in compression than in tension, it is felt that joints with branch axial tension can be designed safely using the recommended interaction equation.

In the course of the analysis of the three interaction equations, it was found that when the interaction equations were applied to the interactive data nondimensionalized by the experimental reference values they required smaller chord thicknesses than when applied to the interactive data

nondimensionalized by the API ultimate strength predictions for the same level of safety. This indicates that some of the conservatism which is present in the ultimate strength equations, especially for DT joints in IPB, can be eliminated with no loss in safety in the interactive design.

Comparison of replicate reference tests for axial compression and OPB with the β=1.0 joints showed significant differences in ultimate loads and joint behavior. A new parameter was found which has a significant effect on the behavior of β=1.0 joints. This parameter is the distance between the weld toes at the saddle points, or the gap. Comparison of the gap size and experimental compressive capacity for tests A21, A22, 028, 023 showed that when the gap is considered to behave as a column the compressive capacity follows the SSRC inelastic buckling curve well. This behavior was also shown when Tests A21 and A22 were modelled using the finite element method. Based on the analysis of the gap influence, and because measurements of the β=1.0 specimens showed a wide variation in the gap distance on nominally identical joints, it is recommended that an additional factor of safety be applied to the ultimate strength equations for β=1.0 specimens in compression or OPB.

7.2 Analytical Conclusions.

7.2.1 Verification of Simple Finite Elemental Model.

Because the experimental data raised several questions which cannot be answered with confidence using the data available, and because a balance between the analytical and experimental approach to the investigation of tubular joints is needed, a simplified finite element model using the ABAQUS finite element program was developed and used to study the ultimate strength behavior of tubular joints. To minimize the cost of computation, simple 4-noded shell elements which neglect transverse shear were used in the model. In addition, the weld was not included in the model. However, both material and geometric nonlinearity was included in the model. The results of several validation runs and comparison to other published finite element solutions showed that the proposed model produced reasonably accurate predictions of ultimate strength and was very economical.

7.2.2 Gap Effect on $\beta = 1.0$ in Compression.

The finite element model was used to investigate several aspects of tubular joint behavior. First, the effect of the gap size on compression strength of a $\beta = 1.00$ joint was studied. The results of the finite element study which indicated that the gap area of the joint can be analyzed as a column, agreed well with the experimental results.

7.2.3 γ Effect in IPB. Because the ultimate strength of Tests I7, I24 and I43 did not agree with the API strength equations and very little DT bending data is available, each test was modeled using the finite element analysis. The results of the analyses agreed well with the experiments and showed that the Billington equation modified by Yura for DT joints provides a much better prediction of IPB strength than the API equations.

7.2.4 Interaction Analysis. The finite element model was extended for use in the production of AI interaction data for a β = 0.67 DT joint. When plotted with the experimental data, the analytical data falls along the outside of the band of experimental data indicating that the finite element predictions are accurate and slightly conservative.

Since the model proved to be applicable to interaction analysis, the case of IO interaction for a β = 0.35 DT joint was analyzed. This case was chosen because the experimental results of this research showed an increase in the OPB strength with the addition of IPB while the results of the TNO research indicated a decrease in strength. The finite element solution showed that the OPB strength of the joint decreased by approximately 10% when approximately 35% of the ultimate IPB moment is applied. This agrees with the TNO results. The overprediction of IO strength which occurred in this (Texas) research was attributed to an

unaccounted for restraint in the experimental setup provided by the anti-twist mechanism.

7.3 Summary

The results of 27 ultimate strength and interaction tests on DT tubular joints with β ratios of 1.0 and 0.35 were presented.

The results of this research indicates that while the interaction curves may be different for joints with different β ratios and for joints with T or DT configurations, the differences in the resulting joint design are minimal. Thus, further experimental research aimed at developing a series of interaction curves is not recommended. Research time and effort would be more effective if directed toward more accurate prediction of the ultimate strength of tubular joints in bending. The results of the analytical study showed that a simplified analytical model using the finite element method could be used to study ultimate strength behavior in tubular joints. It is hoped that the finite element model developed in this work will be further refined and utilized, as it shows promise as a widely applicable and economical method of analyzing the ultimate strength behavior of tubular joints.

A P P E N D I X A

TWO DIMENSIONAL INTERACTION FORMULAE

In order to better understand the data, curves were developed to fit each individual 2-D interaction case. From this point, a three dimensional interaction formula was developed. These 2-D interactions help to determine the loss in accuracy of the formula which occurs when the 2-D cases are lumped into one three dimensional equation.

Axial Compression with OPB: The interaction between axial compression and OPB for all three β ratios used in this project are shown in Fig.A.1. The axial and bending terms are normalized by experimental reference values given in Table 4.2. In the OPB reference tests, a small axial load was required to hold the specimen in the test frame, therefore the data points from Tests 023, 028, 08,and 042 do not fall directly on the bending axis. But, for clarity the axial loads are ignored in the calculation of the OPB reference tests.

Because using a linear interaction as dictated by Test A033 would produce overconservative predictions for the β=0.67 and 0.35 joints, different interaction equations for each β ratio more closely represent the behavior of the joints. The interaction equations can be written in the general form shown below,

$$P/P_u^X + (M/M_u)_{OPB}^Y = 1.0 \qquad (A.1)$$

assuming a nonlinear effect for both axial and bending terms. The values of the exponents were determined by varying X and Y to achieve a lower bound to the data from each β ratio. The resulting values of X and Y are shown in Table A.1 and the resulting equations are plotted in Fig. A.1.

Axial Compression with IPB: The interaction between axial compression and IPB for β = 1.0, 0.67 and 0.35 is shown in Fig. A.2. The axial and IPB terms are normalized by the experimental values shown in Table 4.2 As in the AO interaction, the axial loads are ignored in the calculation of the IPB reference tests.

Using the same general equation as in the AO interaction the AI interaction can be written as,

$$P/P_u^X + (M/M_u)_{IPB}^Z = 1.0 \qquad (A.2)$$

As with the AO interaction, the values of the exponents were determined by varying X and Z to achieve a lower bound to the data from each β ratio. The resulting values of X and Z are shown in Table A.1 and the resulting equations are plotted in Fig.A.2.

IPB with OPB: The results of interaction tests between IPB and OPB are plotted in Fig.A.3. In each of these tests a small axial load was present in the joint; however, because this is a two dimensional analysis, the axial loads are ignored in the development of the interaction equation.

TABLE A.1 EXPONENTS FOR TWO DIMENSIONAL INTERACTIONS

β	Exponent	AO	AI	IO
1.00	X	1.00	1.00	----
	Y	1.00	----	1.10
	Z	----	4.60	2.50
0.67	X	1.00	1.00	----
	Y	1.35	----	1.00
	Z	----	2.40	2.50
0.35	X	2.30	1.00	----
	Y	1.00	----	1.00
	Z	----	4.00	15.00

$$(P/P_u)^X + (M/M_u)^Y_{OPB} + (M/M_u)^Z_{IPB} = 1.0$$

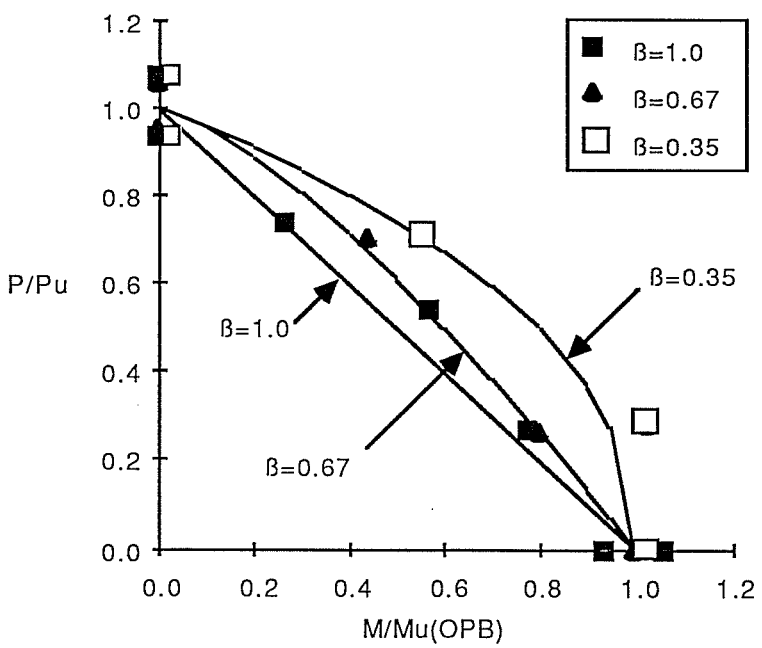

Fig. A1 2-D AO Interaction

Using the same general equation as with the AO, and AI, the failure line can be defined by the following equation;

$$(M/M_u)_{OPB}{}^{Y} + (M/M_u)_{IPB}{}^{Z} = 1.0 \qquad (A.3)$$

As before, the values of the exponents was determined by varying Y and Z to achieve a lower bound to the data from each β ratio. The increase in OPB capacity shown by the β=0.35 tests was neglected so, an upper bound was set at $(M/M_u)_{OPB}$ =1.0 for the β=0.35 interaction.The resulting values of Y and Z are shown in Tabled A.1 and the resulting equations are plotted in Fig. A.3.

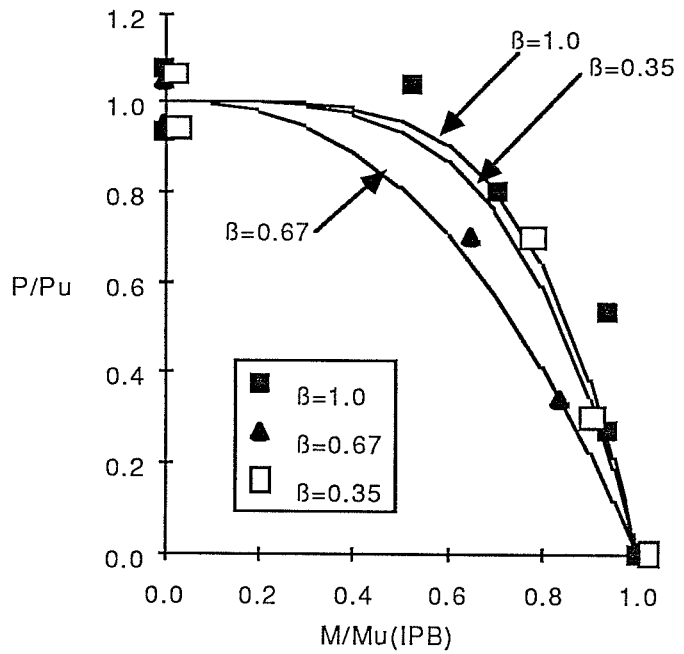

Fig. A.2 2-D AI Interaction

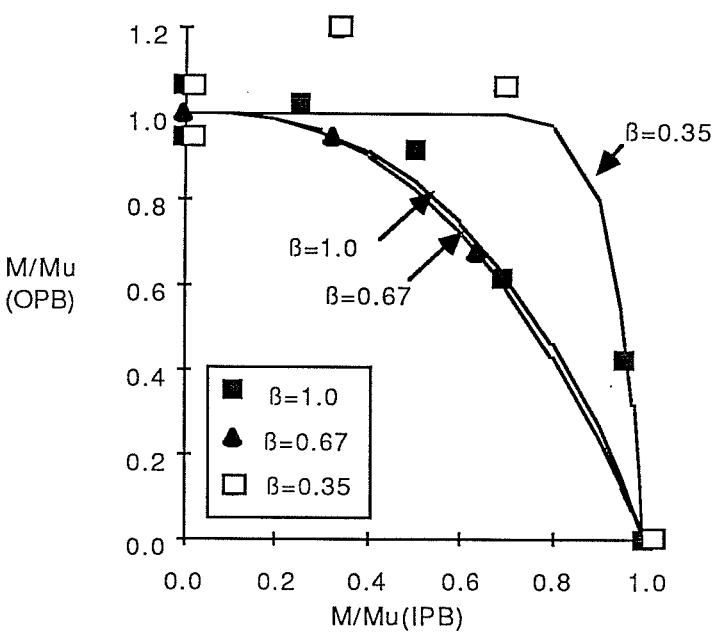

Fig. A.3 2-D IO Interaction

A P P E N D I X B

TABULATED TEST DATA

DATA REDUCTION DEFINITIONS

A_U, A_L = Upper and Lower Axial Loads Respectively (Kips)

L = Moment Arm of Specimen (in.), given in Appendix C

M_{IPB} = IPB Moment (Kip-in.)

M_{OPB} = OPB Moment (Kip-in.)

R = IPB Lateral Load (Kips)

Q = OPB Lateral Load (Kips)

θ_{IPB} = IPB Branch Rotation (Deg.)

θ_{OPB} = OPB Branch Rotation (Deg.)

Δ_{IPB} = IPB Lateral Deflection (in.)

Δ_{OPB} = OPB Lateral Deflection (in.)

DATA REDUCTION CALCULATIONS

$M_{IPB} = (R / 2) \times L \times \cos(\theta_{IPB})$

$M_{OPB} = (Q / 2) \times L \times \cos(\theta_{OPB})$

$P\text{-}\Delta \text{ Moment} = [(A_L + A_U) / 2] \times \Delta$

$\theta_{IPB} = \text{Arcsin} (\Delta_I / L)$

$\theta_{OPB} = \text{Arcsin} (\Delta_O / L)$

TABLE B.1 TEST A22

LOAD STAGE	UPPER AXIAL AU (KIPS)	UPPER DEFL. (IN.)	LOWER AXIAL AL (KIPS)	LOWER DEFL. (IN.)	AVG. DEFL. (IN.)
0	.0	.000	.0	.000	.000
1	18.5	-.028	20.5	.100	.036
2	38.2	-.033	39.9	.135	.051
3	57.7	-.021	58.9	.153	.066
4	76.3	-.018	78.1	.181	.082
5	94.7	-.021	96.7	.214	.097
6	114.0	-.027	116.0	.258	.116
7	132.8	-.038	133.8	.306	.134
8	151.4	-.021	151.5	.379	.179
9	147.7	.096	147.6	.477	.287
10	141.9	.319	141.9	.606	.463
11	139.9	.646	139.6	.660	.653
12	140.2	.754	139.6	.706	.730
13	141.2	.930	140.4	.768	.849
14	70.9	.786	72.5	.723	.755
15	2.1	.670	3.0	.581	.626

TABLE B.2 TEST A51

LOAD STAGE	UPPER AXIAL (KIPS)	UPPER DEFL. (IN.)	LOWER AXIAL (KIPS)	LOWER DEFL. (IN.)	AVG. DEFL. (IN.)
0	.0	.000	.0	.000	.000
1	4.7	.000	6.6	.019	.010
2	12.7	.041	14.6	.025	.033
3	27.6	.093	29.5	.071	.082
4	41.9	.136	43.6	.146	.141
5	48.9	.154	51.4	.223	.189
6	54.5	.186	57.0	.294	.240
7	62.1	.268	64.5	.393	.331
8	66.8	.392	69.3	.499	.446
9	68.5	.595	71.0	.592	.594
10	67.7	.806	70.5	.633	.720
11	66.6	1.163	68.8	.759	.961
12	36.1	1.065	37.4	.546	.806
13	2.2	.827	3.4	.327	.577

TABLE B.3 TEST A40

LOAD STAGE	UPPER AXIAL AU (KIPS)	UPPER DEFL. (IN.)	LOWER AXIAL AL (KIPS)	LOWER DEFL. (IN.)	AVG. DEFL. (IN.)
0	.0	.000	.0	.000	.000
1	6.0	.168	6.8	-.136	.016
2	14.5	.231	16.2	-.059	.086
3	26.1	.330	27.1	.044	.187
4	31.9	.383	32.5	.147	.265
6	38.9	.034	39.9	.773	.404
7	41.3	.329	42.0	.902	.616
8	39.7	.806	40.2	.983	.895
9	39.0	1.206	39.8	1.110	1.158
10	17.6	1.044	18.8	.822	.933
11	.9	.850	2.2	.553	.702

TABLE B.4 TEST 028

LOAD STAGE	LATERAL LOAD Q (KIPS)	UPPER AXIAL AU (KIPS)	LOWER AXIAL AL (KIPS)	OPB DEFL. (IN.)	BRANCH MOMENT (K-IN.)	P-DELTA MOMENT (K-IN.)	OPB ROTATION (DEG.)	TOTAL OPB MOMENT (K-IN.)
1	.0	3.9	6.3	.000	1	0	.00	1
2	1.6	9.3	12.4	.016	48	0	.02	48
3	10.1	9.5	12.4	.087	296	1	.08	297
4	20.0	9.3	12.3	.186	588	2	.18	590
5	30.0	9.4	12.2	.295	878	3	.29	881
6	35.3	9.5	12.3	.361	1033	4	.35	1037
7	40.0	9.5	12.3	.435	1173	5	.43	1178
8	45.1	9.6	12.5	.529	1322	6	.52	1327
9	50.1	9.4	12.3	.714	1468	8	.70	1476
10	49.6	9.4	12.7	.949	1455	10	.93	1465
11	47.4	9.3	12.7	1.186	1389	13	1.16	1402
12	45.2	9.3	12.5	1.648	1323	18	1.61	1341
13	19.6	9.4	12.4	1.363	574	15	1.33	589
14	.8	9.3	12.5	1.114	23	12	1.09	35

TABLE B.5 TEST 042

LOAD STAGE	LATERAL LOAD Q (KIPS)	UPPER AXIAL AU (KIPS)	LOWER AXIAL AL (KIPS)	OPB DEFL. (IN.)	OPB DEFL. + INITIAL (IN.)	BRANCH MOMENT (K-IN.)	P-DELTA MOMENT (K-IN.)	OPB ROTATION (DEG.)	TOTAL OPB MOMENT (K-IN.)
1	.0	2.0	3.3	.001	.40	1	1	.00	2
2	1.3	1.9	3.1	.480	.81	37	2	.47	39
3	2.2	2.0	3.1	1.396	1.80	63	5	1.37	68
4	2.5	2.2	3.1	1.843	2.24	72	6	1.81	78
5	2.8	2.2	3.1	2.361	2.76	82	7	2.32	89
6	3.0	2.2	3.0	3.264	3.66	88	9	3.21	97
7	3.2	2.2	3.0	4.241	4.64	94	12	4.17	107
8	3.5	2.4	3.2	5.292	5.69	101	16	5.21	116
9	3.5	2.3	3.1	6.311	6.71	100	18	6.21	118
10	3.1	2.3	3.0	7.328	7.73	91	20	7.22	111
11	3.1	2.0	3.2	8.734	9.13	91	24	8.61	115
12	2.2	1.9	3.0	7.882	8.28	63	20	7.77	83
13	.7	1.9	3.1	6.880	7.28	19	18	6.78	38

TABLE B.6 TEST I43

LOAD STAGE	LATERAL LOAD R (KIPS)	UPPER AXIAL AU (KIPS)	LOWER AXIAL AL (KIPS)	IPB DEFL. (IN.)	BRANCH MOMENT (K-IN.)	P-DELTA MOMENT (K-IN.)	IPB ROTATION (DEG.)	TOTAL IPB MOMENT (K-IN.)
1	.0	3.0	4.5	.000	1	0	.00	1
2	1.0	2.5	4.5	.166	29	1	.16	30
3	2.2	2.5	4.5	.405	63	1	.40	64
4	4.1	2.4	4.5	.835	118	3	.82	121
5	5.7	2.5	4.6	1.479	164	5	1.46	169
6	6.3	2.5	4.6	1.778	183	6	1.76	190
7	7.2	2.5	4.7	2.497	208	9	2.47	217
8	7.6	2.5	4.7	3.282	220	12	3.24	232
9	7.8	2.6	4.7	4.082	225	15	4.04	240
10	7.8	2.6	4.8	5.237	226	19	5.18	245
11	7.9	2.6	4.8	6.480	228	24	6.41	252
12	7.9	2.6	4.9	7.708	228	29	7.64	257
13	7.9	2.6	4.9	8.866	226	33	8.79	259
14	8.0	2.7	4.9	10.039	229	38	9.97	267
15	3.9	2.8	4.9	9.271	110	36	9.20	146
16	.2	2.7	4.9	8.203	7	31	8.13	38

TABLE B.7 TEST A031

LOAD STAGE	LATERAL LOAD Q (KIPS)	UPPER BRANCH AU (KIPS)	LOWER BRANCH AL (KIPS)	OPB DEFL. (IN.)	BRANCH MOMENT (K-IN.)	P-DELTA MOMENT (K-IN.)	OPB ROTATION (DEG.)	TOTAL OPB MOMENT (K-IN.)
0	.0	.0	.0	.000	0	0	.00	0
4	1.7	41.5	43.7	.020	51	1	.02	52
5	10.2	41.3	43.7	.106	302	4	.10	307
6	20.4	41.4	43.7	.257	603	11	.25	614
7	24.3	41.1	43.7	.456	717	19	.44	736
8	25.3	41.0	43.8	.841	746	36	.82	782
9	25.1	40.9	43.9	1.392	741	59	1.35	800
10	25.2	40.8	43.9	2.033	744	86	1.97	830
13	25.9	40.5	44.1	3.340	763	141	3.24	905
14	26.6	40.5	44.2	4.144	783	175	4.03	958
15	27.3	40.4	44.2	5.240	801	222	5.09	1023
16	27.6	40.4	44.3	6.312	809	267	6.14	1076
17	27.0	40.4	44.4	8.394	789	356	8.18	1144
18	13.7	40.3	44.4	8.169	400	346	7.95	746
19	.3	40.3	44.5	7.867	8	333	7.66	341
20	.3	.3	4.7	7.377	8	19	7.18	26

TABLE B.8 TEST A032

LOAD STAGE	LATERAL LOAD Q (KIPS)	UPPER AXIAL AU (KIPS)	LOWER AXIAL AL (KIPS)	OPB DEFL. (IN.)	BRANCH MOMENT (K-IN.)	P-DELTA MOMENT (K-IN.)	OPB ROTATION (DEG.)	TOTAL OPB MOMENT (K-IN.)
1	.0	18.7	21.1	.000	1	0	.00	1
2	.0	56.5	59.0	.000	1	0	.00	1
3	.0	84.5	86.7	.000	1	0	.00	1
4	3.0	84.2	86.7	.025	88	2	.02	90
5	3.0	84.1	87.7	.027	89	2	.03	91
6	5.3	84.0	87.8	.046	156	4	.04	160
7	10.3	84.0	87.8	.093	302	8	.09	310
8	20.5	83.9	87.8	.212	602	18	.21	620
9	24.6	83.6	87.8	.340	722	29	.33	751
10	25.5	83.6	87.9	.547	748	47	.53	795
11	21.1	83.0	88.2	1.284	620	110	1.25	730
12	19.1	83.4	88.0	2.164	560	185	2.11	746
13	17.8	83.2	88.1	3.202	522	274	3.12	796
14	8.5	83.1	88.1	3.095	249	265	3.02	514
15	.3	82.9	88.0	2.967	8	254	2.89	262
16	.2	.1	4.3	2.636	7	6	2.57	12

TABLE B.9 TEST A033

LOAD STAGE	UPPER AXIAL AU (KIPS)	UPPER DEFL. (IN.)	LOWER AXIAL AL (KIPS)	LOWER DEFL. (IN.)	AVG. DEFL. (IN.)	LATERAL LOAD Q (KIPS)	OPB DEFL. (IN.)	BRANCH MOMENT (K-IN.)	P-DELTA MOMENT (K-IN.)	OPB ROT. (DEG.)	TOTAL OPB MOMENT (K-IN.)
0	.0	.000	.0	.000	.000	.0	.000	0	0	.00	0
1	5.4	.020	7.8	-.018	.001	1.4	.007	42	0	.01	42
2	5.4	.019	7.8	-.015	.002	8.6	.074	253	0	.07	253
3	5.3	.018	7.9	-.015	.002	10.1	.096	297	1	.09	298
4	18.5	.026	21.5	.004	.015	10.1	.091	296	2	.09	298
5	54.9	.063	57.5	.036	.050	10.2	.101	300	6	.10	306
6	85.7	.101	87.9	.060	.081	9.8	.118	288	10	.11	299
7	105.8	.129	107.6	.079	.104	9.5	.147	278	16	.14	294
8	116.9	.143	118.4	.109	.126	10.4	.630	305	74	.61	379
9	107.5	.323	109.1	.148	.236	10.6	1.080	313	117	1.05	430
10	102.8	.469	104.4	.183	.326	10.3	1.692	303	175	1.65	479
11	36.2	.439	38.6	.071	.255	10.1	1.601	296	60	1.56	356
12	3.7	.367	6.2	.051	.209	10.1	1.529	298	8	1.49	305
13	5.3	.370	7.6	.029	.200	.3	1.366	10	9	1.33	19

TABLE B.10 TEST AI34

LOAD STAGE	LATERAL LOAD R (KIPS)	UPPER BRANCH AU (KIPS)	LOWER BRANCH AL (KIPS)	IPB DEFL. (INCHES) (IN.)	BRANCH MOMENT (KIP-IN.)	P-DELTA MOMENT (K-IN.)	IPB ROTATION (DEG.)	TOTAL IPB MOMENT (K-IN.)
0	.1	5.2	6.9	.001	4	0	.00	4
1	.1	18.0	20.7	-.016	2	0	.00	2
2	.1	40.9	43.7	-.012	2	-1	.00	2
3	4.3	41.5	43.7	.059	127	3	.06	129
4	20.5	41.6	43.7	.337	603	14	.33	617
5	39.6	41.6	43.7	.743	1164	32	.72	1196
6	48.9	41.4	43.5	1.074	1438	46	1.05	1483
7	57.0	41.5	43.7	1.457	1674	62	1.42	1736
8	62.7	41.5	44.0	1.926	1842	82	1.88	1924
9	65.9	41.5	43.6	2.451	1933	104	2.39	2037
10	67.4	41.4	43.7	3.307	1977	141	3.23	2118
11	66.3	41.4	43.8	4.259	1942	181	4.16	2123
12	63.6	41.3	43.7	5.372	1860	228	5.25	2088
13	60.7	41.2	43.6	6.320	1774	268	6.18	2042
14	23.6	41.4	43.8	5.656	689	241	5.52	929
15	.4	41.3	44.6	5.116	10	220	5.00	230

Table B.11 Test AI35

LOAD STAGE	LATERAL LOAD R (KIPS)	UPPER BRANCH AU (KIPS)	LOWER BRANCH AL (KIPS)	IPB DEFL. (IN.)	BRANCH MOMENT (K-IN.)	P-DELTA MOMENT (K-IN)	IPB ROTATION (DEG.)	TOTAL IPB MOMENT (K-IN.)
0	.0	.0	.0	-.005	0	0	.00	0
3	.0	27.7	30.9	-.003	0	0	.00	0
4	.0	55.8	59.8	.018	0	1	.02	1
9	5.5	83.1	86.4	.068	161	6	.07	167
10	25.5	83.2	86.4	.404	751	34	.39	785
11	35.1	83.2	86.4	.609	1034	52	.59	1085
12	43.2	82.4	86.3	.818	1274	69	.80	1343
13	50.2	81.6	86.4	1.045	1478	88	1.02	1566
14	56.6	80.8	86.4	1.370	1668	115	1.34	1782
15	61.9	82.9	86.5	1.854	1825	157	1.81	1982
17	59.9	82.9	86.7	4.130	1759	350	4.02	2109
18	58.4	82.8	86.9	4.520	1714	384	4.40	2098
19	53.8	82.8	86.9	5.410	1578	459	5.27	2037
20	47.7	82.8	86.8	6.460	1396	548	6.29	1944
21	42.7	82.7	86.9	7.230	1249	613	7.05	1862
22	19.9	82.6	86.9	6.830	583	579	6.65	1162
23	.3	82.8	87.0	6.350	9	539	6.18	548

TABLE B.12 TEST AI36

LOAD STAGE	UPPER BRANCH AU (KIPS)	UPPER DEFL. (IN.)	LOWER BRANCH AL (KIPS)	LOWER DEFL. (IN.)	AVERAGE AXIAL DEFL. (IN.)	LATERAL LOAD R (KIPS)	IPB DEFL. (IN.)	BRANCH MOMENT (K-IN.)	P-DELTA MOMENT (K-IN.)	IPB ROTATION (DEG.)	TOTAL IPB MOMENT (K-IN.)
0	.0	.000	.0	.000	.000	.0	.000	1	0	.00	1
2	8.8	.036	12.2	.001	.019	17.4	.267	510	3	.26	513
4	36.6	.082	40.1	.030	.056	35.0	.627	1027	24	.61	1052
5	76.4	.114	80.4	.095	.105	35.1	.667	1030	52	.65	1082
6	98.7	.131	101.1	.129	.130	35.1	.695	1031	69	.68	1101
7	117.5	.182	118.5	.131	.157	34.8	.733	1023	87	.72	1110
8	129.2	.216	129.2	.125	.171	35.2	.751	1033	97	.73	1130
9	140.5	.246	141.3	.124	.185	35.1	.774	1030	109	.76	1140
10	155.2	.203	156.4	.222	.213	35.9	.857	1054	134	.84	1187
11	166.2	.288	169.0	.202	.245	35.6	.970	1045	163	.95	1208
12	160.8	.381	163.8	.200	.291	35.4	1.151	1038	187	1.12	1225
13	144.5	.591	146.6	.220	.406	35.4	1.607	1038	234	1.57	1272
14	71.0	.394	75.3	.249	.322	35.4	1.569	1038	115	1.53	1152
15	3.0	.133	6.9	.242	.188	35.4	1.495	1040	7	1.46	1047
16	2.5	.073	6.7	.293	.183	.3	.837	10	4	.82	14

TABLE B.13 TEST AI50

LOAD STAGE	UPPER BRANCH AU (KIPS)	UPPER AXIAL DEFL. (IN.)	LOWER BRANCH AL (KIPS)	LOWER AXIAL DEFL. (IN.)	AVERAGE AXIAL DEFL. (IN.)	LATERAL LOAD R (KIPS)	IPB DEFL. (IN.)	BRANCH MOMENT (K-IN.)	P-DELTA MOMENT (K-IN.)	IPB ROTATION (DEG.)	TOTAL IPB MOMENT (K-IN.)
0	1.2	.000	4.1	.000	.000	.0	.000	0	0	.00	0
1	5.6	-.016	8.6	.034	.009	2.2	.038	63	0	.04	63
2	45.2	-.006	48.4	.131	.063	19.5	.364	571	17	.36	588
3	81.6	-.001	84.9	.239	.119	35.3	.750	1036	62	.73	1099
4	104.8	.002	107.8	.341	.172	43.2	1.140	1267	121	1.11	1389
5	117.9	.045	121.7	.420	.233	47.6	1.577	1397	189	1.54	1586
6	125.2	.144	129.0	.541	.343	45.4	2.117	1331	269	2.07	1600
7	122.7	.722	124.2	.626	.674	32.6	2.946	956	364	2.88	1320
8	110.9	.975	111.2	.741	.858	37.3	3.844	1091	427	3.75	1518
9	51.9	.772	56.9	.705	.714	22.7	3.481	664	189	3.40	854
10	.8	.595	4.7	.562	.579	.2	2.803	5	8	2.74	12

TABLE B.14 TEST I037

LOAD STAGE	UPPER AXIAL AU (KIPS)	LOWER AXIAL AL (KIPS)	LATERAL LOAD Q (KIPS)	OPB DEFL (IN.)	BRANCH MOMENT (K-IN.)	P-DELTA MOMENT (K-IN.)	OPB ROT. (DEG.)	TOTAL OPB MOMENT (K-IN.)	LATERAL LOAD R (KIPS)	IPB DEFL (IN.)	BRANCH MOMENT (K-IN.)	P-DELTA MOMENT (K-IN.)	IPB ROT. (DEG.)	TOTAL IPB MOMENT (K-IN.)
1	11.1	14.9	.1	-.001	2	0	.00	2	.0	.000	1	0	.00	1
2	11.0	15.0	.1	-.001	3	0	.00	3	5.9	.110	172	1	.11	174
6	11.0	15.0	.8	.040	23	1	.04	23	19.4	.613	567	8	.60	575
7	10.9	15.0	10.6	.121	311	2	.12	313	19.3	.610	566	8	.60	574
8	10.9	15.0	20.8	.242	609	3	.24	612	19.2	.621	564	8	.61	572
9	10.8	15.0	30.2	.403	886	5	.39	891	19.3	.665	566	9	.65	574
10	11.0	15.1	35.4	.552	1037	7	.54	1044	19.3	.701	566	9	.69	575
11	11.0	15.1	38.1	.972	1116	13	.95	1129	19.3	.762	566	10	.74	576
12	11.0	15.0	38.8	1.982	1138	26	1.94	1164	19.3	.828	565	11	.81	576
13	11.1	15.1	40.4	2.931	1183	38	2.87	1221	19.3	.875	566	11	.86	577
14	11.2	15.1	42.0	3.889	1228	51	3.80	1279	19.3	.925	566	12	.90	578
15	11.3	15.2	45.9	6.089	1338	81	5.96	1419	19.3	1.098	567	15	1.07	582
16	11.3	15.1	19.8	5.618	579	74	5.50	653	19.3	1.057	567	14	1.03	581
17	11.2	15.2	.3	5.123	7	68	5.01	75	19.4	.930	568	12	.91	580
18	11.3	15.3	.1	5.054	2	67	4.94	70	.1	.598	4	8	.58	12
19	3.6	7.4	.1	4.977	2	27	4.87	29	.1	.595	4	3	.58	8

TABLE B.15 TEST I038

LOAD STAGE	UPPER AXIAL AU (KIPS)	LOWER AXIAL AL (KIPS)	LATERAL LOAD Q (KIPS)	OPB DEFL (IN.)	BRANCH MOMENT (K-IN.)	P-DELTA MOMENT (K-IN.)	OPB ROT. (DEG.)	TOTAL OPB MOMENT (K-IN.)	LATERAL LOAD R (KIPS)	IPB DEFL (IN.)	BRANCH MOMENT (K-IN.)	P-DELTA MOMENT (K-IN.)	IPB ROT. (DEG.)	TOTAL IPB MOMENT (K-IN.)
1	13.1	16.8	.0	.001	1	0	.00	1	.0	.005	1	0	.00	2
6	13.1	17.4	3.7	.084	109	1	.08	110	38.3	.963	1122	15	.94	1137
7	13.1	16.7	10.6	.153	311	2	.15	314	38.2	.964	1122	14	.94	1136
8	13.0	16.4	21.1	.303	619	4	.30	623	38.3	1.007	1123	15	.98	1138
9	13.0	16.4	29.2	.438	856	6	.43	862	38.3	1.060	1123	16	1.03	1139
10	13.1	16.8	37.2	.728	1092	11	.71	1103	38.3	1.187	1125	18	1.16	1143
11	12.9	17.1	38.5	1.091	1131	16	1.07	1147	38.4	1.288	1125	19	1.26	1145
12	13.0	16.8	37.8	1.838	1110	27	1.79	1138	38.4	1.416	1127	21	1.38	1148
13	12.9	17.0	38.4	2.811	1126	42	2.75	1168	38.4	1.509	1127	23	1.47	1150
14	12.9	16.9	39.2	3.776	1148	56	3.69	1204	38.4	1.704	1128	25	1.66	1153
15	12.9	17.2	40.6	5.376	1186	81	5.26	1267	38.5	2.089	1128	31	2.04	1160
16	12.8	17.5	17.8	5.016	521	76	4.90	597	38.5	2.098	1128	32	2.05	1160
17	13.1	17.9	.9	4.666	26	72	4.56	99	38.5	2.060	1130	32	2.01	1162

TABLE B.16 TEST IO39

LOAD STAGE	UPPER AXIAL AU (KIPS)	LOWER AXIAL AL (KIPS)	LATERAL LOAD Q (KIPS)	OPB DEFL. (IN.)	BRANCH MOMENT (K-IN.)	P-DELTA MOMENT (K-IN.)	OPB ROT. (DEG.)	TOTAL OPB MOMENT (K-IN)	LATERAL LOAD R (KIPS)	IPB DEFL. (IN.)	BRANCH MOMENT (K-IN.)	P-DELTA MOMENT (K-IN.)	IPB ROT. (DEG.)	TOTAL IPB MOMENT (K-IN.)
1	13.0	16.3	.1	.003	3	0	.00	4	.1	.004	2	0	.00	2
2	13.3	15.8	10.6	.115	309	1	.11	310	.1	.001	2	0	.00	2
5	13.4	16.7	18.9	.220	554	4	.22	558	2.7	.033	79	1	.03	80
6	13.3	16.0	19.0	.234	557	4	.23	560	20.3	.428	593	7	.42	599
7	13.2	15.9	19.1	.276	558	4	.27	562	40.0	.882	1169	14	.86	1183
8	13.2	15.9	19.1	.387	558	6	.38	564	57.4	1.562	1680	25	1.53	1705
9	13.5	16.6	19.1	.528	559	9	.52	568	66.7	2.246	1950	37	2.20	1987
10	13.2	16.9	19.4	.754	568	12	.74	580	70.9	3.138	2072	51	3.07	2123
11	13.7	16.2	19.3	1.176	564	19	1.15	584	71.9	4.728	2095	78	4.64	2173
12	13.8	16.8	19.5	1.526	570	25	1.49	595	69.9	6.305	2031	105	6.19	2136
13	13.5	17.8	19.5	1.544	571	25	1.51	596	33.9	5.683	988	94	5.57	1082
14	13.1	17.5	19.6	1.563	572	26	1.53	598	.3	5.054	8	83	4.96	90
15	13.3	17.7	1.4	1.322	41	10	1.29	51	.3	4.746	9	35	4.65	44
17	2.1	7.2	1.0	1.297	28	2	1.27	30	.3	4.684	9	7	4.59	16

Table B.17 Test IO26

LOAD STAGE	UPPER AXIAL AU (KIPS)	LOWER AXIAL AL (KIPS)	LATERAL LOAD Q (KIPS)	OPB DEFL. (IN.)	BRANCH MOMENT (K-IN.)	P-DELTA MOMENT (K-IN)	OPB ROT. (DEG.)	TOTAL OPB MOMENT (K-IN.)	LATERAL LOAD R (KIPS)	IPB DEFL. (IN.)	BRANCH MOMENT (K-IN.)	P-DELTA MOMENT (K-IN.)	IPB ROT. (DEG.)	TOTAL IPB MOMENT (K-IN.)
0	3.6	6.8	.2	.003	5	0	.00	5	.1	.000	4	0	.00	4
4	10.7	14.7	2.6	.030	77	0	.03	77	4.3	.113	126	1	.11	127
5	10.4	14.3	11.7	.154	340	2	.15	342	22.9	.503	665	6	.50	672
6	10.6	14.3	19.0	.325	552	4	.32	556	36.6	.930	1061	12	.92	1073
7	10.5	14.4	23.4	.531	678	7	.52	685	45.1	1.314	1309	16	1.30	1325
8	10.6	14.3	25.5	.744	741	9	.73	750	49.9	1.630	1445	20	1.61	1466
9	10.7	14.3	27.1	1.027	787	13	1.01	800	51.8	1.915	1501	24	1.89	1525
10	10.8	14.3	27.3	1.208	791	15	1.19	806	53.0	2.091	1536	26	2.07	1562
11	10.7	14.3	27.9	1.410	809	18	1.39	827	52.8	2.214	1529	28	2.19	1556
12	10.8	14.2	27.6	1.585	800	20	1.57	820	53.5	2.367	1550	30	2.34	1579
13	11.0	15.5	28.3	1.907	819	25	1.88	844	52.3	2.515	1514	33	2.49	1547
15	11.3	15.7	26.8	2.330	778	31	2.30	809	52.2	2.883	1513	39	2.85	1551
16	11.2	14.3	27.2	2.570	789	33	2.54	822	51.8	3.009	1500	38	2.97	1538
17	11.2	14.6	27.6	3.176	800	41	3.14	841	53.4	3.278	1547	42	3.24	1590

TABLE B.18 TEST AO44

LOAD STAGE	LATERAL LOAD Q (KIPS)	UPPER AXIAL AU (KIPS)	LOWER AXIAL AL (KIPS)	OPB DEFL. (IN.)	OPB DEFL. + INITIAL (IN.)	BRANCH MOMENT (K-IN.)	P-DELTA MOMENT (K-IN.)	OPB ROTATION (DEG.)	TOTAL OPB MOMENT (K-IN.)
1	.0	6.6	8.4	.005	.36	1	3	.00	3
3	.4	10.9	12.8	.041	.39	12	5	.04	16
4	1.0	10.8	12.8	.481	.83	29	10	.47	39
5	1.3	10.8	12.8	.763	1.11	38	13	.74	51
6	1.7	10.9	12.9	1.122	1.47	50	18	1.09	67
7	2.1	10.8	12.9	1.512	1.86	63	22	1.47	85
14	2.0	11.1	12.3	2.702	3.05	60	36	2.63	95
15	2.0	11.1	12.4	3.736	4.09	59	48	3.64	107
16	1.8	11.2	12.4	4.803	5.15	54	61	4.68	114
17	1.6	11.3	12.4	5.916	6.27	46	74	5.77	120
18	.9	11.3	12.5	7.811	8.16	28	97	7.63	124
19	.4	11.3	12.5	9.566	9.92	13	118	9.36	130
20	.2	11.2	12.5	9.579	9.93	7	118	9.37	125
21	.3	1.4	2.8	7.469	7.82	9	17	7.30	25

TABLE B.19 TEST AO45

LOAD STAGE	LATERAL LOAD Q (KIPS)	UPPER AXIAL AU (KIPS)	LOWER AXIAL AL (KIPS)	OPB DEFL. (IN.)	OPB DEFL. + INITIAL (IN.)	BRANCH MOMENT (K-IN.)	P-DELTA MOMENT (K-IN.)	OPB ROTATION (DEG.)	TOTAL OPB MOMENT (K-IN.)
1	.0	7.9	9.7	.004	.35	0	3	.00	4
2	.0	17.0	18.9	.036	.38	1	7	.04	8
3	.0	27.0	28.4	.329	.67	0	19	.32	19
6	-.3	28.9	30.2	1.463	1.81	-10	53	1.44	44
7	-.5	27.9	29.4	1.996	2.34	-13	67	1.97	54
8	-1.6	29.0	31.1	3.161	3.51	-46	105	3.12	60
11	-3.5	29.1	30.9	5.220	5.57	-102	167	5.15	65
12	-4.8	29.3	31.2	6.344	6.69	-138	203	6.27	65
13	-5.5	28.5	31.2	7.401	7.75	-158	231	7.32	73
15	.3	.2	2.2	6.111	6.46	8	8	6.03	16

TABLE B.20 TEST AI46

LOAD STAGE	LATERAL LOAD R (KIPS)	UPPER AXIAL AU (KIPS)	LOWER AXIAL AL (KIPS)	IPB DEFL. (IN.)	BRANCH MOMENT (K-IN.)	P-DELTA MOMENT (K-IN.)	IPB ROTATION (DEG.)	TOTAL IPB MOMENT (K-IN.)
0	.0	.0	.0	.000	0	0	.00	0
1	1.1	11.6	13.1	.123	31	2	.12	33
2	3.2	11.5	13.1	.604	93	7	.59	101
3	4.8	11.3	13.0	1.218	141	15	1.20	155
4	5.2	11.7	13.1	1.807	152	22	1.77	174
5	6.0	11.7	13.1	2.710	174	34	2.66	207
6	6.0	11.7	13.1	3.429	176	43	3.37	219
7	6.0	11.7	13.1	4.726	173	59	4.64	232
8	5.4	11.7	13.2	6.064	158	75	5.96	233
9	4.7	11.8	13.2	7.470	137	93	7.35	231
10	4.2	11.9	13.2	8.820	122	110	8.69	233
11	3.4	11.5	13.2	10.078	97	125	9.94	221
12	1.1	11.7	13.4	9.607	30	121	9.47	151
13	.2	11.3	13.2	9.296	6	114	9.16	119
14	.5	1.5	3.4	8.356	14	20	8.23	35

TABLE B.21 TEST AI47

LOAD STAGE	LATERAL LOAD R (KIPS)	UPPER AXIAL AU (KIPS)	LOWER AXIAL AL (KIPS)	IPB DEFL. (IN.)	IPB DEFL. + INITIAL (IN.)	BRANCH MOMENT (K-IN.)	P-DELTA MOMENT (K-IN.)	IPB ROTATION (DEG.)	TOTAL IPB MOMENT (K-IN.)
1	.0	14.0	15.5	-.025	-.2	0	-3	-.02	-3
2	.0	23.2	24.3	-.042	-.242	0	-6	-.04	-6
3	.0	29.1	30.2	-.050	-.25	0	-7	-.05	-7
4	1.2	28.7	30.1	.087	-.113	36	-3	.09	32
5	2.1	28.7	30.1	.344	.144	61	4	.34	65
6	3.2	28.7	30.1	.718	.518	93	15	.70	108
7	4.1	28.7	30.2	1.116	.916	119	27	1.10	146
12	4.5	28.7	30.2	1.708	1.508	131	44	1.68	175
13	4.7	28.7	30.2	2.328	2.128	137	63	2.29	200
14	3.4	26.4	25.6	1.745	1.545	99	40	1.71	139
15	.1	24.7	23.6	1.417	1.217	2	29	1.39	31
16	.1	3.3	4.7	1.306	1.106	2	4	1.28	6

TABLE B.22 TEST I048

LOAD STAGE	UPPER AXIAL AU (KIPS)	LOWER AXIAL AL (KIPS)	LATERAL LOAD Q (KIPS)	OPB DEFL (IN.)	BRANCH MOMENT (K-IN.)	P-DELTA MOMENT (K-IN.)	OPB ROT. (DEG.)	TOTAL OPB MOMENT (K-IN.)	LATERAL LOAD R (KIPS)	IPB DEFL (IN.)	BRANCH MOMENT (K-IN.)	P-DELTA MOMENT (K-IN.)	IPB ROT. (DEG.)	TOTAL IPB MOMENT (K-IN.)
0	.0	.0	.0	.000	0	0	.00	0	.0	0	0	0	.00	0
1	1.1	3.6	.4	.000	11	0	.00	11	.8	.104	24	0	.10	24
5	1.5	3.9	.8	.358	24	1	.35	25	2.7	.491	80	1	.48	81
6	1.6	3.9	1.3	.633	37	2	.62	39	2.7	.466	79	1	.46	80
7	1.9	3.9	1.9	1.072	56	3	1.05	59	2.7	.461	79	1	.45	80
8	2.0	3.9	2.4	1.478	69	4	1.45	73	2.7	.471	79	1	.46	81
9	2.1	4.0	2.7	1.906	79	6	1.87	84	2.7	.491	79	1	.48	80
10	2.2	4.0	3.1	2.521	90	8	2.48	98	2.7	.546	79	2	.54	81
11	2.3	4.0	3.5	3.308	103	10	3.26	113	2.5	.556	73	2	.55	74
12	2.5	4.1	3.8	4.157	111	14	4.09	125	2.5	.622	73	2	.61	75
13	2.6	4.1	4.0	5.399	117	18	5.32	135	2.8	.825	82	3	.81	85
14	2.6	4.1	4.1	6.629	118	22	6.53	140	2.8	.976	82	3	.96	86
15	2.7	4.1	4.0	8.242	114	28	8.13	142	2.9	1.13	83	4	1.11	87
16	2.7	4.1	1.7	7.455	50	25	7.35	75	3.7	1.506	107	5	1.48	112
17	2.8	4.1	.6	6.722	17	23	6.63	40	2.5	1.244	72	4	1.22	76
18	2.8	4.1	.0	6.507	1	22	6.41	24	.3	.764	8	3	.75	11

TABLE B.23 TEST I049

LOAD STAGE	UPPER AXIAL AU (KIPS)	LOWER AXIAL AL (KIPS)	LATERAL LOAD Q (KIPS)	OPB DEFL (IN.)	BRANCH MOMENT (K-IN.)	P-DELTA MOMENT (K-IN.)	OPB ROT. (DEG.)	TOTAL OPB MOMENT (K-IN.)	LATERAL LOAD R (KIPS)	IPB DEFL (IN.)	BRANCH MOMENT (K-IN.)	P-DELTA MOMENT (K-IN.)	IPB ROT. (DEG.)	TOTAL IPB MOMENT (K-IN.)
1	1.6	2.8	.1	.000	2	0	.00	2	1.2	.088	35	0	.09	35
5	1.7	2.9	.7	.169	21	0	.17	21	5.7	1.159	165	3	1.14	168
6	1.8	2.9	1.1	.471	33	1	.46	34	5.7	1.196	166	3	1.18	168
7	1.9	3.0	1.7	.844	48	2	.83	50	5.7	1.247	166	3	1.23	170
8	1.9	3.0	2.0	1.226	59	3	1.21	62	5.7	1.295	166	3	1.27	170
9	1.9	3.0	2.3	1.630	67	4	1.60	71	5.7	1.377	166	3	1.35	170
10	2.0	3.1	2.8	2.471	82	6	2.43	88	5.7	1.528	167	4	1.50	171
11	2.0	3.0	3.0	3.316	86	8	3.26	95	5.7	1.772	167	4	1.74	171
12	2.0	3.2	3.2	4.140	94	11	4.08	105	5.8	1.985	168	5	1.95	173
13	2.1	3.3	3.4	4.993	97	14	4.92	111	5.8	2.251	169	6	2.21	175
14	2.1	3.3	3.4	6.275	99	17	6.18	116	5.8	2.662	169	7	2.62	176
15	2.0	3.5	3.6	7.534	104	21	7.43	125	5.9	3.158	171	9	3.11	179
16	1.8	3.4	1.1	6.729	32	17	6.63	50	5.9	3.209	171	8	3.16	179
17	1.8	3.5	.0	5.917	0	16	5.83	16	5.9	3.214	172	9	3.16	181
18	1.6	3.5	.0	5.809	0	15	5.72	15	2.3	2.785	66	7	2.74	73
19	1.4	3.5	.0	5.692	0	14	5.61	14	.2	2.303	7	6	2.27	12

A P P E N D I X C

SPECIMEN DIMENSIONS

TABLE C.1 MOMENT ARM LENGTHS, L

SPECIMEN	L (in.)	SPECIMEN	L (in.)
A22	-	A40	-
028	58.63	042	58.31
A031	59.03	I43	58.00
A032	58.81	A044	58.19
A033	58.88	A045	58.13
AI34	58.75	AI46	58.38
AI35	58.94	AI47	58.38
AI36	58.72	I048	58.25
AI50	58.69	I049	58.25
I037	58.63		
I039	58.50	A51	58.38
I026	59.03		

TABLE C.2 GAP DIMENSIONS FOR β = 1.0 SPECIMENS

SPECIMEN	COMP. GAP* (in.)	TENS. GAP* (in.)
A21	3.63	3.56
A22	3.31	3.88
O23	4.25	3.69
O28	2.75	3.69
I24	3.31	3.50
AO31	4.25	3.63
AO32	3.25	3.50
AO33	3.50	3.50
AI34	3.75	3.63
AI35	3.56	3.94
AI36	3.00	3.13
AI50	3.50	3.25
IO37	3.81	3.50
IO38	3.44	4.13
IO39	3.50	3.75
IO26	3.75	4.25

* Comp. = OPB compression face
Tens. = OPB tension face

TABLE C.3 INITIAL ALIGNMENT (IN.)

SPECIMEN	A22	028	A031	A032	A033	AI34	AI35	AI36	AI50	I037	I038	I039	I026	A51
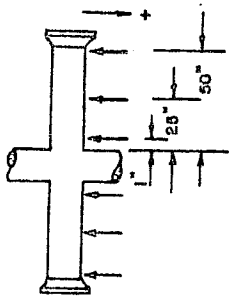	0.05	0.05	-0.15	-0.14	-0.14	-0.15	0.07	0.12	-0.05	-0.15	0.03	-0.05	-0.07	-0.08
	0.07	0.03	-0.10	-0.11	-0.09	-0.13	-0.07	0.09	-0.05	-0.10	-0.02	-0.06	-0.07	-0.04
	0.08	0.02	-0.05	-0.05	-0.02	-0.05	-0.11	0.06	-0.09	-0.05	-0.10	-0.11	-0.03	0.00
	0.15	0.04	0.00	0.06	-0.01	0.00	0.00	0.04	-0.10	-0.05	-0.09	-0.04	0.07	-0.03
	0.07	0.02	0.02	0.02	0.01	0.00	0.00	0.05	-0.02	-0.02	-0.02	-0.02	0.02	-0.03
	0.00	0.00	0.00	0.00	0.00	0.00	0.00	0.00	0.00	0.00	0.00	0.00	0.00	0.00
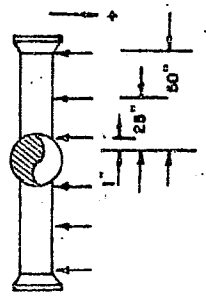	-0.03	0.08	-0.10	-0.03	-0.14	-0.12	-0.11	0.08	0.05	0.03	0.07	0.00	0.03	-0.04
	0.03	0.18	-0.07	0.03	-0.10	-0.17	-0.08	0.08	0.05	0.03	0.10	0.07	0.03	0.15
	0.13	0.35	-0.10	-0.01	-0.09	-0.27	-0.11	0.05	0.13	-0.09	0.15	0.06	0.08	-.—
	0.23	0.34	-0.11	-0.05	-0.05	-0.27	-0.03	0.06	0.19	-0.12	0.00	-0.06	-0.04	0.30
	0.08	0.13	-0.02	-0.01	-0.01	-0.12	-0.01	0.05	0.08	-0.12	0.00	-0.06	-0.04	0.10
	0.00	0.00	0.00	0.00	0.00	0.00	0.00	0.00	0.00	0.00	0.00	0.00	0.00	0.00

TABLE C.3 INITIAL ALIGNMENT (IN.) (CONTINUED)

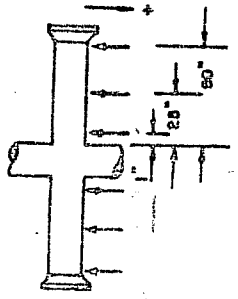

SPECIMEN	A40	O42	I43	AO44	AO45	AI46	AI47	IO48	IO49
	0.10	0.00	0.05	0.05	0.00	0.00	0.00	0.00	0.06
	0.10	-0.05	0.00	0.05	0.00	0.01	-0.03	-0.05	0.12
	0.07	-0.05	-0.05	0.00	-0.05	-0.05	-0.20	-0.05	0.18
	0.00	-0.10	0.06	-0.05	0.00	-0.06	-0.23	0.00	0.10
	-0.02	-0.05	0.02	0.00	0.05	-0.05	0.15	0.00	0.08
	0.00	0.00	0.00	0.00	0.00	0.00	0.00	0.00	0.00

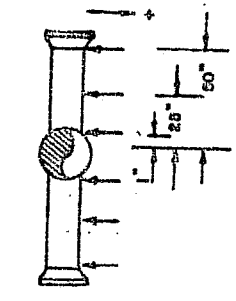

	0.00	0.00	-0.05	0.00	0.00	-0.12	-0.02	-0.00	-0.04
	0.00	0.10	-0.07	0.05	0.10	-0.10	-0.02	0.00	0.02
	-.—	-.—	-.—	-.—	-.—	-.—	-.—	-.—	-.—
	-0.15	0.30	-0.04	0.25	0.21	-0.10	-0.02	0.05	0.28
	0.03	0.15	-0.01	0.08	0.13	-0.06	-0.02	0.01	0.16
	0.00	0.00	0.00	0.00	0.00	0.00	0.00	0.00	0.00

A P P E N D I X D

DERIVATION OF RELATIONSHIP BETWEEN Φ AND T

The basic limit state design criterion can be written as follows:

$$\phi R_n \geq \sum \gamma Q_m \qquad (D.1)$$

where ϕ is the "resistance factor", R_n is the "nominal resistance", γ is the "load factor", and Q_m is the "mean load effect" for a certain limit state.

In order to give an indication of how variations in ϕ will effect the amount of material in the joint, the limit state analysis can be extended to compare the relative chord thicknesses required by each equation for a specific type of joint for a given level of safety. In an interaction analysis the right side of the equation D.1 is represented by the length of the ray from the origin to the point on the interaction diagram corresponding to the design load condition in Fig. 5.1. Similarly the nominal resistance of the joint can also be given by the length of the ray from the origin to the point on the curve in the interaction diagram given by the interaction equation. Thus Eq. D.1 can be written in the following form:

$$\phi[(P/P_u)^2 + (M/M_u)^2_{IPB} + (M/M_u)^2_{OPB}]_R^{1/2} \geq \gamma[(P/P_u)^2 + (M/M_u)^2_{IPB} + (M/M_u)^2_{OPB}]_Q^{1/2} \qquad (D.2)$$

In order for the design point and the point given by the interaction equation to be along the same ray, the ratios of axial and the two bending terms to each other must be the same. Therefore, each term can be taken out of the radical. For example, if the axial term is removed from the radical, Eq. D.2 can be written as shown below:

$$\phi(P/P_u)_R[1 = e^2_{IPB} + e^2_{OPB}]^{1/2} \geq \gamma(P/P_u)_Q \ [1 + e^2_{IPB} + e^2_{OPB}]^{1/2} \quad (D.3)$$

$$e^2_{IPB} = (M/M_u)^2_{IPB}(P/P_u)^2)$$

$$e^2_{OPB} = (M/M_u)^2_{OPB}(P/P_u)^2)$$

Eq. D.3 can then be simplified to:

$$\phi(P/P_u)_R \geq \gamma(P/P_u)_Q \quad (D.4)$$

In Eq. D.4, ϕ is calculated using Eqs. 5.6-5.8 for each interaction. The ratio (P/P_u) is given by the interaction equation based on e^2_{IPB} and e^2_{OPB}, and P_Q is given from the structural analysis; thus, the joint must be designed for a P_u to yield a $(P/P_u)_Q$ which satisfies Eq. D.4. So the relation between P_u (and ϕ can be written as:)

$$\phi(P/P_u)_R(P_Q \geq \gamma(1/P_{uD}) \quad (D.5)$$

For a given joint type, β, D and F_y; P_u is a function of the square of the chord wall thickness. Thus, a relation between ϕ and T is given by the following:

$$\phi(P/P_u)/(P_Q) \geq \gamma(1/CT^2) \quad (D.6)$$

where C is a constant. Because the limit states analyses use mean equation where the interaction equations are mostly lower

bound equations, the error in the prediction of $(P/P_u)_R$ will be accounted for by dividing ϕ by P_m to create an effective ϕ, ϕ_{EFF}. When the error in the prediction of $(P/P_u)_R$ is accounted for, then $(P/P_U)/(P_Q)$ becomes a constant for a given joint and loading. In addition, for a given loading the load factor γ will be a constant. Therefore, Eq. D.6 can be simplified to the following:

$$\phi_{EFF}(K) \geq (1/T^2) \qquad (D.7)$$

where K is a constant. Since the ratios of axial and the two bending terms to each other must be the same for both sides of Eq. D.2, and the ultimate moments are also a function of T^2, Eq. D.7 will also hold for the moment terms i the interaction. It should be emphasized that Eq. D.7 is only intended to given an indication of the variation of T with the interaction equations, and does not represent a method to calculate T for use in design.

APPENDIX E

TABLE E.1 $\beta = 0.35$ and 1.00 tensile coupon results

A - 1 Yield Stress = 48.9 ksi Yield Strain = 0.00169 (in./in.)		A - 2 Yield Stress = 48.7 ksi Yield Strain = 0.00168 (in./in.)		B - 1 Yield Stress = 49 ksi Yield Strain = 0.00168 (in./in.)		B - 2 Yield Stress = 48.7 ksi Yield Strain = 0.00169 (in./in.)	
Stress (ksi)	Plastic Strain (in./in.)	Stress (ksi)	Plastic Strain (in./in.)	Stress (ksi)	Plastic Strain (in./in.)	Stress (ksi)	Plastic Strain (in./in.)
51.5	0.0007	51.5	0.0063	51.1	0.0047	50.0	0.0061
53.6	0.0107	53.6	0.0165	52.2	0.0089	51.1	0.0139
55.8	0.0169	53.6	0.0245	54.3	0.0207	53.2	0.0265
57.9	0.0389	55.8	0.0367	55.4	0.0263	55.3	0.0381
60.1	0.0997	60.1	0.0547	57.6	0.0385	57.4	0.0573
62.2	0.1327	62.2	0.0851	60.9	0.0567	60.6	0.0877
64.2	0.48	64.7	0.46	63.0	0.0867	64.3	0.46
				64.8	0.44		

TABLE E.2 $\beta = 0.67$ tensile coupon results

B Yield Stress = 46.4 ksi Yield Strain = 0.0011 (in./in.)		D Yield Stress = 46.8 ksi Yield Strain = 0.0019 (in./in.)	
Stress (ksi)	Plastic Strain (in./in.)	Stress (ksi)	Plastic Strain (in./in.)
46.8	0.002	47.7	0.0019
48.3	0.004	48.9	0.0041
49.7	0.0074	49.5	0.0068
55.4	0.0243	55.3	0.0238
68.5	0.41	67.9	0.44

TABLE E.3 $\beta = 0.35$ tension branch tensile coupon results

7 Yield Stress = 37.9 ksi Yield Strain = 0.0011 (in./in.)		8 Yield Stress = 41.8 ksi Yield Strain = 0.0010 (in./in.)	
Stress (ksi)	Plastic Strain (in./in.)	Stress (ksi)	Plastic Strain (in./in.)
39.8	0.0033	43.9	0.0032
44.2	0.0092	47.4	0.0092
49.4	0.0172	52.1	0.0169
53.1	0.0252	55.7	0.025
61.2	0.0488	64.1	0.528
64.8	0.0812	68.3	0.08
73.5	0.456	72.1	0.4189

APPENDIX F

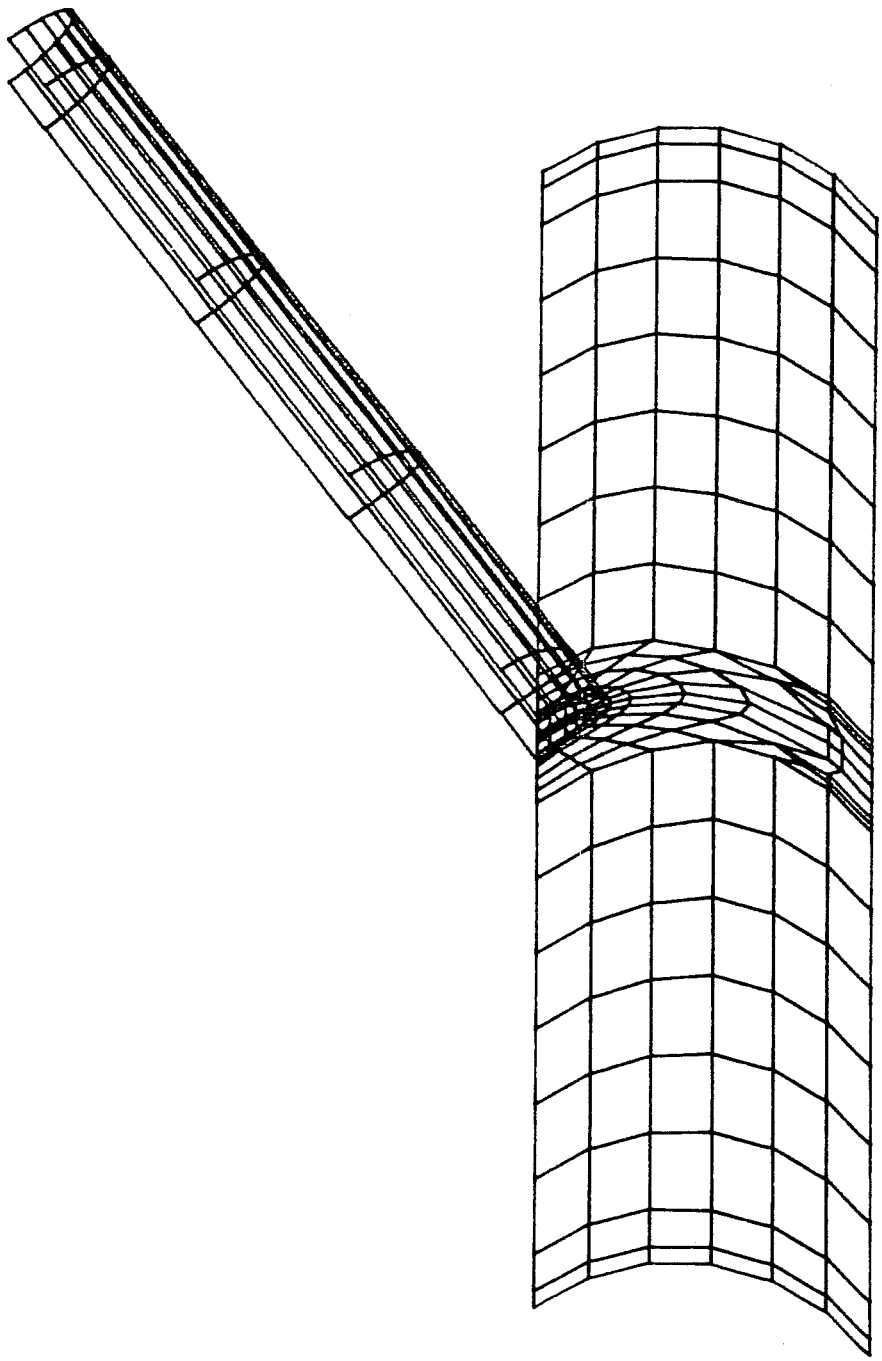

Fig. F.1 $\beta = 0.35$ IPB Mesh - 1/4 specimen.

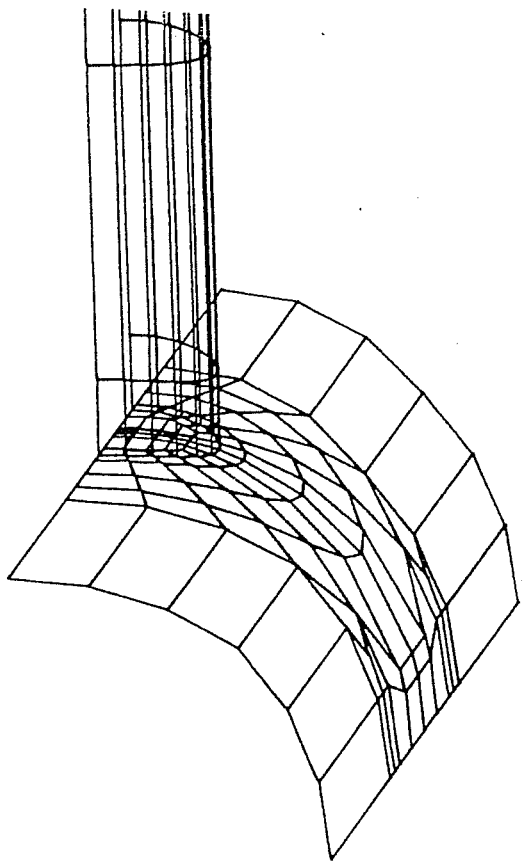

Fig. F.2 $\beta = 0.35$ IPB Mesh - Joint Region

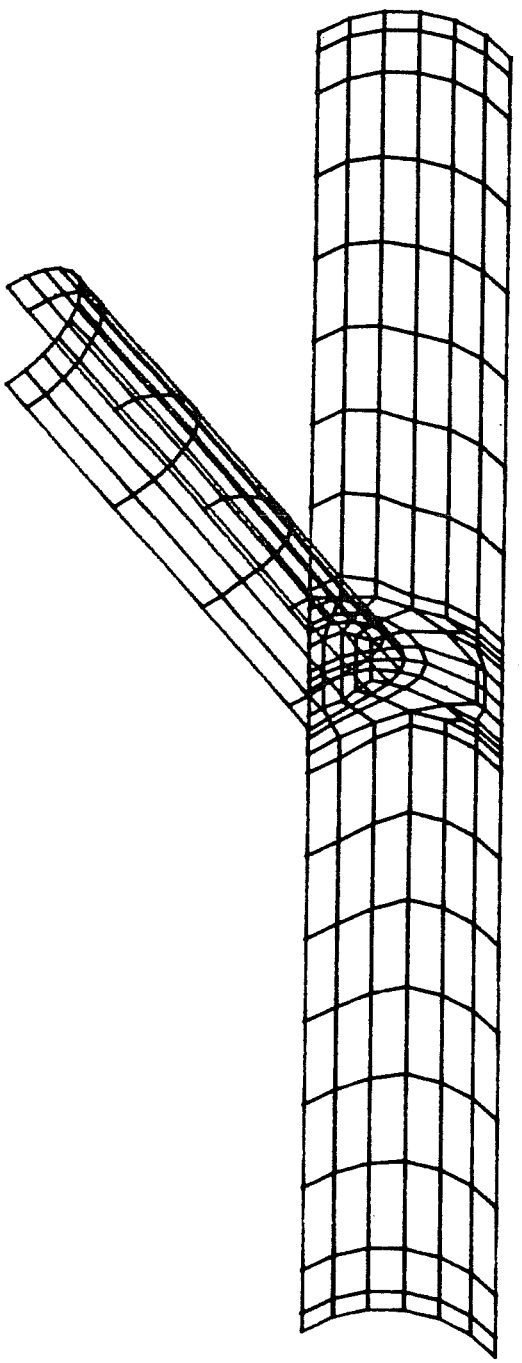

Fig. F.3 β = 0.67 IPB Mesh - 1/4 Specimen

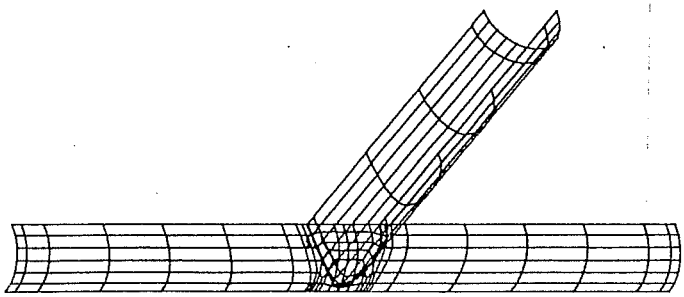

Fig. F.4 β = 1.00 IPB Mesh - 1/4 Specimen

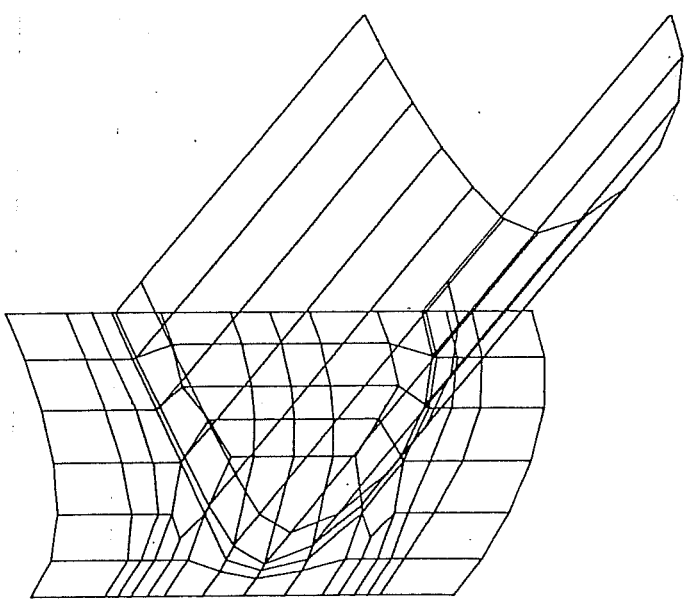

Fig. F.5 β = 1.00 IPB Mesh - Joint Region

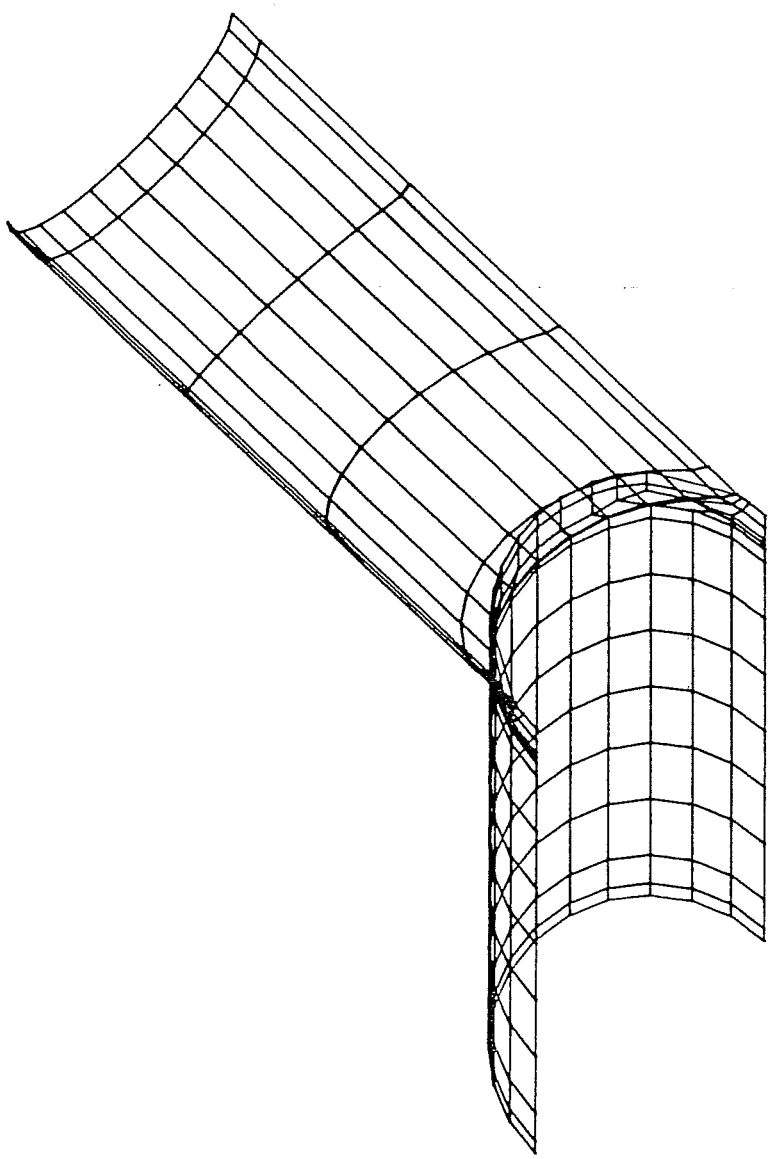

Fig. F.7 β = 0.35 OPB Mesh - 1/4 Specimen

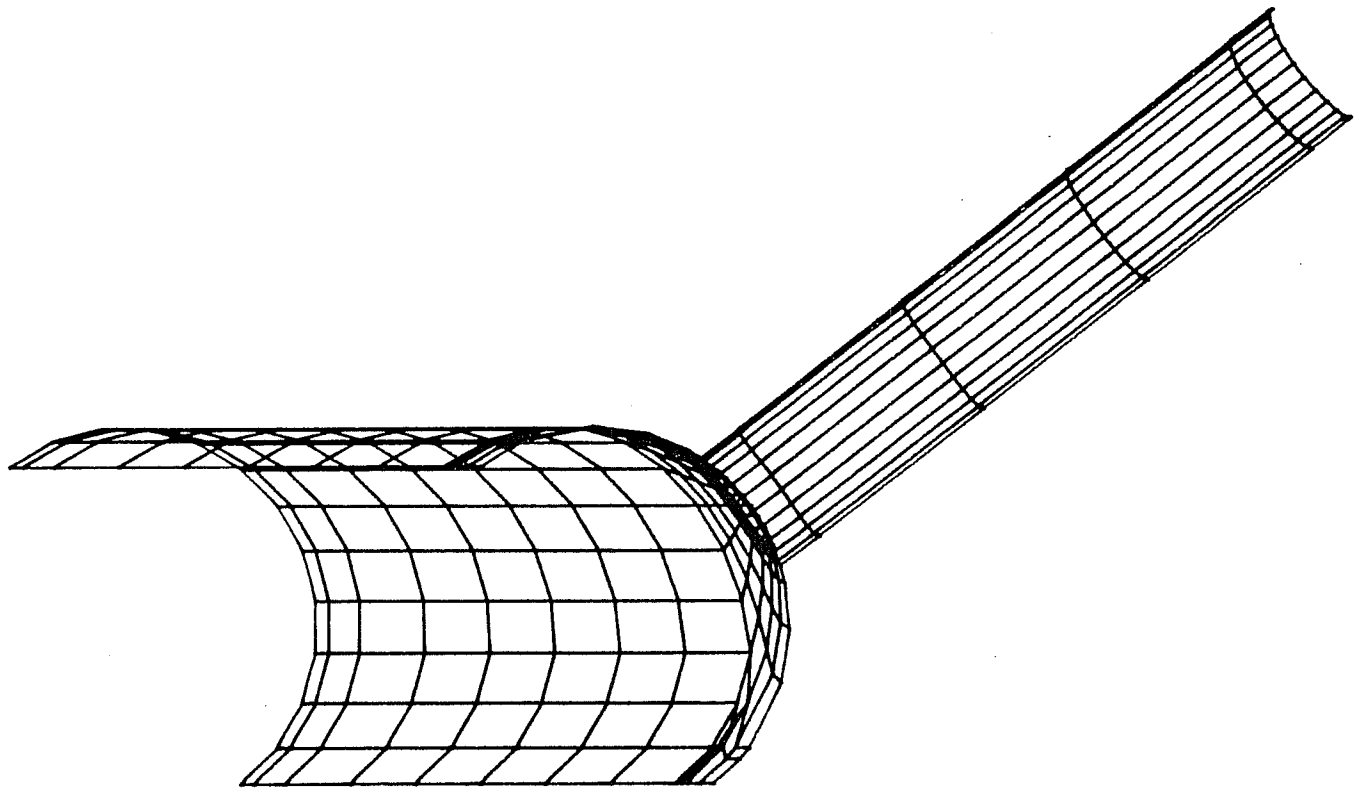

Fig. F.7 β = 0.35 OPB Mesh - 1/4 Specimen

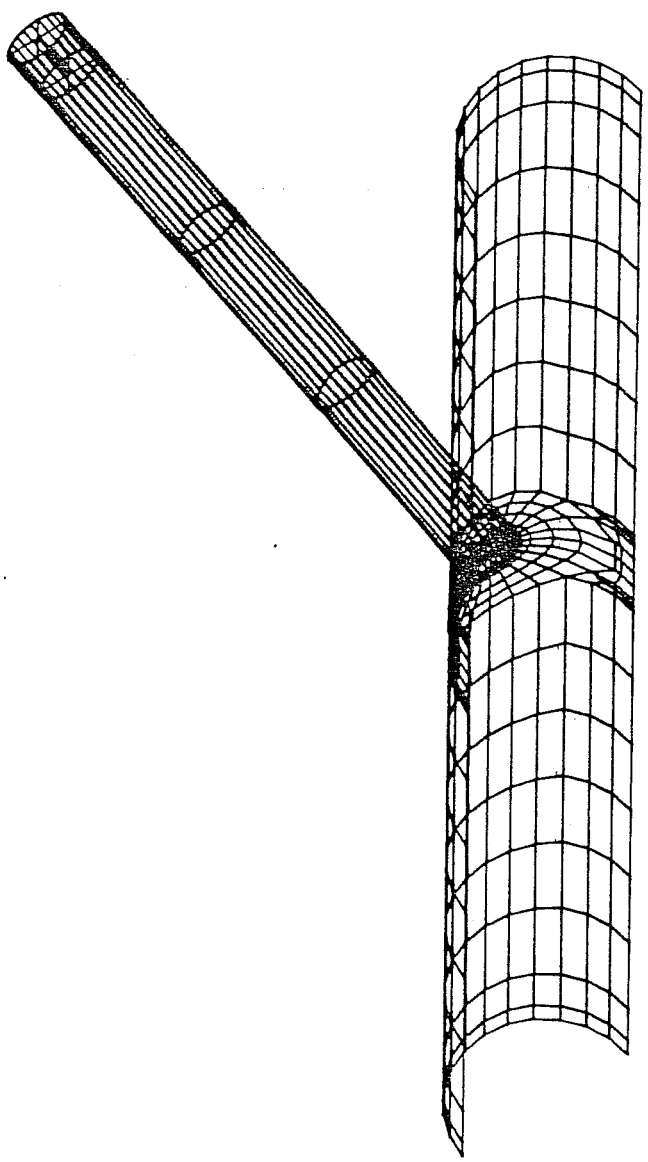

Fig. F.8 β = 0.35 IO Mesh - 1/2 Specimen

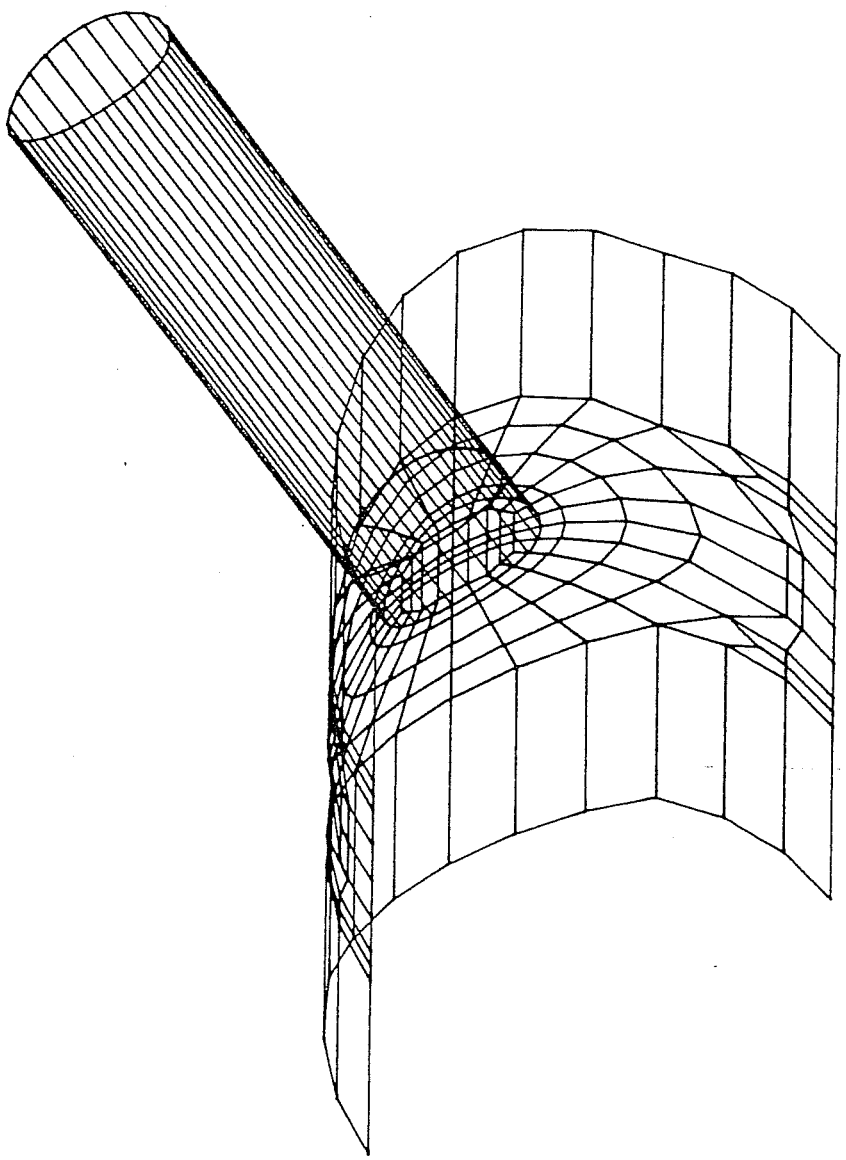

Fig. F.9 β = 0.35 IO Mesh - Joint Region

A P P E N D I X G

Table G.1 FEM "coarse" mesh result $\beta = 0.67$ compression

Axial Load (kips)	Axial Def. (in.)
00.0	0.000
39.1	0.084
61.2	0.163
78.2	0.282
89.5	0.459
92.3	0.634
92.3	0.809
92.3	0.811

Table G.2 FEM "fine" mesh result $\beta = 0.67$ compression

Axial Load (kips)	Axial Def. (in.)
00.0	0.000
30.3	0.067
49.5	0.133
62.0	0.198
70.4	0.263
78.2	0.359
80.3	0.396
81.7	0.432
83.2	0.485
84.8	0.566
85.5	0.687
85.5	0.808
85.5	0.810

Table G.3 FEM results $\beta = 0.35$ axial compression

Axial Load (kips)	Axial Def. (in.)
00.0	0.000
30.6	0.207
46.5	0.411
50.3	0.611
49.0	0.811

Table G.4 FEM Results Test A21

Axial Load (kips)	Axial Def. (in.)	OPB Def. (in.)
0	0.000	0.000
162	0.073	0.005
166	0.08	0.008
169	0.087	0.011
172	0.097	0.025
173	0.100	0.030
172	0.100	0.030
172	0.101	0.035
173	0.102	0.039
173	0.103	0.044
173	0.105	0.051

Table G.5 FEM results Test A22

Axial Load (kips)	Axial Def. (in.)	OPB Def. (in.)
0	0.000	0.000
160	0.073	0.039
166	0.091	0.093
166	0.109	0.160
166	0.110	0.164
166	0.111	0.168
165	0.113	0.174
165	0.115	0.184
165	0.119	0.198
165	0.120	0.204
165	0.122	0.209

Table G.6 FEM results $\beta = 0.35$ axial tension

Axial Load (kips)	Axial Def. (in.)
00.0	0.000
37.3	0.076
66.7	0.150
93.2	0.257
107.9	0.362
111.1	0.388
114.0	0.414
118.1	0.453
123.9	0.511
128.9	0.569
133.5	0.627
137.6	0.685
138.5	0.700
139.5	0.714
140.8	0.736
142.6	0.768
145.3	0.817
146.1	0.833

Table G.7 FEM results $\beta = 1.00$ axial tension

Axial Load (kips)	Axial Def. (in.)
000.0	0.000
285.7	0.118
346.7	0.167
390.2	0.215
412.3	0.246
433.4	0.276
441.2	0.287
448.5	0.299
459.4	0.315
475.4	0.341
496.5	0.379
517.0	0.417
536.3	0.454
555.2	0.492
573.1	0.530
577.1	0.538

Table G.8 FEM results $\beta = 0.35$ IPB

Branch Moment (kip-in.)	P - Δ Moment (kip-in.)	Total Moment (kip-in.)	Rotation (Deg.)
0	0.0	0	0.0
172	7.6	180	1.5
210	15.3	225	3.0
219	22.9	242	4.5
220	30.5	250	6.0

Table G.9 FEM "coarse" mesh result $\beta = 0.67$ IPB

Branch Moment (kip-in.)	P - Δ Moment (kip-in.)	Total Moment (kip-in.)	Rotation (Deg.)
0	0.0	0	0.00
861	16.8	878	1.50
935	21.0	956	1.87
990	25.2	1015	2.25
1049	31.1	1079	2.81
1118	40.8	1159	3.66
1174	50.3	1224	4.49
1219	59.8	1279	5.34
1247	67.1	1314	6.00

Table G.10 FEM "fine" mesh results $\beta = 0.67$ IPB

Branch Moment (kip-in.)	P - Δ Moment (kip-in.)	Total Moment (kip-in.)	Rotation (Deg.)
0	0.0	0	0.0
764	15.6	780	1.50
866	24.2	890	2.33
924	32.8	957	3.16
962	41.4	1003	3.98
989	50.0	1039	4.82
1007	58.6	1066	5.65
1012	62.2	1074	6.00

Table G.11 FEM Results $\beta = 0.67$, γ - 15 IPB

Branch Moment (kip-in.)	P - Δ Moment (kip-in.)	Total Moment (kip-in.)	Rotation (Deg.)
0	0.0	0	0.00
510	3.9	514	0.38
968	7.8	976	0.75
1391	13.6	1404	1.31
1592	19.4	1611	1.87
1718	25.3	1743	2.43
1815	31.0	1846	2.99
1895	36.9	1932	3.56

Table G.12 FEM Results $\beta = 0.67$ IPB - 25% Axial

Branch Moment (kip-in.)	P - Δ Moment (kip-in.)	Total Moment (kip-in.)	Rotation (Deg.)
0	0.0	0	0.00
828	35.0	863	1.50
894	43.7	937	1.87
941	52.4	994	2.25
990	65.6	1056	2.81
1028	78.7	1107	3.37
1059	91.8	1151	3.93
1084	104.9	1189	4.50

Table G.13 FEM Results $\beta = 0.67$ IPB - 50% Axial

Branch Moment (kip-in.)	P - Δ Moment (kip-in.)	Total Moment (kip-in.)	Rotation (Deg.)
0	0.0	0	0.00
728	70.0	798	1.50
781	87.5	868	1.87
813	105.0	918	2.25
843	131.3	974	2.81
856	157.5	1013	3.37
858	183.7	1042	3.93
853	209.9	1063	4.50
837	236.2	1073	5.06

Table G.14 FEM results β = 0.67 IPB-50% Axial-Proportional

Branch Moment (kip-in.)	Axial Load (kips)	P - Δ Moment (kip-in.)	Total Moment (kip-in.)	Rotation (Deg.)
0	0.0	0.0	0	0.00
860	11.5	17.5	877	1.50
924	14.4	27.3	951	1.87
966	17.3	39.3	1005	2.25
998	21.6	61.5	1059	2.81
1010	26.0	88.6	1098	2.27
1005	30.3	120.5	1126	3.93
983	34.6	157.3	1140	4.50
941	38.9	199.1	1140	5.06

Table G.15 FEM results β = 0.67 IPB - 75% Axial

Branch Moment (kip-in.)	P - Δ Moment (kip-in.)	Total Moment (kip-in.)	Rotation (Deg.)
0	0.0	0	0.00
238	26.3	264	0.38
407	53.0	460	0.76
532	92.3	624	1.32
576	131.6	708	1.88
581	171.0	751	2.44
556	210.0	766	3.00
506	249.6	756	3.56

Table G.16 FEM results = 0.35 OPB

Branch Moment (kip-in.)	P - Δ Moment (kip-in.)	Total Moment (kip-in.)	Rotation (Deg.)
0	0.0	0	0.00
56	6.5	63	1.28
81	13.1	94	2.57
91	19.6	111	3.86
94	26.2	120	5.14
93	32.7	126	6.43
91	39.2	130	7.73

Table G.17 FEM results β = 1.00 IPB

Branch Moment (kip-in.)	P - Δ Moment (kip-in.)	Total Moment (kip-in.)	Rotation (Deg.)
0	0.0	0	0.00
842	7.0	861	0.37
1451	14.1	1465	0.75
1892	24.7	1917	1.31
1978	28.6	2006	1.52
2040	32.6	2073	1.73
2118	38.5	2157	2.05
2198	47.4	2246	2.52
2294	60.8	2355	3.23
2323	68.9	2392	3.66
2349	76.9	2426	4.09

Table G.18 FEM results $\beta = 0.35$ OPB-38% IPB

IPB Branch Moment (kip-in.)	IPB P - Δ Moment (kip-in.)	Total IPB Moment (kip-in.)	IPB Rotation (Deg.)	OPB Branch Moment (kip-in.)	OPB P - Δ Moment (kip-in.)	Total OPB Moment (kip-in.)	OPB Rotation (Deg.)
0	0.0	0	0.00	0	0	0	0
44	1.1	45	0.27	0	0	0	0
88	2.2	90	0.54	0	0	0	0
87	2.9	90	0.71	68	8	76	1.93
87	4.2	91	1.01	87	16	103	3.86
85	4.6	90	1.10	89	18	107	4.29
88	5.0	93	1.20	90	20	110	4.82
88	5.4	93	1.29	90	22	112	5.31
88	5.8	93	1.39	89	24	113	5.79
88	6.2	94	1.49	89	26	115	6.27
88	6.6	94	1.60	88	28	116	6.76
88	7.1	95	1.71	87	30	116	7.24
89	7.6	96	1.82	85	32	117	7.73

Table G.18 FEM Results $\beta = 0.35$ $\gamma = 15$ IPB

Branch Moment (kip-in.)	P-Δ Moment (kip-in.)	Total Moment (kip-in.)	Rotation (Deg.)
0	0.0	0	0.00
402	9.8	412	1.93
489	19.6	493	3.86
523	29.4	552	5.79
529	31.9	561	6.27
535	34.3	569	6.76
541	36.8	577	7.24
546	39.2	585	7.73

Table G.19 FEM Results $\beta = 1.00$, $\gamma = 15$ IPB

Branch Moment (kip-in.)	P-Δ Moment (kip-in.)	Total Moment (kip-in.)	Rotation (kip-in.)
0	0.0	0	0.00
1454	7.1	1461	0.38
2696	14.1	2710	0.75
3584	24.7	3609	1.31
3771	28.6	3800	1.52
3919	32.6	3951	1.73
4098	38.5	4137	2.05
4309	47.4	4357	2.52
4473	56.4	4529	3.00
4615	65.3	4680	3.47

REFERENCES

1. American Petroleum Institute, Recommended Practice for Planning, Designing, and Constructing Fixed Offshore Platforms, RP 2A, 15th Edition, October 22, 1984.

2. American Society for Testing Materials, Standard Methods and Definitions for Mechanical Testing of Steel Products, ASTM A370-71.

3. Beale, L. A., and Toprac, A. A., "Analysis of In-Plane T, Y, and K Welded Tubular Connections," Welding Research Council Bulletin, No. 125, Oct. 1967.

4. Beedle, L.S., and Tall, L., "Basic Column Strength," Journal of the Structural Division, ASCE, Vol. 86, ST7, July 1960.

5. Bijlaard,P. P.,"Stresses from Local Loadings in Cylindrical Pressure Vessels," Transactions of the ASME, Journal of Applied Mechanics, Vol. 22, August 1955.

6. Billington, C. J., Lalani, M., Tebbet, I.E.,"Background to new Formulae for the Ultimate Limit State of Tubular Joints," Proceedings, Offshore Technology Conference, Paper OTC #4189, Houston, Texas, May 1982.

7. Boone, T. J., Yura, J. A., and Hoadley, Peter W., "Ultimate Strength of Tubular Joints: Chord Stress Effects," Proceedings Offshore Technical Conference, Vol. 16, Paper OTC #4828, May 1984.

8. Fisher, J.W., Galambos, T.V., Kulak, G.K., and Ravinda, M.K., "Load and Resistance Design Criterion for Connectors," Journal of the Structural Division, ASCE, Vol. 104, No. ST9, Sept.1978.

9. Galambos, T.V., and Ravinda, M.K.,"Load and Resistance Factor Design for Steel," Journal of the Structural Division, ASCE, Vol. 104, No. ST9, Sept.1978.

10. Galambos, T.V., Ravinda, M.K., "Tentative Load and Resistance Factor Design Criteria for Steel Buildings," Research Report No.18, Structural Division, Civil and Environmental Engineering Department, School of Engineering and Applied Science, Washington University, Sept. 1973.

11. Galambos, T.V., and Ravinda, M.K.,"Properties of Steel for Use in LRFD," Journal of the Structural Division, ASCE, Vol. 104, No. ST9, Sept.1978.

12. Graff,W.J., et al,"Review of Design Considerations for Tubular Joints," ASCE International Convention, New York, May 1981.

13. Hibbit, Karlsson, and Sorenson, Inc.," ABAQUS Users Manual," Providence, R.I.

14. Hoadley, P. W., and Yura, J. A., "Ultimate Strength of Tubular Joints Subjected to Combined Loads," Proceedings, Offshore Technology Conference, Paper OTC #4854, Houston, Texas, May 6-9, 1985.

15. Hoadley, P. W., and Yura, J. A., "Ultimate Strength of Tubular joints Subjected to Combined Loads," Ph.D. Dissertation, Dept. of Civil Engineering, University of Texas at Austin,1983.

16. Holsgrove, S. C., Stamenkovic, A.,"Ultimate Load Analysis of Tubular Joints Using The Finite Element Method," Kingston Polytechnic, School of Civil Engineering, July 1984.

17. International Institute of Welding,"Design Recommendations for Hollow Section Joints in Predominatly Statically Loaded Joints," IIW Doc. XV-491-82, Annual Assembly, Portugal,1981.

18. Kurobane, Y., Makino, Y., and Ochi, K.,"Ultimate Resistance of Unstiffened Tubular Joints," Journal of Structural Engineering, ASCE, Vol.110., No. 2., Feb.1984.

19. Lyons, L. P. R.,"LUSAS User's Manual", Finite Element Analysis Ltd., London, 1984

20. Mindlin, R. D.,"Influence of Rotary Inertia and Shear on Flexural Motions of Isotropic, Elastic Plates",Journal of Applied Mechanics, Vol. 18, 1951.

21. MacGregor, J.G.,"Safety and Limit States Design for Reinforced Concrete," Canadian Journal of Civil Engineering, Vol.3, 1976

22. Marshall, P. W.," Basic Considerations for Tubular Joint Design in Offshore Construction," Welding Research Council Bulletin, No. 193, April 1974.

23. Marshall, P.W., Discussion on "Load Interaction in T-Joints of Steel Circular Hollow Sections," Journal of Structural Engineering, ASCE, Vol. 110, No. 11, Nov. 1984.

24. Marshall,P.W.,"Connections for Welded Tubular Structures," Welding of Tubular Structures, Proceedings of the Second International Conference, International Institute of Welding, Pergamon Press, July 1984.

25. Pan, Chan-Ping,"Nonlinear Finite Element Analysis of Tubular Joints," Ph.D. Dissertation, Dept. of Civil Engineering, University of Texas, May 1986.

26. Pan,P.B., et al,"Ultimate Strength of Tubular Joints", Proceedings, Offshore Technology Conference, Paper OTC #2644, Houston, Texas, 1976.

27. Reber,J.B.,"Ultimate Strength Design for Tubular Joints", Proceedings, Offshore Technology Conference, Paper OTC #1664, Houston, Texas, 1972.

28. Sanders, D. H., and Yura, J. A.,"Ultimate Strength and Behavior of Double-Tee Tubular Joints in Tension," Phil M. Ferguson Structural Engineering Laboratory Report 86-2, University of Texas at Austin, 1986.

29. Stamenkovic, A., and Sparrow, K. D.,"Load Interaction in T-Joints of Steel Circular Hollow Sections," Journal of Structural Engineering, ASCE, Vol. 109, No. 9, Sept. 1983.

30. Stol, H.G.A., Puthli, R.S., and Bijlaard, F.S.K., "Experimental Research on Tubular T-Joints Under Proportionally Applied Combined Static Loading," Conference on the Behaviour of Offshore Structures, (BOSS), Delft, The Netherlands, 1-5 July 1985.

31. Stol, H.G.A., Puthli, R.S., and Bijlaard, F.S.K.,"Static Strength of Welded Tubular T-Joints Under Combined Loading",TNO-IBBC report No. B-84-561/63.6.0829, Parts I, II, and III, 1984.

32. Swensson, K. D., et al,"Stress Concentration Factors in Double-Tee Tubular Joints," Phil M. Ferguson Structural Engineering Laboratory Report 86-1, Jan. 1986.

33. Tall, Lambert, et al, Structural Steel Design, John Wiley and Sons, 1974.

34. Underwater Engineering Group, Design of Tubular Joints for Offshore Structures Vol. 2, Page Bros (Norwich) Limited, 1985.

35. Wardiner, J., Hollow Section Joints, Delft University Press, 1982

36. Weinstein, R. M., and Yura, J. A., "The Effect of Chord Stresses on the Static Strength of DT Tubular Connections," Phil M. Ferguson Structural Engineering Laboratory Report 85-1, Jan. 1985.

37. Weinstein, R. M., and Yura, J. A., "The Effect of Chord Stresses on the Static Strength of DT Tubular Connections," Proceedings, Offshore Technology Conference, Paper OTC #5135, Houston, Texas, May 5-8, 1986.

38. Yarmici, E., Yura, J.A.,and Lu, L.W., "Techniques for Testing Structures Permitted to Sway," Experimental Mechanics, Journal of the Society for Experimental Stress Analysis, Vol. 7, No. 8, August 1967

39. Yura, J. A., " Connections with Round Tubes," ASCE Structural Engineering Congress 1985, Symposium - Hollow Structural Sections in Building Construction, Chicago, Ill., Sept. 17-18, 1985.

40. Yura, J.A., Zettlemoyer, N., and Edwards, I.F., "Ultimate Capacity Equations for Tubular Joints," Offshore Technology Conference Proceedings, Vol. 1, No. 3690, 1980.